

Complexity

Advanced Robust Control and Dynamics Modeling for Complex Industrial Systems

Lead Guest Editor: Wonhee Kim

Guest Editors: Kiyong Oh and Minchul Shin





**Advanced Robust Control and Dynamics
Modeling for Complex Industrial Systems**

Complexity

**Advanced Robust Control and Dynamics
Modeling for Complex Industrial
Systems**

Lead Guest Editor: Wonhee Kim


Guest Editors: Kiyong Oh and Minchul Shin



Copyright © 2020 Hindawi Limited. All rights reserved.

This is a special issue published in "Complexity." All articles are open access articles distributed under the Creative Commons Attribution License, which permits unrestricted use, distribution, and reproduction in any medium, provided the original work is properly cited.

Chief Editor

Hiroki Sayama , USA

Associate Editors

Albert Diaz-Guilera , Spain
Carlos Gershenson , Mexico
Sergio Gómez , Spain
Sing Kiong Nguang , New Zealand
Yongping Pan , Singapore
Dimitrios Stamovlasis , Greece
Christos Volos , Greece
Yong Xu , China
Xinggang Yan , United Kingdom

Academic Editors

Andrew Adamatzky, United Kingdom
Marcus Aguiar , Brazil
Tarek Ahmed-Ali, France
Maia Angelova , Australia
David Arroyo, Spain
Tomaso Aste , United Kingdom
Shonak Bansal , India
George Bassel, United Kingdom
Mohamed Boutayeb, France
Dirk Brockmann, Germany
Seth Bullock, United Kingdom
Diyi Chen , China
Alan Dorin , Australia
Guilherme Ferraz de Arruda , Italy
Harish Garg , India
Sarangapani Jagannathan , USA
Mahdi Jalili, Australia
Jeffrey H. Johnson, United Kingdom
Jurgen Kurths, Germany
C. H. Lai , Singapore
Fredrik Liljeros, Sweden
Naoki Masuda, USA
Jose F. Mendes , Portugal
Christopher P. Monterola, Philippines
Marcin Mrugalski , Poland
Vincenzo Nicosia, United Kingdom
Nicola Perra , United Kingdom
Andrea Rapisarda, Italy
Céline Rozenblat, Switzerland
M. San Miguel, Spain
Enzo Pasquale Scilingo , Italy
Ana Teixeira de Melo, Portugal

Shahadat Uddin , Australia
Jose C. Valverde , Spain
Massimiliano Zanin , Spain


Contents

Dynamic Characteristics of an Offshore Wind Turbine with Tripod Suction Buckets via Full-Scale Testing

Yun-Ho Seo, Moo Sung Ryu, and Ki-Yong Oh 




Research Article (16 pages), Article ID 3079308, Volume 2020 (2020)

Investigation of Unmeasured Parameters Estimation for Distributed Control Systems

Hao Wang , Shousheng Xie, Weixuan Wang, Lei Wang, and Jingbo Peng

Research Article (15 pages), Article ID 7518039, Volume 2020 (2020)

Research on Traffic Congestion Based on System Dynamics: The Case of Chongqing, China

Yingsheng Su , Xin Liu , and Xuejun Li 



Research Article (13 pages), Article ID 6123896, Volume 2020 (2020)

Optimal Fault Tolerant Control of Large-Scale Wind Turbines in the Case of the Pitch Actuator Partial Faults

Younes Ait El Maati  and Lhoussain El Bahir 

Research Article (17 pages), Article ID 6210407, Volume 2020 (2020)

Dynamic Modeling and Adaptive Robust Synchronous Control of Parallel Robotic Manipulator for Industrial Application

Haiqiang Zhang , Hairong Fang , Qi Zou, and Dan Zhang

Research Article (23 pages), Article ID 5640246, Volume 2020 (2020)

Application of Supply-Demand-Based Optimization for Parameter Extraction of Solar Photovoltaic Models

Guojiang Xiong , Jing Zhang, Dongyuan Shi , and Xufeng Yuan

Research Article (22 pages), Article ID 3923691, Volume 2019 (2019)

A New Design Method for PI-PD Control of Unstable Fractional-Order System with Time Delay

Min Zheng , Tao Huang , and Guangfeng Zhang 

Research Article (12 pages), Article ID 3253497, Volume 2019 (2019)

Research Article

Dynamic Characteristics of an Offshore Wind Turbine with Tripod Suction Buckets via Full-Scale Testing

Yun-Ho Seo,¹ Moo Sung Ryu,² and Ki-Yong Oh ³

¹Department of System Dynamics, Korea Institute of Machinery and Materials, Daejeon 34103, Republic of Korea

²Korea Electric Power Research Institute, Daejeon 34056, Republic of Korea

³School of Energy System Engineering, Chung-Ang University, Seoul 06974, Republic of Korea

Correspondence should be addressed to Ki-Yong Oh; kiyongoh@cau.ac.kr

Received 3 July 2019; Revised 9 February 2020; Accepted 2 March 2020; Published 30 March 2020

Academic Editor: Dan Selișteanu

Copyright © 2020 Yun-Ho Seo et al. This is an open access article distributed under the Creative Commons Attribution License, which permits unrestricted use, distribution, and reproduction in any medium, provided the original work is properly cited.

The dynamic characteristics of an offshore wind turbine with tripod suction buckets are investigated through finite element analysis and full-scale experiments. In finite element analysis, an integrated framework is suggested to create a simple yet accurate high fidelity model. The integrated framework accounts for not only the strain dependency of the soil but also for all dynamics in the seabed, including those of the soil, suction bucket skirt, and cap. Hence, the model accurately describes the coupling effect of translational and rotational motions of the seabed. The prediction results are compared to the experimental results obtained via full-scale testing in four stages during construction and in several operational conditions. The comparison shows that the stiffness of the suction bucket cap and strain dependency of the soil play a significant role in predicting natural frequency, suggesting that these two factors should be considered in finite element analysis for the accurate prediction of dynamic responses of an offshore wind conversion system. Moreover, dynamic analysis of the strain and acceleration measured during operational conditions shows that strain is more robust than acceleration with regard to the characterization of the overall dynamics of an offshore wind conversion system because the natural frequency of an offshore wind turbine is very low. It can be inferred that the measurement of strain is a more effective way to monitor the long-term evolution of dynamic characteristics. The suggested integrated framework and measurement campaign are useful not only to avoid conservatism that may incur additional costs during load calculation and design phases but also to establish an intelligent operation and maintenance strategy with a novel sensing technique.

1. Introduction

Renewable and sustainable energies are attractive alternatives for mitigating issues related to the consumption of fossil fuels, including the volatility of oil prices, emission of carbon dioxide, and aggravation of air quality due to fine dust emission. Among renewable and sustainable energies, offshore wind power shows a variety of advantages including high energy density, low turbulence, and low wind shear [1]. Technological advances are also making wind energy competitive from the economic perspective [2–9]. In 2018, 409 new offshore wind turbines were commissioned in Europe, which provided an additional capacity of 2,649 MW, and the cumulative capacity of wind farms was 18,499 MW [10].

There are two trends for offshore wind power. One trend is the increase of turbine rated capacity. Most wind farms under construction are using turbines with capacities higher than 6 MW. The other trend is increasing the distance from the shore to mitigate concerns raised by civil complaints as well as to achieve better wind potential. For offshore wind farms under construction in Europe in 2018, the mean distance from the shore is 33 km [10]. However, the farther that a wind farm is from the shore, the deeper the water depth of its candidate site. The average water depth of European offshore wind farms under construction in 2018 is 27.1 m [10]. The long distance from the shore and deep water depth hinder the economic feasibility of wind farms.

To increase the economic feasibility of offshore wind farms, many studies have focused on substructures and

foundations because the cost for these components accounts for 20–40% of the total cost, depending on water depth [11]. With regard to substructures, space frame substructures, including tripods and jacket structures, are the most promising. They provide sufficient strength and stiffness at a competitive cost in transitional water depths at which most new wind farms are permitted for installation nowadays. Regarding foundations, bearing capacity is the most important factor in supporting an offshore wind turbine. To estimate bearing capacity, soil-pile interaction should be exactly elucidated depending on types of foundations: gravitational type, pile type, and rigid bucket.

For the gravitational type, the deformation of bulk soil on the surface is of interest in the sense that the most interactions between the foundation and soil occur at the contact surface between the foundation and soil. However, this type is only feasible for shallow water because the construction cost is proportional to water depth and thus expensive for transitional water depths. Consequently, this type is no longer used for MW-class wind turbines installed in transitional water depths. For the pile type, the ratio of flexibility between soil and a pile is of interest because the ratio of flexibility governs soil-structure interaction [12]. Hence, the ratio of flexibility between soil and the pile is important to determine the specifications of the pile, including size and height [13]. Many current wind farms have been installed in transitional water depths with the pile type because of its proven reliability. Regarding the deep and rigid caisson type, interactions occur only below and beside the foundation. The shape of the foundation (aspect ratio) and soil properties are important to evaluate the influence on the interaction. If the foundation is very rigid compared to the soil, coupling of translational and rotational stiffness should be considered.

Interestingly, a suction bucket has the characteristics of both flexible pile and rigid caisson regarding the interaction with soil [14], making the design and construction more difficult and complex. Several factors affect the interaction between the soil and the suction bucket, including dimension, aspect ratio of a suction bucket, soil properties, and the ratio of flexibility between the soil and the suction bucket. Although designing suction buckets is difficult and complex, suction buckets become more promising than pile foundations in the transitional water depth because suction buckets are economic and offer simple and fast installation [15]. Moreover, suction buckets can help overcome several issues associated with the installation of the pile type including low level of vibration, noise, and suspended sediments.

Several studies have been conducted to deploy suction buckets on the foundations of offshore wind turbines [16, 17]. Design procedures for the installation of suction buckets in sand and clay have been suggested [18, 19]. Experimental studies on the installation of suction buckets have been conducted for sand and clay to validate suggested models and provide appropriate parameters in models [20, 21]. Bearing capacities and resistances of suction buckets under a variety of operational conditions have also been studied [22, 23]. Moreover, the effects of plasticity and cyclic

loads on the behavior of suction buckets have been analyzed to observe operational performance and degradation of stiffness [24, 25]. These intensive studies have elaborated the model accuracy of suction buckets and provided useful information for understanding soil-pile interactions. However, many of the suggested high fidelity models require heavy computational efforts to calculate the static and dynamic responses of offshore wind conversion systems (OWCSs) comprising offshore wind turbines, substructures, and foundations. These heavy calculation efforts hinder the use of these models in the design phases of commercial wind farms because hundreds of load calculations should be conducted in the actual design of substructures and foundations to ensure the reliability and safety of the OWCSs at a variety of operational conditions. Previous experimental studies have been conducted with laboratory model tests or reduced-scale field trials. Hence, uncertainty still exists with regard to the interapplicability of the results obtained from laboratory model tests, field trials with a reduced scale, and full-scale installations. Moreover, significant site-to-site variation of soil properties and the strain dependence of modulus of elasticity cause numerous difficulties and complications in the actual design and construction of a commercial wind farm.

Thus, it is essential to bridge the gap between theory and experiments as well as that between academic research and field applications and thereby mitigate concerns regarding uncertainty and increase prediction accuracy in the development phase of commercial offshore wind farms with multipod suction buckets. To this end, this study suggests a simple yet effective design procedure and its validation method. In particular, an efficient integrated framework is proposed to predict the dynamic responses of OWCSs. This framework also suggests a method of collaboration between civil engineering and mechanical engineering to design a commercial offshore wind farm.

From the civil engineering perspective, a suction bucket was designed in detail to provide sufficient bearing capacity for a selected offshore wind turbine based on an actual soil investigation, including the cone penetration test (CPT) and standard penetration test (SPT). Then, design parameters of the foundation were fed into a three-dimensional (3D) finite element model (FEM) to estimate the equivalent stiffness matrix of the seabed. This matrix accounts for the coupling effect between the translational and rotational motions of the seabed to enhance prediction accuracy. From the mechanical engineering perspective, dynamic analysis was conducted via a high fidelity 3D FEM of the OWCSs with the equivalent stiffness matrix of the seabed that was obtained via civil engineering as the boundary condition.

Two full-scale measurement campaigns were also conducted during the construction and operation. The dynamic characteristics were measured to validate the prediction of the integrated simulation framework when significant progress in construction was achieved. The forces of impact caused by a ship or aero/hydrodynamic excitation forces from winds and waves were used for the excitation of structures in four stages during construction. Moreover, a structural health monitoring (SHM) system was installed to

measure the dynamic characteristics during operation. The data measured using the SHM system were also used for the validation of the integrated simulation framework and evolution of dynamic responses of the OWCS. A comparison between predicted and experimental results suggests that several important features should be accounted for to accurately predict the dynamic responses of the OWCSs, including the stiffness of the cap of the suction bucket and strain dependency of the modulus of elasticity of the soil.

2. Integrated Simulation Framework

Figure 1 shows a schematic of an integrated simulation framework for predicting the dynamic characteristics of an OWCS. Dynamic characteristics of the OWCS should be predicted to determine the specifications of the substructure in the design and load calculation phases because fundamental force frequencies (1P and 3P) should be avoided in the first natural frequency of the OWCS during operation [26, 27]. Hence, prediction accuracy is very important to secure the reliability and safety of OWCSs, given that the design lifespan of an OWCS is more than 20 years. The integrated framework proposed herein is separated into two parts. The first part is estimating a 6×6 stiffness matrix $\mathbf{K}_{\text{Seabed}}$ that represents the stiffness of the seabed including the soil and suction buckets. The method for estimating the stiffness matrix $\mathbf{K}_{\text{Seabed}}$ is described in detail through experiments and simulation in Section 2.1. The second part is predicting the dynamic characteristics of the OWCS and its substructure with a simple yet effective modeling method constrained by boundary conditions from the stiffness matrix $\mathbf{K}_{\text{Seabed}}$. The modeling of the wind turbine system and substructure is described in detail in Section 2.2.

2.1. Soil and Suction Buckets. Figure 2 shows the procedure for estimating the stiffness matrix $\mathbf{K}_{\text{Seabed}}$, accounting for the stiffness of the soil and suction buckets. Hence, the stiffness matrix $\mathbf{K}_{\text{Seabed}}$ represents the dynamic characteristics of the seabed connected to a substructure as a unified model, as shown in Figure 1.

In step 1, soil characteristics of the installation location of the OWCS were investigated. The candidate site is located near a breakwater in a southwestern sea area of the Korean Peninsula. The exact location is $35^{\circ}58'19.43''$ North (latitude) and $126^{\circ}30'53.39''$ East (longitude). The mean sea level of the site is 13.6 m. This site was selected as a testbed of the OWCS to establish the design procedure and criteria for the commercial development of an offshore wind farm with a multipod substructure with suction buckets.

The soil investigation, including the CPT and SPT, was conducted through a site survey. Note that site surveys for conducting the CPT and SPT are indispensable in the design phase for the characterization of the actual soil properties of the site because soil properties are highly nonlinear and vary by site. This nonlinearity includes strain dependency, different dynamic behavior depending on type of soil (i.e., sand or clay), grain size, and pore water pressure. This complexity is the main reason for developing a standard procedure and

code of analysis in the design phase of an offshore wind farm. Bearing resistance, friction resistance, and pore water pressure were measured through CPT, whereas soils were sampled at depth through SPT. The tests were conducted up to a depth of 10.7 m.

In step 2, soil properties of each layer were estimated through laboratory experiments with soil samples collected at depth. Table 1 shows soil properties estimated through laboratory experiments. The results show that the site consists of three layers, with each layer featuring different soil properties. Sand is dominant in the first and third layers, whereas clay is dominant in the second layer (see Table 1).

Using an empirical equation, Young's modulus E , which is a key parameter that describes soil dynamics, can be estimated with the measured cone tip bearing resistance q_c over depth. Different empirical equations should be applied to estimate Young's modulus E for sand and clay because of inherent differences between various types of soils.

To estimate the initial tangent shear modulus G_{max} for the sand layers, 14 empirical models were used. Three models [28–30] directly calculated the initial tangent shear modulus G_{max} . Three models [29, 31, 32] first calculated Young's modulus E ; then, this value was converted to the initial tangent shear modulus G_{max} as

$$G_{\text{max}} = \frac{E}{2(1 + \nu)}. \quad (1)$$

Eight models [33–40] first calculated the velocity of a shear wave traveling V_s through soil with the cone tip bearing resistance q_c ; then, this value was converted to the initial tangent shear modulus G_{max} as

$$G_{\text{max}} = \gamma_d V_s^2. \quad (2)$$

These values were calibrated with the ratio of the secant shear modulus and initial tangent shear modulus, i.e., (G/G_{max}) , with respect to the shear strain considering that Young's (shear) modulus of the soil significantly depends on (shear) strain. The ratio of (G/G_{max}) with respect to shear strain was obtained from laboratory experiments on samples from the Saemangeum Embankment, which is located near the installation site of OWCS [41] (Figure 3(a)).

To estimate Young's modulus E for the clay layer, six empirical models were used. One model [43] calculated the initial tangent shear modulus G_{max} , whereas the remaining five models [44–48] calculated the velocity of a shear wave traveling through soil V_s with the cone tip bearing resistance q_c ; subsequently, the estimated velocity was converted into the initial tangent shear modulus G_{max} using equation (2). All values were calibrated with the ratio of the secant shear modulus and the initial tangent shear modulus (G/G_{max}) with respect to the shear strain to account for strain dependency. Shear strain-shear modulus curves suggested by Vucetic and Dobry [42] were used in this study to calculate Young's modulus E of the clay layer (Figure 3(b)). A plasticity index (PI) of 30 was used for calibrating the modulus because the PI of the clay layer was 29.7 (see Table 1).

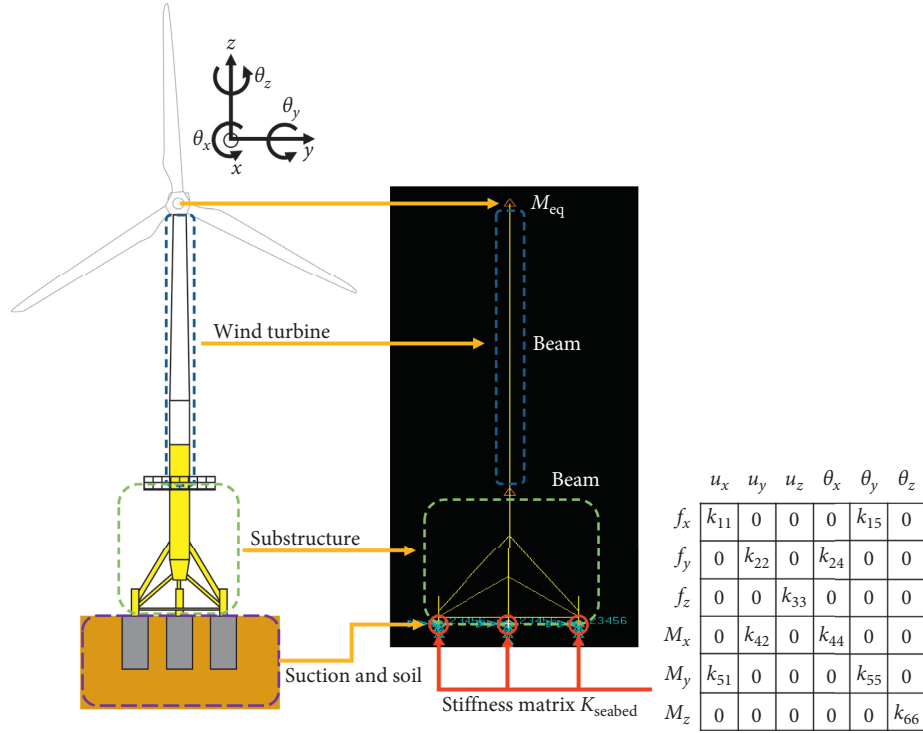


FIGURE 1: Simplified model for an OWCS with a tripod suction buckets.

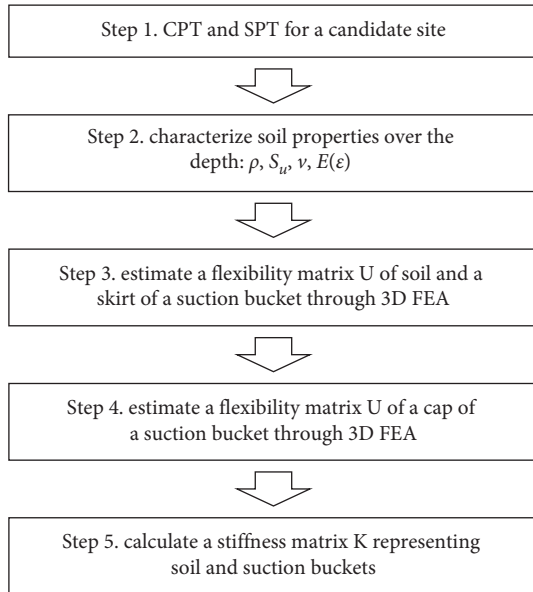


FIGURE 2: Procedure for estimating a stiffness matrix $\mathbf{K}_{\text{Seabed}}$ representing soil and suction buckets.

Finally, all estimated values from different empirical equations, excluding the maximum and minimum values for each layer, were averaged and converted into Young's modulus E with respect to strain (Table 2). Table 2 shows that Young's modulus E significantly decreases with an increasing strain ϵ , suggesting that the strain dependency of Young's modulus E should be considered for soil that supports OWCSs because the large blades in OWCSs

TABLE 1: Soil properties at the site of installation.

Depth (m)	Soil type	γ_d (ton/m ³)	S_u (kPa)	ϕ (°)	ν	PI
0–2.5	Sand	19.0	8	25	0.35	—
2.5–8.3	Clay	18.5	45	0	0.40	29.7
8.3–10.7	Sand	19.0	15	36	0.35	—

γ_d , S_u , ϕ , ν , and PI denote unit weights for zero water content, undrained shear strength, internal friction angle, Poisson's ratio, and the plasticity index.

intensify the aerodynamic force acting on supporting structures, through which significant deformation might occur; other structures installed in the ocean are designed such that the aerodynamic force is minimized.

In step 3, 3D finite element analyses (FEAs) were conducted to elucidate soil-structure interaction between the soil and the skirt of suction buckets. This 3D FEA accounts for multilayer characteristics with different types of soil over depth. Different values of Young's modulus E were also used in case studies to account for the strain dependency of the soil. Then, a flexibility matrix $\mathbf{A}_{\text{soil+suc}_s}$ was calculated for an integrated dynamic analysis, where the subscript suc_s denotes the skirt of the suction bucket. Hence, $\mathbf{A}_{\text{soil+suc}_s}$ is the flexibility matrix of the skirt of the suction bucket embedded in soil. Note that this matrix does not account for the flexibility of the cap of suction buckets. The flexibility of the cap is estimated in the next step.

Regarding 3D FEA, an elaborate model describing the interaction between soil and the skirt was built with hexagonal elements (Figure 4). The diameter and length of the suction buckets are 6 m and 12 m, respectively, and the thickness of the skirt is 19 mm. The following properties of

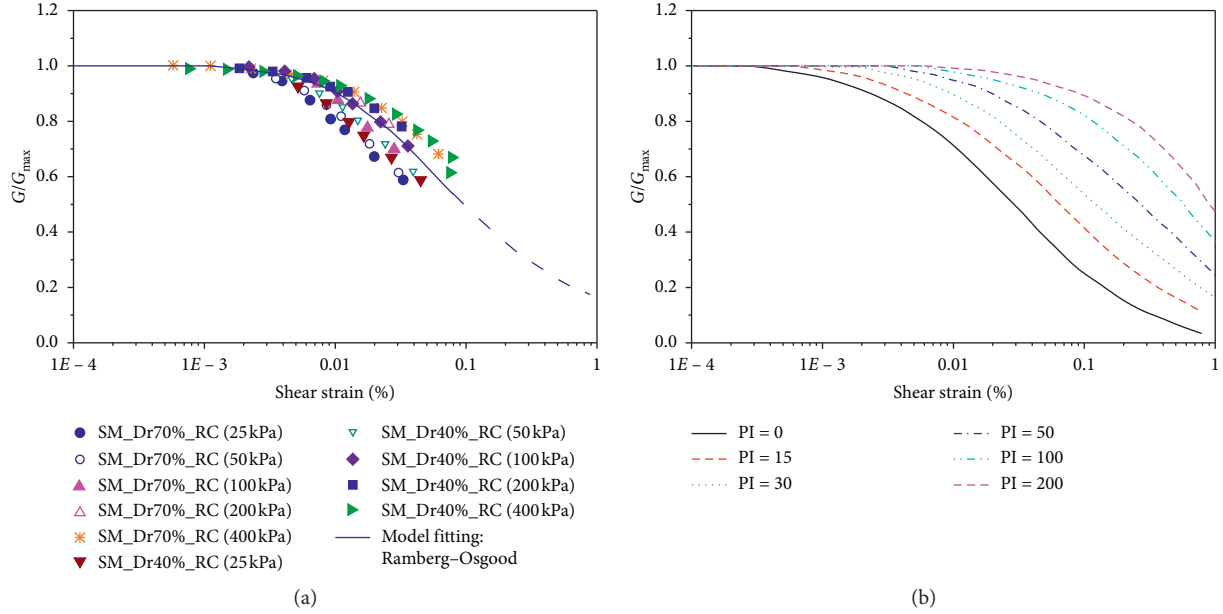


FIGURE 3: Normalized shear modulus over shear strain and PI for (a) soil obtained from Saemangeum Embankment [41] and (b) soil of clay suggested in [42].

TABLE 2: Elastic modulus of each layer with respect to deformation.

Strain ϵ (%)	Young's modulus E (kPa)		
	$<10^{-3}$	0.01	0.1
Sand (upper layer)	17700	16100	8700
Clay	18300	15000	9300
Sand (lower layer)	53300	48500	26100

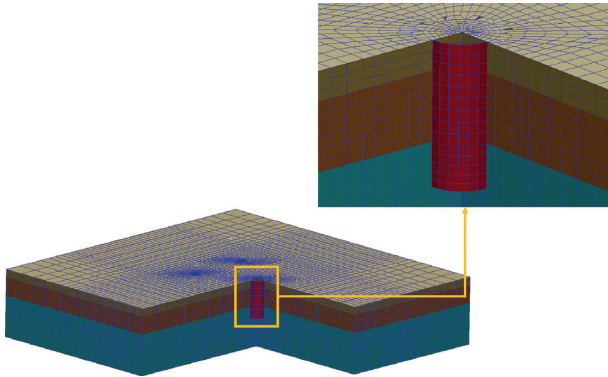


FIGURE 4: Three-dimensional finite element model for soil and a skirt of a suction bucket.

steel were used because the suction bucket is made of steel: Young's modulus = 210 GPa, Poisson's ratio = 0.29, and density = 7850 kg/m³. Boundary conditions of all the surfaces, except the top surface, were clamped to represent nondeformed locations. Further details on the dimensions of the suction buckets are not described herein because they are beyond the scope of this study.

This 3D finite element model was used to calculate a 6×6 flexibility matrix $\mathbf{A}_{\text{Soil+Suc}_s}$ [49], which is defined as

$$\mathbf{A}_{\text{Soil+Suc}_s} = \begin{bmatrix} a_{11} & a_{12} & a_{13} & a_{14} & a_{15} & a_{16} \\ a_{21} & a_{22} & a_{23} & a_{24} & a_{25} & a_{26} \\ a_{31} & a_{32} & a_{33} & a_{34} & a_{35} & a_{36} \\ a_{41} & a_{42} & a_{43} & a_{44} & a_{45} & a_{46} \\ a_{51} & a_{52} & a_{53} & a_{54} & a_{55} & a_{56} \\ a_{61} & a_{62} & a_{63} & a_{64} & a_{65} & a_{66} \end{bmatrix}, \quad (3)$$

where a_{ij} is a flexibility influence coefficient. The flexibility of a suction bucket embedded in soil is similar to that of passive joints [50], suggesting that the flexibility matrix \mathbf{A} includes a number of zero elements as

$$\mathbf{A}_{\text{Soil+Suc}_s} = \begin{bmatrix} a_{11} & 0 & 0 & 0 & a_{15} & 0 \\ 0 & a_{22} & 0 & a_{24} & 0 & 0 \\ 0 & 0 & a_{33} & 0 & 0 & 0 \\ 0 & a_{42} & 0 & a_{44} & 0 & 0 \\ a_{51} & 0 & 0 & 0 & a_{55} & 0 \\ 0 & 0 & 0 & 0 & 0 & a_{66} \end{bmatrix}. \quad (4)$$

A basic assumption in this approach is that force in the x (y) direction and moment in the y (x) direction mainly contribute to deformation in the x (y) direction. In a similar manner, force in the x (y) direction and moment in the y (x) direction mainly contribute to angular displacement in the y (x) direction. Note that a coupling effect between translational and rotational degrees of freedom (DOF) is an actual physical phenomenon in the response of the suction bucket. Therefore, the coupling effect should be considered to accurately evaluate equivalent soil stiffness. Each element of the flexibility matrix \mathbf{A} is calculated by

$$\mathbf{U} = \mathbf{A}\mathbf{F}, \quad (5)$$

where \mathbf{U} and \mathbf{F} denote a displacement vector expressed as $\begin{bmatrix} u_x & u_y & u_z & \theta_x & \theta_y & \theta_z \end{bmatrix}^T$ and a force vector expressed as $\begin{bmatrix} f_x & f_y & f_z & M_x & M_y & M_z \end{bmatrix}^T$. Each element of the flexibility matrix \mathbf{A} is calculated with the displacement vector \mathbf{U} and force vector \mathbf{F} when a unit force (or unit moment) is applied. Specifically, a_{11} and a_{51} are calculated with responses u_x and θ_y , respectively, by 3D FEA when a unit force ($f_x = 1$) is applied with other zero forces and moments. In a similar manner, a_{24} and a_{44} are calculated with responses u_y and θ_x by 3D FEA when a unit moment ($M_x = 1$) is applied with other zero forces and moments.

In step 4, 3D FEAs were conducted to estimate the flexibility matrix $\mathbf{A}_{\text{suc}_c}$ of the cap, where the subscript suc_c denotes the cap of the suction bucket. The diameter of the cap experiences significant changes over depth, whereas the diameter of a mono pile remains unchanged. This significant change of shape occurs in the suction bucket to provide sufficient bearing capacity with relatively small length of the skirt, whereas the mono pile generates a large bearing force with a long length of the pile. This significant change in diameter may induce stress concentration and local flexibility even if the cap is reinforced by many stiffeners. 3D FEA is an efficient solution for calculating the flexibility matrix $\mathbf{A}_{\text{suc}_c}$ because of the complex design of the cap. The cap was modeled as combination of 2D plates and an edge of the cap was assumed to be clamped in the sense that the edge connecting the cap with the skirt is much stiffer than others (Figure 5(a)). Then, a unit force or a unit moment in three directions was applied to calculate the 6×6 flexibility matrix $\mathbf{A}_{\text{suc}_c}$ with deformation of the cap (Figures 5(b) and 5(c)).

In step 5, an equivalent flexibility matrix $\mathbf{A}_{\text{Seabed}}$ representing the flexibility of soil and the suction bucket is calculated as

$$\mathbf{A}_{\text{Seabed}} = \mathbf{A}_{\text{Soil+Suc}_s} + \mathbf{A}_{\text{suc}_c}. \quad (6)$$

This calculation can be explained similar to the case of two spring elements connected in series. One spring represents the stiffness of the soil and the skirt, and the other represents that of the cap. Finally, the equivalent stiffness matrix $\mathbf{K}_{\text{Seabed}}$ of the seabed can be calculated by matrix inversion as

$$\mathbf{K}_{\text{Seabed}} = \mathbf{A}_{\text{Seabed}}^{-1}. \quad (7)$$

This stiffness matrix was used as boundary conditions for a substructure as mentioned earlier.

2.2. Wind Turbine and Substructure. This study modeled the WinDS3000 TC-2 (Doosan Heavy Industries & Construction, South Korea) wind turbine with a tripod substructure. WinDS3000 TC-2 is a 3 MW offshore wind turbine with blades having a diameter of 100 m. Based on the specifications of WinDS3000, which are provided by Doosan Heavy Industry & Construction, the substructure was designed to prevent natural frequencies of the entire system from operational frequencies. Note that specifications of the wind turbine cannot be changed depending the site because

turbine manufacturers require reissue of certificates when any specification of a wind turbine is changed [27]. Table 3 describes the dimensions of the tower and the tripod substructure in detail.

GH Bladed (DNV GL) was used to predict natural frequencies of the OWCS. A tube-shaped tower and a substructure were modeled using beam elements. An assembly of a nacelle, a hub, and blades can be modeled as a point mass. The assembly weighs 186 tons; the nacelle, hub, and blades weigh 128, 28, and 10 tons, respectively. Local flexibility of the blades, tower, and nacelle is negligible because a shape change in the tower or nacelle is small and blades of MW-class OWCS have sufficient stiffness with a sole natural frequency of above 0.6 Hz [51]. The substructures were designed as tripod suction buckets because the cost analysis for the offshore meteorological tower, Herald of the Meteorological and Oceanographic Special Research Unit (HeMOSU)-2, confirmed that the construction cost of tripod suction buckets was half of that of jacket piles, for the same seabed geology, construction, transportation, and supply chain in South Korea [26]. Note that the mean sea level for the candidate site of a 100 MW wind farm is around 20 m, meaning that gravity or monopole types are not economically feasible [52]. The pile type also gives rise to several environmental issues during construction, including vibration, noise, and suspended sediments. Moreover, the construction of HeMOSU-2 took only 6 h, whereas that of HeMOSU-1, in which jacket piles were used, took two months for the installation [53]. The properties of steel described in Section 2.1 were used for the tower and substructure.

The effect of added mass was considered for the submerged substructure, which is defined as the substructure from the depth of the seabed to the depth of the mean sea level because the water added mass has a significant influence on the natural frequencies and mode shapes of a multipod substructure [54]. The inner space of the tube-shaped element below the sea level is filled by seawater and the outer surface is also in contact with seawater, suggesting that the amount of added mass is exactly related to the deformation shape of an element. However, the lowest mode deformation of an element in the finite element analysis can be assumed to be only translational. Therefore, added mass of the inner and the outer water can be set by the area of the element [55].

3. Measurement Campaign

3.1. Measurement under Construction. The evolution of dynamic responses was measured during the construction of the 3 MW-class OWCS. The measurement framework consisted of four stages, as shown in Figure 6. The natural frequency was measured at each stage when significant progress was achieved during construction. Specifically, the natural frequency was measured after completing the installation of tripod suction buckets at stage I (Figure 6(a)) and after completing the installation of bottom and middle towers at stage II (Figure 6(b)). In stage III, the natural frequency was measured after completing the installation of

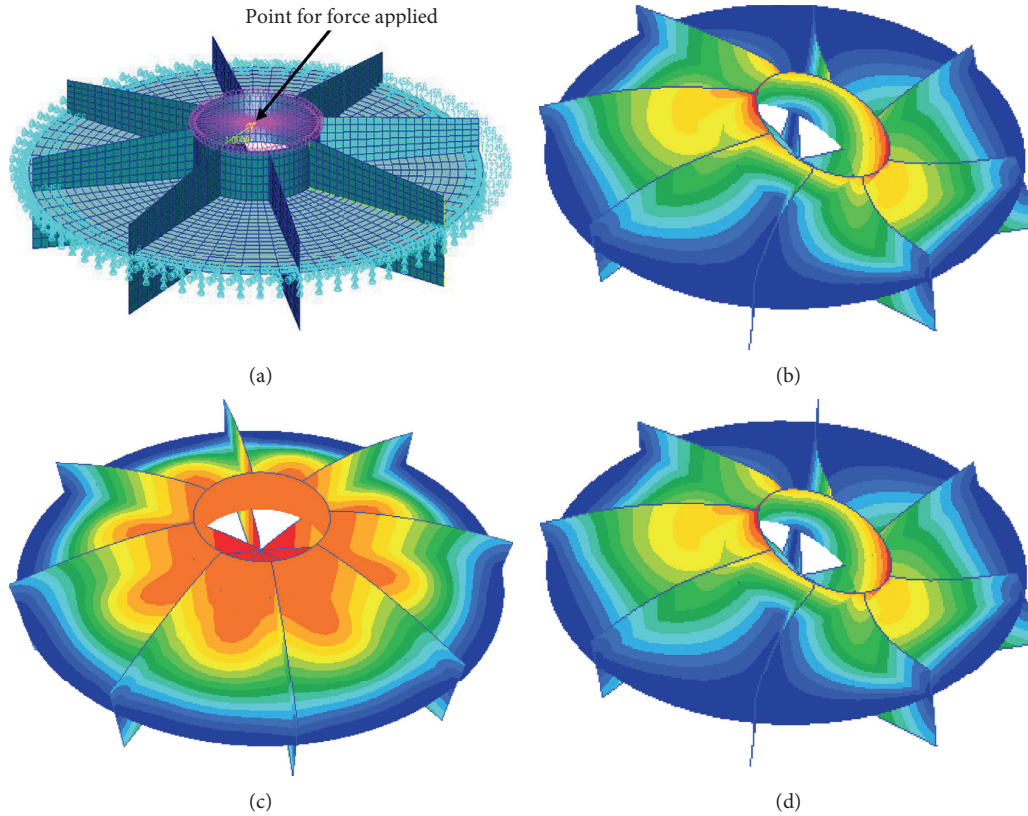


FIGURE 5: Finite element analysis results for calculating the flexibility matrix $A_{suc,c}$ of a cap of a suction bucket: (a) finite element model with the point force applied; relative displacement of the cap for (b) unit horizontal force, (c) unit vertical force, and (d) unit horizontal moment.

TABLE 3: Dimensions of the OWCS model.

Maximum diameter of the tower	4.5 m
Minimum diameter of the tower	3.07 m
Length of the tower	58.5 m
Maximum thickness of the tower walls	46 mm
Minimum thickness of the tower walls	18 mm
Maximum diameter of the main substructure	4.5 m
Minimum diameter of the main substructure	3.0 m
Length of the main substructure	24.9 m
Maximum thickness of the main substructure	54 mm
Minimum thickness of the main substructure	30 mm
Maximum diameter of the supporting structure	1.2 m
Minimum diameter of the supporting structure	0.4 m
Maximum thickness of the supporting structure	30 mm
Minimum thickness of the supporting structure	17.5 mm
Distance from the center of the substructure to the suction buckets	11.5 m

the nacelle on top of the tower (Figure 6(c)). Finally, the natural frequency was measured at stage IV after completing the installation of the hub and three blades (Figure 6(d)).

Two accelerometers with a sensitivity of 10 V/g were installed on the top of the transition piece to measure accelerations along two directions perpendicular to each other. Figure 7(d) shows the installed accelerometers on the transition piece.

In the experiments, the structures were excited in two ways. In one, a ship was used to provide impact force on only the substructure at stage I, whereas in the other, natural

excitation from winds and waves was used to structures under construction from stage II to stage IV. Note that natural exciting forces from winds and waves were not sufficient to excite only the substructure in stage I. Hence, a small ship of 6.6 ton was used to provide impact force to the substructure (Figure 7(c)) because impact force in the time domain is white noise in the frequency domain [56]. The ship slowly approached on landing ladder to excite a substructure (Figures 7(a) and 7(b)); then, the dynamic response was measured. In contrast, structures at stages II, III, and IV were excited sufficiently by natural wind and waves. Hence, the natural frequencies at stages II, III, and IV were determined by measuring acceleration and through subsequent spectral analysis.

3.2. Measurement during Operation. A SHM system was installed to observe long-term variations of the dynamic responses of the OWCS during operation, such as acceleration, strain, temperature, and sea level. The natural frequency of the OWCS with the substructure was calculated using measured accelerations and strains. To measure the accelerations, 10 accelerometers were installed at 5 locations on the tower of the OWCS along the vertical direction (Figure 8(a)). Two accelerometers were installed perpendicular to each other at different heights in each location. For each set, one accelerometer was aligned north-northwest (NNW), the main direction of wind at the site, whereas the

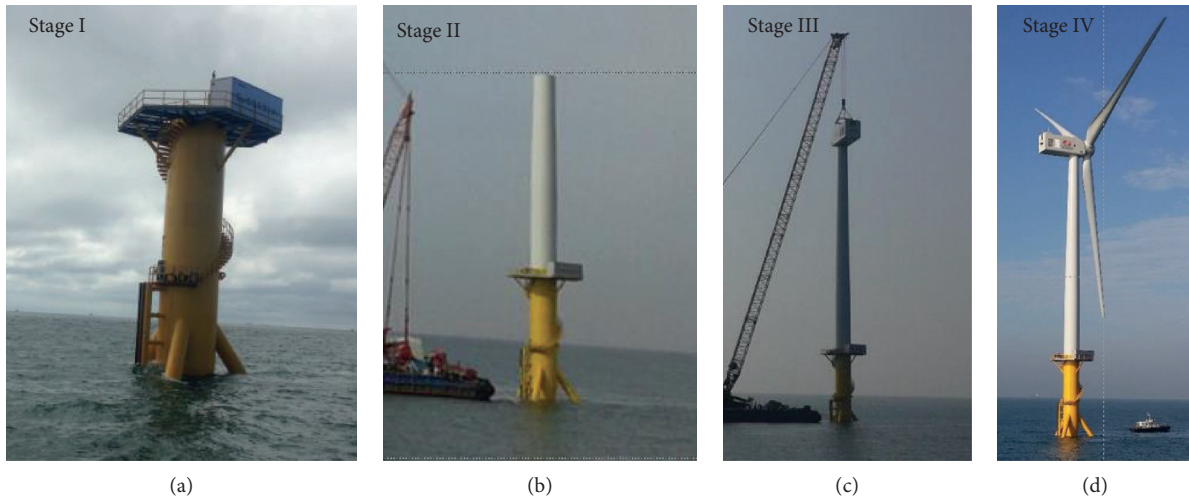


FIGURE 6: Measurement framework consisting of four stages during construction: (a) stage I (b) stage II, (c) stage III, and (d) stage IV.

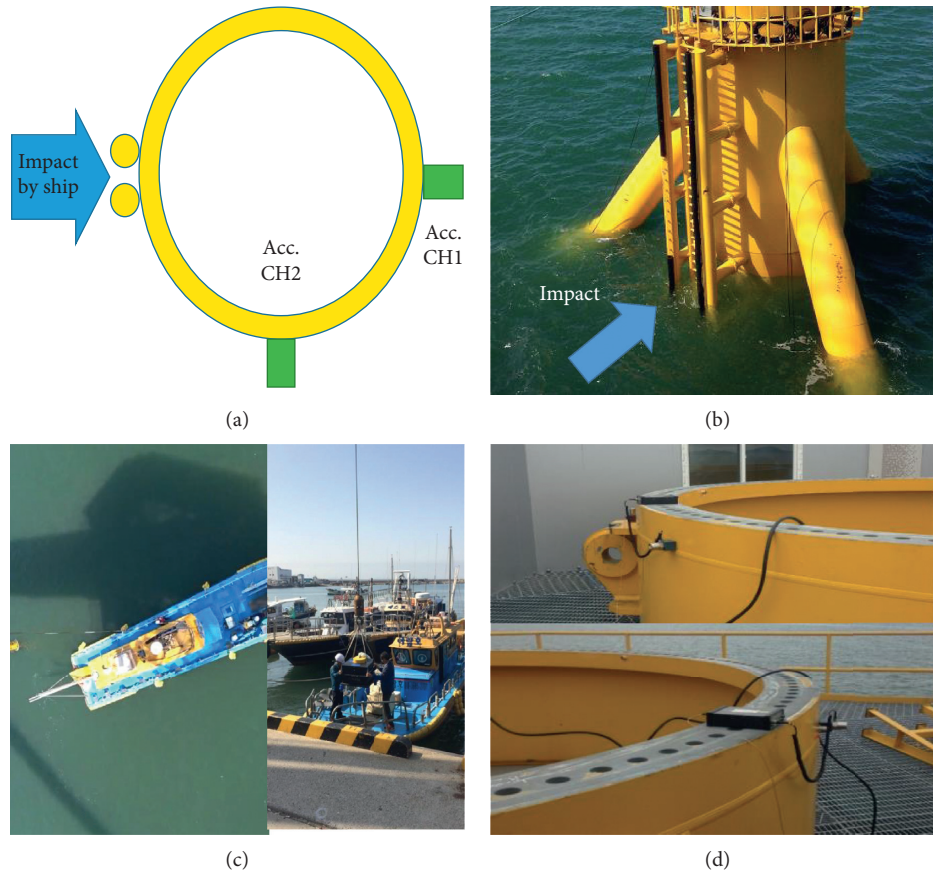


FIGURE 7: Impact tests only with substructure: a schematic diagram with (a) a top view and (b) an isometric view; (c) a ship used to induce impact force on a substructure; (d) accelerometers installed in channel 1 (top) and channel 2 (bottom).

other accelerometer was aligned east-northeast (ENE), perpendicular to the main direction of wind (Figure 8(b)) [57]. In addition, 4 sets of strain gauges were installed near the transition piece between the offshore wind turbine system and the substructure to measure bending

deformation. Two sets of strain gauges were installed +0.5 m from the transition piece; one set was aligned NNW and the other was aligned ENE. Two other sets of strain gauges were installed at -0.5 m from the transition piece. Each set of strain gauges is a full bridge type.

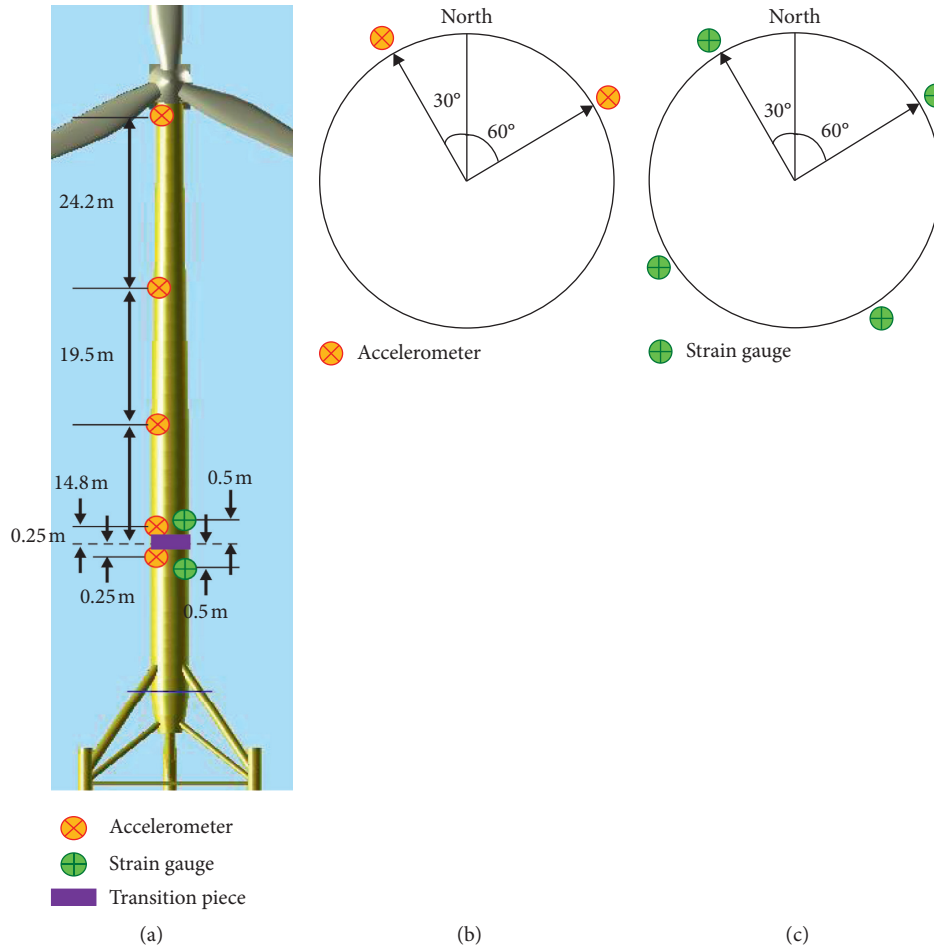


FIGURE 8: Schematics of the structural health monitoring system: (a) installed locations of accelerometers and strain gauges along the vertical direction; installed locations of (b) accelerometers and (c) strain gauges along the horizontal direction.

4. Results and Discussion

4.1. Dynamic Responses under Construction

4.1.1. Stage I. The dynamic response of the tripod suction bucket measured at stage I was compared to that predicted from the integrated framework. To calculate the natural frequency based on an experiment performed at stage I, the measured acceleration (Figure 9(a)) with a record length of 11.8 s and sampling frequency of 256 Hz was converted to the frequency domain via fast Fourier transform (FFT). Then, the maximum peak in the spectrum was determined (Figure 9(b)). Hence, the resolution in the frequency domain for this data is 0.085 Hz. Figure 9(a) shows the measured acceleration in the time domain, which follows the conventional transient response of a second-order system. This observation can be explained by the fact that the first mode is dominant for the tripod suction buckets embedded in the seabed; thus, it governs the overall dynamic behavior of the OWCS. The natural frequency of the tripod substructure determined through spectral analysis is 3.30 Hz, as shown in Figure 9(b).

Four different cases were studied in the integrated framework to compare not only the effect of the cap of the suction bucket but also the strain dependency of the modulus (Table 4). In each case, the flexibility matrix $\mathbf{A}_{\text{soil+suc}_s}$ accounts for only the stiffness of the soil and the suction skirt, as in many previous studies, whereas the flexibility matrix $\mathbf{A}_{\text{Seabed}}$ accounts for all stiffness components, including the soil, suction skirt, and suction cap. In case 1, strain is assumed to be less than 10^{-3} for all layers, whereas in case 2, it is assumed to be approximately 0.01 for all layers. In case 3, the two uppermost layers are considered to experience a large strain of approximately 0.1, whereas the deepest layer experiences a deformation of approximately 0.01, assuming that a smaller deformation occurs in the deeper layer because of relatively high stiffness. In case 4, a large deformation of approximately 0.1 is considered to occur for all layers.

The last two columns of Table 4 show the predicted natural frequencies (and the corresponding errors compared to the measured values that are given in parentheses) calculated with the corresponding flexibility matrix.

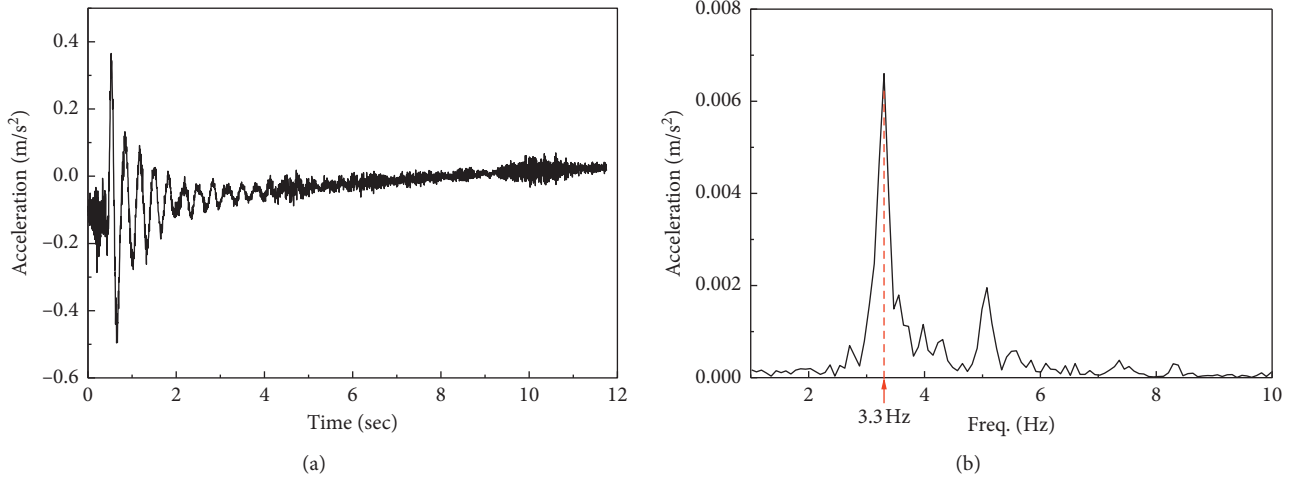


FIGURE 9: Measured acceleration data at stage I: (a) acceleration in the time domain and (b) spectrum in the frequency domain.

TABLE 4: Soil properties for case studies and natural frequencies (NF) predicted via the integrated simulation framework.

Case number	Young's modulus E (kPa)			Natural frequency (Hz) (error w.r.t. measurement %)	
	Sand (upper layer)	Clay	Sand (lower layer)	Flexibility matrix	
				$A_{\text{soil+suc.}}$	A_{Seabed}
1	17700	18300	53300	4.30 (30.3)	3.77 (14.2)
2	16100	15000	48500	4.21 (27.6)	3.71 (12.4)
3	8700	9300	48500	3.98 (20.6)	3.40 (3.03)
4	8700	9300	26100	3.57 (8.18)	3.24 (1.82)

Remarkably, relatively large errors were encountered when only the flexibility matrix $A_{\text{soil+suc.}}$ was considered. The errors ranged from 8.18% to 30.3% when only the flexibility matrix $A_{\text{soil+suc.}}$ was considered, whereas they ranged from 1.82% to 14.2% when the flexibility matrix A_{Seabed} was considered. The errors attributed to this difference were at least double, i.e., 30.3% vs. 14.2% (case 1) or 8.18% vs. 1.82% (case 4), when the same modulus for each layer was applied. The analysis suggests that the stiffness of the cap plays a critical role in the prediction of dynamic responses of the substructure. Therefore, the contribution of the cap should be considered.

From the perspective of strain dependency, the error could be reduced by considering larger deformations in soil. Specifically, the error between the measured and predicted values was 1.82% when the strain for all layers is assumed to be approximately 0.1 (case 4 with the flexibility matrix A_{Seabed}), whereas the error between measurement and prediction was 14.2% when strain is assumed to be less than 10^{-3} (case 1 with the flexibility matrix A_{Seabed}).

The analysis of the dynamic characteristics of the tripod substructure in stage I clearly shows that the stiffness of the cap and Young's modulus, which accounts for strain dependency [58], should be considered to accurately predict the dynamic response of the OWCS and its substructure.

4.1.2. Stages II to IV. The natural frequencies under construction during stages II to IV were also obtained from the

measured acceleration under natural excitation from wind and waves. In stages II to IV, acceleration could be measured over a long period because these experiments were conducted under natural excitation, whereas stage I was conducted using an impact test with a ship. Therefore, analysis could be conducted with high resolution in the frequency domain. The accelerations excited by wind and wave were measured for a period of 125 s with a sampling frequency of 1707 Hz, meaning that the frequency resolution at the analysis is 0.008 Hz. Figure 10 shows results of spectral analyses for stages II to IV. These frequency spectra show one clear peak even though the structure is under natural excitation, suggesting that natural excitation from wind and waves was sufficient for determining the natural frequencies of the structure under construction.

Table 5 shows a comparison between the measured and predicted values of natural frequency. The measured values were compared with the predicted values for cases that showed the largest and smallest errors in stage I, namely, case 1 and case 4, respectively. Similar to the results obtained in stage I, case 4 showed smaller errors than case 1. Moreover, the percentage errors of case 1 with the flexibility matrix $A_{\text{soil+suc.}}$ in stage II were much smaller than those in stage I. This observation suggests that the contribution of the equivalent stiffness of the seabed to the natural frequency of the OWCS during stage II was lesser than that at stage I. In a similar manner, the errors of case 4 with the flexibility matrix $A_{\text{soil+suc.}}$ in stages II, III, and IV decreased compared to those in stage I. The predicted results for case 4 also show

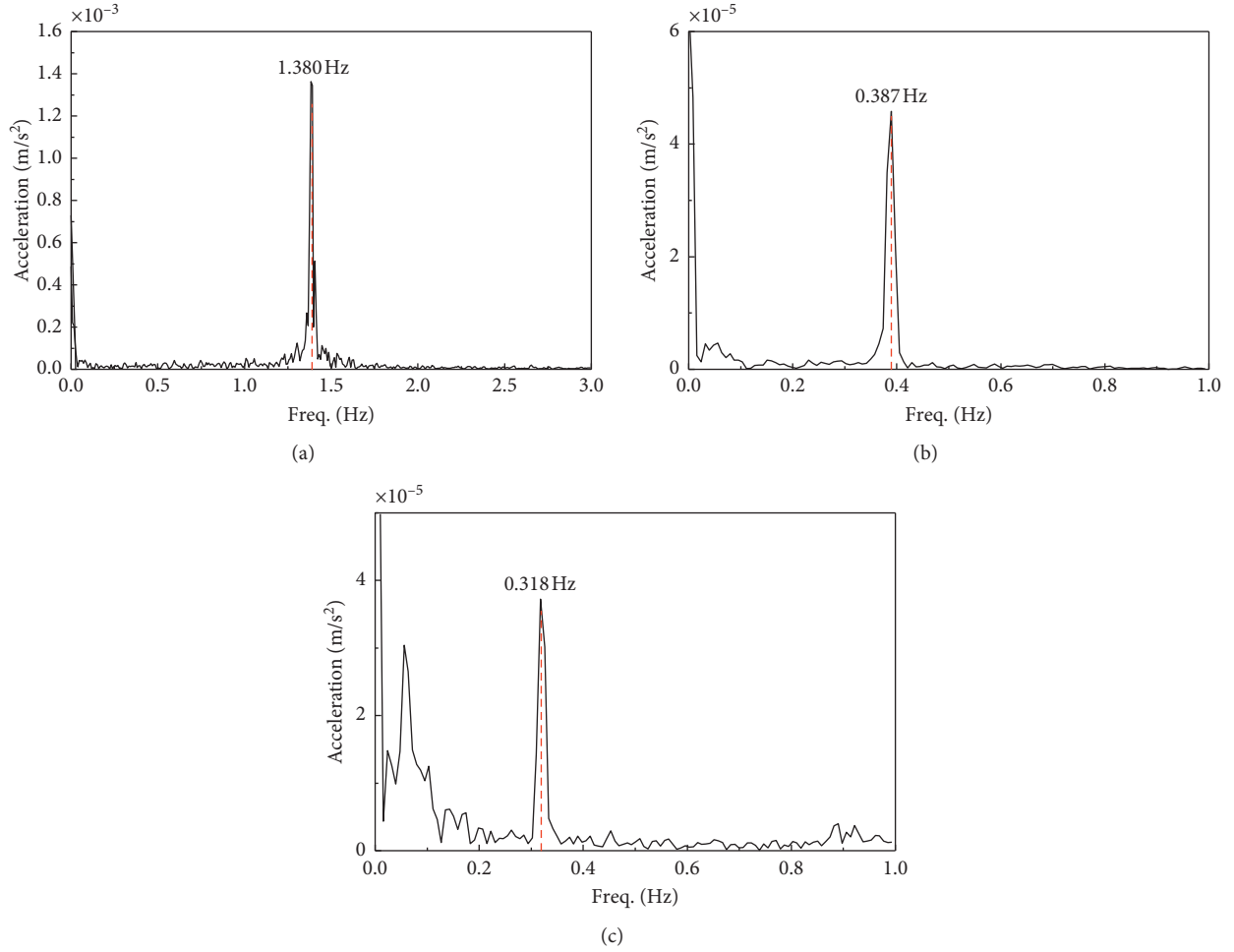


FIGURE 10: Spectral analyses of measured acceleration: (a) stage II, (b) stage III, and (c) stage IV.

TABLE 5: Comparison of measured and predicted values of natural frequency.

		Natural frequency (Hz)		
		Stage II	Stage III	Stage IV
Measurement		1.380	0.387	0.318
Prediction	Case 1 with $\mathbf{A}_{\text{soil+suc}_s}$	1.530	0.391	0.334
	(Error w.r.t. exp., %)	(10.87)	(1.03)	(5.03)
	Case 4 with $\mathbf{A}_{\text{soil+suc}_s}$	1.420	0.380	0.325
	(Error w.r.t. exp., %)	(2.89)	(1.81)	(2.02)
	Case 4 with $\mathbf{A}_{\text{Seabed}}$	1.360	0.374	0.320
	(Error w.r.t. exp., %)	(1.45)	(3.36)	(0.94)

that the flexibility matrix $\mathbf{A}_{\text{Seabed}}$ shows more accurate predictions compared to the flexibility matrix $\mathbf{A}_{\text{soil+suc}_s}$. In conclusion, the model that accounts for the stiffness of the cap and strain dependency demonstrates increased prediction accuracy. The suggested elaborate model and method of predicting the dynamics of a substructure and foundation would be useful in predicting the long-term degradation of soil supporting the OWCS because soil degrades faster than the suction bucket and the substructure [59].

4.2. Dynamic Responses during Operation. Figure 11 shows the results of a spectral analysis of data obtained from a SHM system under idling (stop) and operational conditions. In the idling or stop conditions, the first natural frequency calculated was 0.318 Hz for the spectra of both acceleration and strain measured at various locations, further validating that the first natural frequency measured at stage IV is accurate. Moreover, the spectra did not exhibit location dependency between NNW and ENE. The spectra for ENE are omitted

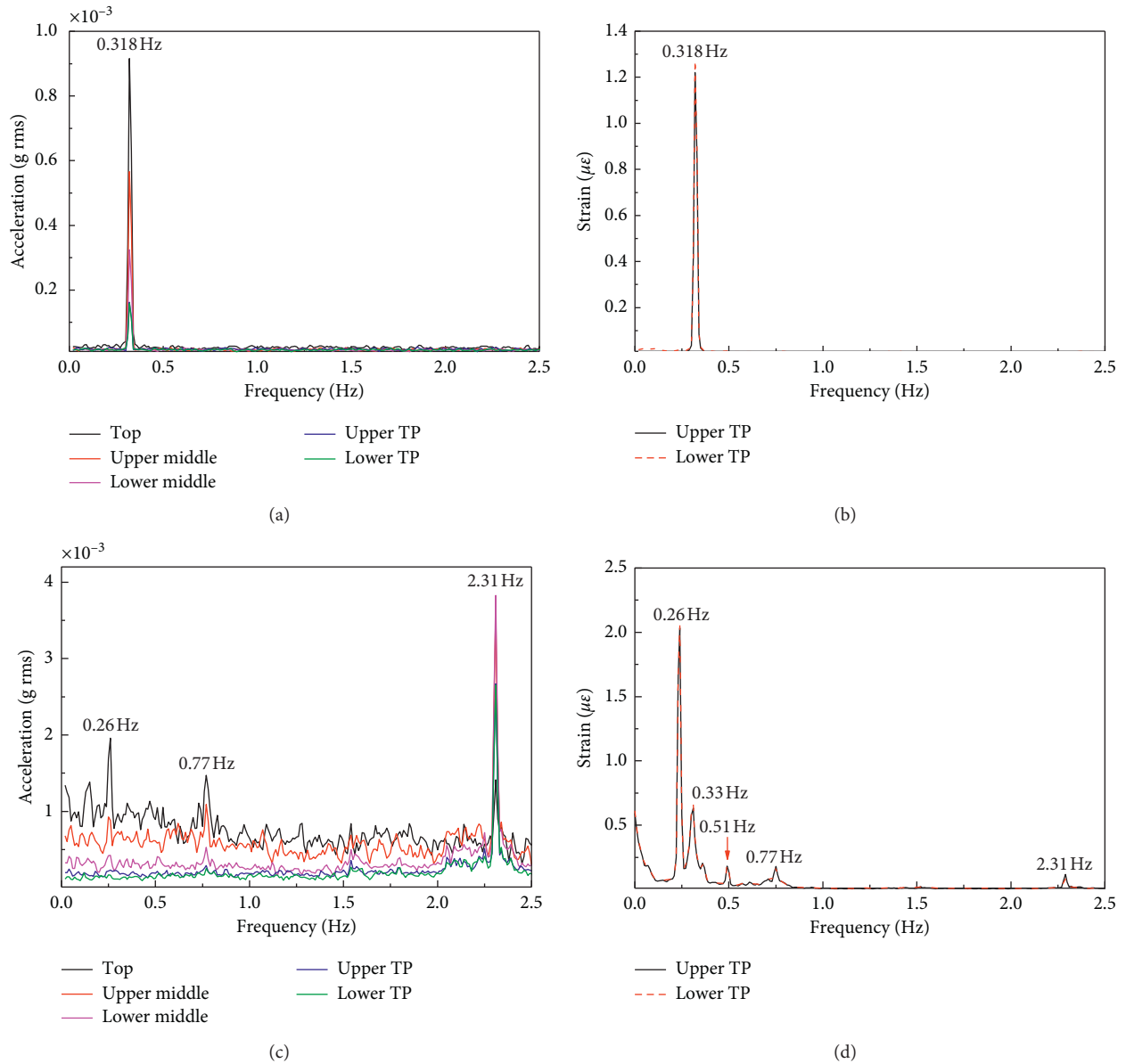


FIGURE 11: Spectral analyses of structural health monitoring system data along NNW direction under idling (stop) condition with (a) accelerometers and (b) strain gauges; rated operations measured in NNW direction with (c) accelerometers and (d) strain gauges.

herein for the sake of brevity. Hence, either of both measured data from accelerometers and strain gauges can be used to monitor natural frequency of the OWCS.

However, measured data under a rated production are different, as shown in Figures 11(c) and 11(d) for the wind turbines operating with a rotational speed of 15.4 rpm (0.26 Hz). The natural frequency does not appear for the measured acceleration (Figure 11(c)). The spectra of acceleration simply show various peaks related to 1P (rotational speed), 3P (blade passing component), and their harmonics. In contrast, the natural frequency clearly appears along with operational forcing frequencies for the measured strain (Figure 11(d)). The same phenomena were observed in the spectra measured using the accelerometers and strain gauges at ENE. This observation can be explained by the fact

that various auxiliary machines, including oil pumps, cooling fans, and electric equipment, are switched on during operation and these machines increase the level of background vibration noise. This could be the reason for previous studies measuring the natural frequency with accelerometers after applying emergency stops [60, 61]. In other words, a significant impact force would be induced in measuring the dynamic responses with the accelerometers [62]. In contrast, the spectra of strain show the natural frequency of the OWCS as well as frequencies associated with operation. Hence, it can be inferred that the measurement of strain using SHM is more effective than that of acceleration in characterizing the dynamic response or monitoring the evolution of natural frequencies of the OWCS because the frequencies of interest in this study are low frequencies. Note

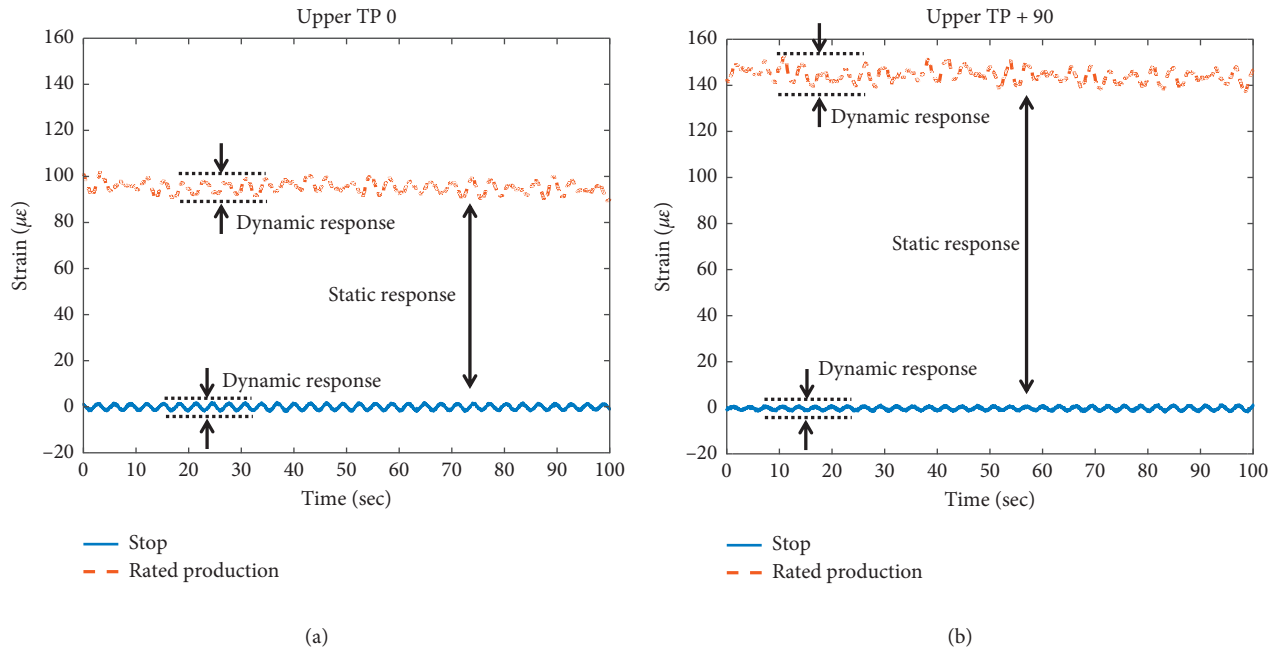


FIGURE 12: Static and dynamic responses measured from strain gauges.

that acceleration is proportional to the second derivative of the displacement with respect to time. This means that the acceleration is proportional to the square of the frequency in the frequency domain. Hence, the strain would be more apparent than the acceleration at low frequencies, but the acceleration would be larger than the strain at high frequencies.

In addition, the natural frequency under the rated operating condition (0.33 Hz) was slightly higher than that under the idling condition (0.32 Hz). This result is similar to that in [63], in which the first natural frequency predicted under the idling or stop conditions was slightly lesser than the measured frequency.

Several analytical approaches have been applied to elucidate the load dependency of the dynamic response, suggesting that the load dependency is primarily relevant to soil-pile interactions. One reason is that the static thrust force induced on the OWCS is significantly larger than the dynamic and cyclic force, as shown in Figure 12. This static load changes the friction angle of soil because of soil-pile interaction [64]. Another reason is that the equivalent stiffness of soil depends on the ratio of the diameter and length of embedding [60]. A relatively large ratio increases the bending stiffness of soil and piles, thereby increasing the first natural frequency with increasing load induced on the OWCS. This phenomenon can explain the slight increase in the natural frequency measured via SHM because the key characteristic of the suction bucket is the relatively large ratio of the diameter with respect to the length of embedding. Sediment transportation at the seabed also results in changes in the dynamic characteristics of the OWCS [61]. The scour depth depends on time because of aero- and hydrodynamic loads and thereby changes the eigenfrequency and modal damping. Compaction of the backfilled

material occurs in the presence of waves, thereby inducing depth compaction. This phenomenon increases the friction angle and thereby shifts the eigenfrequency of the OWCS [64].

This interesting phenomenon might also be related to the pull in and out mechanism of the suction bucket. Under operational conditions, a significant thrust force, which is larger than the cyclic force, as shown in Figure 12, acts against the tip bearing force, which is a major supporting force of the suction bucket. Therefore, the equivalent stiffness of soil, including that of the suction bucket, increases. Note that the suction bucket provides two supporting forces for the structure. One is skin force between the soil and the skirt. The skin force is related to contact friction, which is influenced by pressure and type of soil. The contact friction is independent of the friction angle of the soil, which is defined by the inherent characteristics of the soil. The other is tip bearing force, which is the supporting force from the soil and is transmitted to the perimeter of the suction bucket. The contribution of the tip bearing force would be significant in the sense that the stiffness of the cap plays a critical role, as already shown in case studies. Moreover, the tip bearing force is governed by the friction angle, which is the same as shear strength.

5. Conclusion

This study evaluates the dynamic characteristics of an OWCS through simulation and experiments. An integrated framework was suggested to accurately model the seabed, including the soil, the skirt of a suction bucket, and the cap of a suction bucket. Full-scale experiments were also conducted for various stages under construction as well as under operation. The following conclusions can be drawn:

- (i) The stiffness of the cap of a suction bucket plays a critical role in predicting the natural frequencies of the OWCS. In particular, the contribution of the stiffness of the cap of the suction bucket is more significant when predicting dynamic responses of the substructure embedded in the seabed with suction buckets [65].
- (ii) The strain dependency of the modulus of elasticity of the soil significantly affects the dynamic responses of the substructure. However, the effect of the strain dependency is limited with regard to predicting the dynamic responses of the entire structure. Hence, it can be inferred that the suction bucket embedded in soil should be designed with a focus on providing sufficient bearing capacity, whereas the substructure submerged in seawater should account for the dynamic responses of the OWCS and its substructure. Future work will include a systematic study using a 3D finite element model of the soil and the suction bucket to elucidate the strain with respect to depth and soil-pile interactions.
- (iii) The natural frequency during the operational stage slightly differs from that during stop or idling conditions. This may be attributed to soil-pile interactions in the seabed. Specifically, the tip bearing force governed by thrust forces contributes to the evolution of the natural frequency depending on operational conditions such as stop and rated operation.
- (iv) During operation, strain is more sensitive than acceleration for measuring the dynamic characteristics or long-term evolution of dynamic responses of the OWCS and its substructure. Hence, strain measurement can be used to predict the remaining useful life of the OWCS with the SHM system.

Nomenclature

CPT:	Cone penetration test
FEA:	Finite element analysis
FEM:	Finite element model
ENE:	East-northeast
FFT:	Fast Fourier transform
NNW:	North-northwest
OWCS:	Offshore wind conversion system
SHM:	Structural health monitoring
SPT:	Standard penetration test
PI:	Plasticity index
A:	Flexibility matrix
A_{Seabed} :	Flexibility matrix of seabed
$A_{\text{soil+suc}_s}$:	Flexibility matrix of soil and skirt of suction bucket
A_{suc_c} :	Flexibility matrix of cap of suction bucket
F:	Force vector
K_{Seabed} :	Stiffness matrix of seabed
U:	Displacement vector
E:	Young's modulus

G:	Secant shear modulus
G_{max} :	Initial tangent shear modulus
M_* :	Moment in * direction
S_u :	Undrained shear strength
V_s :	Shear wave velocity
f_* :	Force in * direction
q_c :	Cone tip bearing resistance
u_* :	Displacement in * direction
θ_* :	Angular displacement in * direction
ϕ :	Internal friction angle
ε :	Strain
ν :	Poisson's ratio
γ_d :	Unit weights for zero water content.

Data Availability

The data used to support the findings of this study are available from the corresponding author upon request.

Conflicts of Interest

The authors declare that there are no conflicts of interest.

Acknowledgments

This study was partially supported by the Korea Institute of Energy Technology Evaluation and Planning (KETEP) (grant no. 20183010025730) (Development of diagnosis & maintenance technologies for gear train of a wind turbine) funded by the Korean Ministry of Trade, Industry & Energy (MOTIE) and a National Research Foundation of Korea (NRF) grant funded by the Korean government (MSIT) (no. 2020R1C1C1003829).

References

- [1] G. M. Joselin Herbert, S. Iniyar, E. Sreevalsan, and S. Rajapandian, "A review of wind energy technologies," *Renewable and Sustainable Energy Reviews*, vol. 11, no. 6, pp. 1117–1145, 2007.
- [2] C. Guo and D. Wang, "Frequency regulation and coordinated control for complex wind power systems," *Complexity*, vol. 2019, Article ID 8525397, 12 pages, 2019.
- [3] M. Nasiri, S. Mobayen, and Q. M. Zhu, "Super-twisting sliding mode control for gearless PMSG-based wind turbine," *Complexity*, vol. 2019, Article ID 6141607, 15 pages, 2019.
- [4] R. Jia, F. Ma, J. Dang, G. Liu, and H. Zhang, "Research on multidomain fault diagnosis of large wind turbines under complex environment," *Complexity*, vol. 2019, Article ID 2896850, 13 pages, 2019.
- [5] E. Otaola, A. J. Garrido, J. Lekube, and I. Garrido, "A comparative analysis of self-rectifying turbines for the mutriku oscillating water column energy plant," *Complexity*, vol. 2019, Article ID 636904, 14 pages, 2019.
- [6] S. V. Medina, J. A. Carta, and U. P. Ajenjo, "Performance sensitivity of a wind farm power curve model to different signals of the input layer of ANNs: case studies in the Canary islands," *Complexity*, vol. 2019, Article ID 2869149, 11 pages, 2019.
- [7] Z. Wang, L. Zheng, W. Du et al., "A novel method for intelligent fault diagnosis of bearing based on capsule neural

- network,” *Complexity*, vol. 2019, Article ID 6943234, 17 pages, 2019.
- [8] S. L. Clainche and J. M. Vega, “Analyzing nonlinear dynamics via data-driven dynamic mode decomposition-like methods,” *Complexity*, vol. 2018, Article ID 6920783, 21 pages, 2018.
 - [9] J. M. Torres and R. M. Aguilar, “Using deep learning to predict complex systems: a case study in wind farm generation,” *Complexity*, vol. 2018, Article ID 9327536, 10 pages, 2018.
 - [10] C. Walsh, *Offshore Wind in Europe—Key Trends and Statistics 2018*, WindEurope, Brussels, Belgium, 2019.
 - [11] European Environment Agency, “Europe’s onshore and offshore wind energy potential: an assessment of environmental and economic constraints,” Technical Report No. 6, European Environment Agency, Copenhagen, Denmark, 2009.
 - [12] J. Ryue, K. Baik, and J.-H. Lee, “An analysis of horizontal deformation of a pile in soil using a continuum soil model for the prediction of the natural frequency of offshore wind turbines,” *The Journal of the Acoustical Society of Korea*, vol. 35, no. 6, pp. 480–490, 2016.
 - [13] J. Jonkman, S. Butterfield, W. Musial, and G. Scott, “Definition of a 5 MW reference wind turbine for offshore system development,” Technical Report NREL/TP-500-38060, National Renewable Energy Laboratory, Golden, Co, USA, 2009.
 - [14] J. Ryue, K. Baik, and T.-R. Kim, “An analysis of horizontal deformation of a pile in soil using a beam-on-spring model for the prediction of the eigenfrequency of the offshore wind turbine,” *The Journal of the Acoustical Society of Korea*, vol. 35, no. 4, pp. 261–271, 2016.
 - [15] Center for Wind Energy at James Madison University, *Review of Options for Offshore Foundation Substructures*, Center for Wind Energy at James Madison University, Harrisonburg, VA, USA, 2012.
 - [16] L. B. Ibsen, M. Liingaard, and S. A. Nielsen, *Bucket Foundation, a Status*, Copenhagen offshore wind, Copenhagen, Denmark, 2005.
 - [17] K.-Y. Oh, W. Nam, M. S. Ryu, J.-Y. Kim, and B. I. Epureanu, “A review of foundations of offshore wind energy converters: current status and future perspectives,” *Renewable and Sustainable Energy Reviews*, vol. 88, pp. 16–36, 2018.
 - [18] G. T. Houlsby and B. W. Byrne, “Design procedures for installation of suction caissons in clay and other materials,” *Proceedings of the Institution of Civil Engineers—Geotechnical Engineering*, vol. 158, no. 2, pp. 75–82, 2005.
 - [19] G. T. Houlsby and B. W. Byrne, “Design procedures for installation of suction caissons in sand,” *Proceedings of the Institution of Civil Engineers—Geotechnical Engineering*, vol. 158, no. 3, pp. 135–144, 2005.
 - [20] G. T. Houlsby, R. B. Kelly, J. Huxtable, and B. W. Byrne, “Field trials of suction caissons in sand for offshore wind turbine foundations,” *Géotechnique*, vol. 56, no. 1, pp. 3–10, 2006.
 - [21] L. Wang, L. Yu, Z. Guo, and Z. Wang, “Seepage induced soil failure and its mitigation during suction caisson installation in silt,” *Journal of Offshore Mechanics and Arctic Engineering*, vol. 136, 2014.
 - [22] J. P. Doherty, G. T. Houlsby, and A. J. Deeks, “Stiffness of flexible caisson foundations embedded in nonhomogeneous elastic soil,” *Journal of Geotechnical and Geoenvironmental Engineering*, vol. 131, no. 12, pp. 1498–1508, 2005.
 - [23] M. Achmus, S. T. Akdag, and K. Thieken, “Load-bearing behavior of suction bucket foundations in sand,” *Applied Ocean Research*, vol. 43, pp. 157–165, 2013.
 - [24] F. A. Villalobos, B. W. Byrne, and G. T. Houlsby, “An experimental study of the drained capacity of suction caisson foundations under monotonic loading for offshore applications,” *Soils and Foundations*, vol. 49, no. 3, pp. 477–488, 2009.
 - [25] B. W. Byrne and G. T. Houlsby, “Experimental investigations of the response of suction caissons to transient combined loading,” *Journal of Geotechnical and Geoenvironmental Engineering*, vol. 130, no. 3, pp. 240–253, 2004.
 - [26] IEC 61400-3, *Wind Turbines—Part 3: Design Requirements for Offshore Wind Turbines*, IEC, Geneva, Switzerland, 2009.
 - [27] Det Norske Veritas, *Design of Offshore Wind Turbine Structures*, *Offshore Standard DNV-OS-J101*, DNV, Oslo, Norway, 2011.
 - [28] G. J. Rix and K. H. Stokoe, “Correlation of initial tangent modulus and cone penetration resistance,” in *Proceedings of the First International Symposium on Calibration Chamber Testing/ISOCCCTI*, pp. 351–362, New York, NY, USA, June 1991.
 - [29] Y.-H. Jung, K.-W. Lee, M.-M. Kim, H.-M. Kwon, and C.-K. Chung, “Evaluation of maximum shear modulus of silty sand in Songdo area in the west coast of Korea using various testing methods,” *Journal of the Korean Geotechnical Society*, vol. 21, no. 9, pp. 65–75, 2005.
 - [30] P. K. Robertson, “Interpretation of cone penetration tests—a unified approach,” *Canadian Geotechnical Journal*, vol. 46, no. 11, pp. 1337–1355, 2009.
 - [31] J. H. Schmertmann, “Static cone to compute static settlement over sand,” *Journal of the Soil Mechanics and Foundations Division*, vol. 96, no. 3, pp. 1011–1043, 1970.
 - [32] G. Baldi, R. Bellotti, N. Ghionna, and M. Jamiolkowski, *Stiffness of Sands from CPT, SPT and DMT—A Critical Review in Penetration Testing in the UK*, *Penetration Testing in the UK No. 42*, The Institution of Civil Engineers, Birmingham, UK, 1989.
 - [33] P. K. Robertson, D. J. Woeller, and W. D. L. Finn, “Seismic cone penetration test for evaluating liquefaction potential under cyclic loading,” *Canadian Geotechnical Journal*, vol. 29, no. 4, pp. 686–695, 1992.
 - [34] C. E. Fear and P. K. Robertson, “Estimating the undrained strength of sand: a theoretical framework,” *Canadian Geotechnical Journal*, vol. 32, no. 5, pp. 859–870, 1995.
 - [35] C. E. Wride, P. K. Robertson, K. W. Biggar et al., “Interpretation of in situ test results from the CANLEX sites,” *Canadian Geotechnical Journal*, vol. 37, no. 3, pp. 505–529, 2000.
 - [36] R. D. Andrus, N. P. Mohanan, P. Piratheepan, B. S. Ellis, and T. L. Holzer, “Predicting shear-wave velocity from cone penetration resistance,” in *Proceedings of the 4th International Conference on Earthquake Geotechnical Engineering 2007*, pp. 25–28, Thessaloniki, Greece, June 2007.
 - [37] R. Dobry, “Comparison between clean sand liquefaction charts based on penetration resistance and shear wave velocity,” in *Proceedings of the 5th International Conference on Recent Advances in Geotechnical Earthquake Engineering and Soil Dynamics 2010*, San Diego, CA, USA, 2010.
 - [38] L. Paoletti, Y. Hegazy, S. Monaco, and R. Piva, “Prediction of shear wave velocity for offshore sands using cpt data—Adriatic sea,” in *Second International Symposium on Cone Penetration Testing 2010*, pp. 1–8, Huntington Beach, CA, USA, 2010.
 - [39] M. Karray, G. Lefebvre, Y. Ethier, and A. Bigras, “Influence of particle size on the correlation between shear wave velocity and cone tip resistance,” *Canadian Geotechnical Journal*, vol. 48, no. 4, pp. 599–615, 2011.
 - [40] C.-G. Sun, C.-S. Cho, M. Son, and J. S. Shin, “Correlations between shear wave velocity and in-situ penetration test

- results for Korean soil deposits,” *Pure and Applied Geophysics*, vol. 170, no. 3, pp. 271–281, 2013.
- [41] KAIST, *A Report to Estimate Deformation Modulus of Seabed for Seashore Wind Turbine Construction & Commercialization Embedded Suction Bucket Support Structure*, KAIST, Daejeon, Republic of Korea, 2015.
- [42] M. Vucetic and R. Dobry, “Effect of soil plasticity on cyclic response,” *Journal of Geotechnical Engineering*, vol. 117, no. 1, pp. 89–107, 1991.
- [43] P. Simonini and S. Cola, “Use of piezocone to predict maximum stiffness of Venetian soils,” *Journal of Geotechnical and Geoenvironmental Engineering*, vol. 126, no. 4, pp. 378–382, 2000.
- [44] A. Jaime and M. P. Romo, “The Mexico earthquake of September 19, 1985—correlations between dynamic and static properties of Mexico city clay,” *Earthquake Spectra*, vol. 4, no. 4, pp. 787–804, 1988.
- [45] P. W. Mayne and G. J. Rix, “Correlations between shear wave velocity and cone tip resistance in natural clays,” *Soils and Foundations*, vol. 35, no. 2, pp. 107–110, 1995.
- [46] M. Long and S. Donohue, “Characterization of Norwegian marine clays with combined shear wave velocity and piezocone cone penetration test (CPTU) data,” *Canadian Geotechnical Journal*, vol. 47, no. 7, pp. 709–718, 2010.
- [47] L. Tonni and P. Simonini, “Shear wave velocity as function of cone penetration test measurements in sand and silt mixtures,” *Engineering Geology*, vol. 163, pp. 55–67, 2013.
- [48] G. Cai, A. J. Puppala, and S. Liu, “Characterization on the correlation between shear wave velocity and piezocone tip resistance of Jiangsu clays,” *Engineering Geology*, vol. 171, pp. 96–103, 2014.
- [49] S. S. Rao, *Mechanical Vibrations*, Prentice-Hall, Upper Saddle River, NJ, USA, 5th edition, 2011.
- [50] A. Klimchik, A. Pashkevich, S. Caro, and D. Chablat, “Stiffness matrix of manipulators with passive joints: computational aspects,” *IEEE Transactions on Robotics*, vol. 28, no. 4, pp. 955–958, 2012.
- [51] M. Jureczko, M. Pawlak, and A. Mężyk, “Optimisation of wind turbine blades,” *Journal of Materials Processing Technology*, vol. 167, no. 2-3, pp. 463–471, 2005.
- [52] K.-Y. Oh, J.-Y. Kim, J.-S. Lee, and K.-W. Ryu, “Wind resource assessment around Korean Peninsula for feasibility study on 100 MW class offshore wind farm,” *Renewable Energy*, vol. 42, pp. 217–226, 2012.
- [53] M. S. Ryu, J. S. Lee, D. J. Kwag, and S. Bang, “Comparison of two meteorological tower foundations for off-shore wind turbines,” in *Proceedings of the 26th International Ocean and Polar Engineering Conference*, Rhodes, Greece, July 2016.
- [54] H.-G. Moll, F. Vorpahl, and H.-G. Busmann, “Dynamics of support structures for offshore wind turbines in fully-coupled simulations—influence of water added mass on jacket mode shaper, natural frequencies and loads,” in *Proceedings of the European Wind Energy Conference and Exhibition*, Warsaw, Poland, April 2010.
- [55] Det Norske Veritas, *Modeling and Analysis of Marine Operations*, DNV, Oslo, Norway, 2011.
- [56] D. J. Ewins, *Modal Testing Theory, Practice and Application*, Research Studies Press Ltd., Boston, MA, USA, 2nd edition, 2000.
- [57] K.-Y. Oh, J.-Y. Kim, J.-K. Lee, M.-S. Ryu, and J.-S. Lee, “An assessment of wind energy potential at the demonstration offshore wind farm in Korea,” *Energy*, vol. 46, no. 1, pp. 555–563, 2012.
- [58] J. H. Atkinson and G. Salfors, “Experimental determination of soil properties,” in *Proceedings of the 10th ECSMFE 1991*, vol. 3, Florence, Italy, 1991.
- [59] W. Nam, K.-Y. Oh, and B. I. Epureanu, “Evolution of the dynamic response and its effects on the serviceability of offshore wind turbines with stochastic loads and soil degradation,” *Reliability Engineering & System Safety*, vol. 184, pp. 151–163, 2019.
- [60] L. V. Andersen, M. J. Vahdatirad, M. T. Sichani, and J. D. Sørensen, “Natural frequencies of wind turbines on monopile foundations in clayey soils—a probabilistic approach,” *Computers and Geotechnics*, vol. 43, pp. 1–11, 2012.
- [61] M. Damgaard, L. B. Ibsen, L. V. Andersen, and J. K. F. Andersen, “Cross-wind modal properties of offshore wind turbines identified by full scale testing,” *Journal of Wind Engineering and Industrial Aerodynamics*, vol. 116, pp. 94–108, 2013.
- [62] R. Shirzadeh, C. Devriendt, M. A. Bidakhvidi, and P. Guillaume, “Experimental and computational damping estimation of an offshore wind turbine on a monopile foundation,” *Journal of Wind Engineering and Industrial Aerodynamics*, vol. 120, pp. 96–106, 2013.
- [63] M. B. Zaaijer, “Foundation modelling to assess dynamic behaviour of offshore wind turbines,” *Applied Ocean Research*, vol. 28, no. 1, pp. 45–57, 2006.
- [64] R. Rubak and J. Thirstrup Petersen, “Monopile as part of aeroelastic wind turbine simulation code,” in *Proceedings of Copenhagen Offshore Wind*, Hellerup, Denmark, 2005.

Research Article

Investigation of Unmeasured Parameters Estimation for Distributed Control Systems

Hao Wang , Shousheng Xie, Weixuan Wang, Lei Wang, and Jingbo Peng

Aeronautics Engineering College, Air Force Engineering University, Xi an 710038, China

Correspondence should be addressed to Hao Wang; 15129822645@163.com

Received 11 September 2019; Revised 10 February 2020; Accepted 20 February 2020; Published 29 March 2020

Guest Editor: Wonhee Kim

Copyright © 2020 Hao Wang et al. This is an open access article distributed under the Creative Commons Attribution License, which permits unrestricted use, distribution, and reproduction in any medium, provided the original work is properly cited.

The problem of unmeasured parameters estimation for distributed control systems is studied in this paper. The Takagi–Sugeno fuzzy model which can appropriate any nonlinear systems is employed, and based on the model, an observer-based fuzzy H_∞ filter which has robustness against time-delay, external noise, and system uncertainties is designed. The sufficient condition for the existence of the desired filter is derived in terms of linear matrix inequalities (LMIs) solutions. Moreover, the underdetermined estimation problem in which the number of sensors available is typically less than the number of state variables to be estimated is specifically addressed. A systematic method is proposed to produce a model tuning parameter vector of appropriate dimension for the estimation of the filter, and the optimal transformation matrix is selected via iterative solution to minimize the estimated error. Finally, a simulation example for turbofan aeroengine is given to illustrate the effectiveness of the proposed method, and the estimated error is less than 2.5%.

1. Introduction

Along with the continuous development of computer and network technology, distributed control systems (DCSs) have gradually become a new trend and attract much attention [1, 2]. Compared with traditional point-to-point control systems, DCSs have advantages such as high reliability, reduced weight, low cost, and ease of maintenance [3, 4]. The DCSs provide the low-level processing function via intelligent unit and are more conducive to the implementation of complex control algorithms [5, 6]. However, the signal of DCSs is transmitted via bus network, which brings new challenges, such as networked-induced time-delay, packet dropout, and packet disordering.

In practice, many parameters are difficult to obtain due to the limitation of the system itself (for example, the sensors cannot be installed in poor working conditions) or cost constraints. Thus, the estimation of unmeasured system parameters is significantly important, since the

estimated parameters can not only be used in the design of controller but also for online monitoring [7, 8]. For the estimation problem of unmeasured system parameters, there are two main methods: (1) high-precision mathematical model [9]; (2) filtering technique and its extension methods [10]. The first method is to establish the mathematical model based on the structure of system to solve the unmeasured parameters. However, the modeling process is often cumbersome and complicated. And for some systems, the structure is extremely complicated and cannot be accurately modeled. Moreover, since this method generally requires iterative calculation, the amount of calculation is large.

For the second method, the estimation of unmeasured parameters is based on the value of measurable parameters using the filtering technique. Because this method uses a recursive algorithm, it is easy to implement on computer and meet the requirements of accuracy and real-time. Among the filters, the H_∞ filter stands out because it has robust stability against external noise without priori

knowledge of noise and precise mathematical model [11–13].

However, in some cases, the number of sensors available is typically less than the number of state variables to be estimated, which is an underdetermined estimation problem and cannot be solved directly. A common approach to address this shortcoming is to estimate a subset of the unknown parameters and assuming that others remain unchanged [14–16]. Although this approach enables online filter-based estimation, it will introduce error in the accuracy of overall estimation application. If any of the parameters which are assumed unchanged moves away from their nominal values, the estimates can no longer represent the true parameters. Litt [17] presented a novel approach based on singular value decomposition (SVD) that selects a model tuning parameter vector of low enough dimension. The model tuning parameter vector is constructed as a linear combination of all unmeasured parameters and the transformation matrix is generated by selecting the k most significant terms of singular values, where k is the number of available sensors. Similarly, the SVD is also used in [18] to determine which parts of the systems are observable if the whole system is unobservable. However, the unaccounted terms of singular values may also have great importance on the accuracy of overall estimation application even if they are small under some circumstances.

Furthermore, in [19], the transformation matrix is selected to minimize the theoretical mean squared estimation error at a steady-state open-loop linear design point. But the estimation results are affected by the parameter perturbation, and there are many limitations in application. Moreover, all the approaches above do not consider the impact of time-delay and uncertainties of the

system. Thus, it has great significance and practical value to propose a novel approach for the underdetermined estimation problem.

Besides, due to the strong nonlinear fitting characteristics of complex nonlinear systems, the Takagi–Sugeno (T-S) fuzzy model has been widely used in the study of nonlinear systems since it was proposed [20–22]. Thus in this paper, an observer-based fuzzy H_∞ filter is constructed, and the unmeasured parameters estimation problem for T-S fuzzy distributed control systems with time-delay and parameters perturbation is studied.

The contributions of this paper can be concluded as follows: (i) a model tuning parameter vector of appropriate dimension is produced for the estimation of the filter; (ii) a systematic method is proposed for the selection of optimal transformation matrix to minimize the estimated error via iterative solution; (iii) the parameter perturbation is considered, so that the designed filter has a certain range of margins of disturbance.

The remainder of this paper is organized as follows. Section 2 introduces the modeling method of DCSs and the observer-based fuzzy H_∞ filter. The main results are presented in Section 3, including the analysis and synthesis of the filtering error system. Section 4 presents the approach of optimal transformation matrix selection. Numerical simulation results are shown in Section 5 and finally conclusion and a discussion of further application of the method are presented.

2. Problem Formulation

Consider the DCSs with time-delay, which can be described by a class of T-S fuzzy model as follows:

Plant rule i : If $f_1(t)$ is Φ_1^i and \dots $f_g(t)$ is Φ_g^i , then

$$\begin{aligned}\dot{\mathbf{x}}(t) &= (\mathbf{A}_i + \Delta\mathbf{A}_i)\mathbf{x}(t) + (\mathbf{B}_i + \Delta\mathbf{B}_i)\mathbf{u}(t - \tau(t)) + \mathbf{L}_i\mathbf{h}(t) + (\mathbf{E}_{1i} + \Delta\mathbf{E}_{1i})\mathbf{w}(t), \\ \mathbf{y}(t) &= (\mathbf{C}_i + \Delta\mathbf{C}_i)\mathbf{x}(t) + (\mathbf{D}_i + \Delta\mathbf{D}_i)\mathbf{u}(t - \tau(t)) + \mathbf{M}_i\mathbf{h}(t) + (\mathbf{E}_{2i} + \Delta\mathbf{E}_{2i})\mathbf{w}(t), \\ \mathbf{z}(t) &= (\mathbf{F}_i + \Delta\mathbf{F}_i)\mathbf{x}(t) + (\mathbf{G}_i + \Delta\mathbf{G}_i)\mathbf{u}(t - \tau(t)) + \mathbf{N}_i\mathbf{h}(t) \\ \mathbf{x}(t) &= \phi(t), \\ t &\in [-\tau_m, 0],\end{aligned}\tag{1}$$

where $\Omega_j^i (i = 1, \dots, r; j = 1, \dots, g)$ denotes the fuzzy set, r denotes the number of IF-THEN rules, and $f_j(t)$ denotes the premise variable. $\mathbf{x}(t) \in \mathbb{R}^n$ is the vector of state variables; $\mathbf{u}(t) \in \mathbb{R}^m$ is the vector of control inputs; $\mathbf{y}(t) \in \mathbb{R}^p$ is the vector of measured outputs; $\mathbf{z}(t) \in \mathbb{R}^l$ is the vector of unmeasured outputs and $\mathbf{w}(t)$ is noise signal which belongs to $L_2(0, \infty)$. $\mathbf{A}_i, \mathbf{B}_i, \mathbf{C}_i, \mathbf{D}_i, \mathbf{E}_{1i}, \mathbf{E}_{2i}, \mathbf{F}_i, \mathbf{G}_i, \mathbf{L}_i, \mathbf{M}_i, \mathbf{N}_i$ are matrices with appropriate dimension. $\Delta\mathbf{A}_i, \Delta\mathbf{B}_i, \Delta\mathbf{C}_i, \Delta\mathbf{D}_i, \Delta\mathbf{E}_{1i}, \Delta\mathbf{E}_{2i},$

$\Delta\mathbf{F}_i, \Delta\mathbf{G}_i$ are unknown matrices which represent the time-varying uncertainties of the system. $\mathbf{h}(t) \in \mathbb{R}^q$ is the health parameters of system, which represents the physical characteristics of each component.

Remark 1. The health parameters are considered in this paper, because the performance degradation of each component in the system is inevitable during the

working process. And the system's performance is affected by the level of degradation, which is generally described in terms of unmeasured health parameters such as efficiencies and capacities related to each major module in most cases. If the health parameters move away from their nominal values, the shift in other performance variables will be induced. They may be treated as a set of biases and can be augmented to the system states.

It is assumed that both sensors and actuators are time-driven. The data has timestamp and is transmitted in a single-packet, and incorrect order of the data packet does not exist. Since time-delay is related to the bus load at a certain moment, it is assumed that the time-delay has an upper bound, which is $\tau(t) \leq \tau_m$ (under the above assumption, the upper bound of time-delay can be estimated; see [23] in detail). As a consequence, $\tau(t)$ can be modeled as a finite state Markov stochastic process on a finite set $\Lambda = \{1, 2, \dots, \tau_m\}$. The transition probability from $\tau(t) = i$ at time t to $\tau(t) = j (j \neq i)$ at time $t + \Delta t$ is

$$\Pr(\tau(t + \Delta t) = j | \tau(t) = i) = \begin{cases} \pi_{ij}\Delta t + o(\Delta t), & i \neq j, \\ 1 + \pi_{ii}\Delta t + o(\Delta t), & i = j, \end{cases} \quad (2)$$

where $\Delta t > 0$ and $\lim_{\Delta t \rightarrow 0} (o(\Delta t)/\Delta t) = 0$. $\pi_{ij} \geq 0$ is the transition probability rates from $\tau(t) = i$ at time t to $\tau(t) = j (j \neq i)$ at time $t + \Delta t$, and there is $\sum_{j=1, j \neq i}^{\tau_m} \pi_{ij} = -\pi_{ii}$.

The state feedback controller is applied in this paper, which is $\mathbf{u}(t) = \mathbf{K}_c \mathbf{x}(t)$. Then, by fuzzy blending, the global fuzzy augmented model can be obtained as follows:

$$\left\{ \begin{array}{l} \dot{\mathbf{x}}_h(t) = \sum_{i=1}^r h_i(f(t)) [(\mathbf{A}_{hi} + \Delta \mathbf{A}_{hi})\mathbf{x}_h(t) + (\mathbf{B}_{hi} + \Delta \mathbf{B}_{hi})\mathbf{x}_h \\ \quad \cdot (t - \tau(t)) + (\mathbf{E}_{h1i} + \Delta \mathbf{E}_{h1i})\mathbf{w}(t)], \\ \mathbf{y}(t) = \sum_{i=1}^r h_i(f(t)) [(\mathbf{C}_{hi} + \Delta \mathbf{C}_{hi})\mathbf{x}_h(t) + (\mathbf{D}_{hi} + \Delta \mathbf{D}_{hi})\mathbf{x}_h \\ \quad \cdot (t - \tau(t)) + (\mathbf{E}_{2i} + \Delta \mathbf{E}_{2i})\mathbf{w}(t)], \\ \mathbf{z}(t) = \sum_{i=1}^r h_i(f(t)) [(\mathbf{F}_{hi} + \Delta \mathbf{F}_{hi})\mathbf{x}_h(t) + (\mathbf{G}_{hi} + \Delta \mathbf{G}_{hi}) \\ \quad \cdot \mathbf{x}_h(t - \tau(t))], \\ \mathbf{x}_h(t) = \begin{bmatrix} \phi(t) \\ 0 \end{bmatrix}, \\ t \in [-\tau_m, 0], \end{array} \right. \quad (3)$$

where

$$\begin{aligned} \mathbf{x}(t) &= \begin{bmatrix} \mathbf{x}(t) \\ \mathbf{h}(t) \end{bmatrix}, \\ \mathbf{A}_{hi} &= \begin{bmatrix} \mathbf{A}_i & \mathbf{L}_i \\ 0 & \mathbf{I} \end{bmatrix}, \\ \mathbf{B}_{hi} &= \begin{bmatrix} \mathbf{B}_i \mathbf{K}_c & 0 \\ 0 & 0 \end{bmatrix}, \\ \Delta \mathbf{A}_{hi} &= \begin{bmatrix} \Delta \mathbf{A}_i & 0 \\ 0 & 0 \end{bmatrix}, \\ \Delta \mathbf{B}_{hi} &= \begin{bmatrix} \Delta \mathbf{B}_i \mathbf{K}_c & 0 \\ 0 & 0 \end{bmatrix}, \\ \mathbf{E}_{h1i} &= \begin{bmatrix} \mathbf{E}_{1i} \\ 0 \end{bmatrix}, \\ \mathbf{C}_{hi} &= [\mathbf{C}_i \quad \mathbf{M}_i], \\ \Delta \mathbf{C}_{hi} &= [\Delta \mathbf{C}_i \quad 0], \\ \Delta \mathbf{E}_{h1i} &= \begin{bmatrix} \Delta \mathbf{E}_{1i} \\ 0 \end{bmatrix}, \\ \mathbf{D}_{hi} &= [\mathbf{D}_i \mathbf{K}_c \quad 0], \\ \Delta \mathbf{D}_{hi} &= [\Delta \mathbf{D}_i \mathbf{K}_c \quad 0], \\ \mathbf{E}_{h2i} &= \mathbf{E}_{2i}, \\ \Delta \mathbf{E}_{h2i} &= \Delta \mathbf{E}_{2i}, \\ \mathbf{F}_{hi} &= [\mathbf{F}_i \quad \mathbf{N}_i], \\ \mathbf{G}_{hi} &= [\mathbf{G}_i \mathbf{K}_c \quad 0], \\ \Delta \mathbf{F}_{hi} &= [\Delta \mathbf{F}_i \quad 0], \\ \Delta \mathbf{G}_{hi} &= [\Delta \mathbf{G}_i \mathbf{K}_c \quad 0], \\ h_i(f(t)) &= \frac{\vartheta_i(f(t))}{\sum_{i=1}^r \vartheta_i(f(t))}, \\ \vartheta_i(f(t)) &= \prod_{j=1}^2 \Omega_j^i(f(t)). \end{aligned} \quad (4)$$

For the underdetermined estimation problem, a low-dimensional model tuning parameter vector $\mathbf{q}(t)$ is produced to represent the information of high-dimensional health parameter vector $\mathbf{h}(t)$. The model tuning parameter vector $\mathbf{q}(t)$ is constructed as a linear combination of all health parameters, given by

$$\mathbf{q}(t) = \mathbf{V}^* \mathbf{h}(t), \quad (5)$$

where $\mathbf{h}(t) \in \mathbb{R}^q$, $\mathbf{q}(t) \in \mathbb{R}^k$, $k < q$, and \mathbf{V}^* is a $k \times q$ transformation matrix, which is applied to construct the tuning parameter vector. The selection of optimal \mathbf{V}^* is obtained in Section 4.

Thus, the estimation of the health parameters $\hat{\mathbf{h}}$ can be obtained as

$$\hat{\mathbf{h}} = \mathbf{V}^{*\dagger} \mathbf{q}, \quad (6)$$

where $\mathbf{V}^{*\dagger}$ is the pseudoinverse of \mathbf{V}^* .

The final augmented dynamic fuzzy model can be rewritten as

$$\begin{cases} \dot{\mathbf{x}}_q(t) = \sum_{i=1}^r h_i(f(t)) [(\mathbf{A}_{qi} + \Delta\mathbf{A}_{qi})\mathbf{x}_q(t) + (\mathbf{B}_{qi} + \Delta\mathbf{B}_{qi})\mathbf{x}_q(t - \tau(t)) + (\mathbf{E}_{q1i} + \Delta\mathbf{E}_{q1i})\mathbf{w}(t)], \\ \mathbf{y}(t) = \sum_{i=1}^r h_i(f(t)) [(\mathbf{C}_{qi} + \Delta\mathbf{C}_{qi})\mathbf{x}_q(t) + (\mathbf{D}_{qi} + \Delta\mathbf{D}_{qi})\mathbf{x}_q(t - \tau(t)) + (\mathbf{E}_{2i} + \Delta\mathbf{E}_{2i})\mathbf{w}(t)], \\ \mathbf{z}(t) = \sum_{i=1}^r h_i(f(t)) [(\mathbf{F}_{qi} + \Delta\mathbf{F}_{qi})\mathbf{x}_q(t) + (\mathbf{G}_{qi} + \Delta\mathbf{G}_{qi})\mathbf{x}_q(t - \tau(t))], \\ \mathbf{x}_q(t) = \begin{bmatrix} \phi(t) \\ 0 \end{bmatrix}, \\ t \in [-\tau_m, 0], \end{cases} \quad (7)$$

where

$$\begin{aligned} \mathbf{x}_q(t) &= \begin{bmatrix} \mathbf{x}(t) \\ \mathbf{q}(t) \end{bmatrix}, \\ \mathbf{A}_{qi} &= \begin{bmatrix} \mathbf{A}_i & \mathbf{L}_i \mathbf{V}^{*\dagger} \\ 0 & \mathbf{I} \end{bmatrix}, \\ \mathbf{E}_{q1i} &= \begin{bmatrix} \mathbf{E}_{1i} \\ 0 \end{bmatrix}, \\ \Delta\mathbf{A}_{qi} &= \begin{bmatrix} \Delta\mathbf{A}_i & 0 \\ 0 & 0 \end{bmatrix}, \\ \mathbf{B}_{qi} &= \begin{bmatrix} \mathbf{B}_i \mathbf{K}_c & 0 \\ 0 & 0 \end{bmatrix}, \\ \Delta\mathbf{B}_{qi} &= \begin{bmatrix} \Delta\mathbf{B}_i \mathbf{K}_c & 0 \\ 0 & 0 \end{bmatrix}, \\ \Delta\mathbf{E}_{q1i} &= \begin{bmatrix} \Delta\mathbf{E}_{1i} \\ 0 \end{bmatrix}, \\ \mathbf{C}_{qi} &= [\mathbf{C}_i \quad \mathbf{M}_i \mathbf{V}^{*\dagger}], \\ \Delta\mathbf{C}_{qi} &= [\Delta\mathbf{C}_i \quad 0], \\ \mathbf{D}_{qi} &= [\mathbf{D}_i \mathbf{K}_c \quad 0], \\ \Delta\mathbf{D}_{qi} &= [\Delta\mathbf{D}_i \mathbf{K}_c \quad 0], \\ \mathbf{E}_{q2i} &= \mathbf{E}_{2i}, \\ \Delta\mathbf{E}_{q2i} &= \Delta\mathbf{E}_{2i}, \\ \mathbf{F}_{qi} &= [\mathbf{F}_i \quad \mathbf{N}_i \mathbf{V}^{*\dagger}], \\ \mathbf{G}_{qi} &= [\mathbf{G}_i \mathbf{K}_c \quad 0], \\ \Delta\mathbf{F}_{qi} &= [\Delta\mathbf{F}_i \quad 0], \\ \Delta\mathbf{G}_{qi} &= [\Delta\mathbf{G}_i \mathbf{K}_c \quad 0]. \end{aligned} \quad (8)$$

Remark 2. If the model tuning parameter vector is of appropriate dimension, the augmented system (7) is observable and the observer-based filter can be used to estimate the unknown health and performance parameters. And the key of the estimation is to find the optimal transformation matrix so that the low dimension tuning vector can represent as much of the information as possible. Moreover, different from the method in [17–19], the solution of the optimal transformation matrix is transformed into an optimization problem.

It is assumed that the uncertainties of the system can be described in the following form:

$$\begin{bmatrix} \Delta\mathbf{A}_{qi} & \Delta\mathbf{B}_{qi} & \Delta\mathbf{E}_{q1i} & \Delta\mathbf{F}_{qi}^T \\ \Delta\mathbf{C}_{qi} & \Delta\mathbf{D}_{qi} & \Delta\mathbf{E}_{q2i} & \Delta\mathbf{G}_{qi}^T \end{bmatrix} = \begin{bmatrix} \mathbf{U}_{1i} \\ \mathbf{U}_{2i} \end{bmatrix} \mathbf{S}_i [\mathbf{V}_{1i} \quad \mathbf{V}_{2i} \quad \mathbf{V}_{3i} \quad \mathbf{V}_{4i}], \quad (9)$$

where \mathbf{U}_{1i} , \mathbf{U}_{2i} , \mathbf{V}_{1i} , \mathbf{V}_{2i} , \mathbf{V}_{3i} , \mathbf{V}_{4i} are known matrices and \mathbf{S}_i is a time-varying unknown matrix which satisfies

$$\mathbf{S}_i^T \mathbf{S}_i \leq \mathbf{I}. \quad (10)$$

Then the following observer-based fuzzy filter is constructed:

$$\begin{aligned} \dot{\hat{\mathbf{x}}}(t) &= \sum_{i=1}^r h_i(f(t)) [(\mathbf{A}_{qi} + \Delta\mathbf{A}_{qi})\hat{\mathbf{x}}(t) \\ &\quad + (\mathbf{B}_{qi} + \Delta\mathbf{B}_{qi})\hat{\mathbf{x}}(t - \tau(t)) + \mathbf{K}_i(\mathbf{y}(t) - \hat{\mathbf{y}}(t))], \\ \hat{\mathbf{y}}(t) &= \sum_{i=1}^r h_i(f(t)) [(\mathbf{C}_{qi} + \Delta\mathbf{C}_{qi})\hat{\mathbf{x}}(t) + (\mathbf{D}_{qi} + \Delta\mathbf{D}_{qi})\hat{\mathbf{x}}(t - \tau(t))], \\ \hat{\mathbf{z}}(t) &= \sum_{i=1}^r h_i(f(t)) [(\mathbf{F}_{qi} + \Delta\mathbf{F}_{qi})\hat{\mathbf{x}}(t) + (\mathbf{G}_{qi} + \Delta\mathbf{G}_{qi})\hat{\mathbf{x}}(t - \tau(t))], \end{aligned} \quad (11)$$

where $\tilde{\mathbf{x}}(t)$ is the filter state, and $\hat{\mathbf{y}}(t)$ and $\hat{\mathbf{z}}(t)$ are the filter outputs. \mathbf{K}_i is the filter parameter to be determined.

The estimation error of state is

$$\begin{aligned}\tilde{\mathbf{x}}(t) &= \mathbf{x}_q(t) - \hat{\mathbf{x}}(t) \\ &= (\mathbf{A}_{qi} - \mathbf{K}_i \mathbf{C}_{qi} + \Delta \mathbf{A}_{qi} - \mathbf{K}_i \Delta \mathbf{C}_{qi}) \tilde{\mathbf{x}}(t) \\ &\quad + (\mathbf{B}_{qi} - \mathbf{K}_i \mathbf{D}_{qi} + \Delta \mathbf{B}_{qi} - \mathbf{K}_i \Delta \mathbf{D}_{qi}) \tilde{\mathbf{x}}(t - \tau(t)) \\ &\quad + (\mathbf{E}_{q1i} - \mathbf{K}_i \mathbf{E}_{2i} + \Delta \mathbf{E}_{q1i} - \mathbf{K}_i \Delta \mathbf{E}_{2i}) \mathbf{w}(t).\end{aligned}\quad (12)$$

Define $\boldsymbol{\xi}(t) = [\mathbf{x}_q^T \tilde{\mathbf{x}}^T(t)]^T$ and $\mathbf{e}(t) = \mathbf{z}(t) - \hat{\mathbf{z}}(t)$, and the filtering error system is given by

$$\begin{aligned}\dot{\boldsymbol{\xi}}(t) &= \sum_{i=1}^r h_i(f(t)) [(\bar{\mathbf{A}}_i + \Delta \bar{\mathbf{A}}_i) \boldsymbol{\xi}(t) + (\bar{\mathbf{B}}_i + \Delta \bar{\mathbf{B}}_i) \boldsymbol{\xi}(t - \tau(t)) \\ &\quad + (\bar{\mathbf{E}}_i + \Delta \bar{\mathbf{E}}_i) \mathbf{w}(t)], \\ \dot{\mathbf{e}}(t) &= \sum_{i=1}^r h_i(f(t)) [(\bar{\mathbf{F}}_i + \Delta \bar{\mathbf{F}}_i) \boldsymbol{\xi}(t) + (\bar{\mathbf{G}}_i + \Delta \bar{\mathbf{G}}_i) \boldsymbol{\xi}(t - \tau(t))],\end{aligned}\quad (13)$$

where

$$\begin{aligned}\bar{\mathbf{A}}_i &= \begin{bmatrix} \mathbf{A}_{qi} & 0 \\ 0 & \mathbf{A}_{qi} - \mathbf{K}_i \mathbf{C}_{qi} \end{bmatrix}, \\ \bar{\mathbf{B}}_i &= \begin{bmatrix} \mathbf{B}_{qi} & 0 \\ 0 & \mathbf{B}_{qi} - \mathbf{K}_i \mathbf{D}_{qi} \end{bmatrix}, \\ \Delta \bar{\mathbf{A}}_i &= \begin{bmatrix} \Delta \mathbf{A}_{qi} & 0 \\ 0 & \Delta \mathbf{A}_{qi} - \mathbf{K}_i \Delta \mathbf{C}_{qi} \end{bmatrix}, \\ \bar{\mathbf{E}}_i &= \begin{bmatrix} \mathbf{E}_{q1i} \\ \mathbf{E}_{q1i} - \mathbf{K}_i \mathbf{E}_{2i} \end{bmatrix}, \\ \Delta \bar{\mathbf{B}}_i &= \begin{bmatrix} \Delta \mathbf{B}_{qi} & 0 \\ 0 & \Delta \mathbf{B}_{qi} - \mathbf{K}_i \Delta \mathbf{D}_{qi} \end{bmatrix}, \\ \Delta \bar{\mathbf{E}}_i &= \begin{bmatrix} \Delta \mathbf{E}_{q1i} \\ \Delta \mathbf{E}_{q1i} - \mathbf{K}_i \Delta \mathbf{E}_{2i} \end{bmatrix}, \\ \bar{\mathbf{F}}_i &= [0 \ \mathbf{F}_{qi}], \\ \Delta \bar{\mathbf{F}}_i &= [0 \ \Delta \mathbf{F}_{qi}], \\ \bar{\mathbf{G}}_i &= [0 \ \mathbf{G}_{qi}], \\ \Delta \bar{\mathbf{G}}_i &= [0 \ \Delta \mathbf{G}_{qi}].\end{aligned}\quad (14)$$

Define the following parameters:

$$\begin{aligned}\bar{\mathbf{A}} &= \sum_{i=1}^r h_i(f(t)) \bar{\mathbf{A}}_i, \\ \Delta \bar{\mathbf{A}} &= \sum_{i=1}^r h_i(f(t)) \Delta \bar{\mathbf{A}}_i, \\ \bar{\mathbf{B}} &= \sum_{i=1}^r h_i(f(t)) \bar{\mathbf{B}}_i, \\ \Delta \bar{\mathbf{B}} &= \sum_{i=1}^r h_i(f(t)) \Delta \bar{\mathbf{B}}_i, \\ \bar{\mathbf{E}} &= \sum_{i=1}^r h_i(f(t)) \bar{\mathbf{E}}_i, \\ \Delta \bar{\mathbf{E}} &= \sum_{i=1}^r h_i(f(t)) \Delta \bar{\mathbf{E}}_i, \\ \bar{\mathbf{F}} &= \sum_{i=1}^r h_i(f(t)) \bar{\mathbf{F}}_i, \\ \Delta \bar{\mathbf{F}} &= \sum_{i=1}^r h_i(f(t)) \Delta \bar{\mathbf{F}}_i, \\ \bar{\mathbf{G}} &= \sum_{i=1}^r h_i(f(t)) \bar{\mathbf{G}}_i, \\ \Delta \bar{\mathbf{G}} &= \sum_{i=1}^r h_i(f(t)) \Delta \bar{\mathbf{G}}_i.\end{aligned}\quad (15)$$

The goal is to design a filter in form of (11) so that the filtering error system can meet the following requirements simultaneously:

- (1) The filtering error system is asymptotically stable when $\mathbf{w}(t) = 0$
- (2) Under the zero initial condition, the filtering error system satisfies

$$\|\mathbf{e}(t)\|_2 \leq \gamma \|\mathbf{w}(t)\|_2, \quad (16)$$

for any nonzero $\mathbf{w}(t) \in L_2(0, \infty)$.

3. Main Results

In this section, the sufficient condition for the existence of the desired filter is derived in terms of LMIs solutions. Before proceeding with the study, the following Lemma is needed.

Lemma 1 (see [24]). *$\mathbf{D}, \mathbf{E}, \mathbf{F}$ are real matrices with appropriate dimensions, and \mathbf{F} is a time-varying unknown matrix which satisfies $\mathbf{F}^T \mathbf{F} \leq \mathbf{I}$. Then for a scalar $\varepsilon > 0$, the following inequality*

$$\mathbf{D}\mathbf{F} + \mathbf{E} + \mathbf{E}^T \mathbf{F}^T \mathbf{D}^T \leq \varepsilon^{-1} \mathbf{D}\mathbf{D}^T + \varepsilon \mathbf{E}^T \mathbf{E}, \quad (17)$$

always holds.

Theorem 1. If there exist positive matrices $\mathbf{P} > 0, \mathbf{Q} > 0, \mathbf{R} > 0$, and matrix \mathbf{W} such that the following inequality holds:

$$\bar{\Psi} = \begin{bmatrix} \Gamma & \mathbf{P}(\bar{\mathbf{B}} + \Delta\bar{\mathbf{B}}) + \mathbf{W} & \mathbf{P}(\bar{\mathbf{E}} + \Delta\bar{\mathbf{E}}) & \tau_m \mathbf{W} & \tau_m (\bar{\mathbf{A}} + \Delta\bar{\mathbf{A}})^T \mathbf{R} & (\bar{\mathbf{F}} + \Delta\bar{\mathbf{F}})^T \\ * & -\mathbf{Q} & 0 & 0 & \tau_m (\bar{\mathbf{B}} + \Delta\bar{\mathbf{B}})^T \mathbf{R} & (\bar{\mathbf{G}} + \Delta\bar{\mathbf{G}})^T \\ * & * & -\gamma^2 \mathbf{I} & 0 & \tau_m (\bar{\mathbf{E}} + \Delta\bar{\mathbf{E}})^T \mathbf{R} & 0 \\ * & * & * & -\tau_m \mathbf{R} & 0 & 0 \\ * & * & * & * & -\tau_m \mathbf{R} & 0 \\ * & * & * & * & * & -\mathbf{I} \end{bmatrix} < 0, \quad (18)$$

where

$$\Gamma = \mathbf{P}(\bar{\mathbf{A}} + \Delta\bar{\mathbf{A}}) + (\bar{\mathbf{A}} + \Delta\bar{\mathbf{A}})^T \mathbf{P} + \mathbf{Q} - \mathbf{W} - \mathbf{W}^T, \quad (19)$$

then the filtering error system is asymptotically stable and the prescribed H_∞ performance γ can be guaranteed.

Proof. Select the Lyapunov function as

$$V(t) = V_1(t) + V_2(t) + V_3(t), \quad (20)$$

where

$$\begin{aligned} V_1(t) &= \xi^T(t) \mathbf{P} \xi(t), \\ V_2(t) &= \int_{t-\tau(t)}^t \xi^T(\alpha) \mathbf{Q} \xi(\alpha) d\alpha, \\ V_3(t) &= \int_{-\tau_m}^0 \int_{t+\beta}^t \dot{\xi}^T(\alpha) \mathbf{R} \dot{\xi}(\alpha) d\alpha d\beta. \end{aligned} \quad (21)$$

When $w(t) = 0$, the derivation of $V(t)$ is

$$\begin{aligned} \dot{V}_1(t) &= 2\xi^T(t) \mathbf{P} ((\bar{\mathbf{A}} + \Delta\bar{\mathbf{A}})\xi(t) + (\bar{\mathbf{B}} + \Delta\bar{\mathbf{B}})\xi(t - \tau(t))), \\ \dot{V}_2(t) &\leq \xi^T(t) \mathbf{Q} \xi(t) - \xi^T(t - \tau(t)) \mathbf{Q} \xi(t - \tau(t)), \\ \dot{V}_3(t) &\leq \tau_m \dot{\xi}^T(t) \mathbf{R} \dot{\xi}(t) - \int_{t-\tau(t)}^t \dot{\xi}^T(\alpha) \mathbf{R} \dot{\xi}(\alpha) d\alpha. \end{aligned} \quad (22)$$

It is obvious that there is

$$\xi(t - \tau(t)) = \xi(t) - \int_{t-\tau(t)}^t \dot{\xi}^T(\alpha) d\alpha. \quad (23)$$

Thus, $V(t)$ can be further rewritten as

$$\begin{aligned} \dot{V}(t) &\leq 2\xi^T(t) \mathbf{P} ((\bar{\mathbf{A}} + \Delta\bar{\mathbf{A}})\xi(t) + (\bar{\mathbf{B}} + \Delta\bar{\mathbf{B}})\xi(t - \tau(t))) + \xi^T(t) \mathbf{Q} \xi(t) - \xi^T(t - \tau(t)) \mathbf{Q} \xi(t - \tau(t)) \\ &\quad + \tau_m \dot{\xi}^T(t) \mathbf{R} \dot{\xi}(t) - \int_{t-\tau(t)}^t \dot{\xi}^T(\alpha) \mathbf{R} \dot{\xi}(\alpha) d\alpha + 2\xi^T(t) \mathbf{W} \left(\xi^T(t - \tau(t)) - \xi^T(t) + \int_{t-\tau(t)}^t \dot{\xi}^T(\alpha) d\alpha \right) \\ &\leq \frac{1}{\tau(t)} \int_{t-\tau(t)}^t \begin{bmatrix} \xi(t) \\ \xi(t - \tau(t)) \\ \dot{\xi}(\alpha) \end{bmatrix}^T \Psi_0 \begin{bmatrix} \xi(t) \\ \xi(t - \tau(t)) \\ \dot{\xi}(\alpha) \end{bmatrix}, \end{aligned} \quad (24)$$

where

$$\Psi_0 = \left(\begin{bmatrix} \Gamma & \mathbf{P}(\bar{\mathbf{B}} + \Delta\bar{\mathbf{B}}) + \mathbf{W} & \tau_m \mathbf{W} \\ * & -\mathbf{Q} & 0 \\ * & * & -\tau_m \mathbf{R} \end{bmatrix} + \tau_m \begin{bmatrix} (\bar{\mathbf{A}} + \Delta\bar{\mathbf{A}})^T \\ (\bar{\mathbf{B}} + \Delta\bar{\mathbf{B}})^T \\ 0 \end{bmatrix} \mathbf{R} \begin{bmatrix} (\bar{\mathbf{A}} + \Delta\bar{\mathbf{A}})^T \\ (\bar{\mathbf{B}} + \Delta\bar{\mathbf{B}})^T \\ 0 \end{bmatrix} \right)^T. \quad (25)$$

By the Schur complement, if the inequality (24) holds, it can be obtained that there is $\Psi_0 < 0$. Thus, there is $\dot{V}(t) < 0$ and the filtering error system is asymptotically stable.

Secondly, define a new function

$$J = \int_0^T [\mathbf{e}^T(t) \mathbf{e}(t) - \gamma^2 \mathbf{w}^T(t) \mathbf{w}(t)] dt, \quad (26)$$

where T is a scalar which satisfies $T > 0$.

Thus, under the zero initial condition, there is

$$\begin{aligned}
J &= \int_0^T [\mathbf{e}^T(t)\mathbf{e}(t) - \gamma^2 \mathbf{w}^T(t)\mathbf{w}(t) + \dot{V}(t)] dt - V(T) \\
&\leq \int_0^T [\mathbf{e}^T(t)\mathbf{e}(t) - \gamma^2 \mathbf{w}^T(t)\mathbf{w}(t) + \dot{V}(t)] dt \\
&\leq \begin{bmatrix} \xi(t) \\ \xi(t - \tau(t)) \\ w(t) \\ \dot{\xi}(\alpha) \end{bmatrix}^T \Psi_1 \begin{bmatrix} \xi(t) \\ \xi(t - \tau(t)) \\ w(t) \\ \dot{\xi}(\alpha) \end{bmatrix}, \tag{27}
\end{aligned}$$

where

$$\begin{aligned}
\Psi_1 &= \begin{bmatrix} \Gamma & \mathbf{P}(\bar{\mathbf{B}} + \Delta\bar{\mathbf{B}}) + \mathbf{W} & \mathbf{P}(\bar{\mathbf{E}} + \Delta\bar{\mathbf{E}}) & \tau_m \mathbf{W} \\ * & -\mathbf{Q} & 0 & 0 \\ * & * & -\gamma^2 \mathbf{I} & 0 \\ * & * & * & -\tau_m \mathbf{R} \end{bmatrix} \\
&+ \tau_m \begin{bmatrix} (\bar{\mathbf{A}} + \Delta\bar{\mathbf{A}})^T \\ (\bar{\mathbf{B}} + \Delta\bar{\mathbf{B}})^T \\ (\bar{\mathbf{E}} + \Delta\bar{\mathbf{E}})^T \\ 0 \end{bmatrix} \mathbf{R} \begin{bmatrix} (\bar{\mathbf{A}} + \Delta\bar{\mathbf{A}})^T \\ (\bar{\mathbf{B}} + \Delta\bar{\mathbf{B}})^T \\ (\bar{\mathbf{E}} + \Delta\bar{\mathbf{E}})^T \\ 0 \end{bmatrix}^T \\
&+ \begin{bmatrix} (\bar{\mathbf{F}} + \Delta\bar{\mathbf{F}})^T \\ (\bar{\mathbf{G}} + \Delta\bar{\mathbf{G}})^T \\ 0 \\ 0 \end{bmatrix} \begin{bmatrix} (\bar{\mathbf{F}} + \Delta\bar{\mathbf{F}})^T \\ (\bar{\mathbf{G}} + \Delta\bar{\mathbf{G}})^T \\ 0 \\ 0 \end{bmatrix}^T. \tag{28}
\end{aligned}$$

According to the Schur complement, it follows that

$$\Psi_1 < 0 \Leftrightarrow \bar{\Psi} < 0. \tag{29}$$

Thus, if the inequality $\bar{\Psi} < 0$ holds, there is $J < 0$ and equation (16) holds for any nonzero $\mathbf{w}(t) \in L_2[0, \infty]$. The proof is completed.

Theorem 2. For a given scalar $\gamma > 0$, the filtering problem is solvable under the conditions above with a H_∞ performance level γ , if there exist positive matrices $\mathbf{P}_1, \mathbf{P}_2, \mathbf{Q}_1, \mathbf{Q}_2, \mathbf{R}_1, \mathbf{R}_2$, matrices $\mathbf{W}_1, \mathbf{W}_2, \mathbf{Z}_i$ and scalars $\varepsilon_{1i}, \varepsilon_{2i}, \varepsilon_{3ij}, \varepsilon_{4i}, \varepsilon_{5i} > 0 (1 \leq i \leq j \leq r)$ such that the following inequalities hold:

$$\Omega_{ii} < 0, \quad i = 1, 2, \dots, r, \tag{30}$$

$$\Omega_{ij} + \Omega_{ji} < 0, \quad i < j, i, j = 1, 2, \dots, r, \tag{31}$$

where

$$\begin{aligned}
\Theta_{1i} &= \begin{bmatrix} (\mathbf{P}_1 \mathbf{U}_{1i})^T & (\mathbf{P}_2 \mathbf{U}_{1i})^T & 0 & 0 & 0 & 0 & 0 & (\tau_m \mathbf{R}_1 \mathbf{U}_{1i})^T & (\tau_m \mathbf{R}_2 \mathbf{U}_{1i})^T & 0 \end{bmatrix}^T, \\
\Xi_{1i} &= \begin{bmatrix} \mathbf{V}_{1i} & 0 & \mathbf{V}_{2i} & 0 & \mathbf{V}_{3i} & 0 & 0 & 0 & 0 & 0 \end{bmatrix}, \\
\Theta_{2i} &= \begin{bmatrix} 0 & (\mathbf{P}_2 \mathbf{U}_{1i})^T & 0 & 0 & 0 & 0 & 0 & (\tau_m \mathbf{R}_2 \mathbf{U}_{1i})^T & 0 \end{bmatrix}^T, \\
\Xi_{2i} &= \begin{bmatrix} 0 & \mathbf{V}_{1i} & 0 & \mathbf{V}_{2i} & 0 & 0 & 0 & 0 & 0 & 0 \end{bmatrix}, \\
\Theta_{3ij} &= \begin{bmatrix} 0 & (\mathbf{P}_2 \mathbf{K}_i \mathbf{U}_{2i})^T & 0 & 0 & 0 & 0 & 0 & (\tau_m \mathbf{R}_2 \mathbf{K}_i \mathbf{U}_{2i})^T & 0 \end{bmatrix}^T, \\
\Xi_{3i} &= \begin{bmatrix} 0 & \mathbf{V}_{1i} & 0 & \mathbf{V}_{2i} & \mathbf{V}_{3i} & 0 & 0 & 0 & 0 & 0 \end{bmatrix}, \\
\Theta_{4i} &= \begin{bmatrix} 0 & 0 & 0 & 0 & 0 & 0 & 0 & 0 & 0 & \mathbf{U}_{1i}^T \end{bmatrix}^T, \\
\Xi_{4i} &= \begin{bmatrix} 0 & \mathbf{V}_{4i} & 0 & 0 & 0 & 0 & 0 & 0 & 0 & 0 \end{bmatrix}, \\
\Theta_{5i} &= \begin{bmatrix} 0 & 0 & 0 & 0 & 0 & 0 & 0 & 0 & 0 & \mathbf{U}_{2i}^T \end{bmatrix}^T, \\
\Xi_{5i} &= \begin{bmatrix} 0 & 0 & 0 & \mathbf{V}_{4i} & 0 & 0 & 0 & 0 & 0 & 0 \end{bmatrix}, \\
\Gamma_{11} &= \mathbf{P}_1 \mathbf{A}_{qi} + \mathbf{A}_{qi}^T \mathbf{P}_1 + \mathbf{Q}_1 - \mathbf{W}_1 - \mathbf{W}_1^T, \\
\Gamma_{22} &= \mathbf{P}_2 \mathbf{A}_{qi} - \mathbf{Z}_{1i} \mathbf{C}_{qi} + \mathbf{A}_{qi}^T \mathbf{P}_2 - \mathbf{C}_{qi}^T \mathbf{Z}_{1i}^T + \mathbf{Q}_2 - \mathbf{W}_2 - \mathbf{W}_2^T, \\
\Gamma_{13} &= \mathbf{P}_1 \mathbf{B}_{qi} + \mathbf{W}_1, \\
\Gamma_{24} &= \mathbf{P}_2 \mathbf{B}_{qi} - \mathbf{Z}_{1i} \mathbf{D}_{qi} + \mathbf{W}_2, \\
\Gamma_{25} &= \mathbf{P}_2 \mathbf{E}_{qi} - \mathbf{Z}_{1i} \mathbf{E}_{2i}, \\
\Omega_{ij} &= \begin{bmatrix} \Omega_{0ij} + \varepsilon_{1i} \Xi_{1i}^T \Xi_{1i} + \varepsilon_{2i} \Xi_{2i}^T \Xi_{2i} - \varepsilon_{3ij} \Xi_{3i}^T \Xi_{3i} + \varepsilon_{4i} \Xi_{4i}^T \Xi_{4i} + \varepsilon_{5i} \Xi_{5i}^T \Xi_{5i} & \Theta_{1i} & \Theta_{2i} & \Theta_{3ij} & \Theta_{4i} & \Theta_{5i} \\ * & -\varepsilon_{1i} & 0 & 0 & 0 & 0 \\ * & * & -\varepsilon_{1i2} & 0 & 0 & 0 \\ * & * & * & \varepsilon_{3ij} & 0 & 0 \\ * & * & * & * & -\varepsilon_{4i} & 0 \\ * & * & * & * & * & -\varepsilon_{5i} \end{bmatrix},
\end{aligned}$$

$$\mathbf{\Omega}_{0ij} = \begin{bmatrix} \Gamma_{11} & 0 & \Gamma_{13} & 0 & \mathbf{P}_1 \mathbf{E}_{q1i} & \tau_m \mathbf{W}_1 & 0 & \tau_m \mathbf{A}_{qi}^T \mathbf{R}_1 & 0 & 0 \\ * & \Gamma_{22} & 0 & \Gamma_{24} & \Gamma_{25} & 0 & \tau_m \mathbf{W}_2 & 0 & \tau_m [\mathbf{A}_{qi}^T \mathbf{R}_2 - \mathbf{C}_{qi}^T \mathbf{Z}_{2i}] & \mathbf{F}_{qi}^T \\ * & * & -\mathbf{Q}_1 & 0 & 0 & 0 & 0 & \tau_m \mathbf{B}_{qi}^T \mathbf{R} & 0 & 0 \\ * & * & * & -\mathbf{Q}_2 & 0 & 0 & 0 & 0 & \tau_m [\mathbf{B}_{qi}^T \mathbf{R}_2 - \mathbf{D}_{qi}^T \mathbf{Z}_{2i}] & \mathbf{G}_{qi}^T \\ * & * & * & * & -\gamma^2 \mathbf{I} & 0 & 0 & \tau_m \mathbf{E}_{q1i}^T \mathbf{R}_1 & \tau_m [\mathbf{E}_{q1i}^T \mathbf{R}_2 - \mathbf{E}_{2i}^T \mathbf{Z}_{2i}] & 0 \\ * & * & * & * & * & -\tau_m \mathbf{R}_1 & 0 & 0 & 0 & 0 \\ * & * & * & * & * & * & -\tau_m \mathbf{R}_2 & 0 & 0 & 0 \\ * & * & * & * & * & * & * & -\tau_m \mathbf{R}_1 & 0 & 0 \\ * & * & * & * & * & * & * & * & -\tau_m \mathbf{R}_2 & 0 \\ * & * & * & * & * & * & * & * & * & -\mathbf{I} \end{bmatrix}, \quad (32)$$

Moreover, the filter parameter can be solved by

$$\mathbf{K}_i = \mathbf{P}_2^{-1} \mathbf{Z}_{1i}. \quad (33)$$

Proof. Let

$$\begin{aligned} \mathbf{P} &= \text{diag}\{\mathbf{P}_1, \mathbf{P}_2\}, \\ \mathbf{Q} &= \text{diag}\{\mathbf{Q}_1, \mathbf{Q}_2\}, \\ \mathbf{R} &= \text{diag}\{\mathbf{R}_1, \mathbf{R}_2\}, \\ \mathbf{W} &= \text{diag}\{\mathbf{W}_1, \mathbf{W}_2\}. \end{aligned} \quad (34)$$

Then $\bar{\Psi}$ can be rewritten as

$$\bar{\Psi} = \begin{bmatrix} \Upsilon_{11} & \Upsilon_{12} & \Upsilon_{13} & \tau_m \mathbf{W} & \tau_m \Upsilon_{15} & (\bar{\mathbf{F}} + \Delta \bar{\mathbf{F}})^T \\ * & -\mathbf{Q} & 0 & 0 & \tau_m \Upsilon_{25} & (\bar{\mathbf{G}} + \Delta \bar{\mathbf{G}})^T \\ * & * & -\gamma^2 \mathbf{I} & 0 & \tau_m \Upsilon_{35} & 0 \\ * & * & * & -\tau_m \mathbf{R} & 0 & 0 \\ * & * & * & * & -\tau_m \mathbf{R} & 0 \\ * & * & * & * & * & -\mathbf{I} \end{bmatrix}, \quad (35)$$

where

$$\begin{aligned} \Upsilon_{11} &= \text{diag}\{\boldsymbol{\delta}_1, \boldsymbol{\delta}_2\}, \\ \boldsymbol{\delta}_1 &= \mathbf{P}_1 (\mathbf{A}_{qi} + \Delta \mathbf{A}_{qi}) + (\mathbf{A}_{qi} + \Delta \mathbf{A}_{qi})^T \mathbf{P}_1 + \mathbf{Q}_1 - \mathbf{W}_1 - \mathbf{W}_1^T, \\ \boldsymbol{\delta}_2 &= \mathbf{P}_2 (\mathbf{A}_{qi} + \Delta \mathbf{A}_{qi}) - \mathbf{P}_2 \mathbf{K}_i (\mathbf{C}_{qi} + \Delta \mathbf{C}_{qi}) + (\mathbf{A}_{qi} + \Delta \mathbf{A}_{qi})^T \\ &\quad \cdot \mathbf{P}_2 - (\mathbf{C}_{qi} + \Delta \mathbf{C}_{qi})^T \mathbf{K}_i^T \mathbf{P}_2 + \mathbf{Q}_2 - \mathbf{W}_2 - \mathbf{W}_2^T, \\ \Upsilon_{12} &= \text{diag}\{\mathbf{P}_1 (\mathbf{B}_{qi} + \Delta \mathbf{B}_{qi}) + \mathbf{W}_1, \mathbf{P}_2 (\mathbf{B}_{qi} + \Delta \mathbf{B}_{qi}) \\ &\quad - \mathbf{P}_2 \mathbf{K}_i (\mathbf{D}_{qi} + \Delta \mathbf{D}_{qi}) + \mathbf{W}_2\}, \\ \Upsilon_{13} &= \begin{bmatrix} \mathbf{P}_1 (\mathbf{E}_{q1i} + \Delta \mathbf{E}_{q1i}) \\ \mathbf{P}_2 (\mathbf{E}_{q1i} + \Delta \mathbf{E}_{q1i}) - \mathbf{P}_2 \mathbf{K}_i (\mathbf{E}_{2i} + \Delta \mathbf{E}_{2i}) \end{bmatrix}, \\ \Upsilon_{15} &= \text{diag}\{(\mathbf{A}_{qi} + \Delta \mathbf{A}_{qi})^T \mathbf{R}_1, (\mathbf{A}_{qi} + \Delta \mathbf{A}_{qi})^T \mathbf{R}_2 - (\mathbf{C}_{qi} + \Delta \mathbf{C}_{qi})^T \mathbf{K}_i^T \mathbf{R}_2\}, \\ \Upsilon_{25} &= \text{diag}\{(\mathbf{B}_{qi} + \Delta \mathbf{B}_{qi})^T \mathbf{R}_1 (\mathbf{B}_{qi} + \Delta \mathbf{B}_{qi})^T \mathbf{R}_2 - (\mathbf{D}_{qi} + \Delta \mathbf{D}_{qi})^T \mathbf{K}_i^T \mathbf{R}_2\}, \\ \Upsilon_{35} &= [(\mathbf{E}_{q1i} + \Delta \mathbf{E}_{q1i})^T \mathbf{R}_1 (\mathbf{E}_{q1i} + \Delta \mathbf{E}_{q1i})^T \mathbf{R}_2 - (\mathbf{E}_{2i} + \Delta \mathbf{E}_{2i})^T \mathbf{K}_i^T \mathbf{R}_2]. \end{aligned} \quad (36)$$

Then, for further analysis, based on equation (9) and Lemma 1, equation (35) can be decomposed into

$$\begin{aligned} \bar{\Psi} &= \sum_{i=1}^r \sum_{j=1}^r h_i(f(t)) h_j(f(t)) \left\{ \mathbf{\Omega}_{0ij} + \boldsymbol{\Theta}_{1i} \mathbf{S}_i \boldsymbol{\Xi}_{1i} + \boldsymbol{\Xi}_{1i}^T \mathbf{S}_i^T \boldsymbol{\Theta}_{1i}^T \right. \\ &\quad + \boldsymbol{\Theta}_{2i} \mathbf{S}_i \boldsymbol{\Xi}_{2i} + \boldsymbol{\Xi}_{2i}^T \mathbf{S}_i^T \boldsymbol{\Theta}_{2i}^T - \boldsymbol{\Theta}_{3ij} \mathbf{S}_i \boldsymbol{\Xi}_{3i} - \boldsymbol{\Xi}_{3i}^T \mathbf{S}_i^T \boldsymbol{\Theta}_{3ij}^T \\ &\quad \left. + \boldsymbol{\Theta}_{4i} \mathbf{S}_i \boldsymbol{\Xi}_{4i} + \boldsymbol{\Xi}_{4i}^T \mathbf{S}_i^T \boldsymbol{\Theta}_{4i}^T + \boldsymbol{\Theta}_{5i} \mathbf{S}_i \boldsymbol{\Xi}_{5i} + \boldsymbol{\Xi}_{5i}^T \mathbf{S}_i^T \boldsymbol{\Theta}_{5i}^T \right\} \\ &\leq \sum_{i=1}^r \sum_{j=1}^r h_i(f(t)) h_j(f(t)) \left\{ \mathbf{\Omega}_{0ij} + \frac{1}{\varepsilon_{1i}} \boldsymbol{\Theta}_{1i} \boldsymbol{\Theta}_{1i}^T + \varepsilon_{1i} \boldsymbol{\Xi}_{1i}^T \boldsymbol{\Xi}_{1i} \right. \\ &\quad + \frac{1}{\varepsilon_{2i}} \boldsymbol{\Theta}_{2i} \boldsymbol{\Theta}_{2i}^T + \varepsilon_{2i} \boldsymbol{\Xi}_{2i}^T \boldsymbol{\Xi}_{2i} - \frac{1}{\varepsilon_{3ij}} \boldsymbol{\Theta}_{3ij} \boldsymbol{\Theta}_{3ij}^T - \varepsilon_{3ij} \boldsymbol{\Xi}_{3i}^T \boldsymbol{\Xi}_{3i} \\ &\quad \left. + \frac{1}{\varepsilon_{4i}} \boldsymbol{\Theta}_{4i} \boldsymbol{\Theta}_{4i}^T + \varepsilon_{4i} \boldsymbol{\Xi}_{4i}^T \boldsymbol{\Xi}_{4i} + \frac{1}{\varepsilon_{5i}} \boldsymbol{\Theta}_{5i} \boldsymbol{\Theta}_{5i}^T + \varepsilon_{5i} \boldsymbol{\Xi}_{5i}^T \boldsymbol{\Xi}_{5i} \right\}. \end{aligned} \quad (37)$$

Moreover, define

$$\begin{aligned} \mathbf{Z}_{1i} &= \mathbf{P}_2 \mathbf{K}_i, \\ \mathbf{Z}_{2i} &= \mathbf{K}_i^T \mathbf{R}_2. \end{aligned} \quad (38)$$

By applying the Schur complement, equation (37) is equivalent to

$$\sum_{i=1}^r h_i^2(f(t)) \boldsymbol{\Omega}_{ii} + \sum_{i<j}^r h_i(f(t)) h_j(f(t)) (\boldsymbol{\Omega}_{ij} + \boldsymbol{\Omega}_{ji}) < 0. \quad (39)$$

Thus, the inequalities (30) and (31) hold. The proof is completed.

4. Optimal Transformation Matrix Selection

It can readily be obtained that the estimation precision is directly affected by the estimation of the unknown states

(health parameters). Thus, the key of the parameters estimation is to find an optimal transformation matrix \mathbf{V}^* , which can ensure that the low-dimensional tuning vector \mathbf{q} can represent as much of the information of the health parameters as possible.

In this paper, the optimization objective is to find an optimal transformation matrix \mathbf{V}^* , which can ensure that the estimation error of the measured outputs $\rho = (\mathbf{y} - \hat{\mathbf{y}})^T (\mathbf{y} - \hat{\mathbf{y}})$ is minimum.

Thus, the optimization problem can be described as

$$\begin{aligned} \min \quad & \rho \\ \text{s.t.} \quad & \rho = (\mathbf{y} - \hat{\mathbf{y}})^T (\mathbf{y} - \hat{\mathbf{y}}). \end{aligned} \quad (40)$$

And the method based on iterative solution is used in this paper, and the process of optimal transformation matrix selection is shown in Figure 1:

- (1) To begin with, the initial value of \mathbf{V}^* is given randomly. And during the estimation process, the optimal \mathbf{V}^* of the last moment is used as the initial value to reduce the quantity of calculation. In order to avoid the calculation converging to a poorly scaled result, the Frobenius norm of \mathbf{V}^* must satisfy $\|\mathbf{V}^*\|_F = 1$.
- (2) With reference to equation (7), construct the reduced-order state-space model.
- (3) Solve the parameters of the H_∞ filter.
- (4) Calculate estimated error using equation (40).
- (5) Determine whether the estimated error ρ achieves convergence within a tolerance (user-specified):
 - (1) If converged, skip step 6 and proceed directly to step 7.
 - (2) If not converged, proceed to step 6.
 - (3) If the number of iterations exceeds 100, skip step 6 and proceed directly to step 7 to meet the real-time requirements.
- (6) Use the MATLAB *lsqnonlin* function to update \mathbf{V}^* , and the new value still needs to satisfy $\|\mathbf{V}^*\|_F = 1$.
- (7) Return the optimal value of \mathbf{V}^* , and ends.

5. Simulation Example

Before proceeding with the simulation, the high-precision aero-thermodynamic mathematical model of aeroengine in full envelope is the basis of the simulation. It can not only build the small deviation dynamic state space models, but can also replace the real engine in simulation. The detailed modeling process is carried out by reference to [25, 26]. This paper takes a type of double-rotor turbofan engine as research object and uses modeling method based on component characteristics. The afterburner is not considered in this engine model. For greater adaptability, faster calculation speed, and stronger convergence, the self-tuning Broyden quasi-Newton method [27] is used to solve equilibrium equations in the component-

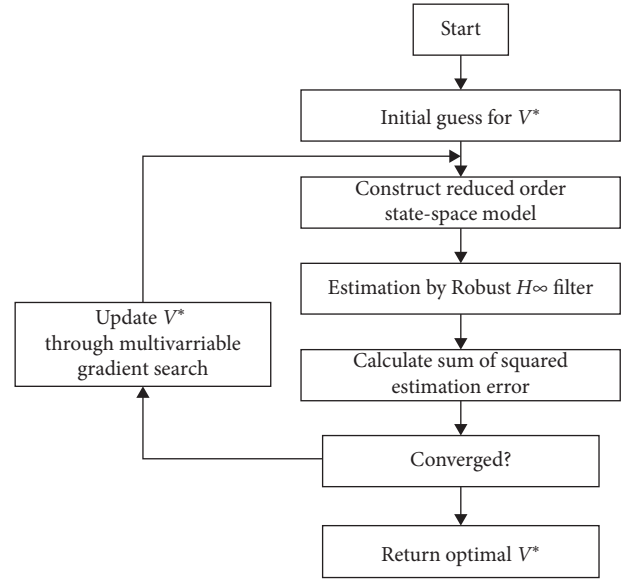


FIGURE 1: Flowchart of \mathbf{V}^* iterative search.

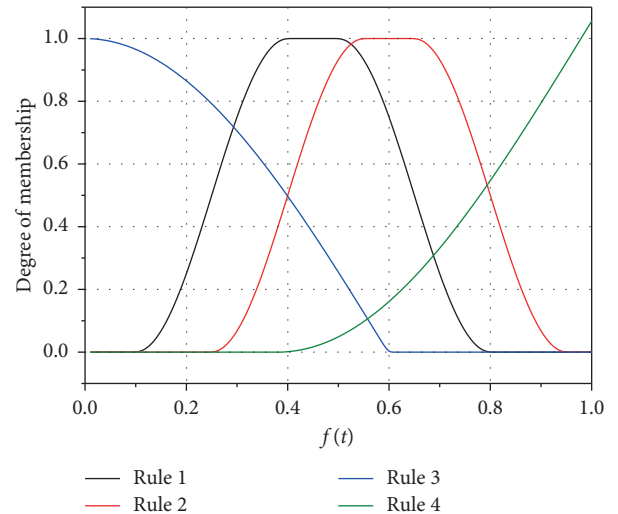


FIGURE 2: Initial membership function.

level mathematical model. And the small deviation dynamic model is solved by fitting method [28–30].

Assuming that the aeroengine works in the maximum state and then based on the methods of flight envelop division in [31–33], a T-S fuzzy model is constructed and the initial membership function is shown in Figure 2. In this paper, the T-S fuzzy model has two state variables, four health parameters, two control inputs, five measured outputs, and three unmeasured outputs, all shown in Table 1.

Then the four T-S fuzzy rules with the selection of H_f and Ma can be obtained as follows:

Rule 1. If H_f is about 0 km and Ma is about 0, then

TABLE 1: Variables of aeroengine T-S fuzzy model.

State variables	Health parameters	Control inputs	Measured outputs	Unmeasured outputs
n_l —low-pressure spool speed	Low-pressure compressor (LPC) efficiency	wf —fuel flow	n_l —low-pressure spool speed	T_5 —LPT exit total temperature
	LPC flow capacity		n_h —high-pressure spool speed	F_n —net thrust
n_h —high-pressure spool speed	Low-pressure turbine (LPT) efficiency	A_8 —nozzle area	P_{2b} —LPC exit total pressure	
	LPT flow capacity		T_{2b} —LPC exit total temperature	Π_T —turbine pressure ratio
			T_3 —HPC exit total temperature	

$$\begin{aligned}
\mathbf{A}_1 &= \begin{bmatrix} -1.26 & 1.02 \\ -0.14 & -1.24 \end{bmatrix}, \\
\mathbf{B}_1 &= \begin{bmatrix} 0.35 & 0.54 \\ 0.36 & 0.32 \end{bmatrix}, \\
\mathbf{L}_1 &= \begin{bmatrix} -1.02 & 0.90 & -0.62 & 0.51 \\ -0.26 & -0.11 & 0.28 & 0.23 \end{bmatrix}, \\
\mathbf{E}_{11} &= \begin{bmatrix} -0.5 \\ 1.0 \end{bmatrix}, \\
\mathbf{C}_1 &= \begin{bmatrix} 1 & 0 \\ 0 & 1 \\ 0.55 & -0.29 \\ 0.51 & -0.07 \\ 0.36 & 0.54 \end{bmatrix}, \\
\mathbf{D}_1 &= \begin{bmatrix} 0 & 0 \\ 0 & 0 \\ 0.19 & -0.82 \\ 0.05 & -0.22 \\ 0.04 & -0.16 \end{bmatrix}, \\
\mathbf{M}_1 &= \begin{bmatrix} 0 & 0 & 0 & 0 \\ 0 & 0 & 0 & 0 \\ 0.94 & -0.18 & 0.02 & -0.07 \\ 0.24 & -0.39 & 0.01 & -0.02 \\ 0.13 & -0.23 & -0.09 & -0.08 \end{bmatrix}, \\
\mathbf{E}_{21} &= \begin{bmatrix} 0 \\ 0 \\ 0.2 \\ 0.1 \\ 0.15 \end{bmatrix}, \\
\mathbf{F}_1 &= \begin{bmatrix} 0.25 & -0.54 \\ -0.14 & 1.27 \\ 0.40 & 0.04 \end{bmatrix}, \\
\mathbf{G}_1 &= \begin{bmatrix} 0.45 & 0.09 \\ -0.10 & 0.39 \\ 0.24 & 0.40 \end{bmatrix}, \\
\mathbf{N}_1 &= \begin{bmatrix} -0.23 & -0.29 & 0.07 & -0.18 \\ -0.09 & 0.26 & -0.33 & -0.19 \\ 0.81 & -0.08 & 0.04 & -0.08 \end{bmatrix}.
\end{aligned} \tag{41}$$

Rule 2. If H_f is about 4.8 km and Ma is about 1.24, then

$$\begin{aligned}
\mathbf{A}_2 &= \begin{bmatrix} -2.66 & 1.10 \\ -0.61 & -1.39 \end{bmatrix}, \\
\mathbf{B}_2 &= \begin{bmatrix} 0.39 & 0.42 \\ 0.36 & 0.33 \end{bmatrix}, \\
\mathbf{L}_2 &= \begin{bmatrix} -0.86 & 0.87 & -0.64 & 0.52 \\ -0.28 & -0.10 & 0.27 & 0.23 \end{bmatrix}, \\
\mathbf{E}_{12} &= \begin{bmatrix} -0.3 \\ 0.1 \end{bmatrix}, \\
\mathbf{C}_2 &= \begin{bmatrix} 1 & 0 \\ 0 & 1 \\ 2.03 & -0.34 \\ 0.66 & -0.06 \\ 0.42 & 0.58 \end{bmatrix}, \\
\mathbf{D}_2 &= \begin{bmatrix} 0 & 0 \\ 0 & 0 \\ 0.14 & -0.67 \\ 0.02 & -0.11 \\ 0.02 & -0.10 \end{bmatrix}, \\
\mathbf{M}_2 &= \begin{bmatrix} 0 & 0 & 0 & 0 \\ 0 & 0 & 0 & 0 \\ 0.92 & -0.16 & 0.02 & -0.05 \\ 0.15 & -0.30 & 0 & -0.01 \\ 0.08 & -0.18 & -0.09 & -0.07 \end{bmatrix}, \\
\mathbf{E}_{22} &= \begin{bmatrix} 0 \\ 0 \\ 0.3 \\ 0.25 \\ 0.1 \end{bmatrix}, \\
\mathbf{F}_2 &= \begin{bmatrix} -0.34 & -0.52 \\ -0.06 & 1.26 \\ 2.10 & 0.12 \end{bmatrix}, \\
\mathbf{G}_2 &= \begin{bmatrix} 0.45 & 0.09 \\ -0.10 & 0.43 \\ 0.54 & -0.57 \end{bmatrix}, \\
\mathbf{N}_2 &= \begin{bmatrix} -0.31 & -0.22 & 0.08 & -0.17 \\ 0 & 0.19 & -0.34 & -0.19 \\ 0.94 & -0.18 & 0.09 & -0.19 \end{bmatrix}.
\end{aligned} \tag{42}$$

Rule 3. If H_f is about 12.8 km and Ma is about 0.7, then

$$\begin{aligned}
 \mathbf{A}_3 &= \begin{bmatrix} -0.31 & 0.19 \\ -0.05 & -0.28 \end{bmatrix}, \\
 \mathbf{B}_3 &= \begin{bmatrix} 0.11 & 0.11 \\ 0.09 & 0.09 \end{bmatrix}, \\
 \mathbf{L}_3 &= \begin{bmatrix} -0.24 & 0.21 & -0.16 & 0.13 \\ -0.07 & -0.02 & 0.07 & 0.06 \end{bmatrix}, \\
 \mathbf{E}_{13} &= \begin{bmatrix} 0.2 \\ 0.3 \end{bmatrix}, \\
 \mathbf{C}_3 &= \begin{bmatrix} 1 & 0 \\ 0 & 1 \\ 0.53 & -0.18 \\ 0.49 & -0.04 \\ 0.35 & 0.55 \end{bmatrix}, \\
 \mathbf{D}_3 &= \begin{bmatrix} 0 & 0 \\ 0 & 0 \\ 0.19 & -0.84 \\ 0.05 & -0.21 \\ 0.04 & -0.15 \end{bmatrix}, \\
 \mathbf{M}_3 &= \begin{bmatrix} 0 & 0 & 0 & 0 \\ 0 & 0 & 0 & 0 \\ 0.94 & -0.17 & 0.02 & -0.08 \\ 0.23 & -0.41 & 0.01 & -0.02 \\ 0.13 & -0.25 & -0.10 & -0.09 \end{bmatrix}, \\
 \mathbf{E}_{23} &= \begin{bmatrix} 0 \\ 0 \\ 0.1 \\ 0.2 \\ 0.1 \end{bmatrix}, \\
 \mathbf{F}_3 &= \begin{bmatrix} 0.22 & -0.31 \\ -0.10 & 1.04 \\ 0.59 & 0.12 \end{bmatrix}, \\
 \mathbf{G}_3 &= \begin{bmatrix} 0.45 & 0.12 \\ -0.08 & 0.36 \\ 0.45 & -0.58 \end{bmatrix}, \\
 \mathbf{N}_3 &= \begin{bmatrix} -0.25 & -0.25 & 0.07 & -0.20 \\ -0.07 & 0.21 & -0.34 & -0.19 \\ 1.05 & -0.15 & 0.07 & -0.17 \end{bmatrix}.
 \end{aligned} \tag{43}$$

Rule 4. If H_f is about 18.8 km and Ma is about 1.72, then

$$\begin{aligned}
 \mathbf{A}_4 &= \begin{bmatrix} -0.63 & 0.24 \\ -0.13 & -0.29 \end{bmatrix}, \\
 \mathbf{B}_4 &= \begin{bmatrix} 0.08 & 0.10 \\ 0.08 & 0.07 \end{bmatrix}, \\
 \mathbf{L}_4 &= \begin{bmatrix} -0.20 & 0.19 & -0.14 & 0.11 \\ -0.06 & -0.02 & 0.06 & 0.05 \end{bmatrix}, \\
 \mathbf{E}_{14} &= \begin{bmatrix} 0.3 \\ 0.5 \end{bmatrix}, \\
 \mathbf{C}_4 &= \begin{bmatrix} 1 & 0 \\ 0 & 1 \\ 2.29 & -0.36 \\ 0.73 & -0.07 \\ 0.46 & 0.58 \end{bmatrix}, \\
 \mathbf{D}_4 &= \begin{bmatrix} 0 & 0 \\ 0 & 0 \\ 0.14 & -0.66 \\ 0.03 & -0.12 \\ 0.03 & -0.11 \end{bmatrix}, \\
 \mathbf{M}_4 &= \begin{bmatrix} 0 & 0 & 0 & 0 \\ 0 & 0 & 0 & 0 \\ 0.95 & -0.16 & 0.02 & -0.05 \\ 0.18 & -0.30 & 0 & -0.01 \\ 0.09 & -0.17 & -0.09 & -0.08 \end{bmatrix}, \\
 \mathbf{E}_{24} &= \begin{bmatrix} 0 \\ 0 \\ 0.2 \\ 0.1 \\ 0.1 \end{bmatrix}, \\
 \mathbf{F}_4 &= \begin{bmatrix} -0.37 & -0.50 \\ -0.07 & 1.25 \\ 2.00 & 0.14 \end{bmatrix}, \\
 \mathbf{G}_4 &= \begin{bmatrix} 0.46 & 0.05 \\ -0.11 & 0.47 \\ 0.61 & -0.43 \end{bmatrix}, \\
 \mathbf{N}_4 &= \begin{bmatrix} -0.28 & -0.21 & 0.07 & -0.18 \\ -0.02 & 0.18 & -0.33 & -0.18 \\ 0.79 & -0.20 & 0.09 & -0.22 \end{bmatrix}.
 \end{aligned} \tag{44}$$

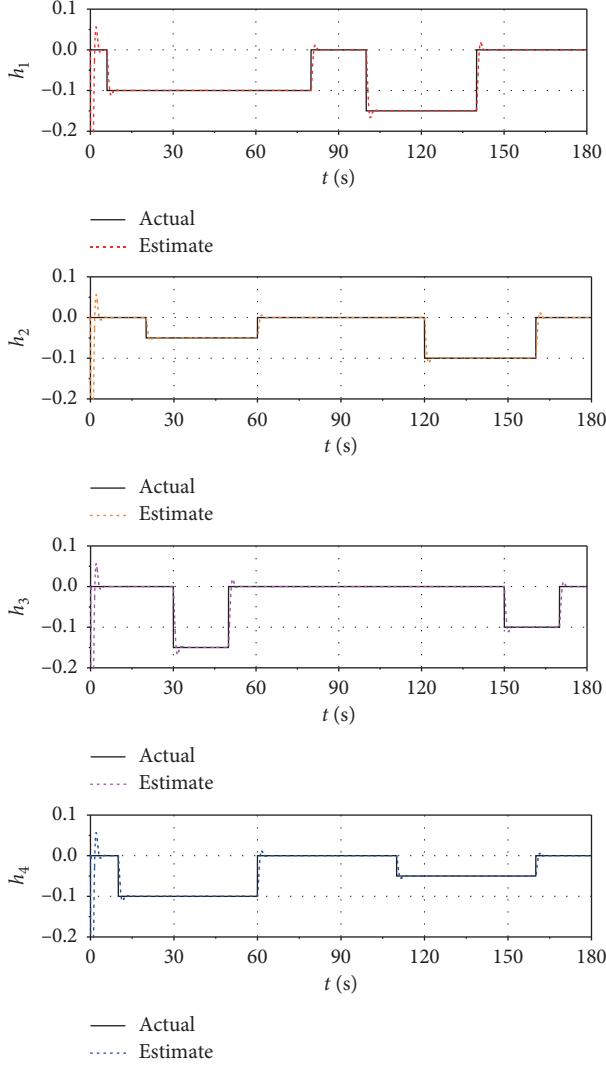


FIGURE 3: The estimation of health parameters for Type I.

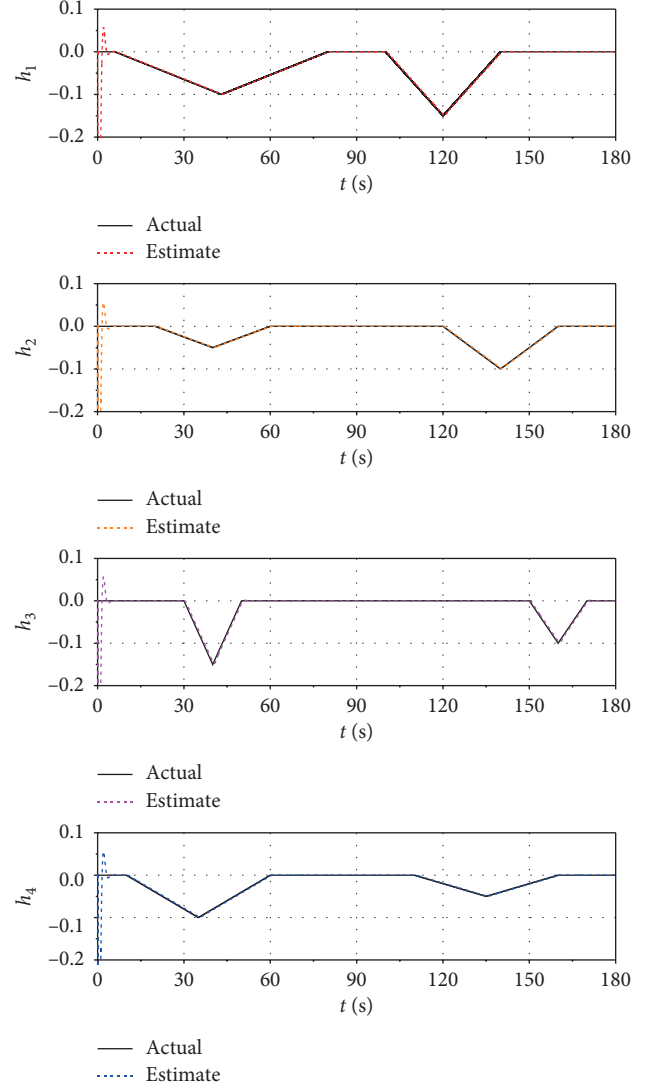


FIGURE 4: The estimation of health parameters for Type II.

Moreover, the uncertainties of the system are

$$\begin{aligned}
 \mathbf{U}_{1i} &= [0.2 \quad -0.3 \quad 0 \quad 0 \quad 0]^T, \\
 \mathbf{V}_{4i} &= [-0.1 \quad 0.2 \quad 0.15], \\
 \mathbf{U}_{2i} &= [0.1 \quad 0.3 \quad -0.1 \quad 0.2 \quad 0.05]^T, \\
 \mathbf{V}_{3i} &= 0.1, \\
 \mathbf{V}_{1i} &= [0.1 \quad 0.5 \quad 0 \quad 0 \quad 0], \\
 \mathbf{V}_{2i} &= [0.2 \quad -0.1 \quad 0 \quad 0 \quad 0], \\
 (i &= 1, 2, 3, 4).
 \end{aligned} \tag{45}$$

The system sampling period is set as $T = 20$ ms, and the external disturbance $w(t)$ is

$$w(t) = \frac{0.3 \sin(0.8t)}{5 \sin(6t) + 3 \cos(8t)}. \tag{46}$$

The state space of time-delay is $\tau(t) \in \{1, 2, 3\}$, and the state transition matrix of $\tau(t)$ is

$$\mathbf{\Pi} = \begin{bmatrix} -0.6 & 0.4 & 0.2 \\ 0.3 & -0.5 & 0.2 \\ 0.1 & 0.4 & -0.5 \end{bmatrix}. \tag{47}$$

The working condition is chosen as $H=5$ km and $Ma=0.3$. The given value of γ is $\gamma = 2$.

Two types of performance degradation are selected to simulate, which are slow varying and sudden change of health parameters. For the sudden change type (Type I), there is a step change for health parameters, and this type is used to represent the sudden damage, such as foreign objects damage. And the slow varying type (Type II) is defined as the linear variation of health parameters to represent the gradual performance degradation during using process. These two types can cover almost all the health parameters changes in practice, and they are simulated respectively to illustrate the effectiveness of the method proposed in this paper.

The results are shown in Figures 3–6. It can be seen that the method proposed in this paper can effectively simulate

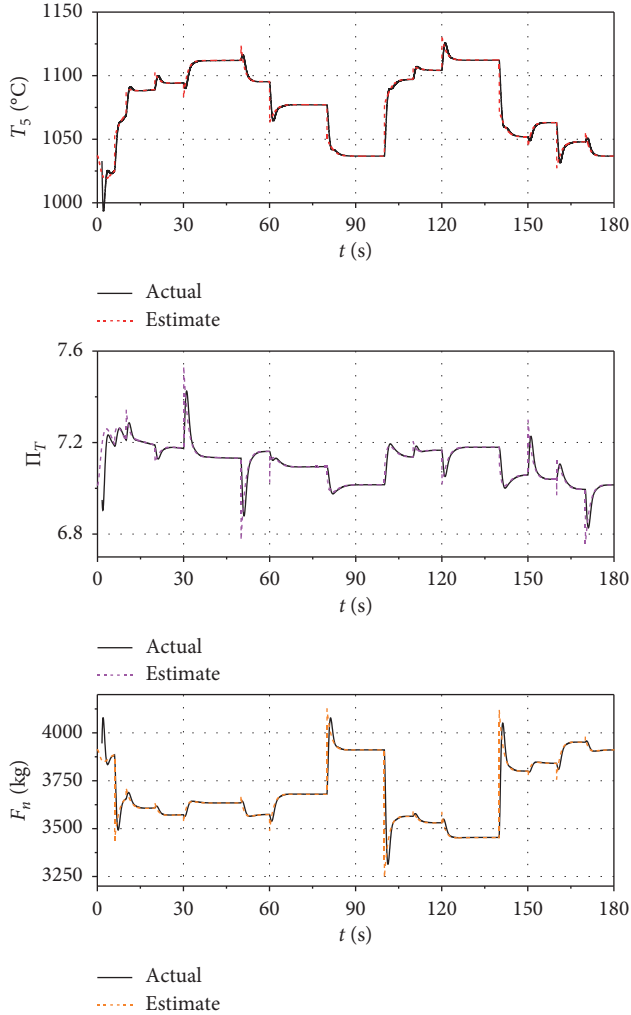


FIGURE 5: The estimation of performance parameter for Type I.

the health and performance parameters of the aeroengine. The estimated values can accurately track the changes as the health parameters shift.

By comparing the results of the two types of health parameters change, it can be concluded that the estimated values for slow varying type are more accurate. For the type of sudden change, it takes a while for the estimated values to stabilize and the overshoot is slightly larger.

Table 2 shows the average estimated error of the health and performance parameters. It can be seen that the estimated error is within 2.5% for all types. At the same time, the results are more accurate except for the beginning of simulation.

Furthermore, the results show that the method proposed in this paper can accurately estimate most system parameters of interest. On this basis, the method can also be used in the investigations of direct control, fault diagnosis, health management, and online monitoring. And for aeroengine, there are already some researches which indicate that the changes of health parameters can characterize specific faults, allowing for online monitoring and alerting [34–36].

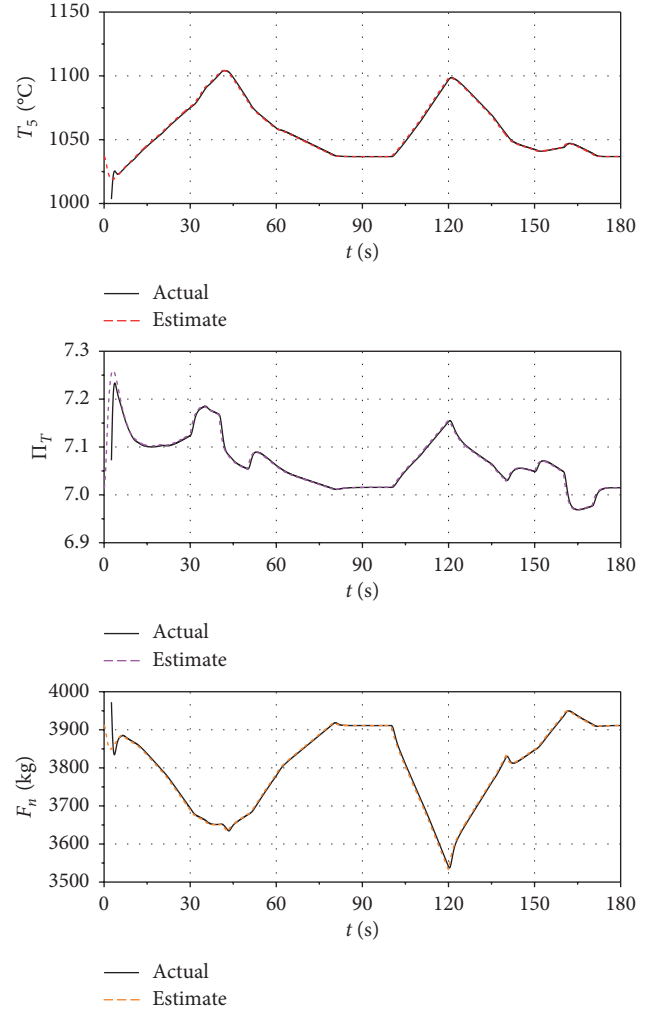


FIGURE 6: The estimation of performance parameter for Type II.

TABLE 2: Estimated errors of health and performance parameters.

Estimated error	Type I (%)	Type II (%)
h_1	0.46	0.40
h_2	0.38	0.31
T_5	1.27	0.98
F_n	1.95	1.57
Π_T	2.46	2.03

6. Conclusion

In this paper, a method is proposed for the underdetermined estimation problem of the distributed control systems. First, the T-S fuzzy model for DCSs is constructed and a model tuning parameter vector of appropriate dimension is produced. Then an observer-based fuzzy filter is designed and the sufficient condition for the existence of the designed filter is derived in terms of LMIs solutions. Besides, the method based on iterative solution is used to select the optimal transformation matrix to minimize the estimated error. Finally, the results of the simulation show that the proposed method can effectively estimate unmeasured parameters of the aeroengine and the estimated error is less than 2.5%.

Data Availability

The data used to support the findings of this study are included within the article.

Conflicts of Interest

The authors declare that they have no conflicts of interest.

Acknowledgments

This work was supported by the National Natural Science Foundation of China (51476187, 51606219, and 51506221).

References

- [1] M. Khalgui and O. Mosbahi, "Intelligent distributed control systems," *Information and Software Technology*, vol. 52, no. 12, pp. 1259–1271, 2010.
- [2] A. Behbahani and B. Tulpule, "Perspective for distributed intelligent engine controls of the future," in *Proceeding of the 46th AIAA/ASME/SAE/ASEE Joint Propulsion Conference & Exhibit*, Nashville, TN, USA, July 2010.
- [3] J. P. Hespanha, P. Naghshtabrizi, and Y. Xu, "A survey of recent results in networked control systems," *Proceedings of the IEEE*, vol. 95, no. 1, pp. 138–162, 2007.
- [4] G. C. Goodwin, E. I. Silva, and D. E. Quevedo, "A brief introduction to the analysis and design of networked control systems," *Automatica*, vol. 18, pp. 810–820, 2008.
- [5] F. Kazempour and J. Ghaisari, "Stability analysis of model-based networked distributed control systems," *Journal of Process Control*, vol. 23, no. 3, pp. 444–452, 2013.
- [6] Y. Kao, J. Xie, C. Wang, and H. R. Karimi, "A sliding mode approach to H_{∞} non-fragile observer-based control design for uncertain Markovian neutral-type stochastic systems," *Automatica*, vol. 52, pp. 218–226, 2015.
- [7] D. L. Simon and A. W. Rinehart, "Sensor selection for aircraft engine performance estimation and gas path fault diagnostics," *Journal of Engineering for Gas Turbines and Power*, vol. 138, no. 7, pp. 1–11, 2016.
- [8] J. T. Csank and J. W. Connolly, "Model-based engine control architecture with an extended kalman filter," in *Proceedings of the AIAA Guidance, Navigation and Control Conference*, San Diego, CA, USA, January 2016.
- [9] G. Liao, Y. Jiao, Q. Li, and J. Huang, "Research on high accuracy real-time component-level modeling method for turbo-shaft engine," *Journal of Propulsion Technology*, vol. 37, no. 1, pp. 25–33, 2016.
- [10] D. L. Simon, J. B. Armstrong, and S. Garg, "Application of an optimal tuner selection approach for on-board self-tuning engine models," *Journal of Engineering for Gas Turbine and Power*, vol. 134, no. 4, pp. 1–11, 2012.
- [11] Z. Zhang, C. Lin, and B. Chen, "New decentralized H_{∞} filter design for nonlinear interconnected systems based on Takagi-Sugeno fuzzy models," *IEEE Transactions on Cybernetics*, vol. 45, no. 12, pp. 2914–2924, 2015.
- [12] G. H. Yang and X. G. Guo, "Brief paper: insensitive H_{∞} filter design for continuous-time systems with respect to filter coefficient variations," *Automatica*, vol. 46, pp. 1860–1869, 2010.
- [13] Y. Chen, Z. Wang, and Y. Yuan, "Distributed H_{∞} filtering for switched stochastic delayed systems over sensor networks with fading measurements," *IEEE Transactions on Cybernetics*, vol. 50, no. 1, pp. 2–14, 2020.
- [14] T. Brotherton, A. Volponi, R. Luppold, and D. L. Simon, "eSTORM: enhanced self turning on-board real-time engine model," in *Proceedings of the 2003 IEEE Aerospace Conference*, Big Sky, MT, USA, March 2003.
- [15] T. Kobayashi and D. L. Simon, "Application of a bank of Kalman filters for aircraft engine fault diagnostics," in *Proceedings of the ASME Turbo Exposition*, Atlanta, GA, USA, June 2003.
- [16] T. Kobayashi and D. L. Simon, "Evaluation of an enhanced bank of Kalman filters for in-flight aircraft engine sensor fault diagnostics," in *Proceedings of the ASME Turbo Exposition*, Vienna, Austria, June 2004.
- [17] J. S. Litt, "An optimal orthogonal decomposition method for kalman filter-based turbofan engine thrust estimation," *Journal of Engineering for Gas Turbine and Power*, vol. 130, pp. 1–12, 2008.
- [18] R. C. Magana and A. Medina, "Time domain transient state estimation using singular value decomposition Poincare map and extrapolation to the limit cycle," *International Journal of Electrical Power & Energy Systems*, vol. 53, pp. 810–817, 2013.
- [19] D. L. Simon and S. Garg, "Optimal tuner selection for kalman filter based aircraft engine performance estimation," *Journal of Engineering for Gas Turbine and Power*, vol. 132, pp. 1–10, 2010.
- [20] Y. Yu, H. K. Lam, and K. Y. Chan, "T-S fuzzy model based output feedback tracking control with control input saturation," *IEEE Transactions on Fuzzy Systems*, vol. 26, no. 6, pp. 3514–3523, 2018.
- [21] N. Rong, Z. Wang, and H. Zhang, "Finite-time stabilization for discontinuous interconnected delayed systems via interval type-2 T-S fuzzy model approach," *IEEE Transactions on Fuzzy Systems*, vol. 27, no. 2, pp. 249–261, 2019.
- [22] C. Peng, S. Ma, and X. Xie, "Observer-based non-PDC control for networked T-S fuzzy systems with an event-triggered communication," *IEEE Transactions on Cybernetics*, vol. 47, no. 8, pp. 2279–2287, 2017.
- [23] N. Vatanski, J. Georges, and C. Aubrun, "Networked control with delay measurement and estimation," *Control Engineering Practice*, vol. 17, no. 2, pp. 231–244, 2008.
- [24] T. Iwasaki and R. E. Skelton, "All controllers for the general H_{∞} control problem: LMI existence condition and state space formulas," *Automatica*, vol. 30, pp. 1307–1317, 1994.
- [25] G. Q. Luo, *Numerical Methods for Aviation Gas Turbine Engine Simulation*, National Defence Industry Press, Beijing, China, 2007.
- [26] R. John, "Real-time simulation of F100-PW-100 turbofan engine using the hybrid computer," *Computer-Aided Design*, vol. 8, no. 2, pp. 1–8, 1976.
- [27] Y. Wang, Q. Li, and X. Huang, "Numerical calculation of aero-engine model based on self-tuning Broyden quasi-Newton method," *Journal of Aerospace Power*, vol. 31, no. 1, pp. 249–256, 2016.
- [28] Q. Li and J. Sun, "Aero-engine variable modeling based on the genetic algorithm," *Journal of Aerospace Power*, vol. 24, no. 2, pp. 427–431, 2006.
- [29] T. Zheng and X. Wang, "Modified method of establishing the state space model of aero-engine," *Journal of Propulsion Technology*, vol. 26, no. 1, pp. 46–49, 2005.
- [30] N. Sugiyama, "Deviation of ABCD system matrices from nonlinear dynamic simulation of jet engines," in *Proceedings of the AIAA Conference*, Nashville, TN, USA, July 1992.
- [31] L. Wang, S. Xie, and Z. Miao, "Identification of T-S fuzzy model for aero-engine based on flight envelop division,"

- Journal of Aerospace Power*, vol. 28, no. 5, pp. 1159–1165, 2013.
- [32] X. Zhai, S. Xie, and Z. Miao, “Fault detection of aero-engine non-linear distributed control system based on T-S fuzzy model,” *Journal of Aerospace Power*, vol. 28, no. 6, pp. 1429–1435, 2013.
- [33] L. Wang, S. Xie, and L. Ren, “Fault diagnosis of sensors in distributed control system based on T-S fuzzy KPCA model,” *Journal of Propulsion Technology*, vol. 35, no. 7, pp. 988–995, 2014.
- [34] A. Stamatis, K. Mathioudakis, and K. D. Papailiou, “Adaptive simulation of gas turbine performance,” *Journal of Engine Gas Turbines Power*, vol. 112, pp. 168–175, 1990.
- [35] A. Tsalavoutas, K. Mathioudakis, and A. Stamatis, “Identifying faults in the variable geometry system of a gas turbine compressor,” *Journal of Turbomachinery*, vol. 123, pp. 33–39, 2001.
- [36] S. Ogaji, S. Sampat, and R. Singh, “Parameter selection for diagnosing a gas-turbine’s performance deterioration,” *Applied Energy*, vol. 73, no. 1, pp. 25–46, 2002.

Research Article

Research on Traffic Congestion Based on System Dynamics: The Case of Chongqing, China

Yingsheng Su ¹, Xin Liu ¹ and Xuejun Li ²

¹School of Statistics, Southwestern University of Finance and Economics, Chengdu 611130, China

²Jincheng School, Sichuan University, Chengdu 611731, China

Correspondence should be addressed to Yingsheng Su; suys@swufe.edu.cn

Received 27 September 2019; Revised 2 January 2020; Accepted 13 February 2020; Published 17 March 2020

Guest Editor: Kiyong Oh

Copyright © 2020 Yingsheng Su et al. This is an open access article distributed under the Creative Commons Attribution License, which permits unrestricted use, distribution, and reproduction in any medium, provided the original work is properly cited.

With the rapid development of society, urban traffic congestion has gradually become an important social problem that many cities need to solve. For Chongqing, traffic congestion not only affects residents' normal travel but also brings more serious environmental pollution. Aiming at the problem of urban traffic congestion and automobile exhaust pollution, this paper adopts the system dynamics method to establish a model for studying urban traffic congestion system from the perspectives of private cars, trucks, and public transportation. First, we determine city motor vehicle trips as an indicator of the degree of traffic congestion in this paper. Second, we analyze the causal relationship between the growth of private cars, the travel of trucks, public transportation, population, and other factors and then build a model and test the stability of the model. Then, we add some practical policies to the model for policy analysis. Finally, it is concluded that the private car restriction policy is effective in controlling the amount of private car travel, and the purchase restriction policy controls the growth of the number of private cars from the root cause, but the development of public transportation is the most effective treatment measure in the long run.

1. Introduction

With the rapid development of China's economy and the improvement of people's income level, motor vehicles are more needed in all aspects of clothing, food, housing, and transportation. The rapid development of the use of motor vehicles has brought convenience to people and changed the pattern of the entire transportation system. The increasing popularity of online shopping has promoted the development of the logistics industry, which has led to the increasing use of freight cars and increased traffic pressure. In addition, with the convenience of take-away distribution, many delivery staff ride motorcycles to shuttle through the streets and lanes every day, causing a lot of traffic problems. More importantly, economic development promotes the improvement of people's living standards, and the per capita possession of private cars has also continued to increase, which is a major source of road traffic pressure.

When traffic congestion occurs, the vehicle travels very slowly, and the behavior of rapid braking will result in

insufficient combustion of fuel oil and a large amount of harmful exhaust gas, which will increase air pollution. And the number of traffic accidents is increasing. Therefore, how to take effective measures to control traffic congestion is an urgent problem to be solved in many cities.

Baidu Maps had released a report called "Research report on urban traffic in China in the third quarter of 2018" in January 2019. It was concluded from the analysis of various data indicators that Chongqing's congestion index was as close as that of Beijing and Harbin. Moreover, in Baidu Map's "fourth quarter of 2018 congestion ranking," Chongqing was one of the "top three," becoming the most congested big city after Beijing and Harbin.

In addition, Baidu Map also divides cities into several categories according to the number of motor vehicles: more than 3 million, more than 2 million, more than 1 million, and less than 1 million. Chongqing ranks second in terms of congestion in cities with more than 3 million categories, second only to Beijing. For Chongqing, traffic congestion is a problem that needs to be improved immediately.

In this paper, we try to find the cause of traffic congestion and further write a model of traffic congestion to find some ways to actually manage. What are the indicators for measuring traffic congestion? How to analyze the factors affecting traffic congestion indicators? These problems are what this article needs to solve.

The structure of this paper is as follows. Section 2 presents the early literature on the study of the causes of traffic congestion and the system dynamics. Section 3 contains the basic construction of the model and some assumptions and premise. Section 4 presents the addition of initial data and the simulation of the model. Section 5 adopts several policies to optimize the results. Finally, Section 6 compares the policies and draws conclusions.

2. Literature Review

Traffic congestion is a qualitative indicator, and its evaluation is subjective in daily life. In academic research, scholars often choose a quantitative indicator instead of qualitative indicator for analysis. Guo et al. [1] selected the road network traffic congestion index, the road network congestion level mileage ratio, the time-based road network congestion level, and the number and distribution of key congestion points to establish a macroindex system for traffic congestion assessment, which can be obtained from actual data.

Based on the study of traffic congestion, the second step is to find out the causes. Many scholars have carried out research studies from the economic, social, and other aspects. The reasons for traffic congestion are analyzed as follows.

Wright and Orenstein think that the main reason for traffic congestion is traffic bottleneck [2]. There are two kinds of traffic bottlenecks: the first is the traffic bottleneck caused by the road itself and the traffic capacity difference caused by the unclear road shape, road width, or road sign. The second reason is the unstable change of road demand. The road supply cannot meet the congestion caused by the change of demand. This type of congestion is caused by uncontrollable weather conditions. Such bottlenecks are few and far between but will lead to even greater congestion. Anthony concluded that traffic congestion was mainly caused by the following problems [3]. First, because of the rapid increase in the number of people, the demand for travel has increased significantly. Secondly, with the increase of the number of motor vehicles, more and more people choose to travel by motor vehicles. Third, occasional severe traffic congestion is caused by the random occurrence of emergency. After explaining the main reasons for the deterioration of infrastructure due to traffic congestion, Diakaki et al. briefly outlined the proposed and implemented control strategies, covering three areas: urban road networks, highway networks, and route guidance [4]. Liu et al. put forward domestic policies for reference according to the experience of "traffic congestion control" in foreign cities [5], such as strengthening the management of traffic road supply and vigorously developing urban public transportation.

Research on traffic congestion management includes those as below. Taylor believes that charging for roads is a way to alleviate traffic problems [6]. McKnight believes that conventional traffic management and improvement of vehicle standards are not particularly effective in the reality of rapidly increasing demand for road use. He also believes that the control of the use and purchase of private cars is the key to effectively control traffic congestion. Coomber et al. proposed different charging methods and prices for parking lots with different functions in the city to alleviate traffic congestion [7]. Muanmas et al. proposed from the perspective of economics that through congestion pricing [8], people can pay the marginal social cost generated when they travel, to internalize the externality of the transportation system and effectively reduce traffic congestion. Fishman et al. studied the mechanism of shared bikes on traffic congestion [9]. Research results showed that bike sharing can not only enhance physical health but also reduce urban traffic congestion and environmental pollution. From the perspective of system dynamics, Heung et al. designed a dynamic programming method to control traffic problems. By installing a local fuzzy logic controller (FLC) at each intersection, a dynamic programming (DP) technology was proposed to derive the green light time at each stage of the traffic light cycle [10].

This paper takes city motor vehicle trips as the index to measure the degree of traffic congestion to simulate and analyze the degree of easing the congestion caused by various policies. System dynamics is a discipline of analyzing and studying information feedback founded by Forrester W of Massachusetts institute of technology in 1956. Its ability to deal with higher order, nonlinear, multiple feedback, complex time-varying system problems and policy simulation has made it widely used in various fields of economic and social development. [11] Modeling steps based on system dynamics are shown in Figure 1. Kaparias and Bell analyzed the successes and pitfalls of London's congestion charging and identified potential future opportunities based on the latest technological developments in the field of cooperative intelligent transportation systems (ITS) [12].

Some literatures also try to find solutions to traffic congestion by using system dynamics method. Wang and Jia analyzed the main factors that affect the demand for private cars [13] and studied the changes of people's demand for private cars after China's entry into WTO. Fan and Yan conducted a simulation analysis of private car ownership in Beijing and compared the impact of existing governance measures on demand [14]. They concluded that actively developing urban public transportation is the most effective way to reduce private cars. Yang et al. [15] selected Beijing city as the research object, established a system dynamics model for analysis, and concluded that controlling the number of motor vehicles is helpful to control traffic congestion. Dang studied that the automobile license plate auction system in Shanghai is effective in reducing the demand for private cars [16]. Jia et al. used system dynamics method to establish traffic congestion pricing management model from the perspective of environmental and social benefits [17]. Through dynamic simulation and comparison, reasonable schemes to alleviate

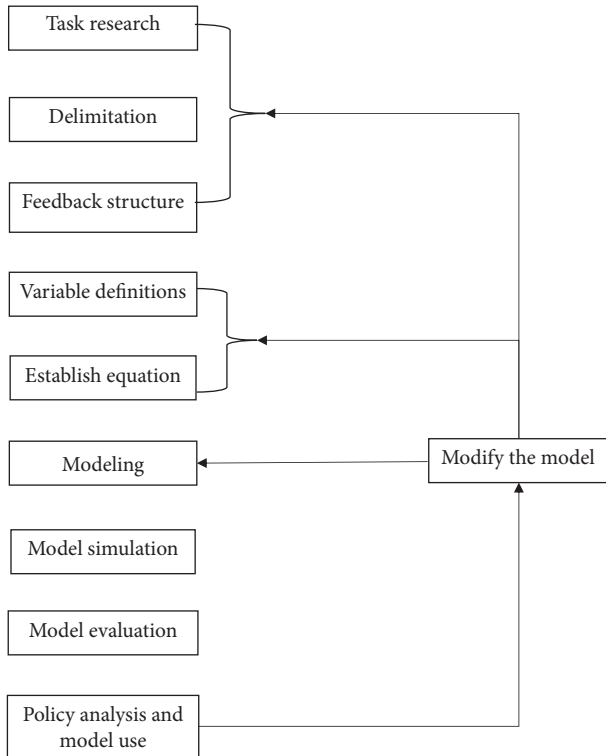


FIGURE 1: System dynamics modeling process.

traffic congestion and environmental pollution were obtained. Zhang et al. [18] built the system dynamics model of urban green transportation and proposed to improve public transportation and reduce the emission of carbon.

This paper starts from the city motor vehicle trips, considering the travel volume of private cars, buses, trucks, and other motor vehicles and mainly establishes a system from the two perspectives of residents' private car travel and logistics use. Based on the application of system dynamics, this paper uses causal diagram, flowchart, and corresponding data parameters to complete the qualitative analysis and completes the programming with the support of Vensim software. Then, in the simulation, different policy variables are added, and experiments are carried out. Finally, quantitative results of research objects based on time changes can be obtained. Taking Chongqing as an example, the core of this paper is to analyze private car restriction policy, private car purchase restriction policy, and freight car limit policy and estimate the impact of improving the public transport sharing rate. Through the simulation of the above policies, effective suggestions can be put forward to reduce the amount of city motor vehicle travel so as to improve the valuable reference for solving the traffic congestion problem.

3. Model Description

3.1. The Basic Model. At present, there are many indicators for the quantitative analysis of traffic congestion. For example, the congestion ranking of Baidu Map is based on the commuting peak index. This paper mainly measures the city motor vehicle trips to measure congestion.

System dynamics analyzes the interdependent interaction of internal elements of the system and assumes that factors outside the system do not have a significant impact on the elements within the system; therefore, variables that are important to the complex problem being studied are included in the system. Factors that are not significantly related to the problem are excluded from the system.

In order to analyze city motor vehicle travels, this article has established a complex system that not only contains the ownership of private cars, buses, freight cars, and other motor vehicles but also has a close relationship with other aspects of urban population, economy, environment, policy, etc. According to the research purpose of this paper, the analysis factors in the system are finally determined as shown in Table 1.

After determining the boundary of the system, the causal relationship shown in Figure 2 is determined by analyzing the factors. “+” means positive effect and “-” means negative effect. The variables of the city motor vehicle travel system mainly include city's economy (GDP), resident population, urban logistics, private car travel, bus travel, freight car trips, and other motor vehicle trips. By analyzing the relationship between the variables, the causal relationship of the main variables can be established as shown in Figure 2. As the city's economy and population grow, the demand for people to buy vehicles increases. The growth rate of motor vehicle ownership far exceeds the growth rate of urban road area, resulting in greater traffic congestion. The increase in the amount of motor vehicles will emit more exhaust gas, resulting in greater environmental pollution, which in turn will reduce the growth of private cars. This paper attempts to mitigate the implementation of urban policy, such as controlling the growth of private car trips and freight car trips, in order to reduce the number of motor vehicle trips and alleviate traffic congestion. There are some main causal circuits as follows:

City motor vehicle trips \rightarrow waste gas pollution \rightarrow environmental pollution \rightarrow private car growth rate \rightarrow private car ownership \rightarrow private car travel \rightarrow city motor vehicle trips

City motor vehicle trips \rightarrow urban motor vehicle ownership \rightarrow traffic factor \rightarrow private car growth rate \rightarrow private car ownership \rightarrow private car travel \rightarrow city motor vehicle trips

This paper determines the system boundary and establishes a system inventory flow graph based on causality. The causal relationship only illustrates the positive and negative effects between the two variables. In the system dynamics model, the variables are also divided into state variables, rate variables, and so on. To illustrate the relationship that is not illustrated in the causal diagram, to further quantify the entire model, we use Vensim to plot the stock flow (Figure 3). In the policy analysis, after adding various policies, the new SD model is shown in Figure 4.

3.2. Some Formulas

(1) Bus ownership = INTEG (bus ownership * bus growth rate, initial value of bus ownership)

TABLE 1: Determination of system boundaries.

System category	Specific variables
Residents' travel	Private car ownership
	Private car travel
	Private car growth rate
	Private car scrap rate
	Bus ownership
	Bus growth rate
	Other motor vehicle ownership
Urban logistics	Other motor vehicle growth rate
	Related governance policy
	City freight volume
	Urban freight growth rate
	Car ownership
Others	Freight car trips
	Urban freight growth
	Related governance policy
	Permanent residents
	Resident population growth rate
	Total household registration population
	Household registration population growth rate
	Total car purchase price
	Car tax
	Fuel cost
	Fuel cost growth rate
	Parking fee
	Total road area of the city
	Average road area
	Annual growth rate of urban road area
City GDP	
GDP growth rate	
NO ₂ stock	
Each vehicle emits NO ₂ per year	
Motor vehicle contribution rate to NO ₂ emissions	

- (2) City motor vehicle trips = bus ownership + other motor vehicle travel + private car travel + freight car travel
- (3) Consumer psychological factor = demonstration effect^{0.4} * economic factors^{0.6}
- (4) Total purchase price = car purchase price + other fees
- (5) Income-to-price ratio = per capita GDP / total car purchase price
- (6) Total household registration population = total household registration population * household registration population growth rate
- (7) Per capita GDP = city GDP / total household registration population
- (8) City GDP = INTEG (GDP growth volume, initial GDP value)
- (9) Growth rate of private car = traffic factor^{0.15} * economic factor^{0.4} * consumer psychological factor^{0.32} * (1 - environmental factor)^{0.13} * degree of consumption satisfaction
- (10) Fuel costs = INTEG (fuel cost growth rate * fuel costs, initial value of fuel cost)

- (11) Private car ownership = INTEG (annual demand for private cars - annual private cars scrap rate, initial value of private cars)
- (12) Annual demand for private cars = private car ownership * growth rate of private cars
- (13) Annual scrap number of private cars = private car ownership * private car scrap rate
- (14) Permanent residents = INTEG (permanent residents * population growth rate, initial value of permanent residents)
- (15) Per capita ownership = private car ownership / resident residents
- (16) Other fees = parking fee + fuel fee + car purchase tax
- (17) Car tax = purchase price * purchase tax rate

3.3. Assumption and Notation

- (1) The assumption of the average emission of NO₂ vehicles: taking the vehicle with the emission level of "National Phase IV Motor Vehicle Pollutant Emission Standard" as an example, the emission of light vehicles is about 1.6l, and the maximum emission of NO₂ cannot exceed 0.08 g/km. If the annual driving distance is 15000 km, NO₂: 0.08 kg/km * 15000 km / 1000 = 1.2 kg.
- (2) The model assumes sustained and stable economic growth.
- (3) Urban material flow in the model is replaced by urban freight volume; in the model, NO₂ production was selected as the environmental pollution index. The share rate of public transport is actually the share rate of public transport motorization. Environmental pollution is expressed by the content of NO₂. All growth rates are sequential.
- (4) Assume that all growth rates are constant.
- (5) Private cars, buses, and trucks are mainly considered in surface traffic volume, while the rest are included in other motor vehicles.
- (6) Traffic factors only consider the influence of the average road area of vehicles. Environmental factors are positively correlated with the total number of motor vehicles. Economic factors are expressed as a table function of the ratio of income to car purchase price. The above indexes are obtained by table functions. Consumer psychology is the exponential function of economic factor and demonstrative effect.
- (7) The growth rate of private cars is derived from the formula given in [12] and combined with the actual situation of the research object in this paper; it is concluded that the growth rate of private cars = traffic factor^{0.15} * economic factor^{0.4} * consumer psychological factor^{0.32} * (1 - environmental pressure)^{0.12} * consumer satisfaction degree. The degree of consumption satisfaction is determined

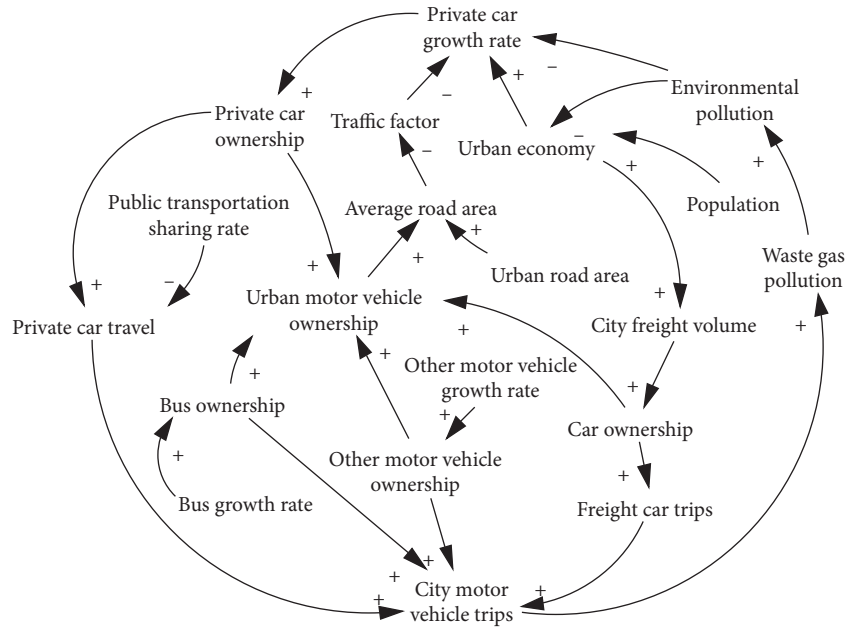


FIGURE 2: Causal cycle diagram.

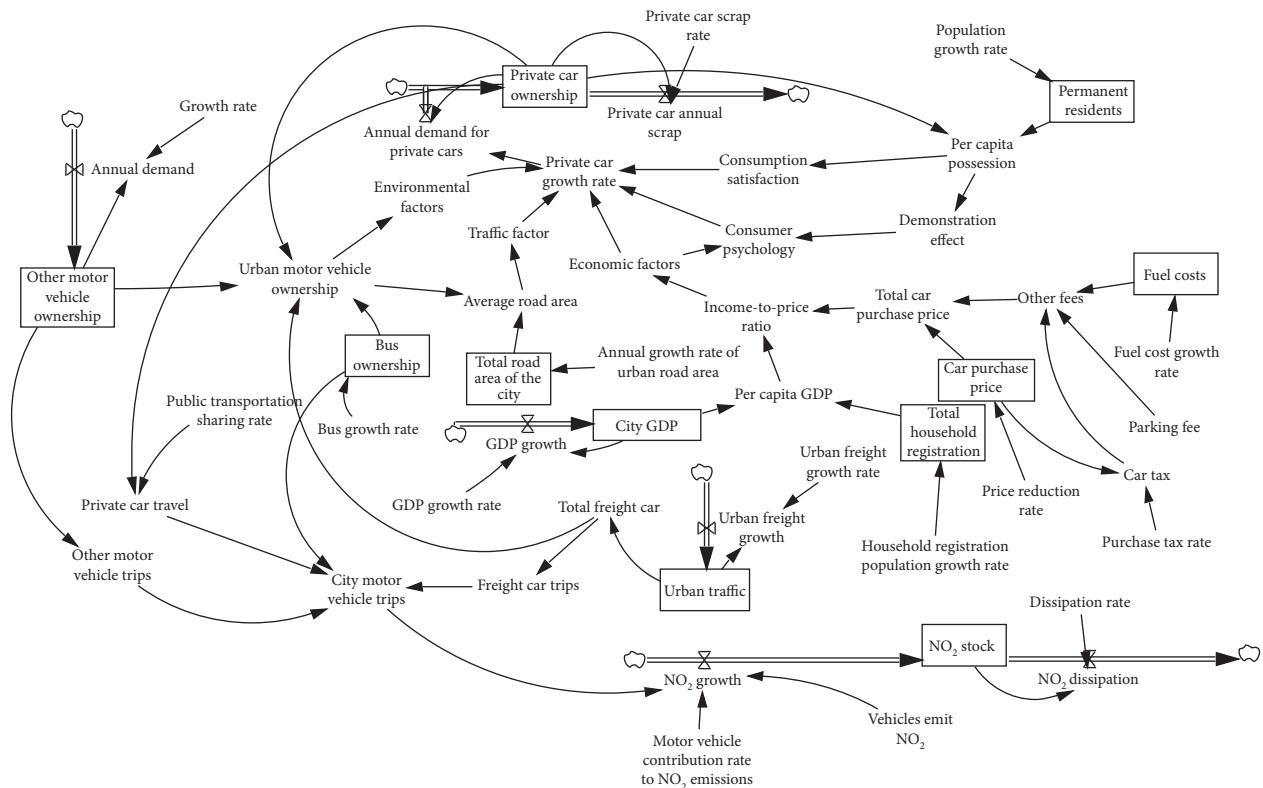


FIGURE 3: System dynamics diagram (without policy).

by per capita ownership. When per capita ownership is 0, the degree of consumer satisfaction is 0, and people are eager to buy cars. When per capita ownership is above 1, consumers' demand for cars is not high, so the degree of consumer satisfaction tends to be 1.

(8) The assumption of the restriction policy: each restriction of a tail number will reduce the number of vehicle trips by 10%. Similarly, when two tail numbers are restricted, about 20% of private car trips will be reduced. The parity-number limit policy is rotated once every two days, reducing the trip rate by 50%.

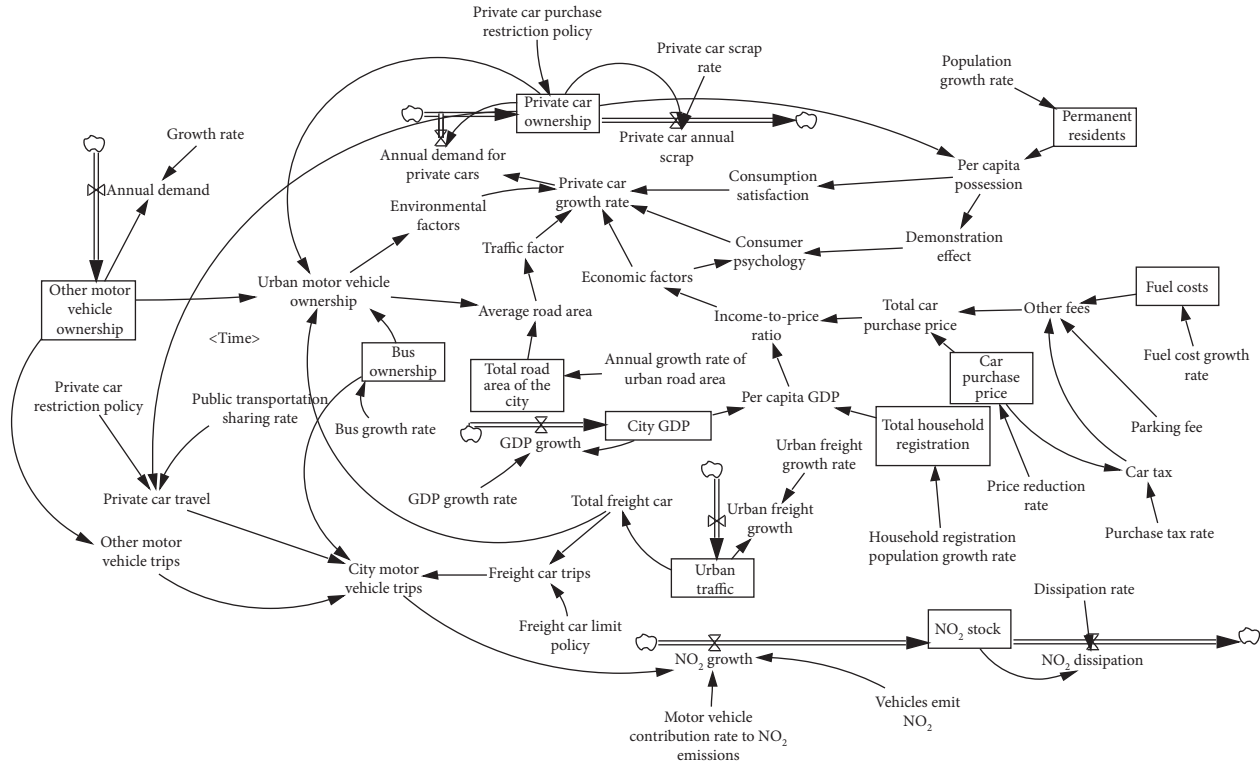


FIGURE 4: System dynamics diagram (with policy).

- (9) The winning rate of private purchase restriction policy is assumed to be 30%.
- (10) In the process of operation, the policy of vigorously developing public transportation is translated into the annual increase of public transportation sharing rate, which is shown in the form of table function.

4. Model Simulation

4.1. *Parameter Estimation.* The parameter estimation methods adopted in this model are as follows:

- (1) Adopt the linear fitting method
- (2) Quote relevant data of statistical yearbook
- (3) Estimate parameter values according to the model’s reference behavior characteristics
- (4) Methods of expert evaluation and references

Take the logarithm of Chongqing’s GDP from 2011 to 2016 and use Excel to get the trend (Figure 5). According to the trend chart, the logarithm of GDP and time basically conforms to the linear relationship, and the determination coefficient is 0.9971, with a high degree of fitting, as follows:

$$y = 0.1126x - 217.13, \tag{1}$$

$$R^2 = 0.9971.$$

The GDP growth rate of Chongqing is 11.26%. Similarly, according to the data of statistical yearbook, logarithmic fitting was carried out for each level variable, and the values were obtained as shown in Table 2.

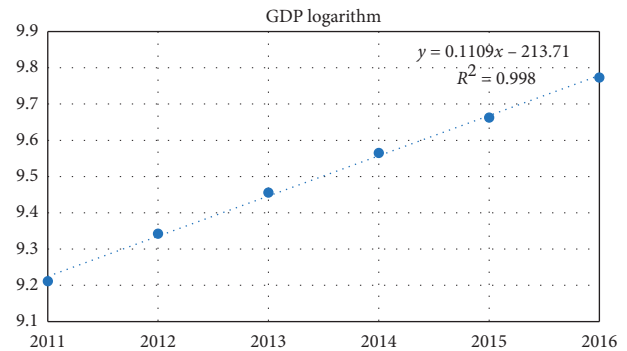


FIGURE 5: GDP growth rate fitting chart.

TABLE 2: Setting of constant values of the model.

Variable	Initial value set %
The GDP growth rate	11.26
Permanent population growth rate	0.84
Registered population growth rate	0.35
Fuel rate growth rate	10.17
Bus growth rate	11.83

The initial values of the Chongqing traffic simulation model are shown in Table 3 which refer to the relevant data of Chongqing in China statistical yearbook 2011 [19].

4.2. *Model Simulation.* Different step sizes of 0.25 (step 2), 0.5 (step 0), and 1 (current) are selected for the system dynamics model, which represent quarter, half year, and

TABLE 3: Initial values of the model.

Variable (unit)	The initial value
Private car ownership (10,000)	89.89
Bus ownership (vehicle)	8118
Other car holdings (ten thousand)	39.69
Purchase price (yuan)	150000
Per capita GDP (yuan/person)	34500
Total household registration population (10,000)	3392
Permanent residents (10,000)	3048
Total area of the city (ten thousand square kilometers)	17776
Purchase tax rate	0.1
Private car scrap rate	0.11
Total freight car (ten thousand)	26.01
Fuel costs (yuan)	5000
Cargo volume (ten thousand tons)	9.68
NO ₂ dissipation rate	0.1
Initial time	2011
Final time	2030
Time step	1
Units for time	Year

year, respectively. The results are shown in Figure 6. According to the trend in the figure, it can be concluded that the system is basically stable, and the operation of the model does not cause morbidity.

This paper takes the 2011–2016 Chongqing Statistical Yearbook data as the initial value and makes a medium and long-term simulation of the development of the number of motor vehicles in Chongqing. In Table 4, the simulation results of some variables in 2017 are compared with the actual statistical values. Compared with the prediction results, the error of each simulation value is small, and all do not exceed 5%. The behavior described by the model is basically consistent with the actual system behavior, and the model is basically effective.

4.3. Trend Forecast. As can be seen from Figure 7, without the use of policy adjustments, travel of all types of motor vehicles will continue to increase. And because private cars are the largest number of all types of motor vehicles and demand growth is growing rapidly, its continuous increase will increase the traffic burden without any control policy. But it can also be seen that the rapid growth of private cars will gradually slow down around 2025. Although the overall trend is still rising, the growth rate has been declining slowly.

Buses can reduce the number of private cars and increase the number of total motor vehicles. However, as the growth of private cars is much faster than the growth of buses, the natural growth rate of buses cannot alleviate the traffic pressure that the growing number of private cars brought.

It can be analyzed that with the increase of city GDP and the increase of per capita income, the consumption level of people is also increasing. As online shopping has become the most commonly shopping method, the demand for logistics has also increased accordingly. In addition to long-distance transportation such as aviation and trains, the number of freight cars is also increasing. The large-scale freight cars are

heavy in weight, slow in speed, and low in fuel combustion, which also causes air pollution and traffic pressure.

As shown in Figure 8, the growth rate set by the model decreases with time. The automobile demand may gradually decrease. As a result, the growth rate may continue to decline. However, since the per capita vehicle cannot reach 1 in a short period of time, the consumer satisfaction level will not be zero during the simulation period, so the growth rate will decrease later and then approach a constant so that the number of private cars still grows and traffic stress will not be alleviated.

5. Policy Optimization

5.1. Private Car Restriction Policy. At present, Chongqing has not yet implemented a large-scale limit policy and only implemented the double-number restriction policies on the bridges of the Fujian-Macau Bridge, the Huanghua Garden Bridge, and the Jiahua Bridge. This article mainly refers to three possibilities. Most of the existing domestic limit policies have been implemented to restrict the tail numbers during the weekdays and not to restrict them on weekends. Moreover, buses, taxis, official vehicles, and most freight vehicles are not affected by this policy. Therefore, in this article, it is assumed that the traffic restriction policy only has impact on the travel of private cars.

We set the parameters, fill in the model, and run the simulation three times separately to get the trend (Figure 9).

As can be seen from Figure 9, the restriction policy has a significant effect on reducing the amount of private car travel. In theory, the more restricted the tail numbers, the less the travel and the smaller the traffic burden. However, it can also be seen from the figure that after adopting parity-number restriction policy, the number of motor vehicle trips in cities has been reduced by almost half. With the implementation of the private car restriction policy, the development of public transportation may not keep up with people's travel needs.

5.2. Private Car Purchase Restriction Policy. Chongqing has not yet taken specific measures in terms of restricting the purchase of vehicles. However, in theory, rather than trying to adopt other policies to reduce the number of private cars, it is better to reduce the purchase of vehicles from the root cause. In order to curb the excessive growth of private cars, different restrictions on purchases have been adopted in various places, which are mainly divided into three types: Beijing's random lottery purchase policy, Shanghai's license auction policy, and Guangzhou Auction + Rocking Policy. This paper mainly adopts Beijing's policy to analyze.

In recent years, Beijing has been ranked among the top three in the country, both in terms of the number of motor vehicles and the degree of traffic congestion. On December 23, 2010, Beijing began to implement the policy of determining the private car purchase indicators by lottery.

The specific implementation principle of the lottery policy is a certain number of vehicles is allocated for each period, and the number is assigned before the lottery and drawn. The selected number in the pumping period also has

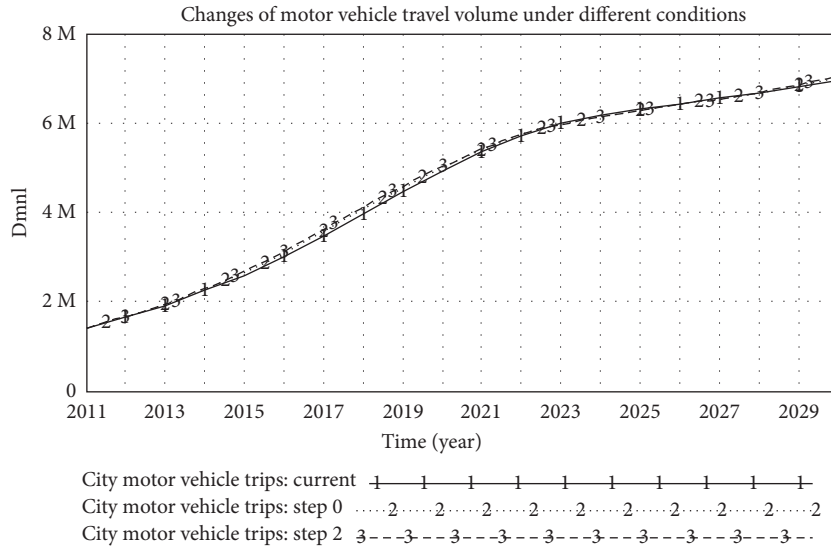


FIGURE 6: Historical test.

TABLE 4: Comparison of model simulation predictions with real values (2017).

Variable (unit)	Predictive value	Actual value	Error (%)
Private car (10,000 cars)	324.51	320.14	1.37
Private car (10,000 cars)	18975	19015	-0.21
City GDP (100 million yuan)	18990.2	19500.27	-2.62
Permanent residents (10,000 people)	3069.24	3075.16	-0.19
Total household registration population (10,000 people)	3400.35	3389.82	0.31
NO ₂ stock (10,000 tons)	214031	203954.91	4.94

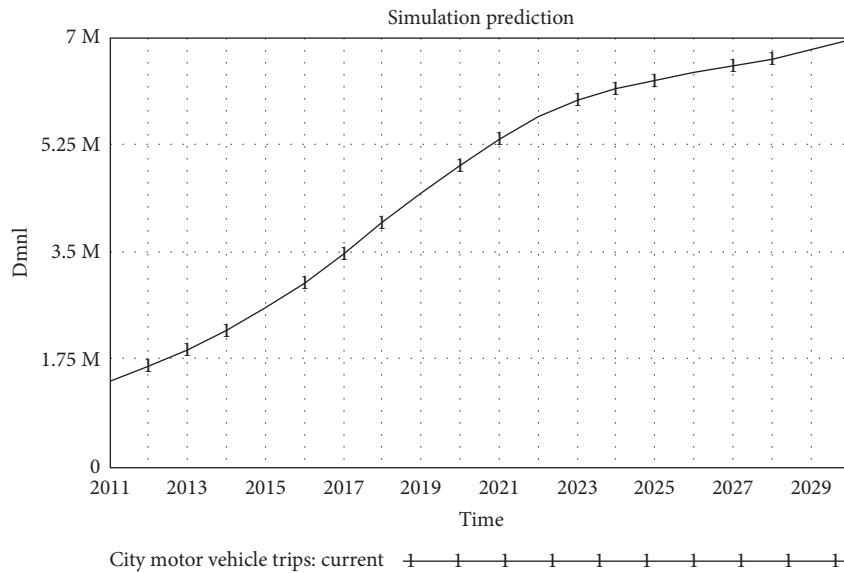


FIGURE 7: Changes in city motor vehicles trips over time.

a shelf life. If it is not used until the deadline, the quota will be invested in the next time. Referring to the previous period of Beijing, the allocated number of vehicles given in each

period is x , and the number of people participating in the survey is y . The winning rate is $x/y * 100\%$. After investigation, it was found that not all of the people involved in the

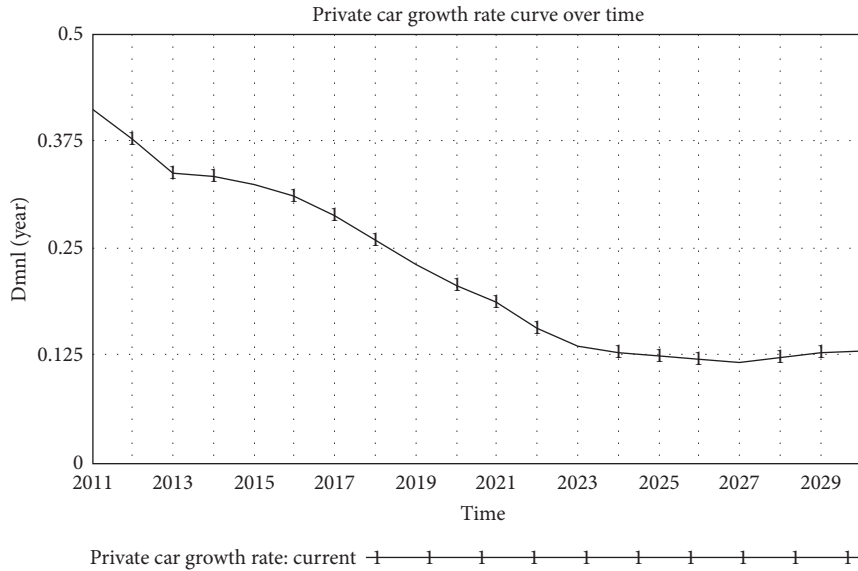


FIGURE 8: Changes in the growth rate of private cars.

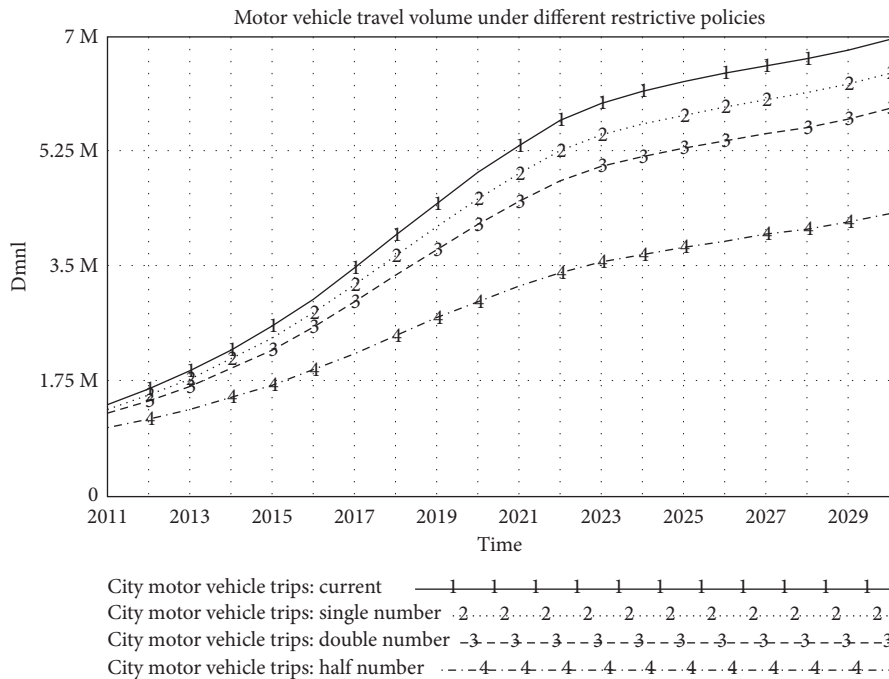


FIGURE 9: Vehicle traffic in cities under different restrictions.

extraction were those who had the demand for car purchases. Due to the lower and lower rate of winning in recent years, many people will choose queue for a long time, so $y \geq$ the annual demand for private cars.

As shown in Table 5 and Figure 10, the car purchase restriction policy is a good measure to limit the total number of private cars. In the case of each period, you can effectively limit the number of cars you buy. Regardless of other factors, the purchase of a car is an effective policy to alleviate traffic congestion.

TABLE 5: Comparison of the number of private cars with and without implementation of the private car purchase restriction policy.

Time	Without policy (10,000 units)	With policy (10,000 units)
2012	117.163	94.867
2013	148.558	100.457
2014	182.229	106.752
2015	222.717	113.452
2016	270.452	120.868
2017	324.719	128.637

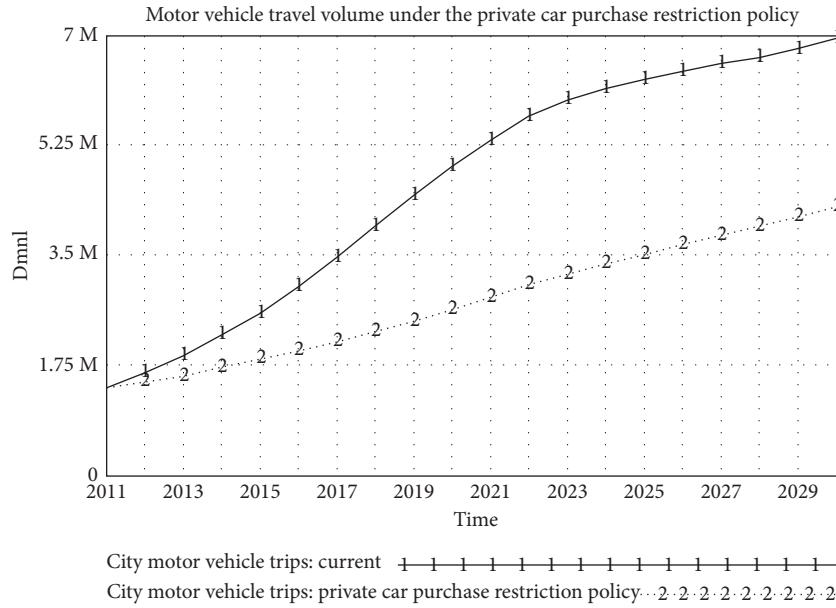


FIGURE 10: The number of motor vehicle trips in the city under the swaying policy.

TABLE 6: Travel mode selection and travel distance [9].

Travel mode (km) (%)	0–2	2–5	5–8	8–10	10–20	>20
Walk	56.41	4.5	0.43	0.36	0	0
Bicycle	3.05	30.01	14.21	13.03	5.1	1.23
Public transit	3.07	31.32	46.16	47.88	38.88	36.75
Private car	7.6	30.17	40.3	43.98	43.98	63.97
Others	3.54	2.33	2.33	0.81	0.81	2.66

5.3. Focus on the Development of Public Transportation.

In addition to private cars, public transportation is also an indispensable way for contemporary travel. Public transportation has the advantages of being cheap, convenient, and green. Promoting public transportation can not only reduce traffic congestion but also reduce environmental pollution. In this paper, when the initial value of the model is set, it is assumed that the public transportation sharing rate is constant. In fact, this is impossible because the government invests a large amount of money every year to build public transportation. For example, in recent years, more and more bus lines have been established in Chongqing. The light rail line has formed a network, and most of the landmark locations and business districts in the main city are included.

From Table 6, it can be found that when travelling more than two kilometers and less than twenty kilometers, people choose public transportation with a similar probability to private cars, so we think that transportation and private cars can be substituted. In an increasingly convenient public transportation network, people are more inclined to choose public transportation because of the difficulty of parking and the trouble of traffic jams.

Therefore, while vigorously developing public transportation, the sharing rate of public transportation to private

car travel is also constantly rising. The article assumes that the public transportation sharing rate is a variable that changes over time. After adjusting the function, we perform simulation analysis, and the result is shown in Figure 11. With the continuous development of public transportation, city motor vehicle trips have been greatly reduced.

5.4. Freight Car Limit Policy.

In order to restrict the passage of freight vehicles in urban areas, the Chongqing Municipal Government has also adopted some restrictions on freight cars. The main restrictions are as follows: first, every day from 7:00 to 22:00, all freight cars with registered addresses not in Chongqing are prohibited. In Chongqing, the three-axis (including) freight cars that do not hold valid passports are forbidden to enter the main section. Second, 24 hours a day, all freight cars are prohibited from entering the following sections: Yubei District Shuanghu Road (the intersection of Huangjiaoping Park and Shenghu Tianyu Road), Baiguo Road, and Qihang Avenue; it is forbidden to approve the trucks with a load of more than 1 ton (inclusive) and enter the Xingsheng Avenue of Yubei District.

However, because the base of freight cars is too small, the proportion of travels in the whole city is not large, and there is no obvious change in the amount of motor vehicles. The

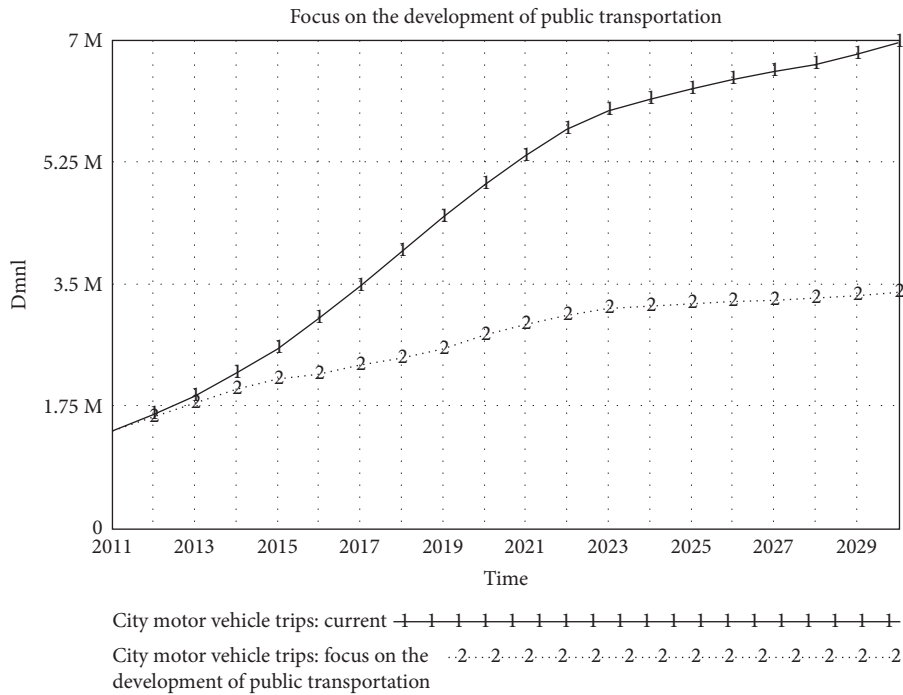


FIGURE 11: Focus on the development of public transportation.

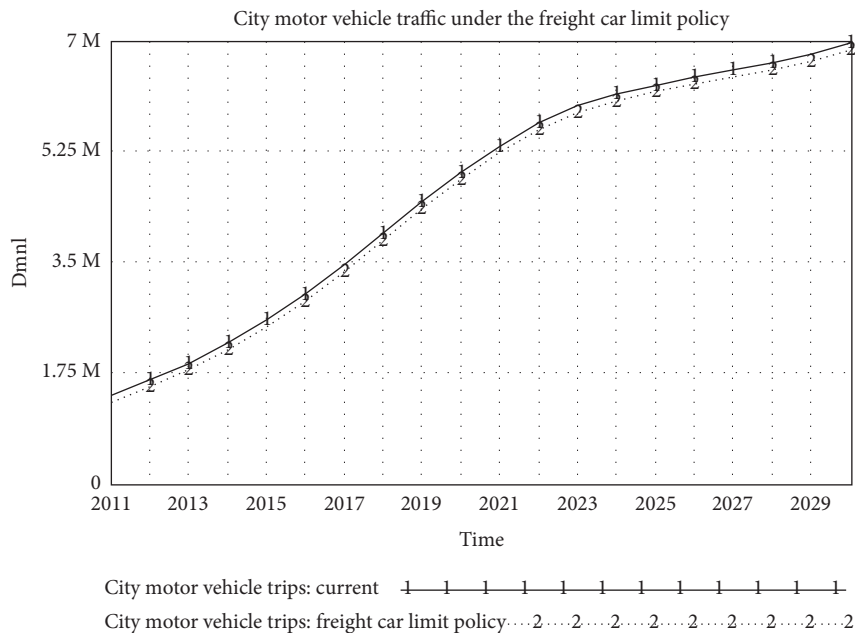


FIGURE 12: City motor vehicle trips under the restricted truck policy.

results after the simulation are shown in Figure 12. Moreover, since the freight car is closely related to the logistics industry, if the road section of the truck entering the city center is greatly restricted, it will have a great impact on the city logistics circulation.

Based on the comparison of the city motor vehicle trips under the above four different policies, we can get Figure 13.

6. Conclusions

In the previous section, we analyzed four types of restrictive policies. We found that these four policies have certain impacts on urban motor vehicle travel. The main purpose of this paper is to provide reasonable policy recommendations for Chongqing's current congestion caused by motor vehicles, so the final step is to compare policies.

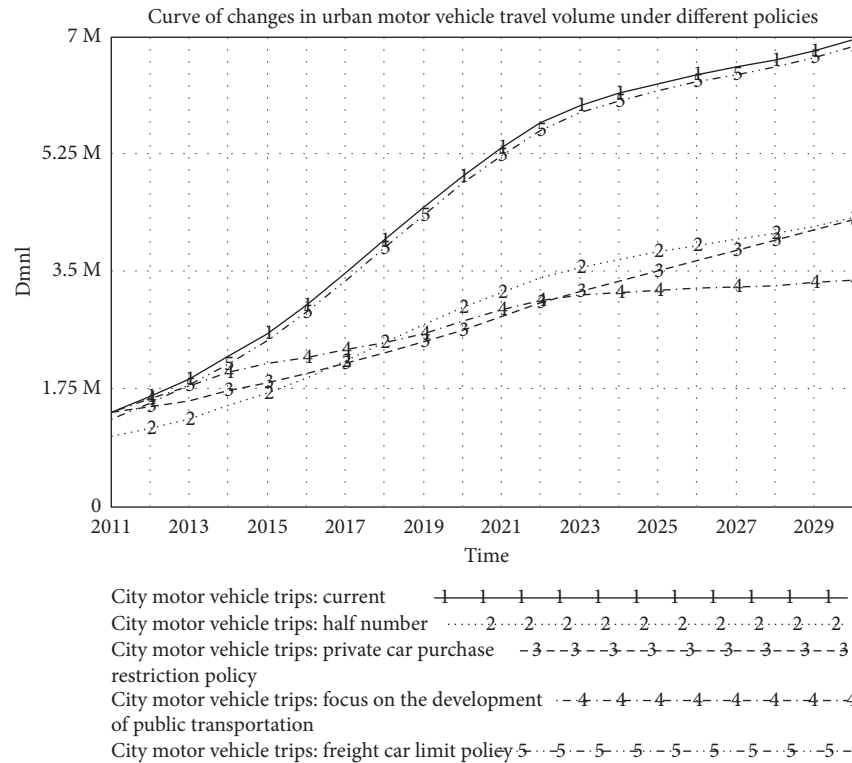


FIGURE 13: City motor vehicle travel volume under policy comparison.

From Figure 13, we found that each policy has a certain effect on controlling the amount of motor vehicle travel in the city, and the effect of the freight car limit policy is the weakest. In the short term, the private car restriction policy has the best effect. The effect of the purchase restriction policy has been very good, indicating that restricting car purchase is a rooted solution. The method of developing public transportation is not as effective as the private car restriction policy and the purchase restriction policy in the early stage. However, it will show its advantages in the later period, and it is also an effective way to control the growth of motor vehicle travel.

When no policies are used, the simulation results show that in the future, the growth rate of private car growth will gradually flatten. Although its overall trend is still growing, the demand for private cars will gradually flatten due to the increase in consumer satisfaction.

It can be concluded that the number of private cars will be reduced if Chongqing implements the restriction policy of private cars. Neither single-number limit nor double-number limit is less effective than the parity-number restriction policy. Therefore, the parity-number limit is a measure that can reduce traffic congestion in a short period of time. The purchase restriction policy has reduced the number of private cars from the root cause and so it is a valid measure. Developing public transportation is a long-term solution to solve the problem of traffic congestion. It is known that ordinary people choose to walk when they travel normally for less than two kilometers. In the ordinary travel of more than two kilometers, the ratio of people choosing public transportation and private car travel is generally close.

Considering that the supply of parking spaces in today’s cities is small, if public transportation is convenient enough, people may be more inclined to choose convenient travel. Therefore, the government should plan more funds and plans for public transportation, which not only helps to manage traffic congestion but also helps control environmental pollution. The control effect of the truck limit policy on traffic congestion is not obvious.

But because the model is a simplification of the actual transportation system, many related factors and policies are also ignored. First of all, it is common sense to measure the degree of traffic congestion with city motor vehicle trips as an indicator, but it is not comprehensive enough. The actual traffic congestion may also be due to factors such as road network density and road width. Secondly, when considering the policy of controlling traffic congestion, this paper mainly considers factors such as controlling the amount of private car travel and improving the replacement rate of public transportation.

For the implementation of the restriction policy and the limit policy, the article is simplified into a linear relationship, which has a certain deviation from the actual impact. The research on the impact of truck traffic is also related to the development of urban logistics industry. This paper only considers the city’s daytime limit policy and has certain limitations. Finally, in order to control traffic congestion and environmental pollution, the government has to come up with a variety of new methods that are closely related to the development of science and technology. For example, some foreign cities have begun to adopt congestion pricing policies. Therefore, in the future, factors such as parking charges

and road construction can be considered to improve the construction of the transportation system.

Data Availability

The data used to support the findings of this study are available from the corresponding author upon request.

Conflicts of Interest

The authors declare that they have no conflicts of interest.

Acknowledgments

This study was supported by the Major Projects of the National Social Science Fund (no. 16ZDA010), Sichuan Science and Technology Program (nos. 2019JDR0210 and 2019JDR0030), and Scientific Research Project of Central University of Southwest University of Finance and Economics (no. JBK170503).

References

- [1] J. Guo, M. Liu, L. Yu et al., "Development and application of Beijing traffic congestion macro evaluation index system," in *Proceedings of the 3rd China Intelligent Transportation Annual Conference*, Nanjing, China2007, in Chinese.
- [2] C. Wright and P. R. Orenstein, "Simple models for traffic jams and congestion control," *Proceedings of the Institution of Civil Engineers-Transport*, vol. 135, no. 3, pp. 123–130, 1999.
- [3] D. Anthony, "Can traffic congestion be cured?" *The Washington Post*, vol. 4, pp. 955–974, 2006.
- [4] P. Diakaki, D. Kotsialos, and Wang, "Review of road traffic control strategies," *Proceedings of the IEEE*, vol. 91, no. 12, pp. 2041–2042, 2004.
- [5] Z. Liu, X. Yue, and R. Zhao, "The causes and countermeasures of urban traffic congestion in China," *Urban Development Research*, vol. 18, no. 11, pp. 90–96, 2011, in Chinese.
- [6] J. Taylor, "Urban congestion and pollution. is road pricing the answer?" *Proceedings of the Institution of Civil Engineers-Municipal Engineer*, vol. 93, no. 4, pp. 227–228, 1992.
- [7] D. Coomber, P. Guest, J. Bates et al., "Study of parking and traffic demand: I. the research programme," *Traffic Engineering and Control*, vol. 38, no. 2, pp. 62–67, 1997.
- [8] W. Muanmas, M. G. H. Bell, and H. Yang, "Impact of congestion charging on the transit market: an inter-modal equilibrium model," *Transportation Research. Part A: Policy and Practice*, vol. 41, no. 7, pp. 703–713, 2007.
- [9] E. Fishman, S. Washington, and N. Haworth, *An Evaluation Framework for Assessing the Impact of Public Bicycle Share Schemes*, Transportation Research Board, Washington, DC, USA, 2012.
- [10] T. H. Heung, T. K. Ho, and Y. F. Fung, "Coordinated road-junction traffic control by dynamic programming," *IEEE Transactions on Intelligent Transportation Systems*, vol. 6, no. 3, pp. 341–350, 2005.
- [11] Q. Wang, *System Dynamics*, Tsinghua University Press, Beijing, China, 1994, in Chinese.
- [12] I. Kaparias and M. G. H. Bell, "London congestion charging: successes, gaps and future opportunities offered by cooperative ITS," in *Proceedings of the 2012 15th International IEEE Conference on Intelligent Transportation Systems*, Anchorage, AK, USA, September 2012.
- [13] Q. Wang and J. Jia, "Study on the influence of China's entry into the WTO on China's car market demand," *Systems Engineering Theory and Practice*, vol. 3, pp. 56–62, 2002, in Chinese.
- [14] J. Fan and G. Yan, "Simulation and control of total private cars in Beijing based on system dynamics," *Journal of Highway and Transportation Technology*, vol. 26, no. 12, pp. 120–125, 2009, in Chinese.
- [15] H. Yang, K. Lin, Y. Zhou, and X. Du, "The governance of urban traffic jam based on system dynamics: in case of Beijing, China," *LTLGB 2012*, Springer, Berlin, Germany, 2013.
- [16] Z. Dang, "Testing the effect of Shanghai auto license auction system based on system dynamics," *Market Weekly (Theory Research)*, vol. 5, pp. 21–23, 2015, in Chinese.
- [17] S. Jia, G. Yan, A. Shen, and J. Zheng, "A system dynamics model for determining the traffic congestion charges and subsidies," *Arabian Journal for Science and Engineering*, vol. 42, no. 12, pp. 5291–5304, 2017.
- [18] Y. Zhang, L. J. Wan, L. Zhang, and D. X. Cheng, "Forecast of energy consumption and carbon emission of urban traffic by using system dynamics," *Advanced Materials Research*, vol. 989–994, pp. 1248–1251, 2014.
- [19] Chongqing Municipal Bureau of Statistics, *Chongqing Statistical Yearbook*, China Statistics Press, Beijing, China, 2011.

Research Article

Optimal Fault Tolerant Control of Large-Scale Wind Turbines in the Case of the Pitch Actuator Partial Faults

Younes Ait El Maati  and Lhoussain El Bahir 

Cadi Ayad University, Laboratory of Electrical Engineering and Control Systems (LGECOS), National School of Applied Sciences, Av. Abdelkarim El Khattabi B.P 575, Marrakech 40000, Morocco

Correspondence should be addressed to Younes Ait El Maati; aitelmaati.younes@gmail.com

Received 24 September 2019; Revised 30 December 2019; Accepted 11 January 2020; Published 12 February 2020

Guest Editor: Kiyong Oh

Copyright © 2020 Younes Ait El Maati and Lhoussain El Bahir. This is an open access article distributed under the Creative Commons Attribution License, which permits unrestricted use, distribution, and reproduction in any medium, provided the original work is properly cited.

In this paper, an adaptive fault tolerant control strategy is proposed to deal with the three pitch actuator faults in the large-scale wind turbines. Firstly, a simultaneous state and fault estimation was performed through a suitable LMI (linear matrix inequality) based optimal strategy. Hereafter, the new control law is designed using the previously estimated fault information. The actuator efficiency estimator uses as design parameters, respectively, the performance index γ against the wind and the learning rate Ξ . of the fault estimation algorithm. The study shows that the choice of the previous two parameters impacts the response time of the fault estimation and the correlation of the tracking error with the wind. The aim is to choose a small fault estimation response time while keeping a weak correlation between the tracking error and the wind turbulence noise. Finally, a tuning strategy is elaborated to choose the suitable γ and Ξ to match the reconfiguration objective.

1. Introduction

The increasing energy demand leads to the production of large wind turbines. Thus, more and more vibrational behaviors could be expected in the different degrees of freedom (DOFs). Figures 1 and 2 show the most important DOF. The excitation of the DOFs leads to increase in loads and forces on the structure. The aim is to reduce the loads in order to protect the structure against fatigue and damage.

The wind turbine operates in two different regions, low and high winds. In the first region, so called partial load region, the aim is to maximize the extracted power [1, 2]. This was achieved by controlling the generator torque to maintain an optimum ratio between the tip speed of the blades and the operating wind speed [3]. In the second region, so called full load region, the wind turbine was controlled to reduce loads and keep the power at its rated value. Practically, the constant power was maintained through a fixed speed and a fixed generator torque. This has

been obtained by pitching the blades from or toward wind to adjust the speed of the rotor, while applying a constant generator torque [4]. For example, the authors in [5] proposed an anticipative control scheme of a wind turbine working in the maximum power region. The idea is to use the wind speed as a generator of the set point of the MPP (maximal power point) control.

1.1. The Pitch Actuator Control of Wind Turbines in the Full Load Region. In the full load region, the high turbulence occurs and produces big deflection movements on the blades. The pitch actuators were used to attenuate the loads in the full load region [6–8].

Many papers have studied the loads exerted by the wind on the different parts of the wind turbine structure. In [9], the authors discussed and identified which wind turbine components can benefit from advanced control algorithms and also presented results from a preliminary loads case analysis using a baseline controller.

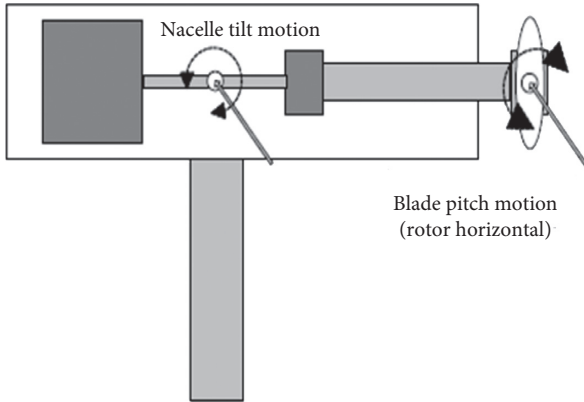


FIGURE 1: Blade pitch degree of freedom.

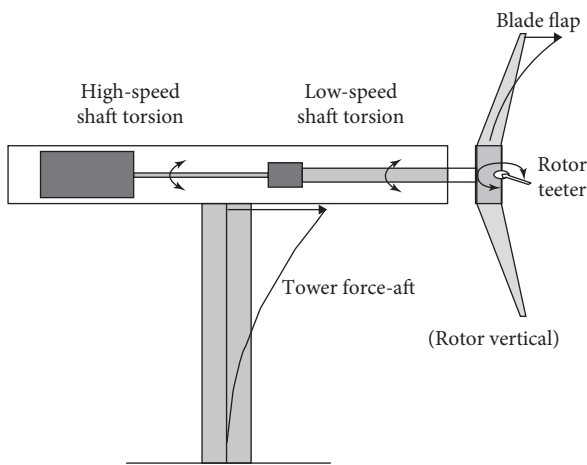


FIGURE 2: Blade flap and tower fore-aft degrees of freedom.

From the discussed papers above, it can be noticed that the wind turbines in the megawatt size are expensive, and hence their reliability is expected to be high to generate as much energy as possible. This type of wind turbines is expected to have reduced downtimes while keeping energy production. Usually, the turbines are turned off even during simple faults to wait for service.

1.2. Fault Detection and Tolerant Control in Wind Turbines.

The statistics in [10] show that gearbox faults are the most critical ones in wind turbines, essentially due to its relatively high stopping time and severity on the whole structure. Another type of wind turbine faults is of electrical root. For example, the wind turbine can face short circuit faults in the wires or inverter over voltage faults. It can also experience hard over fault in the generator or some sensor faults like drift or bias.

The last reason creates the need to introduce fault detection, isolation, and accommodation systems within the existing classical control systems in order to reduce stop time even with limited energy production [11]. Early detection has been the spot of the control industry studies especially using residual generation and fault analysis. The paper [12] presents an overview of the fault diagnosis

method categories, with an application to the wind turbine pitch fault control. For more details, see also [13, 14].

The model-based methods are one of the most suitable methods for the study of the fault tolerant control of the wind turbines. In fact, the availability of the large-scale wind turbine model is no longer a problem especially with the existence of highly trusted wind environment software and emulators such as FAST (Fatigue, Aerodynamics, Structures, and Turbulence).

In this paper, the FAST code is used to test the proposed strategy. FAST is an aeroelastic simulator capable of predicting the fatigue loads of two- and three-bladed flexible with 24 degrees of freedom [15, 16]. The code uses a modal approach in combination with Kane dynamics to develop the equations of motion. FAST helps considerably researchers and engineers in testing wind load reduction algorithms [17]. This software provides a linearized model parameter about a chosen operating point with more than 40 measures of outputs (rotor speed, generator speed, and tower and blade displacement).

The pitch servomotor is the most critical actuator in the wind turbine [18, 19]. As discussed earlier, it is used to regulate the power and to attenuate the vibrations in the high wind region. If this actuator loses its efficiency, it will no longer provide the sufficient control efforts to attenuate the vibrations and regulate the power. Based on the last reason, a new control law is to be constructed to deal with the fault. The new control efforts could be produced by online tuning of the controller parameters or by changing the baseline control law using an estimation of the fault [20–22].

In the wind turbines' control field, in the pitch actuator fault, the authors inference [23] proposed a fault tolerant control strategy to deal with the drop of the hydraulic liquid in the servo pitches of the rotor. In the same field, another type of fault is the imbalance in the rotor due to icing or destruction of one or more blades. This fault not only reduces the aerodynamic efficiency of the turbine and its power output but can also lead to large increases of loads on the drivetrain, blades, and tower. For this, the authors in [24] used the FAST software to model aerodynamic imbalance in a sample 5 MW offshore wind turbine. It has been concluded that the combination of blade and nacelle measurements, obtained from instrumentation already placed on the structure, can be formulated into an algorithm used to detect and locate the imbalance (see also [25]).

Another essential component is the anemometer. The anemometers are used in the feedforward control of the wind turbines. In [26], the authors proposed a new method to estimate the wind speed that could be substituted for anemometers in control loops. Moreover, the authors in [27] proposed a robust observer to generate residuals for the fault turbine moment sensors which provides a measurement of the loads applied on the structure. In [28], the authors have proposed a method to estimate the gearbox efficiency in the wind turbines. The idea is to detect the drop in the efficiency and generate a suitable residual to indicate the fault occurrence (see also [29, 30]).

Given the very disturbed wind nature, several optimization methods could be used to minimize the effect of the

disturbance on the outputs. In [31], a multiagent optimal method based on reinforcement learning was proposed to control a grid connected energy system.

The fault isolation and tolerant control applied to the wind turbines has been illustrated in many papers. For example, in [32, 33], a codesign of the observers and decision mechanisms for satisfying certain trade-off between different isolation performance indices has been established. The performance indices were the false isolation rates, the isolation times, and the minimum size of the isolable faults. The considered fault was additive on the pitch actuator. The paper [34] used jump observers to detect and isolate the faults. The false alarm rate is upper bounded by means of Markov's inequality. The trade-offs between the minimum detectable faults, the false alarm rate, and the response time to faults of the fault diagnoser have been explored. In the previous cited works, the assumption of slow dynamics faults was considered which limits the usage of the strategies to slow faults dynamics.

In this paper, the following contributions have been developed:

- (i) An integrator-based simultaneous states and fault estimator algorithm is designed.
- (ii) The stability and the robustness of the algorithm is proven for the partial fault of the pitch actuators using Lyapunov theory.
- (iii) A fault tolerant control including a baseline multiobjective state feedback regulator is designed. The performance of the method depends on two parameters to be tuned, γ and Ξ .
- (iv) To ensure a best performance of the proposed control solution, two mappings are proposed to tune the design parameters γ and Ξ .
- (v) The evaluation of the proposed control strategy is performed on the 1.5 MW wind turbine benchmark model.

This paper is organized as follows. In Section 2, the wind turbine model used in the benchmark is presented. In Section 3, the wind turbine fault and state estimation is performed and the nominal multiobjective regulator is designed. The wind turbine adaptive fault tolerant control in the faulty production is studied and the tuning strategy is proposed in Section 4. Some concluding remarks are presented in Section 5.

2. The Wind Turbine Model

The wind turbine model used for the control contains seven wind turbine states as follows:

- (i) The rotor speed
- (ii) The blade i flap wise deflection
- (iii) The blade i flap wise deflection velocity

where $i = 1, 2, 3$.

The state space model of the rotor about the operating point is given by

$$\begin{cases} \delta\dot{x} = A\delta x + B\delta u + D_d\omega \\ \delta y = C\delta x \end{cases} \quad (1)$$

The operator δ means a variation about the operating point. A is the dynamics matrix, B is the input matrix, D_d is the disturbance matrix, and C is the measured output matrix. The numerical values of the matrices A , B , C , and D_d are given in the Appendix.

The state vector and the pitch actions are, respectively, represented by the vectors δx and δu :

$$\begin{aligned} \delta x &= [\delta\Omega_r, \delta x_{\text{def}_1}, \delta\dot{x}_{\text{def}_1}, \delta x_{\text{def}_2}, \delta\dot{x}_{\text{def}_2}, \delta x_{\text{def}_3}, \delta\dot{x}_{\text{def}_3}]^T, \\ \delta u &= [\delta\beta_1, \delta\beta_2, \delta\beta_3]^T, \end{aligned} \quad (2)$$

where δx_{def_i} and $\delta\dot{x}_{\text{def}_i}$ are, respectively, the blade deflection and deflection velocity associated to the i^{th} blade. δy represents the measured rotor speed and deflection velocity. The vector ω is the wind disturbance on the considered states and is given by

$$\omega = V(t) - V_0, \quad (3)$$

where $V(t)$ is the instantaneous wind speed and V_0 is the operating wind speed which is equal to 18 m/s in the high wind region. The vector is the rotor speed about the operating point and is given by

$$\delta\Omega_r = \Omega_r(t) - \Omega_{r0}, \quad (4)$$

where $\Omega_r(t)$ is the measured rotor speed and the operating rotor speed is $\Omega_{r0} = 40$ rpm. The input pitches about operating point are equal to $\delta\beta_1 = \delta\beta_2 = \delta\beta_3 = \beta(t) - \beta_0$. $\beta(t)$ is the measured pitch angle and the operating pitch angle is $\beta_0 = 9^\circ$.

The numerical values of variables in the international system of measurement units are given.

It is assumed that the measured outputs are the rotor speed and the blade flap deflection velocities of the three blades. In actual application like wind turbine blade analysis, the deflection velocities could be obtained using the derivative of the deflection displacement measure. This information could be directly obtained using a MEMS gyroscope sensor as in [35], or estimated using ultra-wideband signals as proposed in [36].

The considered turbine is a Wind PACT 1.5 MW large scale. More details about the parameters of this wind turbine could be found in [37, 38]. The turbine parameters summary is given in Table 1.

3. Wind Turbine Control Strategy in the Nominal Production

The nominal controller is designed for two objectives. On the one hand, the rotor speed should be regulated despite the wind changes. On the other hand, the blade's deflections should be attenuated to prevent the structure from being damaged. The control scheme is summarized in Figure 3. The blades' deflection velocity and the rotor speed are both measured and fed to the robust state observer. Finally, the

TABLE 1: Wind turbine parameters.

Characteristics	Value
Rated power (MW)	1.5
M_b : Blade mass (kg)	4,230
D_b : Blade stiffness (N·m/rad)	20760
Total rotor mass (kg)	32,016
J_r : rotor inertia (kg·m ²)	$2.9624 * 10^6$
J_g : generator inertia (kg·m ²)	$53.036 * Ng^2$
N_g : gearbox ratio	87.965
R : rotor radius (m)	35

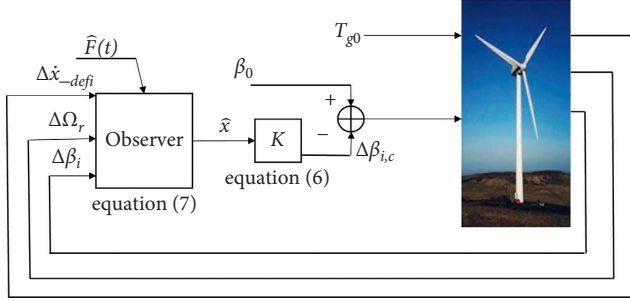


FIGURE 3: The wind turbine control objective scheme.

state feedback controller uses the estimated states to generate the necessary pitch angle variations responsible for regulating rotor speed and attenuating blade deflections. The adjective nominal means the baseline or the fault free situation. The system is linearized about the nominal operating point, and then the nominal controller is derived based on the pole placement method to achieve the nominal production. The opposite to nominal is faulty, which means the situation in which the fault occurs.

3.1. The Global Wind Turbine State Space Model. The global state space representation in the equation (5) takes into account the pitch actuator faults. The actuator effectiveness fault is modeled as a multiplication of the input matrix B by an unknown fault matrix F , and the faulty system is then given by

$$\begin{cases} \dot{x}(t) = Ax(t) + BF(t)u(t) + D_1\omega(t), \\ y(t) = Cx(t) + D_2\omega(t), \end{cases} \quad (5)$$

where $x(t) \in \mathbb{R}^n$ is the state vector; $u(t) \in \mathbb{R}^m$ is the input vector; $y(t) \in \mathbb{R}^p$ is the measured output with $p \geq m$; and C and B have full rank ($\text{rank}(C)=p$ and $\text{rank}(B)=m$). $F(t) \in \mathbb{R}^{m \times m}$, and $F(t) = \text{diag}(f_1(t), f_2(t), \dots, f_m(t))$ is the vector of faults on the actuators.

3.2. The Observer and the Baseline Controller Design. The three-blade flap deflection amplitude reduction and the rotor speed regulation are performed through a pole placement state feedback [39] as in equation (6). In fact, the nominal control law in equation (6) is based on the fault free

(nominal) situation, in which the fault matrix $F(t)$ equals the identity matrix which is constant.

$$u = \Delta\beta_{i-c} = K\hat{x}. \quad (6)$$

The variable \hat{x} in equation (6) is the state vector to estimate. The gains of controller K are design parameters to achieve the multiobjective wind turbine control. The variable \hat{x} should be estimated robustly in the next paragraph.

In Figure 3, T_{g0} is the generator torque input at the operating point and is kept constant in the region of high winds, β_0 is the pitch angle input at the operating point, $\Delta\beta_{i-c}$ is the pitch angle input variations from the operating point ($i=1, 2, 3$), K is the control gain, $\Delta\dot{x}_{\text{def}_i}$ are the deflection velocity variations from the operating point ($i=1, 2, 3$), $\Delta\Omega_r$ is the rotor speed variations from the operating point, $\Delta\beta_i$ is the measured pitch angles and are input to the state observer, and $F(t)$ is the fault matrix.

3.2.1. The Robust State Observer. The structure of the state observer is given by system (7) and illustrated by Figure 4:

$$\dot{\hat{x}}(t) = A\hat{x}(t) + BF(t)u(t) - L(C\hat{x}(t) - y(t)), \quad (7)$$

where $y(t)$ corresponds to the vector containing the measured deflection velocities $\Delta\dot{x}_{\text{def}_i}$ and rotor speed $\Delta\Omega_r$. The vector $u(t)$ corresponds to the measured three blade pitch angles. $F(t)$ is the matrix of the faults. $\hat{x}(t)$ is the output of the observer.

$\hat{x}(t) \in \mathbb{R}^n$ are the observer states, $\hat{y}(t) \in \mathbb{R}^n$ are the observed outputs, $\hat{F}(t) \in \mathbb{R}^{m \times m}$ is the estimate of $F(t)$, and $L(t) \in \mathbb{R}^{n \times p}$ is the estimator gain to be designed.

3.2.2. The Fault Matrix Estimator. The fault matrix $F(t)$ has to be estimated. This estimate is $\hat{F}(t) \in \mathbb{R}^{m \times m}$ and has the following diagonal form: $\hat{F}(t) = \text{diag}(\hat{f}_1, \hat{f}_2, \hat{f}_3)$, where \hat{f}_i is the estimation of the pitch fault on the actuator of index i . The following integrator-based algorithm is proposed:

$$\dot{\hat{f}}_i = -\xi_i r_i e_y(t) u_i(t), \quad (8)$$

where $i=1, 2, 3$; $\Xi = \text{diag}(\xi_1, \xi_2, \dots, \xi_m)$; $\Xi \in \mathbb{R}^{m \times m}$ is called the learning rate; and $r_i \in \mathbb{R}^{1 \times p}$. The parameter p is the number of measurements. $u_i(t)$ is the control input in the direction to the pitch actuator number i .

The adaptability of the estimation consists in the update of the fault estimate dynamics with time by acting on the learning rate Ξ or the matrix $R = [r_1 \ r_2 \ r_3]^T$. The matrix R is an additional degree of freedom that can be used to refine the approximation $B^T P = RC$ in equation (15) in Section 3.2.3. An application of this matrix could be to refine equation (15) only in the direction of a selected measurement from matrix C for a fixed η . For example, to refine equation (15) in the direction of the blade deflections, R could be chosen equal to $\begin{bmatrix} 0 & -470.4158 & 0 & 0 \\ 0 & 0.001 & -470.4158 & 0 \\ 0 & 0 & 0 & -470.4158 \end{bmatrix}$ and the resulting product RC will then be equal to

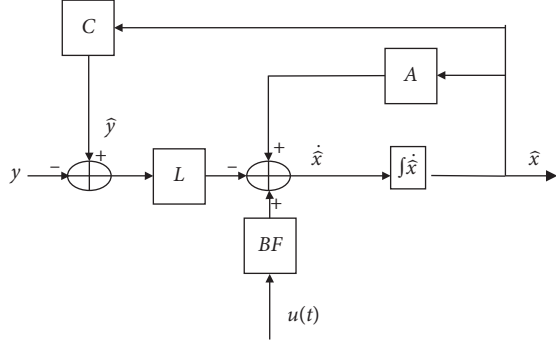


FIGURE 4: The state observer structure.

$$\begin{bmatrix} 0 & 0 & -470.4158 & 0 & 0 & 0 & 0 \\ 0 & 0 & 0 & 0 & -470.4158 & 0 & 0 \\ 0 & 0 & 0 & 0 & 0 & 0 & -470.4158 \end{bmatrix}. \quad \text{In the}$$

resulting matrix RC , the second row vector became null. Indeed, this row represents the contribution of the rotor speed in the product matrix RC . The remaining vector rows 3, 5, and 6 represent the blade deflection velocities contribution in the product matrix RC . Another alternative could be to compute an initial guess of R using YALMIP and refine it according to the need. In the present paper, R was extracted using YALMIP.

The learning rate Ξ is selected and handled by the user to ensure the fault estimation performance requirements. It allows to achieve a compromise between a quick fault accommodation and the disturbance amplification. Indeed, for high values of Ξ , high frequency information, namely, disturbances, is integrated in the learning process and vice versa. The variable $e_y(t)$ is the output tracking error and is equal to the difference $\hat{y}(t) - y(t)$.

3.2.3. Stability and Robustness of the Observer. Consider the states tracking error $e_x(t) = \hat{x}(t) - x(t)$, the output tracking error $e_y(t) = \hat{y}(t) - y(t)$, and the fault tracking error $e_f(t) = \hat{F}(t) - F(t)$.

The states' tracking error dynamics are given by the state space representation in the following equation:

$$\begin{cases} \dot{e}_x(t) = (A - LC)e_x(t) + Be_f(t)u(t) + (LD_2 - D_1)\omega(t), \\ e_y(t) = Ce_x(t) - D_2\omega(t). \end{cases} \quad (9)$$

The first objective is to have $e_x(t) \rightarrow 0$ and $e_f(t) \rightarrow 0$ when $t \rightarrow +\infty$. The tracking errors' convergence and stability could be ensured using the Lyapunov function $V_e(t)$:

$$V_e(t) = e_x^T(t)Pe_x(t) + \text{tr}(e_f^T(t)\Xi^{-1}e_f(t)). \quad (10)$$

The condition of validity of $V_e(t)$ is that Ξ is chosen invertible.

P is a symmetric positive definite matrix. The idea of the Lyapunov function choice is as the learning rate increases, the quadratic fault tracking error $e_f(t)$ decreases and the fault estimate tends to the actual fault. Finally, as the P

matrix decreases, the quadratic state tracking error $e_y(t)$ decreases and tends to the null vector.

The second objective is to minimize the effect of the wind turbulence on the output tracking error $e_y(t)$, using a performance index $\gamma > 0$ as

$$\|e_y(t)_2\| \leq \gamma \|\omega(t)_2\|. \quad (11)$$

The minimization of the wind turbulence $\omega(t)$ effect on the output error could be performed using the following objective function:

$$J = \int_{t_f}^{\infty} \frac{1}{\gamma} [e_y^T(t)e_y(t) - \gamma\omega^T(t)\omega(t)] dt. \quad (12)$$

The considered fault is time invariant. This means that $\dot{F}(t) = 0$ and then $\dot{e}_f(t) = \dot{\hat{F}}(t)$. The derivative of $V_e(t)$ with respect to time is given by

$$\begin{aligned} \dot{V}_e(t) &= e_x^T(t)(P(A - LC) + (A - LC)^T P)e_x(t) \\ &\quad + 2e_x^T(t)PBe_f(t)u(t) + 2e_x^T(t)P(LD_2 - D_1)\omega(t) \\ &\quad + 2\text{tr}(e_f(t)\Xi^{-1}\dot{\hat{F}}(t)). \end{aligned} \quad (13)$$

Writing equation (8) as a matrix form gives the following:

$$\Xi^{-1}\dot{\hat{F}} = Re_y(t)u^T(t) = RCe_x(t)u^T(t). \quad (14)$$

To eliminate the term containing both $e_x^T(t)$ and $u(t)$, equation (15) could be adopted. Indeed, by adopting (15) the second and fourth term in the development of the derivative of the Lyapunov cancel each other.

$$B^T P = RC. \quad (15)$$

In order to solve the condition (15), its LMI version is used as in the following lemma.

Lemma 1 (see [40]). *The condition $B^T P = RC$ has an LMI equivalent writing:*

$$\text{minimize } \eta \text{ subject to } \begin{bmatrix} \eta I_r & B^T P - RC \\ * & \eta I_n \end{bmatrix} > 0, \quad (16)$$

where η is a dimensionless constant used to approximate $B^T P = RC$ as an LMI. The smaller η is, the accurate $B^T P = RC$ is in LMI writing.

In the sequel, the symbol ‘*’ means the transposition of the term in the same diagonal as ‘*.’ For example, in equation (16), ‘*’ is the transposition of the term $B^T P - RC$.

The derivative of the Lyapunov function becomes

$$\begin{aligned} \dot{V}_e(t) &= e_x^T(t)(P(A - LC) + (A - LC)^T P)e_x(t) \\ &\quad + 2e_x^T P(LD_2 - D_1)\omega(t). \end{aligned} \quad (17)$$

By replacing the Lyapunov function derivatives in the cost function expression, the following inequality is obtained:

$$\begin{aligned}
J &\leq \int_{t_f}^{\infty} \frac{1}{\gamma} e_y^T(t) e_y(t) - \gamma \omega(t)^T \omega(t) dt + \dot{V}_e(t) \\
&= \int_{t_f}^{\infty} \frac{1}{\gamma} [e_y^T(t) e_y(t) - \gamma \omega(t)^T \omega(t)] dt + e_x^T(t) (P(A-LC) \\
&\quad + (A-LC)^T P) e_x(t) + 2e_x^T P (LD_2 - D_1) \omega(t). \tag{18}
\end{aligned}$$

There is no direct action of the wind on the outputs; then, $D_2 = 0$. The objective function inequality:

$$\begin{aligned}
J &\leq \frac{1}{\gamma} e_y^T(t) e_y(t) - \gamma \omega^T(t) \omega(t) dt - 2e_x^T(t) P D_1 \omega(t) \\
&\quad + e_x^T(t) (P(A-LC) + (A-LC)^T P) e_x(t) \tag{19} \\
&= \int_{t_f}^{\infty} \zeta(t)^T \Upsilon \zeta(t) dt,
\end{aligned}$$

where

$$\begin{aligned}
\zeta(t) &= \begin{bmatrix} e_x(t) \\ \omega(t) \end{bmatrix}, \\
\Upsilon &= \begin{bmatrix} P(A-LC) + (A-LC)^T P + \frac{1}{\gamma} C^T C & -PD_1 \\ * & -\gamma I_d \end{bmatrix}. \tag{20}
\end{aligned}$$

Finally, to ensure the stability of the states' tracking error dynamics and the minimization of the wind turbulence on the output tracking error, the following inequality should hold:

$$\Upsilon < 0. \tag{21}$$

Using the Schur complement, the same previous inequality becomes

$$\begin{bmatrix} PA + A^T P - YC - C^T Y^T & -PD_1 & C^T \\ * & -\gamma I_d & 0 \\ * & * & -\gamma I_p \end{bmatrix} < 0, \tag{22}$$

where $Y = PL$, and then the error dynamic (9) satisfies the H_{∞} performance.

Remark 1. The adaptive algorithm (8) is proposed with the assumption that the input vector $u_i(t)$ satisfies the persistent excitation condition, which means that there exist positive scalars μ_1 , μ_2 , and t_0 such that for all t , the following inequality holds:

$$\mu_1 \leq \int_t^{t+t_0} u_i(s) u_i(s) ds \leq \mu_2. \tag{23}$$

The poles of the designed observer could be placed through the linear matrix inequality in the following lemma.

Lemma 2 (see [41]). *The eigenvalues of closed loop observed system dynamic matrix $(A-LC) \in \mathbb{R}^{n \times n}$ $A \in \mathbb{R}^{n \times n}$ belong to*

the circular region $D(\alpha, \tau)$ with center $\alpha + j0$ and radius τ if and only if there exists a symmetric positive definite matrix $P \in \mathbb{R}^{n \times n}$ $P \in \mathbb{R}^{n \times n}$ such that the following condition holds:

$$\begin{bmatrix} -P & P(A-LC - \alpha I_n) \\ * & -\tau^2 P \end{bmatrix} < 0. \tag{24}$$

The final integrated problem to be solved for the symmetric positive definite matrix P is as the following lemma.

Lemma 3. *Assume D_2 is null matrix and let a prescribed H_{∞} performance level γ be given. If there exists a symmetric positive definite matrix $P \in \mathbb{R}^{n \times n}$ and matrices $Y \in \mathbb{R}^{n \times p}$ and $R \in \mathbb{R}^{m \times p}$ such that the following condition holds:*

$$\begin{aligned}
&\begin{bmatrix} PA + A^T P - YC - C^T Y^T & -PD_1 & C^T \\ * & -\gamma I_d & 0 \\ * & * & -\gamma I_p \end{bmatrix} < 0 \\
&\begin{bmatrix} -P & P(A-LC - \alpha I_n) \\ * & -\tau^2 P \end{bmatrix} < 0, \tag{25} \\
&\text{minimize } \eta \text{ subject to } \begin{bmatrix} \eta I_r & B^T P - RC \\ * & \eta I_n \end{bmatrix} > 0,
\end{aligned}$$

where $Y = PL$, then the error dynamic (9) satisfies the H_{∞} performance and the poles of the robust state observer are within the region $D(\alpha, \tau)$.

3.2.4. The State Observer and Fault Simulation Results. The natural frequency of the blade is $f_n = (1/2\pi) \sqrt{(D_b/M_b)} = 1.511$ Hz. M_b is the blade mass and D_b is the stiffness of the blade. It gives a natural pulsation of $\omega_n = 9.49$ rad/s. All the frequencies above the natural frequency should be filtered by the observer. However, the observer should amplify the gain corresponding to ω_n for the estimation of the blades' deflections. The Bode diagrams of the designed observer in the system (7) are illustrated in Figures 5(a) and 5(b). The considered channel links the pitch actuator's input ($u_1(t) = \Delta\beta_1$ in Figure 4) with the blade deflection observed state ($y_3(t) = \Delta x_{\text{def}_1}$ in Figure 4).

Figures 5(a) and 5(b) illustrate the designed observer Bode diagram function of the performance level γ corresponding to the system in equation (7). The Bode diagrams are divided into two main regions. The first region is about the natural pulsation of the blades $\omega_n = 9.49$ rad/s. In this region, the magnitude presents maximal values, which means that the blades' deflections are perfectly observed. The second region is where the pulsations are less than the natural pulsation of the blades. As γ becomes smaller (closer to values near 0), the gain of the observer is reduced and the low frequencies of the wind speed are not amplified. The advantage is to prevent penetrating the amplified low frequencies contained in the rotor speed to the fault estimation algorithm through the residual $e_y(t)$. The effect of the amplified low frequencies is reducing the convergence speed of the estimation algorithm in equation (8). As a conclusion, the convergence speed of the fault estimation could be tuned

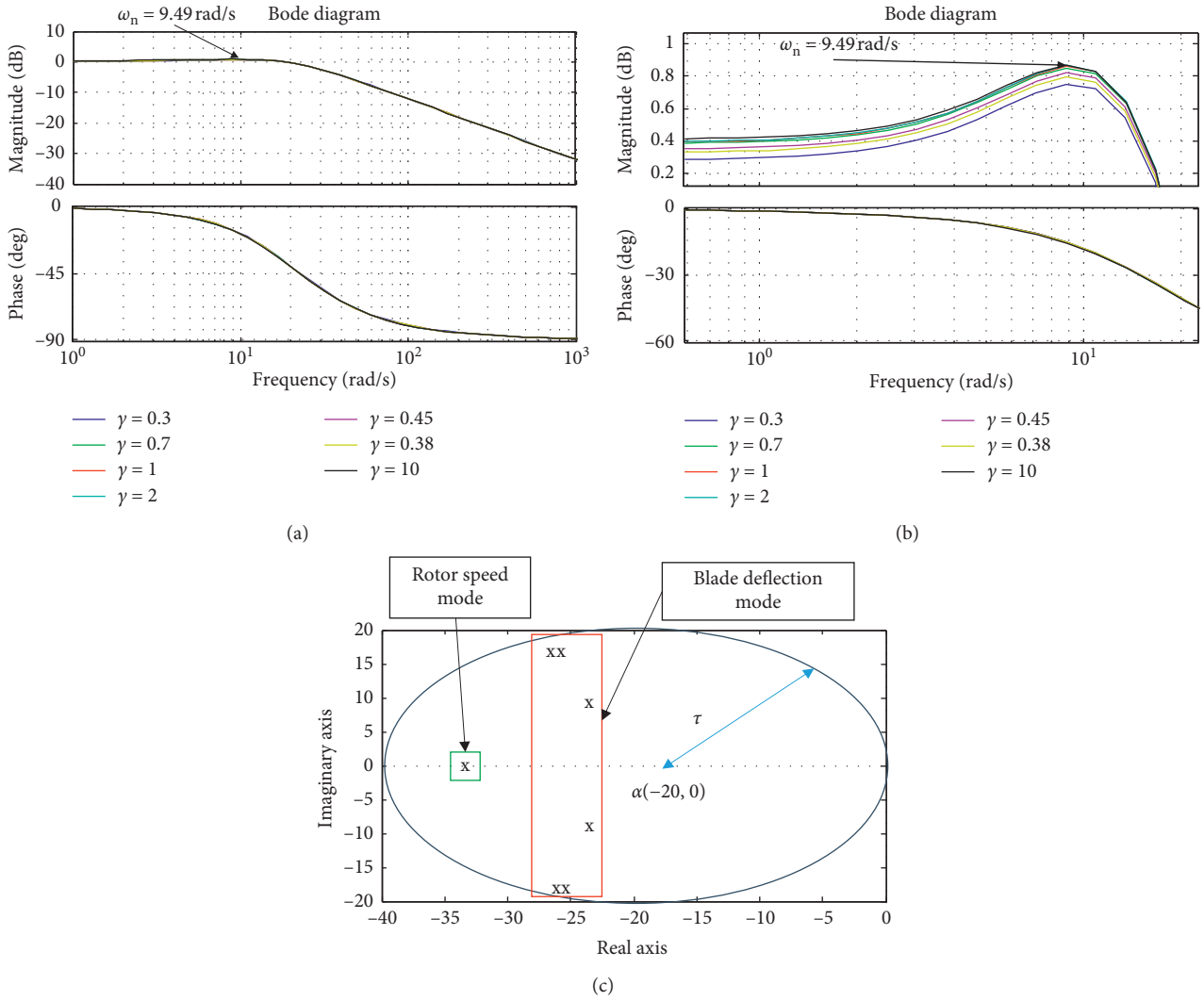


FIGURE 5: (a) Bode diagrams of the designed observer for different performance levels. (b) Zoom on the Bode diagrams of the designed observer for different performance levels. (c) The state observer pole placement for LMI region $(\alpha, \tau) = (-20, 20)$ in the complex axis.

by the performance index γ in addition to the tuning by the learning rate Ξ as illustrated in Figure 6(a), where the learning rate is fixed at 0.1 and γ takes the values 3, 1, and 0.3.

Figures 7 and 8 illustrate the tracking errors in the faulty and the fault tolerant case for the rotor speed and the blade 1 deflection velocity as samples. The observation quality is defined by the states' tracking error. It could be noticed that a sufficient level of observation is achieved for $\gamma = 0.3$ and $\xi_i = 0.1$ ($i = 1, 2, 3$).

For the rotor speed, in the fault tolerant case, the tracking error has a mean value of -3.96×10^{-4} rad/s and a standard deviation of 6.841×10^{-4} rad/s. For the faulty case, the mean value increases to -0.002 rad/s with a standard deviation of 9.8893×10^{-4} rad/s. For the blade deflection velocity, in the fault tolerant case, the tracking error has a mean of -0.058 m/s and a standard deviation of 0.4973 m/s. For the faulty case, the mean value increases to -0.0823 m/s and a standard deviation of 0.6595 m/s.

Figure 5(c) illustrates the result of pole placement of the state observer. The chosen region is of center 20 and radius 20.

The resulting closed loop eigenvalues are $(-33.4089; -24.7069 \pm 8.6379i; -26.6204 \pm 18.7259i; -26.6204 \pm 18.7259i)^T$.

In Figure 6(a), the effectiveness of actuator number 1 means $1 - f_1$. f_1 represents the decrease in the output of the actuator.

In Figures 7 and 8, the notations e_{y_1} correspond to the rotor speed component and e_{y_2} corresponds to the blade deflection velocity component in the tracking error vector e_y .

Figures 6(a) and 8 correspond to the first faulty scenario of Section 4 and Figure 7 corresponds to the third faulty scenario.

Figure 6(b) illustrates the fault estimation of the blade 1 actuator for several values of learning rate ξ_1 . As the learning rate increases, the estimate of the fault converges rapidly to the actual fault (magenta).

Remark: There is a coupling effect between the fault estimation and the state observer due to the fault tolerant control (FTC) correction. Such an effect can be neglected as long as the state observer is slower than the fault estimation. This can be achieved by choosing properly the learning rate.

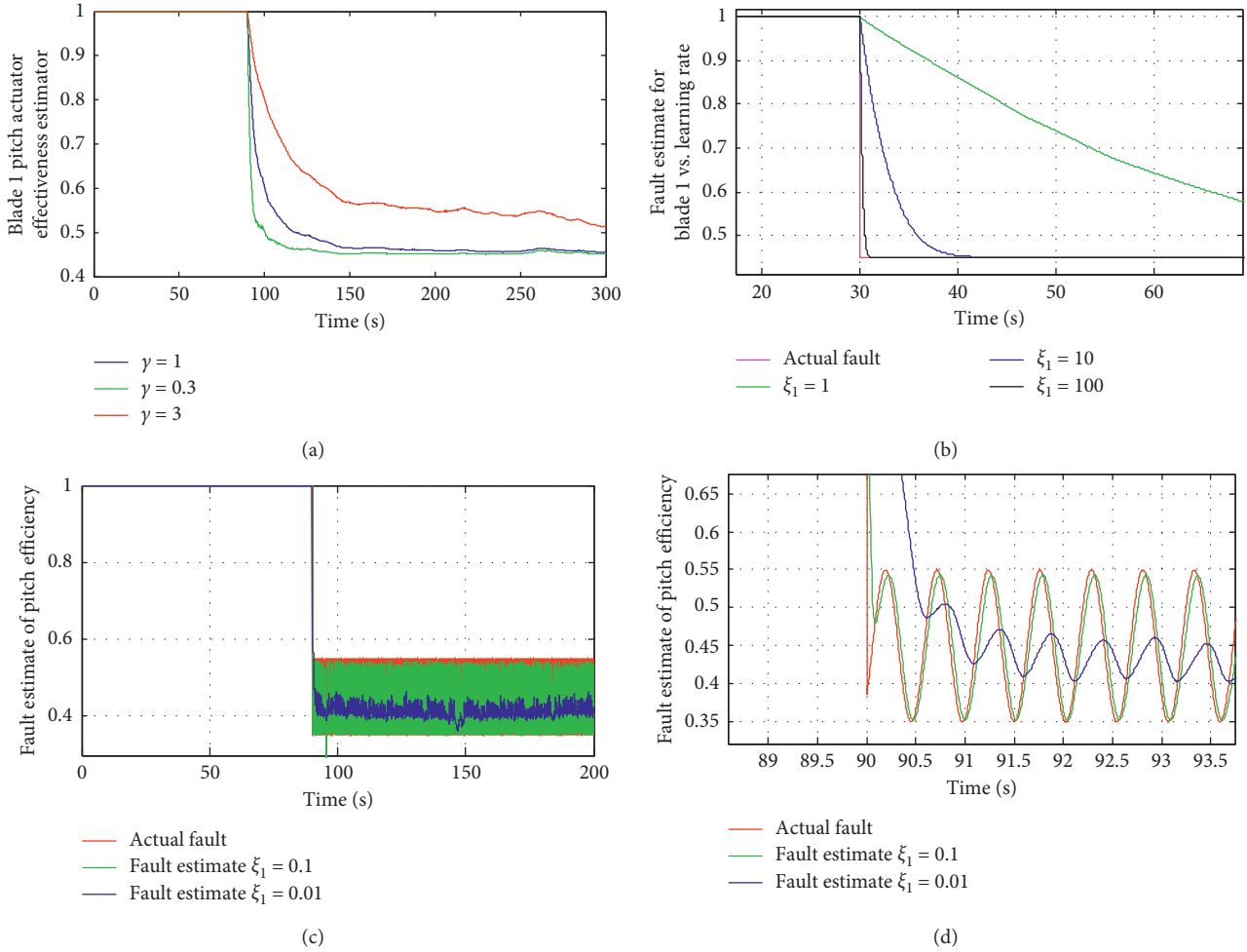


FIGURE 6: (a) Estimation of the pitch 1 actuator effectiveness for different performance levels. (b) Estimation of the pitch 1 actuator effectiveness for different learning rates. (c) Fault estimate with dynamics faster than system dynamics. (d) Zoom on fault estimate with dynamics faster than system dynamics.

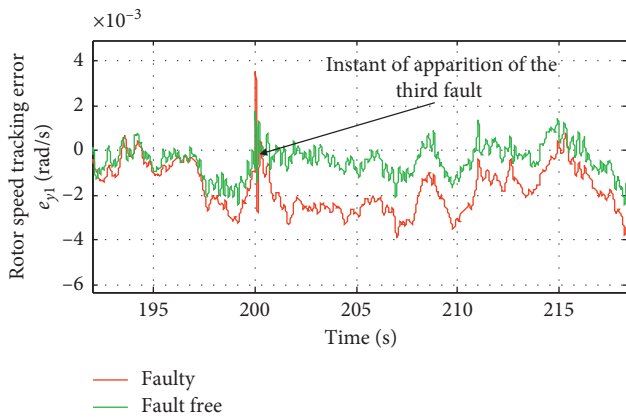


FIGURE 7: The rotor speed tracking error.

3.2.5. Fault Scenario with Dynamics Faster than the System Dynamics. In this section, a sinusoidal loss of efficiency is considered with frequency higher than 1.5 Hz of blades. Figures 6(c) and 6(d) show the result of fault estimation in that case. In the proposed strategy, by only tuning the learning

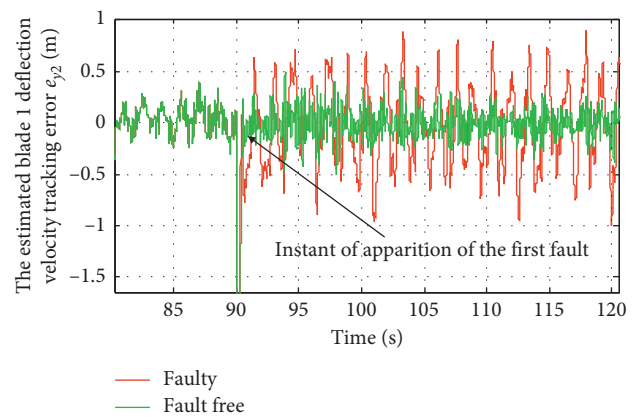


FIGURE 8: The estimated blade 1 deflection velocity tracking error.

rate to suitable higher values, the faults with dynamics faster than the system dynamics could be reconfigured without need to redesign the fault estimate algorithm as recommended in [33]. The amplitude of the fault is 0.1 and the frequency is 12 rad/s higher than 9.49 rad/s of the blades.

In Figure 7, the most important issue is the change of the mean rotor speed error. This information is the only one needed by the algorithm about the fault on the rotor speed. In Figure 8, the change is obvious on the amplitude of the blades at the natural frequency 1.5 Hz. This last information could be easily deduced by computing the value 1/period. Indeed, in Figure 8, the period of the signals is equal to 0.66 seconds giving the blades a natural frequency of 1.5 Hz.

In the faulty case, this increase in the mean and the standard deviation of the tracking error is integrated by the algorithm in equation (8) to deduce the fault amplitude.

3.2.6. *The Baseline Controller Design.* Initially, the eigenvalues of the dynamics matrix A of the system are equal to the vector λ_0 as follows:

$$\lambda_0 = [-0.1043 \quad -5.2649 \pm 8.1929i \quad -5.1247 \pm 7.9957i \quad -5.2649 \pm 8.1929i]^T. \quad (26)$$

The eigenvalue -0.1043 corresponds to the rotor speed dynamic. The last three eigenvalues represent the three blades' dynamics. These eigenvalues are double conjugates because the blades represent an oscillatory system. The objective of the control is to reduce the oscillations of the blades by choosing new eigenvalues bigger in absolute value than the initial eigenvalues and with negative real parts to ensure stability of the closed loop. The design control parameter K is computed so that the closed loop eigenvalues $\lambda_{(A+BK)}$ match the desired eigenvalues λ_d :

$$\lambda_d = \lambda_{(A+BK)}. \quad (27)$$

In the present paper, the desired eigenvalues of the nominal closed loop are

$$\lambda_d = [-0.2 \quad -24.7 \quad -24.7 \quad -26 \quad -26 \quad -27.3 \quad -27.3]^T. \quad (28)$$

The design steps of the nominal control are as follows:

- (i) The controllability matrix of the pair (A, B) is of full rank 7. So, the system is controllable.
- (ii) The control gain is defined as $K = \begin{pmatrix} K_{11} & \dots & K_{17} \\ K_{21} & \dots & K_{27} \\ K_{31} & \dots & K_{37} \end{pmatrix}$.

The gain K is then substituted in the desired characteristic polynomial equation:

$$\det(sI_n - A - BK) = \prod_{j=1}^7 (s - \lambda_{d,j}), \quad (29)$$

where I_n is the identity matrix and s is the Laplace operator. The integer n is the number of states; it is equal to 7 in this paper. $\lambda_{d,j}$ is the j th element of the desired closed loop eigenvalue vector λ_d .

- (i) Equation (29) is solved by equating the identical powers on both sides. This allows extracting the value of the control matrix K .

Finally, the obtained control gain K is applied to the system according to the scheme of Figure 3. The results of the regulation are depicted in Figures 9–12. Figures 9 and

10 illustrate that the speed regulation objective is achieved. In fact, as the rotor speed increases (decreases), the blade pitch angle increases (decreases) in order to prevent wind from driving the wind turbine (in order to provide more wind to drive the wind turbine). The expected achieved performance is of 90% of attenuation. In the open loop, a difference from the operating point of 10 rpm at the instant 150 s is denoted. After applying the control strategy, the difference becomes 1 rpm, which corresponds to 90% of attenuation.

Figures 11 and 12 show that when the deflection increases (the red signal), the pitch action (green) increases to attenuate the deflection as presented in the same figure (blue signal). It can be concluded that the blade pitch action is composed of two signals: a low frequency control action responsible for rotor speed regulation and a high frequency control action responsible for mitigating the blade deflections.

Figures 9–12 correspond to the nominal case (healthy case). In this case, no fault is occurring.

4. Wind Turbine Optimal Adaptive Fault Tolerant Control in the Faulty Operation

The considered fault is the loss of efficiency in the three pitch actuators. The scenario created in the FAST software is a drop of 55% in the effectiveness of the pitch actuator 1 at the instant 90 s, 40% in the effectiveness of the pitch actuator 2 at the instant 150 s, and 60% in the effectiveness of the pitch actuator 3 at the instant 200 s.

4.1. *The Fault Mechanism.* The considered pitch actuator is hydraulic based. In Figure 13(a), the prefix p denotes the piston side, the prefix r denotes the rod side, and the prefix v denotes the proportional valve side. A_p and A_r correspond, respectively, to the surfaces of the piston side and the rod side. The pump pumps oil from the accumulator with a pressure p_s which passes across the proportional valve with a mass flow Q_v . Finally, the air arrives to the piston side with the pressure p_p and thrusts the rod linked to the blades. The trust force is F_{cyl} and is given by

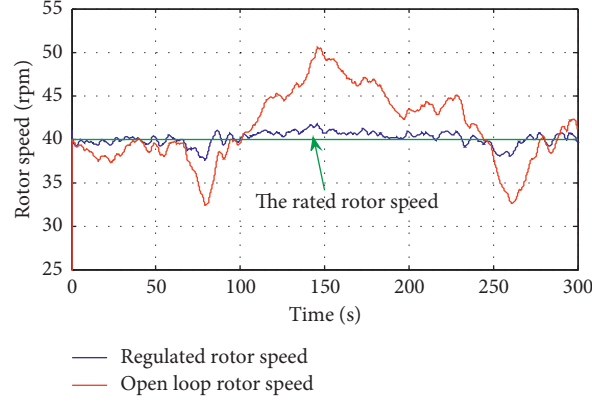


FIGURE 9: Rotor speed (rpm).

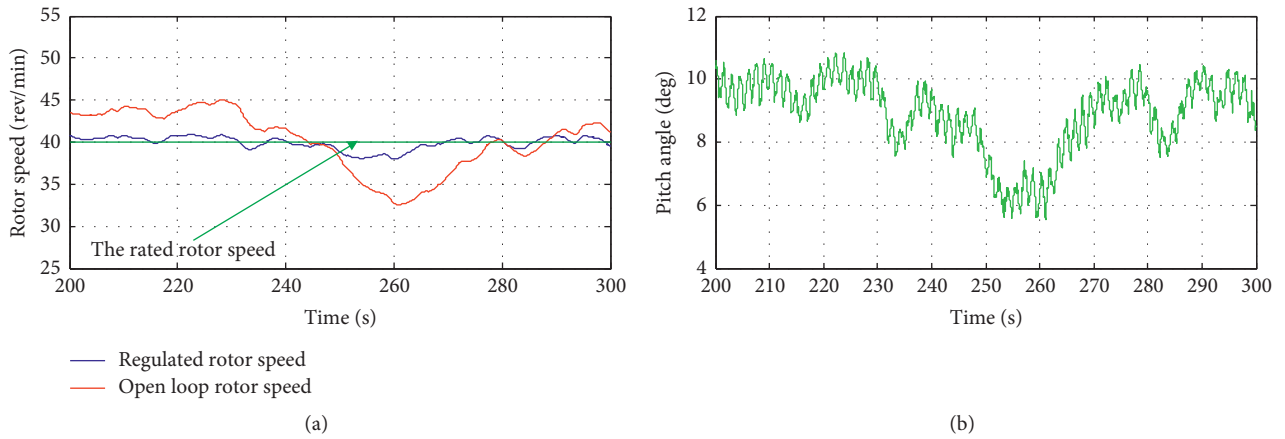


FIGURE 10: Zoom on the rotor speed (rpm) and the blade pitch angles (degrees) in the region [200, 300] sec.

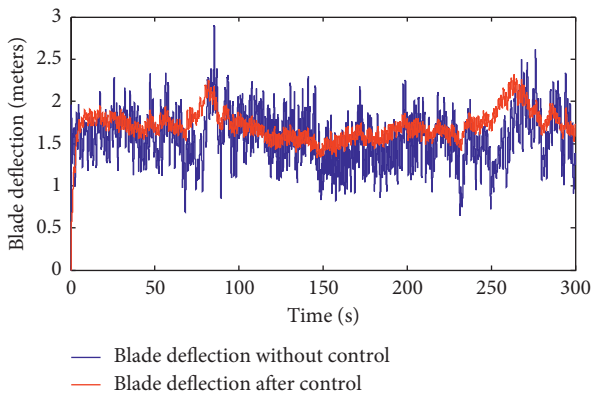


FIGURE 11: Blade deflection (meters).

$$F_{cyl} = p_p A_p - p_r A_r - F_{fric}, \quad (30)$$

where F_{fric} is the friction force of the piston on the cylinder and is linearly dependent to the displacement velocity of the piston.

For the same rod pressure p_r and friction F_{fric} , the considered pitch loss of efficiency fault occurs when the pressure p_p drops due to the ageing of the pump station. This ageing appears for example because of excessive Joule effect (heat) losses in the wirings of the pump motor. Under these

conditions, the thrust force F_{cyl} of the rod on the blade is no longer sufficient to actuate the blade. The thrust force F_{cyl} is represented by the action matrix B in equation (5). The fault is modeled as a loss of efficiency percentage (equal or less than 100%) multiplied by the action matrix B . As a result, the pitch efforts are no longer sufficient for damping the oscillations of the blades. The aim of the algorithm in equation (8) is to track that multiplicative percentage with a sufficient precision and response time.

After that, equation (31) comes to amplify the supplied power (control) to the pump to compensate the lost energy due to Joule effect. The amplification is performed mathematically by dividing the old control signal by the estimated faulty efficiency.

4.2. The Fault Tolerant Controller. The fault tolerant control signal is obtained by dividing the initial baseline control signal by the estimated fault:

$$u_f(t) = \hat{F}(t)^{-1}u(t). \quad (31)$$

To avoid the division by zero in the case of zero efficiency, $\hat{F}(t)$ should be replaced by a small number (for example, 10^{-4}). The scheme of the global fault tolerant control is given by Figure 13(b).

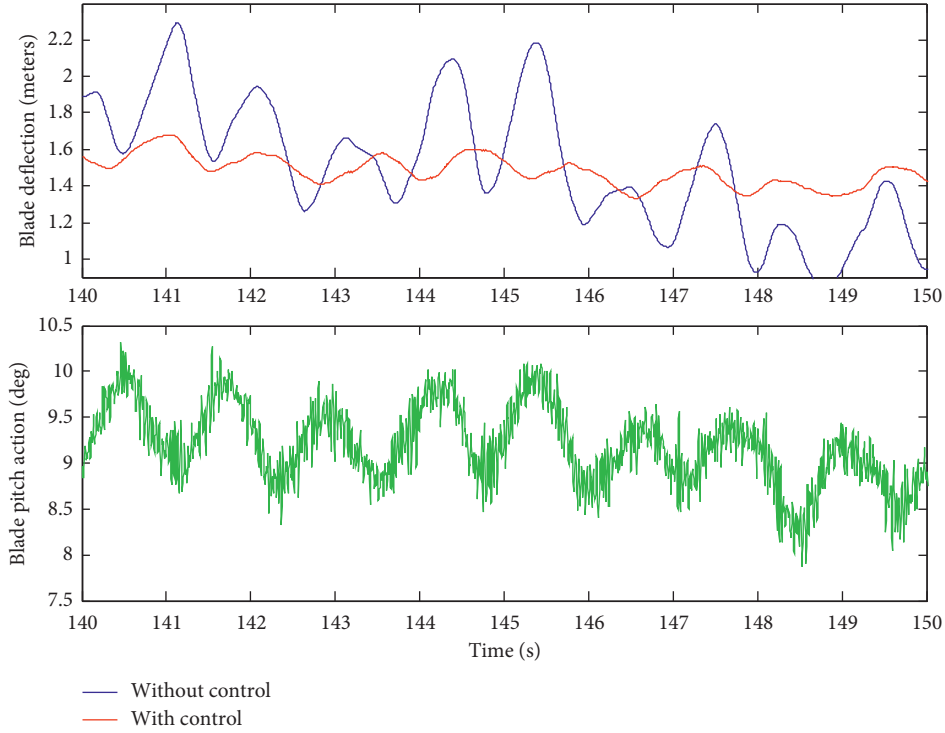


FIGURE 12: Blade 1 deflection (meters) and blade 1 pitch action.

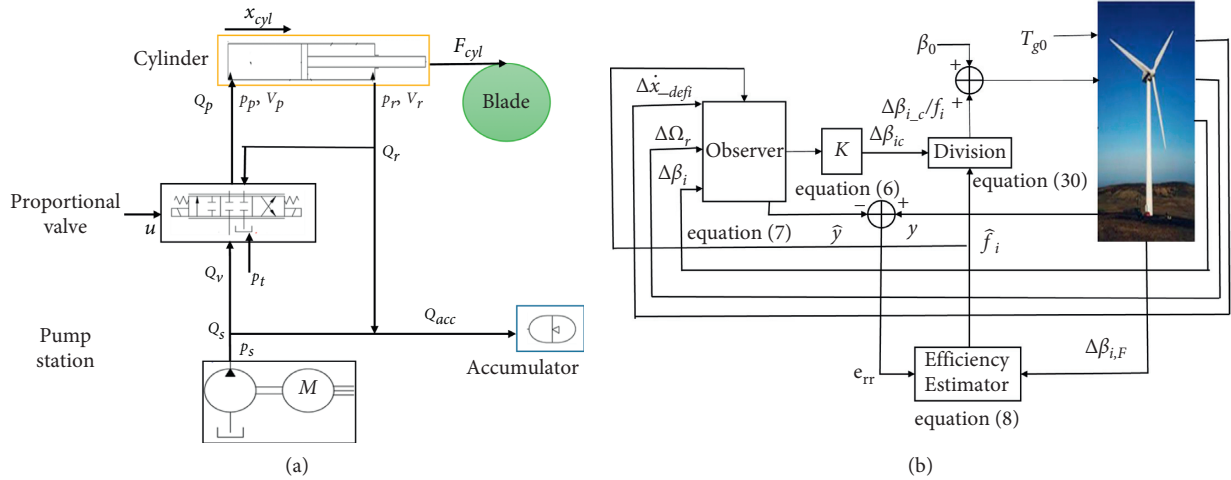


FIGURE 13: (a) The pitch actuator model. (b) The wind turbine control objective scheme.

Before being fed to the pitch actuator, the effectiveness is estimated by the adaptive algorithm. Then, the control signal is divided by the estimated efficiency to compensate the drop in the actual efficiency of the pitch actuator.

Remark: The different LMIs of the algorithm are resolved through the YALMIP tool [42].

$\Delta\beta_i$ is the pitch angle input variations from the operating point for the i^{th} actuator ($i = 1, 2, 3$), $\Delta\dot{x}_{defi}$ are the deflection velocity variations from the operating point for the i^{th} blade, and $\Delta\Omega_r$ is the rotor speed variations from the operating point.

$\Delta\beta_{i,F}$ is the faulty pitch angle input variations from the operating point for each actuator, \hat{f}_i is the estimated

efficiency for the i^{th} actuator, and \hat{x} is the estimated state variations of the wind turbine from the operating point.

4.3. *The Three Pitch Actuators Loss of Effectiveness Faulty Scenario.* Let us consider the blade without loss of generality. Figure 14 illustrates the blade 1 deflection.

In the faulty situation, the deflections increase from 1.5 meters to 4 meters because the pitch actuator could not answer completely to the corrective action of the baseline regulator against the wind. According to [43], the maximal allowable industrial deflection for the considered wind turbine is of 3 m. In the faulty case, this limit is exceeded which increases the risk of damage of the blade.

After applying the fault tolerant control strategy, the blade deflections are perfectly reconfigured.

Let $F(s)$ be the effect of the pitch angle i on the blade i deflection. The effect of the strategy on the blades deflections is interpreted as an additional zero at the origin in the transfer function $F(s)$. In Figure 15, it can be noticed that when s tends to zero, $sF(s)$ tends to zero. The reconfiguration time for each fault estimation of index i is dictated by the product $\xi_i \times r_i$.

The rapidity of the algorithm depends on the learning rate Ξ and the matrix R . As studied earlier in the paper, in addition to the learning rate Ξ , even the performance level γ could influence the response time of the fault estimation through the low frequencies of the wind. In fact, for a given γ , a matrix P depending on γ could be found through the LMI in equation (22). Then, by using the LMI in equation (15), the matrix R is obtained and used to compute the estimation $\hat{F}(t)$ using equation (8). As a conclusion, the parameter γ influences the response time of the algorithm through the matrix R .

The derivative form of the block between $\Delta\beta_{i,c}$ and $F(s)$ in Figure 15 has a risk of turbulence amplification. For this reason, a study to choose the learning rate Ξ and the performance level γ function of the correlation between the tracking error $e_{y-2}(t)$ (blade 1 deflection velocity as an example) and the wind turbulence is proposed in the next section.

4.4. The Choice of γ and Γ Based on the Correlation with Turbulence and the Estimation Response Time Criteria. In this section, empirical boundaries are proposed for choosing the performance level γ and the learning rate Ξ based on two criteria. Namely, the correlation between the wind speed ω and the residual e_y is considered. This variable is crucial to investigate because it could be amplified if decided to use the performance level γ to tune the estimation response time. The second criterion is the rapidity of convergence which is important to ensure because only short times of convergence are recommended for a fast recovery of the fault.

4.4.1. The Correlation between the Wind Turbulence and the Residual e_y . The expression of the correlation of the two signals is given by

$$\text{Corr} = \frac{E[e_y \times \omega] - E[e_y]E[\omega]}{SD_{e_y} \times SD_{\omega}}, \quad (32)$$

where $E[x]$ denotes the expectation of the signal x and SD_x denotes the standard deviation of the signal x . The correlation Corr belongs to the interval $[-1, 1]$. It obeys to the weak and strong correlation. If the coefficient $\text{Corr} \in [-0.5, 0] \cup [0, 0.5]$, it is called a weak correlation. If the coefficient $\text{Corr} \in [-1, -0.5] \cup [0.5, 1]$, it is called a strong correlation.

4.4.2. The Estimation Response Time of the Algorithm. The response time of the fault estimation algorithm in equation (8) for each actuator of index i is given by

$$v_i = \xi_i \times r_i. \quad (33)$$

Many simulations have been made on the FAST software in order to derive empirical data on v and Corr helping to choose the appropriate values of the two parameters γ and Ξ . Then, an interpolation between data points has been performed to define mappings linking the tracking error and the wind disturbance.

Figures 16 and 17 show the evolution of the correlation and fault estimation response time with the performance level and the learning rate for the considered wind turbine in Table 1. From Figure 18, one can conclude that for γ less than 1, this parameter influences the correlation more than the response time of the algorithm. However, when γ exceeds 2.5, the correlation becomes more influenced also by Ξ as γ increases. For γ less than 2.25, the response time of the algorithm is influenced by both Ξ and γ . But, as γ increases, only Ξ influences the response time of the algorithm. In order to guarantee a fast reconfiguration of the system performance, one should choose a small response time of the algorithm by choosing a suitable pair (γ, Ξ) . However, one should guaranty that neither the resulting performance level nor the learning rate amplifies the correlation between the tracking error e_y and the wind turbulence ω .

For the last reason, the two parameters should obey to the following empirical law. For example, if γ is in $[0.9, 1.4]$ interval, Ξ should not be in $[2.21, 9.84]$ (zone 1 in Figure 18) to avoid high correlation, and with the same idea, if γ is chosen in $[1.4, 2.02]$, Ξ should not be in the interval $[8.317, 9.84]$ (zone 2 in Figure 18).

An example of a choice of the pair (γ, Ξ) leading to a fast and less correlated response time is indicated in Figure 19 by $(\gamma, \Xi) = (2.25, 1.25)$.

4.4.3. Discussion with respect to Some Existing Methods. The proposed strategy is not complicated and uses an integral structure with one Lyapunov function to prove stability and convergence of both state estimation error and fault estimation error. The proposed approach uses a reduced number of measurements. Indeed, only the rotor speed and the individual blades' deflection velocity are needed. This reduces the information needs with respect to other techniques such as the one in [44] (requiring also the generator speed measurement). It does not either require the information about the presumed fault size as in [45].

The residual-based techniques in [45–47] deal only with fault detection tasks. Contrariwise, the proposed approach deals with both fault estimation and fault isolation suitable for active fault tolerant control strategies. Indeed, the individual deflection velocity measurement of each blade allows a natural isolation of the fault blade without the need of additional isolation methods. This method avoids the intrinsic delays of online least-squares methods, which could have a negative impact on the fault estimation response time.

The proposed strategy is equipped with a tuning method to avoid amplification of wind turbulence in the direction of the high learning rates. This issue is not sufficiently discussed in other works related to wind turbines.

Contrariwise to other strategies, the proposed method could deal with faults having dynamics faster than the system dynamics only by tuning the learning rate suitably.

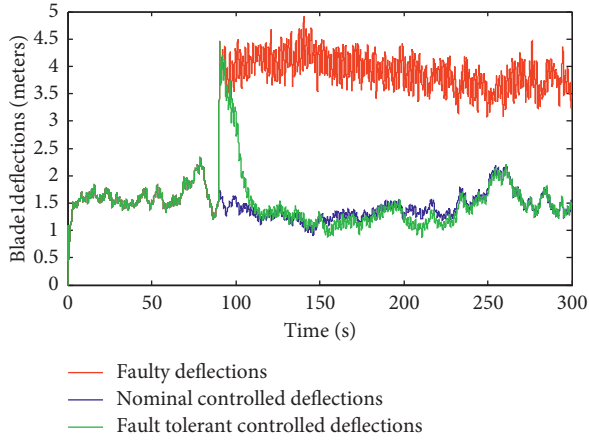


FIGURE 14: The blade deflections in the faulty deflections, nominal deflections, and fault tolerant deflections.

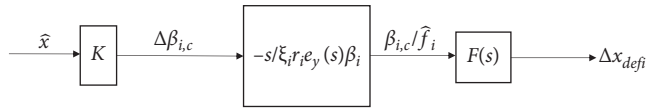


FIGURE 15: The effect of the reconfiguration on the blades.

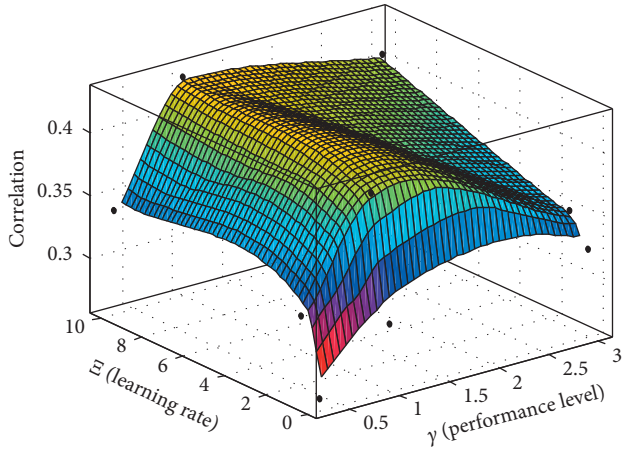


FIGURE 16: The correlation between measuring error and the turbulence with respect to the learning rate and the performance level.

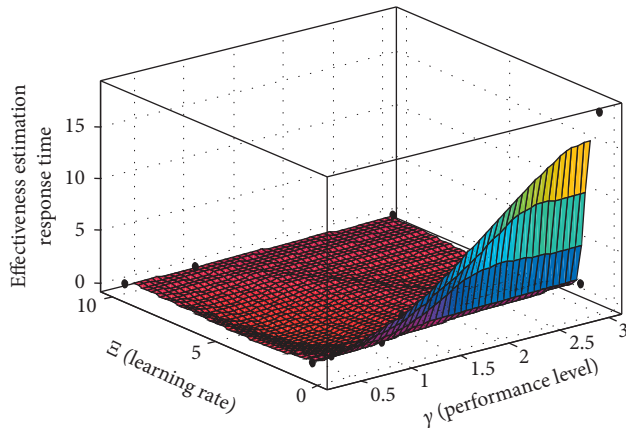


FIGURE 17: The effectiveness estimation response time with respect to the learning rate and the performance level.

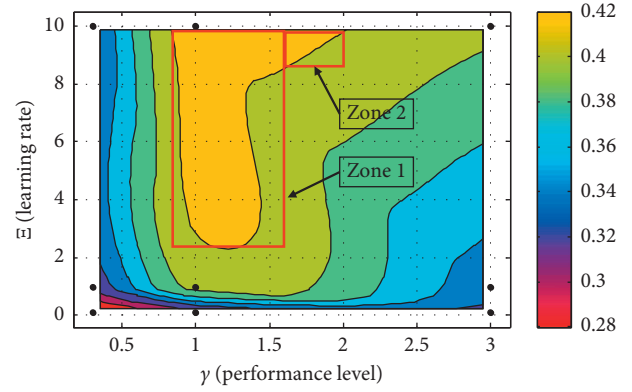


FIGURE 18: Maximal correlation zones vs. learning rate and performance level.

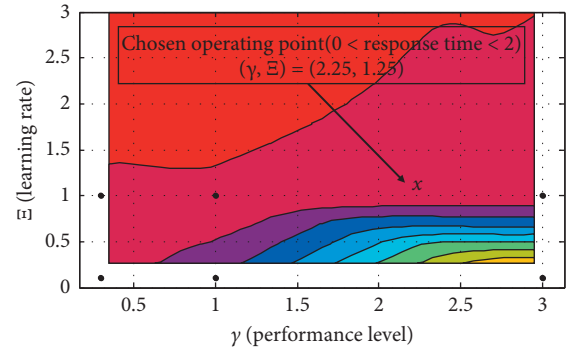


FIGURE 19: The effectiveness estimation algorithm response time vs. learning rate and performance level.

4.4.4. *Comparison of the Proposed Strategy with the Virtual Actuator with State Residual Integrator.* A new scenario of pitch fault on blade 1 is considered for the comparison between the proposed strategy and a virtual actuator-based strategy (details of this method are not the objective of the paper, [48]). In this section, the considered fault happens at the instant 15 seconds. This fault represents pitch actuator loss of efficiency of 55%.

Figure 20 illustrates the structure of the strategy used for comparison. The principle of this strategy is to use a model reference and to compute the difference between the estimated faulty states and the model reference states. This difference is integrated and used as new control law. Equation (8) was used to derive the faulty matrix B_f . The difference with respect to the proposed strategy is in the integration of the state residual x_Δ instead of the division in equation (30) and the use of reference model.

Figure 21 illustrates a comparison between the proposed strategy and the virtual actuator with integrating the state residual in terms of blade fault reconfiguration. In some regions where the wind speed makes high amplitudes of high frequencies, which means the effort needed for integration is higher, the performance of the virtual actuator becomes poor in the interval [16 s; 26 s]. This could be explained by the existence of two integrators, the first presented in equation (8) used to estimate the fault needed by B_f and the second to integrate the state residual. In conclusion, the

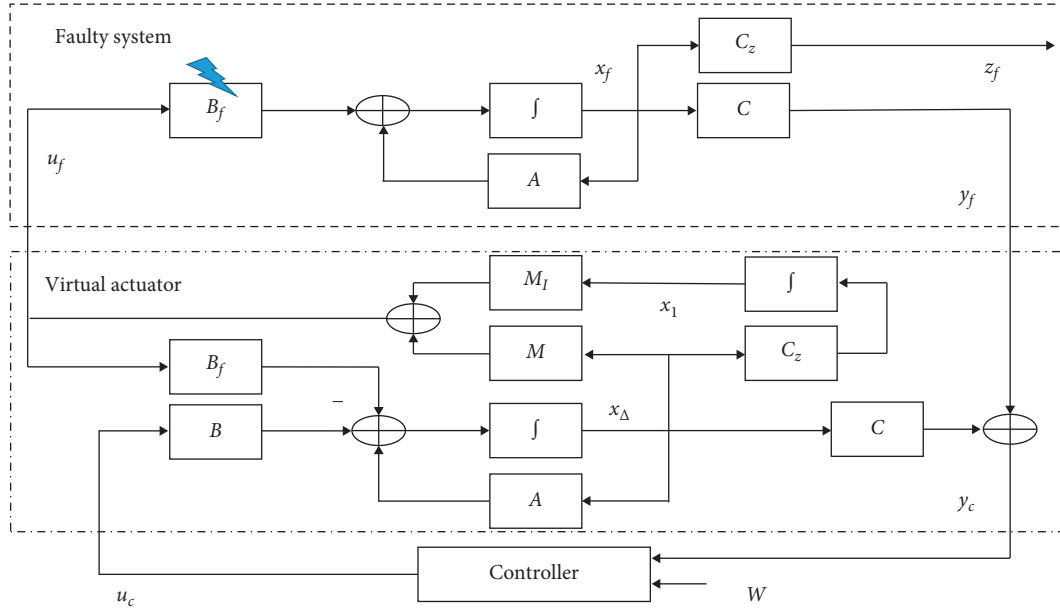


FIGURE 20: The simplified virtual actuator strategy with state residual x_Δ integration.

virtual actuator with integration of state residual is not always suitable for integrator-based fault estimators.

4.4.5. Digital Implementation of the Strategy. The equations to be implemented are the baseline control law in equation (6), the observer in equation (7), and the fault estimation in equation (8). In order to digitalize the continuous equations, the first-order approximation in equation (34) is used. If \dot{z} is the derivative, it could be approximated by

$$\dot{z}(t) = \frac{z(t+T) - z(t)}{T}, \quad (34)$$

where T is the sampling step. Hence, the strategy could be digitalized for each iteration of index k as follows.

The digitalized baseline controller (from equation (6)) is given by

$$u_k = K\hat{x}_k. \quad (35)$$

The digitalized robust observer (from equation (7)) is given by

$$x_{k+1} = A_d\hat{x}_k + B_dF_k u_k + L_d(\hat{y}_k - y_k), \quad (36)$$

where A_d , B_d , and L_d are, respectively, the state matrix, the input matrix, and the observer matrix. The expressions of the previous matrix are given by $A_d = I_n + TA$; $B_d = TB$; and $L_d = TL$.

The digitalized fault estimation (equation (8)) for each actuator of index i is given by

$$f_{k+1,i} = f_{k,i} + T\xi_{k,i}r_{k,i}e_{y,k,i}u_{k,i}. \quad (37)$$

5. Conclusion

In this paper, the partial failure of pitch actuators in wind turbine was considered. The LMI-based fault tolerant

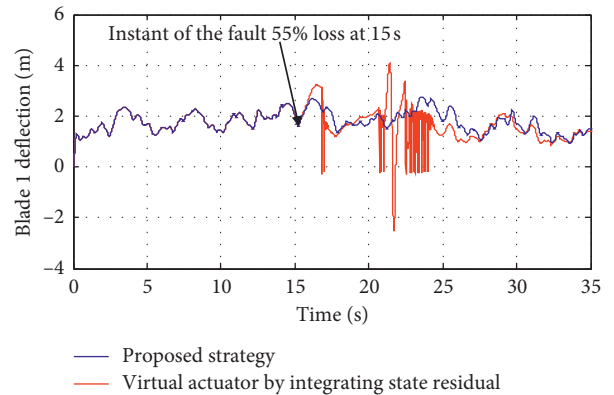


FIGURE 21: The comparison of the faulty blade 1 deflection between the proposed FTC and the residual integration FTC.

control was applied to the considered fault. The method presents the advantages that it estimates at the same time the states and the fault. The method convergence is proved through Lyapunov theory. Two key design parameters were identified in the integrated design, namely, the performance level and the learning rate. It has been shown that the performance level γ of the observer and the learning rate Ξ impact indirectly the loads on the turbine. The parameters have an effect on the availability time of the fault estimation. In some zones of the pair (γ, Ξ) , it has been found that as the learning rate increases, the fault becomes quickly available and the fault tolerant strategy accommodates rapidly the prefault load reduction. In other zones, the robustness γ enhances the loads reduction. Moreover, the performance level γ provides another degree of freedom to the adaptive algorithm in addition to the learning rate Ξ . An empirical design method was proposed to impose both a given correlation of the measuring error to the wind turbulence and a given response time of the effectiveness estimation algorithm. The proposed method helps choosing the desired short

response time of the effectiveness estimation algorithm with sufficiently good correlation level to the wind turbulence.

Appendix

$$\begin{aligned}
 A &= \begin{bmatrix} 0.0328 & 0.1046 & 0.0087 & 0.1046 & 0.0087 & 0.1046 & 0.0087 \\ 0 & 0 & 1 & 0 & 0 & 0 & 0 \\ -41.4716 & -91.8644 & -10.3888 & -1.6712 & -0.1391 & -1.6712 & -0.1391 \\ 0 & 0 & 0 & 0 & 1 & 0 & 0 \\ -41.4712 & -1.6712 & -0.1391 & -91.8644 & -10.3888 & -1.6712 & -0.1391 \\ 0 & 0 & 0 & 0 & 0 & 0 & 1 \\ -41.4721 & -1.6712 & -0.1391 & -1.6712 & -0.1391 & -91.8644 & -10.3888 \end{bmatrix}, \\
 B &= \begin{pmatrix} 0.0015 & 0.0015 & 0.0015 \\ 0 & 0 & 0 \\ -2.0553 & -0.0234 & -0.0234 \\ 0 & 0 & 0 \\ -0.0234 & -2.0553 & -0.0234 \\ 0 & 0 & 0 \\ -0.0234 & -0.0234 & -2.0553 \end{pmatrix}; \\
 C &= \begin{pmatrix} 1 & 0 & 0 & 0 & 0 & 0 & 0 \\ 0 & 0 & 1 & 0 & 0 & 0 & 0 \\ 0 & 0 & 0 & 0 & 1 & 0 & 0 \\ 0 & 0 & 0 & 0 & 0 & 0 & 1 \end{pmatrix}, \\
 D_d &= \begin{pmatrix} 0.0317 & 0.0317 & 0.0317 \\ 0 & 0 & 0 \\ 1.5187 & -0.5062 & -0.5062 \\ 0 & 0 & 0 \\ -0.5062 & 1.5187 & -0.5062 \\ 0 & 0 & 0 \\ -0.5062 & -0.5062 & 1.5187 \end{pmatrix}; \quad \gamma = 0.3; \quad \eta = 1, \\
 E &= \begin{pmatrix} 0.01 & 0 & 0 \\ 0 & 0.01 & 0 \\ 0 & 0 & 0.01 \end{pmatrix}, \\
 P &= \begin{pmatrix} 0.0514 & -0.0001 & 0 & -0.0001 & 0 & -0.0001 & 0 \\ -0.0001 & 1.4086 & 0 & 0.1383 & 0 & -0.1618 & 0 \\ 0 & 0 & 0 & 0 & 0 & 0 & 0 \\ -0.0001 & 0.1383 & 0 & 1.2979 & 0 & 0.0837 & 0 \\ 0 & 0 & 0 & 0 & 0 & 0 & 0 \\ -0.0001 & -0.1618 & 0 & 0.0837 & 0 & 0.5037 & 0 \\ 0 & 0 & 0 & 0 & 0 & 0 & 0 \end{pmatrix}, \\
 L &= \begin{pmatrix} 34.3109 & 0.0237 & 0.0237 & 0.0237 \\ 0.0021 & 1 & 0 & 0 \\ -429.7260 & 19.0461 & -0.4400 & -0.4399 \\ 0.0012 & 0 & 0.9999 & 0 \\ -429.7430 & -0.4400 & 19.0465 & -0.4400 \\ 0.0050 & 0 & 0 & 0.9999 \\ -429.7193 & -0.4399 & -0.4400 & 19.0463 \end{pmatrix}, \\
 R &= \begin{pmatrix} 0.2114 & -157.5057 & 0.1955 & 0.1951 \\ 0.1633 & 0.1955 & -157.5057 & 0.1953 \\ 0.2212 & 0.1951 & 0.1954 & -157.5067 \end{pmatrix}, \\
 K &= 10^3 \begin{pmatrix} -2.1347 & 4.3367 & 0.2346 & -2.3593 & -0.1786 & -2.5160 & -0.1820 \\ -0.0108 & 0.0142 & 0.0009 & 2.1925 & 0.1172 & -2.2166 & -0.1185 \\ 0.0077 & 0.0283 & 0.0014 & -2.1936 & -0.1173 & 2.2145 & 0.1184 \end{pmatrix}.
 \end{aligned} \tag{A.1}$$

Data Availability

No data were used to support this study.

Conflicts of Interest

The authors declare that they have no conflicts of interest.

References

- [1] M. Ors, "Maximum power point tracking for small scale wind turbine with self-excited induction generator," *Control Engineering and Applied Informatics*, vol. 11, no. 2, pp. 30–34, 2009.
- [2] N. A. Cutululis and E. Ceanga, "Robust control of an autonomous wind power system," *Control Engineering and Applied Informatics*, vol. 6, no. 4, pp. 3–12, 2004.
- [3] H. P. Wang, A. Pintea, N. Christov, P. Borne, and D. Popescu, "Modelling and recursive power control of horizontal variable speed wind turbines," *Control Engineering and Applied Informatics*, vol. 14, no. 4, pp. 33–41, 2012.
- [4] E. A. Bossanyi, A. Kumar, and O. Hugues-Salas, "Wind turbine control applications of turbine-mounted LIDAR," *Journal of Physics: Conference Series*, vol. 555, 2012.
- [5] C. Vlad, I. Munteanu, A. I. Bratcu, and E. Ceangă, "Anticipative control of low-power wind energy conversion systems for optimal power regime," *Control Engineering and Applied Informatics*, vol. 11, no. 4, pp. 26–35, 2009.
- [6] T. K. Barlas, W. van Wingerden, A. W. Hulskamp, G. A. M. van Kuik, and H. E. N. Bersee, "Smart dynamic rotor control using active flaps on a small-scale wind turbine: aeroelastic modeling and comparison with wind tunnel measurements," *Wind Energy*, vol. 16, no. 8, 2012.
- [7] E. A. Bossanyi, "Individual blade pitch control for load reduction," *Wind Energy*, vol. 6, no. 2, pp. 119–128, 2003.
- [8] I. Houtzager, J. W. van Wingerden, and M. Verhaegen, "Wind turbine load reduction by rejecting the periodic load disturbances," *Wind Energy*, vol. 16, no. 2, pp. 235–256, 2013.
- [9] P. J. Darrow, *Wind Turbine Control Design to Reduce Capital Costs*, Colorado School of Mines Golden, Golden, CO, USA, 2009.
- [10] J. Ribrant and L. M. Bertling, "Survey of failures in wind power systems with focus on Swedish wind power plants during 1997-2005," *IEEE Transactions on Energy Conversion*, vol. 22, no. 1, pp. 167–173, 2007.
- [11] T. Jain, J. J. Yame, and D. Sauter, "A novel approach to real-time fault accommodation in NREL's 5-MW wind turbine systems," *IEEE Transactions on Sustainable Energy*, vol. 4, no. 4, pp. 1082–1090, 2013.
- [12] R.-E. Precup, P. Angelov, B. S. J. Costa, and M. Sayed-Mouchaweh, "An overview on fault diagnosis and nature-inspired optimal control of industrial process applications," *Computers in Industry*, vol. 74, pp. 75–94, 2015.
- [13] J. Sá da Costa, B. M. S. Santos, and M. J. G. C. Mendes, "A design approach to FD/FTC of complex networked control systems," *Control Engineering and Applied Informatics*, vol. 3, no. 4, pp. 3–11, 2015.
- [14] A. A. Ozdemir, P. Seiler, and G. J. Balas, "Wind turbine fault detection using counter-based residual thresholding," *IFAC Proceedings Volumes*, vol. 44, no. 1, pp. 8289–8294, 2011.
- [15] J. M. Jonkman and M. L. Buhl, "Fast user's guide," 2005, <https://nwtc.nrel.gov/fast7>.
- [16] J. M. Jonkman and M. L. Buhl, "TurbSim user's guide," 2007, <https://nwtc.nrel.gov/turbsim>.
- [17] L. Jong-Won, K. Joong-Kwan, H. Jae-Hung, and S. Hyung-Kee, "Active load control for wind turbine blades using trailing edge flap," *Wind and Structures*, vol. 16, no. 3, pp. 263–278, 2013.
- [18] E. E. Bachynski, M. Etemaddar, M. I. Kvittem, C. Luan, and T. Moan, "Dynamic analysis of floating wind turbines during pitch actuator fault, grid loss, and shutdown," *Energy Procedia*, vol. 35, pp. 210–222, 2013.
- [19] V. Rezaei and F. R. Salmasi, "Robust adaptive fault tolerant pitch control of wind turbines," *Wind Engineering*, vol. 38, no. 6, pp. 601–612, 2014.
- [20] P. F. Odgaard, J. Stoustrup, M. Kinnaert, and M. Kinnaert, "Fault-tolerant control of wind turbines: a benchmark model," *IEEE Transactions on Control Systems Technology*, vol. 21, no. 4, pp. 1168–1182, 2013.
- [21] D. Belkhiat, D. Jabri, and I. Kilani, "Fault tolerant control for a class of switched linear systems using generalized switched observer scheme," *Control Engineering and Applied Informatics*, vol. 17, no. 4, pp. 90–101, 2015.
- [22] R. Ebrahimi Bavili, M. J. Khosrowjerdi, and R. Vatankhah, "Active fault tolerant controller design using model predictive control," *Control Engineering and Applied Informatics*, vol. 17, no. 3, pp. 68–76, 2015.
- [23] V. Rezaei and K. E. Johnson, "Robust fault tolerant pitch control of wind turbines," in *Proceedings of the 52nd IEEE Conference on Decision and Control*, Florence, Italy, December 2013.
- [24] J. Kusnick, D. E. Adams, and D. T. Griffith, "Wind turbine rotor imbalance detection using nacelle and blade measurements," *Wind Energy*, vol. 18, no. 2, pp. 267–276, 2015.
- [25] G. Ramtharan, N. Jenkins, O. Anaya-Lara, and E. Bossanyi, "Influence of rotor structural dynamics representations on the electrical transient performance of FSIG and DFIG wind turbines," *Wind Energy*, vol. 10, no. 4, pp. 293–301, 2007.
- [26] Y. A. Elmaati, L. El Bahir, and K. Fatah, "An integrator based wind speed estimator for wind turbine control," *Wind and Structures*, vol. 21, no. 4, pp. 443–460, 2015a.
- [27] X. Wei and M. Verhaegen, "Sensor and actuator fault diagnosis for wind turbine systems by using robust observer and filter," *Wind Energy*, vol. 14, no. 4, pp. 491–516, 2011.
- [28] Y. A. Elmaati, L. E. L. Bahir, and K. Fatah, "Residual generation for the gearbox efficiency drop fault detection in the NREL 1.5 WindPact turbine," in *Proceedings of the IEEE International Conference on Electrical and Information Technologies*, Marrakech, Morocco, March 2015.
- [29] E. Nabil, A. A. Sobaih, and B. Abou-Zalam, "Constrained Kalman filter based detection and isolation of sensor faults in a wind turbine," in *Proceedings of the IEEE Tenth International Conference on Computer Engineering and Systems (ICCES)*, pp. 67–72, Cairo, Egypt, December 2015.
- [30] Y. A. Elmaati, L. E. L. Bahir, and K. Fatah, "fault tolerant control of internal faults in wind turbine: case study of gearbox efficiency decrease," *International Journal of Rotating Machinery*, vol. 2018, Article ID 9538489, 8 pages, 2018.
- [31] F.-D. Li, M. Wu, Y. He, and X. Chen, "Optimal control in microgrid using multi-agent reinforcement learning," *ISA Transactions*, vol. 51, no. 6, pp. 743–751, 2012.
- [32] E. Sales-Setién and I. Peñarrocha-Alós, "Multiobjective performance-based designs in fault estimation and isolation for discrete-time systems and its application to wind turbines," *International Journal of Systems Science*, vol. 50, no. 6, pp. 1252–1274, 2019.
- [33] E. Sales-Setien and I. Peñarrocha, "Robust estimation and diagnosis of wind turbine pitch misalignments at a wind farm

- level,” *Renewable Energy*, vol. 146, no. 2020, pp. 1746–1765, 2019.
- [34] D. Dolz, I. Penarrocha, and R. Sanchis, “Performance tradeoffs for networked jump observer-based fault diagnosis,” *IEEE Transactions on Signal Processing*, vol. 63, no. 10, pp. 2692–2703, 2015.
- [35] X. Fu, L. He, and H. Qiu, “MEMS gyroscope sensors for wind turbine blade tip deflection measurement,” in *Proceedings of the Instrumentation and measurement Technology Conference (I2MTC)*, May 2013.
- [36] T. Lindstrim, M. Lomholt, J. Ostergaard et al., “Online estimation of wind turbine blade deflection with UWB signals,” in *Proceedings of the 2015 23rd European Signal Processing Conference (EUSIPCO)*, August–September, 2015.
- [37] R. Poore and T. Lettenmaier, *Alternative Design Study Report: WindPACT Advanced Wind Turbine Drive Train: Designs Study*, Global Energy Concepts, LLC, Kirkland, WA, USA, 2002.
- [38] D. Perfiliev, J. Hämäläinen, and J. Backman, “Robust analyzing tools for wind turbine blades coupled with multi-objective optimization,” *Journal of Energy and Power Engineering*, vol. 7, pp. 1831–1836, 2013.
- [39] V. Cirtoaje, A. S. Baiesu, and S. F. Mihalache, “Two controller design procedures using closed-loop Pole placement technique,” *Control Engineering and Applied Informatics*, vol. 11, no. 1, pp. 34–43, 2009.
- [40] H. Wang and S. Daley, “Actuator fault diagnosis: an adaptive observer-based technique,” *IEEE Transactions on Automatic Control*, vol. 41, no. 7, pp. 1073–1078, 1996.
- [41] J. Bernussou and G. Garcia, “Pole assignment for uncertain systems in a specified disk by output feedback,” *Mathematics of Control, Signals and Systems*, vol. 9, no. 2, pp. 152–161, 1996.
- [42] Yalmip: 2015, <http://users.isy.liu.se/johanl/yalmip/>.
- [43] D. A. Griffin, *Blade System Design Studies Volume II: Preliminary Blade Designs and Recommended Test Matrix*, Global Energy Concepts, Kirkland, WA, USA, 2004.
- [44] S. Simani, S. Farsoni, and P. Castaldi, “Identification for wind turbine benchmark fault diagnosis,” *Machines*, vol. 2, no. 4, pp. 275–298, 2014.
- [45] A. B. Borchers, J. A. Larsen, and J. Stoustrup, “Fault detection and load distribution for the wind farm challenge,” *IFAC Proceedings Volumes*, vol. 47, no. 3, pp. 4316–4321, 2014.
- [46] J. Blesa, P. Jimenez, D. Rotondo, F. Nejjari, and V. Puig, “An interval NLPV parity equations approach for fault detection and isolation of a wind farm,” *IEEE Transactions on Industrial Electronics*, vol. 62, no. 6, pp. 3794–3805, 2015.
- [47] L. S. Duviella and M. Sayed-Mouchaweh, “An evolving classification approach for fault diagnosis and prognosis of a wind farm,” in *Proceedings of the 2nd Conference on Control and Fault-Tolerant Systems (SysTol)*, pp. 377–382, Nice, France, October 2013.
- [48] D. Rotondo, F. Nejjari, and V. Puig, “A virtual actuator and sensor approach for fault tolerant control of LPV systems,” *Journal of Process Control*, vol. 24, no. 3, pp. 203–222, 2014.

Research Article

Dynamic Modeling and Adaptive Robust Synchronous Control of Parallel Robotic Manipulator for Industrial Application

Haiqiang Zhang ^{1,2}, Hairong Fang ¹, Qi Zou,² and Dan Zhang²

¹School of Mechanical, Electronic and Control Engineering, Beijing Jiaotong University, Beijing, China

²Lassonde School of Engineering, York University, Toronto, Ontario M3J 1P3, Canada

Correspondence should be addressed to Haiqiang Zhang; haiqiang@yorku.ca

Received 29 July 2019; Revised 28 October 2019; Accepted 14 November 2019; Published 7 February 2020

Guest Editor: Kiyong Oh

Copyright © 2020 Haiqiang Zhang et al. This is an open access article distributed under the Creative Commons Attribution License, which permits unrestricted use, distribution, and reproduction in any medium, provided the original work is properly cited.

Control of parallel manipulators is very hard due to their complex dynamic formulations. If part of the complexity is resulting from uncertainties, an effective manner for coping with these problems is adaptive robust control. In this paper, we proposed three types of adaptive robust synchronous controllers to solve the trajectory tracking problem for a redundantly actuated parallel manipulator. The inverse kinematic of the parallel manipulator was firstly developed, and the dynamic formulation was further derived by mean of the principle of virtual work. Furthermore, linear parameterization regression matrix was determined by virtue of command function “equationsToMatrix” in MATLAB. Secondly, the three adaptive robust synchronous controllers (i.e., sliding mode control, high gain control, and high frequency control) are developed, by incorporating the camera sensor technique into adaptive robust synchronous control architecture. The stability of the proposed controllers was proved by utilizing Lyapunov theory. A sequence of simulation tests were implemented to prove the performance of the controllers presented in this paper. The three proposed controllers can theoretically guarantee the errors including trajectory tracking errors, synchronization errors, and cross-coupling errors asymptotically converge to zero for a given trajectory, and the estimated unknown parameters can also approximately converge to their actual values in the presence of unmodeled dynamics and external uncertainties. Moreover, all the simulation comparative results were presented to illustrate that the adaptive robust synchronous high-frequency controller possess a much superior comprehensive performance than two other controllers.

1. Introduction

Compared to counterpart serial manipulators, parallel manipulators exhibit much greater advantages such as high stiffness, lower inertia, high loading capability, high precision, high acceleration, and high dexterity, which are desirable properties for application in high-speed machine, high-precision-assisted surgery, and high-speed pick and place of Delta robots, and some other applications [1–4]. However, small workspace and abundant singularities within the workspace limit their wide applications. Under such circumstances, parallel manipulators with redundant actuation are expected to tackle their shortcomings, as redundant actuation can eliminate or decrease singularities, increase the dexterous workspace, optimize the

configuration of driving force, and so on. At present, the research studies on redundant actuation mainly focus on the singularities and the workspace [5, 6]. However, the intelligent control strategies in the existing literature are seldom studied, which just have gotten more attention to make the most use of their advantages, especially for high-speed, high-accuracy machine tools. Some advanced intelligent control strategies, such as adaptive control and robust control, are very essential for more prosperous application in industries [7–11].

Redundant actuation can be achieved with two different methods, one is to add the kinematic chain including nonconstrained subchains or constrained subchains without increasing the degree of freedom, and the other is to change the passive joint into active joint [12]. Liu et al. [13] studied

exhaustively the force/motion transmissibility of redundantly actuated parallel manipulators, and six simulation examples illustrate that the actuation redundancy can significantly improve the kinematic performance and enlarge the singularity-free workspace. Yao et al. [14] presented a redundant actuated 5UPS-PRPU parallel manipulator by adding an actuator to the middle PRPU passive constraint branch to form a redundant branch; the simulations illustrated that redundant actuation can greatly improve the performance of the parallel manipulator. Boudreau et al. [15, 16] presented the dynamic model of a cinematically redundant planar parallel manipulator and optimized to make the actuator torques minimize when the end-effector is performing the trajectory tracking. Wang et al. [17] derived the inverse dynamic model of a spatial 3-DOF parallel manipulator with redundant actuation by adding actuators to passive rotational joints, and the driving force was optimized in terms of the Moore–Penrose inverse matrix. The motion control is very complicated for the coupled dynamics of the parallel manipulator with redundant actuation. The preliminary success of controllers design resulted from planar manipulator and Stewart platform with different adaptive control methods. Ren et al. [18] proposed a novel adaptive synchronized control for a planar parallel manipulator with parametric uncertainty and applied it to improve the tracking accuracy. Shang and Cong [19] developed a nonlinear adaptive controller in the task space for the trajectory tracking of a 2-DOF redundantly actuated parallel manipulator, and the control law including dynamics compensation, adaptive friction compensation and error elimination items was designed simultaneously. In [20], Babaghasabha et al. addressed the design and implementation of adaptive control on a planar cable-driven parallel manipulator with uncertainties in dynamic and kinematic parameters based on simplified hypothesis. Zhang and Wei [21] indicated that adaptive control is generally divided into three categories, model reference control, self-tuning control and gain schedule control, and presented a review and discussion on the model reference control of parallel manipulator. Wang et al. [22] proposed an adaptive back-stepping technique for point control of a planar parallel robot, and experimental results showed that the adaptive back-stepping controller outperforms all the other controllers (mentioned in the paper, i.e., back-stepping controller, adaptive controller, adaptive PD controller, and PD controller) in terms of steady-state errors. Honegger et al. [23] proposed a nonlinear adaptive control algorithm and conducted parameters identification of a 6-PSS parallel manipulator employed as a high-speed milling machine. Zhao et al. [24] developed a fully adaptive feed-forward feedback synchronized tracking control approach for precision tracking control of six-degree-of-freedom Stewart Platform, and the simulation results illustrated that the proposed cross-coupling approach can guarantee both position error and synchronization error converge to zero asymptotically. Hence, synchronous control is expected to be applied to improve trajectory tracking accuracy.

In recent years, robust control method has been widely employed in dealing with nonlinear control with

uncertainties and disturbances [25]. Yime et al. [26] proposed a robust adaptive control for the Stewart Gough platform, and the performance of the control law was evaluated by using a sinusoidal path for position and orientation of the upper platform. Zhu et al. [27] presented an adaptive robust posture controller for a parallel manipulator driven by pneumatic muscles with a redundant degree of freedom, which can be utilized to deal with parametric uncertainties and uncertain nonlinearities in the dynamics. Subsequently, a new adaptive robust control architecture for a class of uncertain Euler–Lagrange system was proposed to apply to the wheeled mobile robot, and the experimental results demonstrated that the proposed controller improves control performance in comparison to the adaptive sliding mode control [28]. The control scheme makes full advantage of the adaptive control theory and parameters identification, which played the key role in adaptive strategy; many effective parameter estimation techniques were integrated into adaptive controller design [29]. In addition, the Lyapunov design method emerged as a popular method for estimation in an adaptive algorithm. In this method, the parameter update law was designed in such a way that the time derivative of Lyapunov function was nonpositive [30]. To achieve the proposed tracking trajectory and chattering phenomenon elimination, a robust control strategy was designed for the robotic manipulator based on the sliding mode function and a continuous adaptive control law. And the robustness and stability of the systems had been verified by the Lyapunov theory in [31].

The motivation of this research is to design a stable adaptive robust synchronous control scheme for tracking control of the parallel manipulator with a guaranteed error convergence and without a requirement for prior knowledge of the dynamics of the parallel manipulator. The main contribution of this paper is proposing an alternative adaptive robust synchronous high-frequency control scheme for a 3-DOF parallel manipulator. The synchronization errors and cross-coupling errors are incorporated into adaptive robust control architecture through position and orientation error compensations. The proposed adaptive robust synchronous high-frequency control scheme can obtain the stable tracking performances and synchronization performances in the presence of external uncertainties. A series of simulations were conducted to demonstrate that the proposed control scheme possesses better comprehensive performance than other controllers.

The reminder of this paper is organized as follows. In Section 2, the structure of the redundantly actuated 2RPU-2SPR parallel manipulator (in which R, P, U, and S stand for rotational, prismatic, universal, and spherical kinematic joints, respectively, and the underline format (P) represents the actuated joint) and the coordinate frames are developed. The kinematic relations of the parallel manipulator are presented in detail in Section 3. In Section 4, the explicit dynamic model is derived in terms of the principle of virtual work and d’Alembert formulation. Next, in Section 5, three adaptive robust synchronous controllers are introduced and deduced in considerable detail. In Section 6, the comparative simulation cases are given to verify the effectiveness of the

proposed three controllers. Finally, some concluding remarks and future work are presented in Section 7.

2. System Description

The parallel manipulator has three degrees of freedom and mainly consists of the fixed platform, the moving platform, and four limbs with two of the same identical kinematic configuration. The parallel manipulator module is a good candidate for engineering application, what's more, it can connect X-Y linear rail in series to achieve five-axis serial-parallel hybrid kinematic machine tool, which can complete the complex special-shaded surface free machining (as shown in Figure 1).

In order to conduct experimental verification analysis, we fabricated a scaled-test prototype (as depicted in Figure 2) whose kernel module is a 2RPU-2SPR parallel manipulator with redundant actuation because the number of actuators is greater than that of the degree of freedom. The structural diagram is depicted in Figure 3. The prismatic joints described by the linear joint variables d_i connect the fixed platform to the moving platform by a rotational joint followed by a universal joint or a spherical joint followed by a rotational joint. It is worth noting that the used spherical joint is designed by means of three mutually perpendicular rotational joints in order to enlarge the rotation range.

For modeling purposes, as shown in Figure 3, we assume a fixed coordinate system $B-xyz$ at the centered point \mathbf{B} of the fixed platform and a moving coordinate system $A-uvw$ on the square moving platform at the centered point \mathbf{A} , along the z -axis and w -axis perpendicular to the platform and the x -axis and y -axis parallel to the u -axis and v -axis, respectively. Both $A_1A_2A_3A_4$ and $B_1B_2B_3B_4$ are designed to be squares to yield a symmetric architecture of the parallel manipulator. With these geometric conditions satisfied, the moving platform of parallel manipulator will possess with three degrees of freedom in the Cartesian space by controlling the movement of four actuators, that is, two rotational degrees of freedom around x -axis and v -axis, and one translational degree of freedom along z axis; in this case, the spatial rotations are coupled along with the change of four nonidentical limbs. The mobility analysis of the parallel manipulator including initial configuration and general configuration has been addressed in detail in our previous work [32] by resorting to the screw theory and modified Grubler–Kutzbach (G–K) criterion. To avoid repetition, herein, the mobility regarding the parallel manipulator is not described in this paper.

3. Kinematics Analysis

The moving platform can move along z direction and rotate around the x -axis and v -axis with the consideration of mobility characteristics. The homogeneous transformation matrix \mathbf{T} of the position coordinate point \mathbf{p} can be expressed as follows:

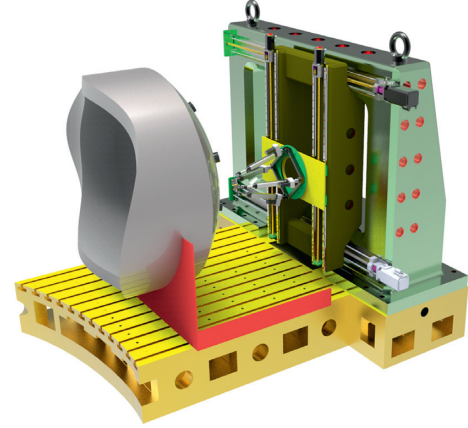


FIGURE 1: A five-axis hybrid kinematic machine tool.

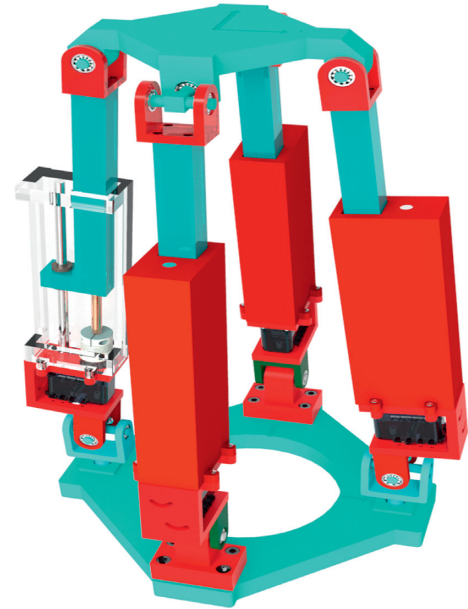


FIGURE 2: The 3D model of parallel manipulator.

$$\mathbf{T} = \begin{bmatrix} \mathbf{R} & \mathbf{p} \\ 0 & 1 \end{bmatrix} = \text{Rot}(x, \alpha) \text{Trans}(z, d) \text{Rot}(v, \beta)$$

$$= \begin{bmatrix} \cos \beta & 0 & \sin \beta & x \\ \sin \alpha \sin \beta & \cos \alpha & -\sin \alpha \cos \beta & y \\ -\sin \beta \cos \alpha & \sin \alpha & \cos \alpha \cos \beta & z \\ 0 & 0 & 0 & 1 \end{bmatrix}, \quad (1)$$

where $\mathbf{p} = [x, y, z]^T$ is the position coordinates of point \mathbf{A} in the fixed coordinate system, α is the rotation angle around the x -axis, and β is the rotation angle around the v -axis.

Additionally, once the rotation matrix \mathbf{R} is obtained, then the rotational Euler angles will be obtained by

$$\begin{cases} \alpha = \arctan 2(R(3, 2), R(2, 2)), \\ \beta = \arctan 2(R(1, 3), R(1, 1)), \end{cases} \quad (2)$$

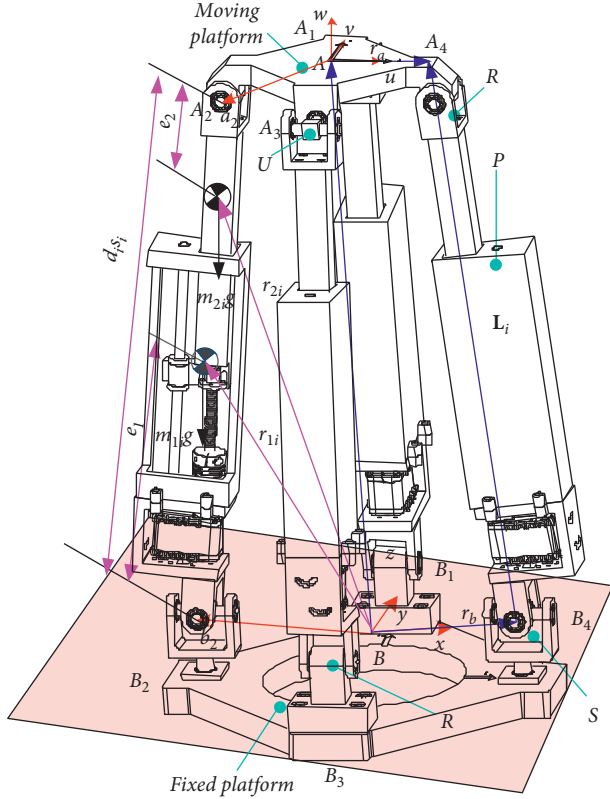


FIGURE 3: Structure diagram of parallel manipulator.

where $R(\cdot, \cdot)$ represents the row and column elements of the rotation matrix \mathbf{R} .

Moreover, referring to the aforementioned relations in (1), the coupling relationships can be outlined as

$$\begin{cases} x = 0, \\ y = -hs\alpha, \\ z = hsa, \end{cases} \quad (3)$$

where h is the movement distance along the z direction. So it is very easy to obtain the parasitic motion of the parallel manipulator:

$$y = -z \tan \alpha. \quad (4)$$

Referring to Figure 3, the closed vector constraint equation of i -th limb can be written as

$$\mathbf{L}_i = \mathbf{d}_i \cdot \mathbf{s}_i = \mathbf{p} + \mathbf{a}_i - \mathbf{b}_i. \quad (5)$$

In (5), \mathbf{b}_i is the description of the position vector in the fixed coordinate system, and ${}^A\mathbf{a}_i$ is the description of the position vector in the moving coordinate system, and \mathbf{a}_i is the representation of vector ${}^A\mathbf{a}_i$ in the fixed coordinate

system, namely, $\mathbf{a}_i = \mathbf{R} \cdot {}^A\mathbf{a}_i$. To prevent graphics confusion, we only represent \mathbf{a}_2 and \mathbf{b}_2 in Figure 3 as representative.

The position and orientation of the moving platform can be represented by independent parameters $\mathbf{X} = [z \ \alpha \ \beta]^T$, the velocity of the i -th limb in the inverse kinematics can be derived by differentiating (5) with regard to time and dot-multiplying both sides of (5) by \mathbf{s}_i , as follows [33]:

$$\begin{bmatrix} \dot{d}_1 \\ \dot{d}_2 \\ \dot{d}_3 \\ \dot{d}_4 \end{bmatrix} = \begin{bmatrix} \mathbf{s}_1^T [\mathbf{a}_1 \times \mathbf{s}_1]^T \\ \mathbf{s}_2^T [\mathbf{a}_2 \times \mathbf{s}_2]^T \\ \mathbf{s}_3^T [\mathbf{a}_3 \times \mathbf{s}_3]^T \\ \mathbf{s}_4^T [\mathbf{a}_4 \times \mathbf{s}_4]^T \end{bmatrix} \begin{bmatrix} v_p \\ w_p \end{bmatrix}, \quad (6)$$

where $v_p = [\dot{x} \ \dot{y} \ \dot{z}]^T$ and $w_p = [w_x \ w_y \ w_z]^T$ are the linear and angular velocity of the moving platform defined in the fixed coordinate system, respectively.

$$\begin{bmatrix} w_x \\ w_y \\ w_z \end{bmatrix} = \begin{bmatrix} 1 & 0 \\ 0 & \cos \alpha \\ 0 & \cos \beta \end{bmatrix} \begin{bmatrix} \dot{\alpha} \\ \dot{\beta} \end{bmatrix}. \quad (7)$$

It is useful to represent (6) in matrix form as

$$\dot{\mathbf{q}} = \mathbf{J}_0 \dot{\mathbf{X}} = \mathbf{J}_q \mathbf{J}_p \dot{\mathbf{X}}, \quad (8)$$

where $\dot{\mathbf{q}} = [\dot{d}_1, \dot{d}_2, \dot{d}_3, \dot{d}_4]^T$, \mathbf{J}_0 is the velocity Jacobain matrix of the parallel manipulator, and

$$\mathbf{J}_q = \begin{bmatrix} \mathbf{s}_1^T [\mathbf{a}_1 \times \mathbf{s}_1]^T \\ \mathbf{s}_2^T [\mathbf{a}_2 \times \mathbf{s}_2]^T \\ \mathbf{s}_3^T [\mathbf{a}_3 \times \mathbf{s}_3]^T \\ \mathbf{s}_4^T [\mathbf{a}_4 \times \mathbf{s}_4]^T \end{bmatrix}, \quad (9)$$

$$\mathbf{J}_p = \begin{bmatrix} \mathbf{J}_{vp} \\ \mathbf{J}_{wp} \end{bmatrix} = \begin{bmatrix} 0 & 0 & 0 \\ -\tan \alpha & -z \cdot \sec^2 \alpha & 0 \\ 1 & 0 & 0 \\ 0 & 1 & 0 \\ 0 & 0 & \cos \alpha \\ 0 & 0 & \sin \alpha \end{bmatrix}.$$

The derivative of independent coordinate parameters can be written in the current case:

$$\dot{\mathbf{X}} = [\dot{z} \ \dot{\alpha} \ \dot{\beta}]^T. \quad (10)$$

By differentiating both sides of (8), the acceleration between the actuated joints and corresponding end-effector can be expressed as

$$\ddot{\mathbf{q}} = \dot{\mathbf{J}}_0 \dot{\mathbf{X}} + \mathbf{J}_0 \ddot{\mathbf{X}}, \quad (11)$$

where

$$\mathbf{j}_0 = \begin{bmatrix} [\mathbf{w}_1 \times \mathbf{s}_1]^T & [(\mathbf{w}_p \times \mathbf{a}_1) \times \mathbf{s}_1 + \mathbf{a}_1 \times (\mathbf{w}_1 \times \mathbf{s}_1)]^T \\ [\mathbf{w}_2 \times \mathbf{s}_2]^T & [(\mathbf{w}_p \times \mathbf{a}_2) \times \mathbf{s}_2 + \mathbf{a}_2 \times (\mathbf{w}_2 \times \mathbf{s}_2)]^T \\ [\mathbf{w}_3 \times \mathbf{s}_3]^T & [(\mathbf{w}_p \times \mathbf{a}_3) \times \mathbf{s}_3 + \mathbf{a}_3 \times (\mathbf{w}_3 \times \mathbf{s}_3)]^T \\ [\mathbf{w}_4 \times \mathbf{s}_4]^T & [(\mathbf{w}_p \times \mathbf{a}_4) \times \mathbf{s}_4 + \mathbf{a}_4 \times (\mathbf{w}_4 \times \mathbf{s}_4)]^T \end{bmatrix} \cdot \mathbf{J}_p + \mathbf{J}_q \cdot \begin{bmatrix} 0 & 0 & 0 \\ (-1 - \tan^2 \alpha) \cdot \dot{\alpha} & -\left(\dot{z} \cdot \sec^2 \alpha + \frac{2z \cdot \sin \alpha}{\cos^3 \alpha} \cdot \dot{\alpha}\right) & 0 \\ 0 & 0 & 0 \\ 0 & 0 & 0 \\ 0 & 0 & -\sin \alpha \cdot \dot{\alpha} \\ 0 & 0 & \cos \alpha \cdot \dot{\alpha} \end{bmatrix}, \quad (12)$$

where \mathbf{w}_i is the angular velocity of the i -th limb defined in the fixed coordinate system.

The structural diagram of the i -th limb is depicted in Figure 3 as well, each of that consists of an upper sublimb and a lower sublimb. Let e_1 be the distance between the centroid B_i and the center of mass of the lower sublimb, while e_2 be the distance of the centroid A_i and the center of mass of the upper sublimb. The position vectors of the centers of mass of the i -th limb are given with respect to the fixed coordinate system:

$$\mathbf{r}_{1i} = \mathbf{b}_i + e_1 \mathbf{s}_i, \quad (13)$$

$$\mathbf{r}_{2i} = \mathbf{b}_i + (\mathbf{d}_i - e_2) \mathbf{s}_i. \quad (14)$$

The inverse kinematics (5) should be differentiated with respect to time, and the velocity of kinematic joints A_i connected to the moving platform can be obtained in the fixed coordinate system:

$$\mathbf{v}_{ai} = \mathbf{v}_p + \boldsymbol{\omega}_p \times \mathbf{a}_i = \mathbf{J}_{ai} \cdot \mathbf{J}_p \cdot \dot{\mathbf{X}}, \quad (15)$$

where

$$\mathbf{J}_{ai} = \begin{bmatrix} 1 & 0 & 0 & 0 & a_{iz} & -a_{iy} \\ 0 & 1 & 0 & -a_{iz} & 0 & a_{ix} \\ 0 & 0 & 1 & a_{iy} & -a_{ix} & 0 \end{bmatrix}. \quad (16)$$

The angular velocity of the i -th limb

$$\boldsymbol{\omega}_i = \frac{\mathbf{s}_i \times \mathbf{v}_{ai}}{\mathbf{d}_i} = \mathbf{J}_{wi} \dot{\mathbf{X}}, \quad (17)$$

where $\mathbf{J}_{wi} = \tilde{\mathbf{s}}_i \mathbf{J}_{ai} \mathbf{J}_p / \mathbf{d}_i$, and $\tilde{\mathbf{s}}_i$ is the antisymmetric operator corresponding to the vector \mathbf{s}_i .

Taking the derivative of (13) and (14) with respect to time, the velocity of the mass center of the lower sublimb and

upper sublimb can be obtained in the fixed coordinate system:

$$\mathbf{v}_{1i} = e_1 \boldsymbol{\omega}_i \times \mathbf{s}_i = \mathbf{J}_{v1i} \dot{\mathbf{X}}, \quad (18)$$

where

$$\begin{aligned} \mathbf{J}_{v1i} &= -e_1 \cdot \tilde{\mathbf{s}}_i \mathbf{J}_{wi}, \\ \mathbf{v}_{2i} &= (\mathbf{d}_i - e_2) \boldsymbol{\omega}_i \times \mathbf{s}_i + \dot{\mathbf{d}}_i \cdot \mathbf{s}_i = \mathbf{J}_{v2i} \dot{\mathbf{X}}, \\ \mathbf{J}_{v2i} &= (e_2 - \mathbf{d}_i) \cdot \tilde{\mathbf{s}}_i \mathbf{J}_{wi} + \mathbf{s}_i \mathbf{J}_{di} \mathbf{J}_p. \end{aligned} \quad (19)$$

Combining (17)–(19), one can obtain

$$\begin{aligned} \mathbf{J}_{v\omega 1i} &= \begin{bmatrix} \mathbf{J}_{v1i} \\ \mathbf{J}_{wi} \end{bmatrix}, \\ \mathbf{J}_{v\omega 2i} &= \begin{bmatrix} \mathbf{J}_{v2i} \\ \mathbf{J}_{wi} \end{bmatrix}, \end{aligned} \quad (20)$$

where $\mathbf{J}_{v\omega 1i}$ and $\mathbf{J}_{v\omega 2i}$ are the velocity Jacobian matrices of the i -th limb.

Turning to accelerations, the acceleration of the point A_i can be carried out by differentiating (15) with respect to time:

$$\dot{\mathbf{v}}_{ai} = \dot{\mathbf{v}}_p + \dot{\boldsymbol{\omega}}_p \times \mathbf{a}_i + \boldsymbol{\omega}_p \times (\boldsymbol{\omega}_p \times \mathbf{a}_i). \quad (21)$$

The angular acceleration velocity of the i -th limb can be expressed as

$$\dot{\boldsymbol{\omega}}_i = \frac{\mathbf{s}_i \times \dot{\mathbf{v}}_{ai} - 2\dot{\mathbf{d}}_i \boldsymbol{\omega}_i}{\mathbf{d}_i} = \mathbf{J}_{wi} \ddot{\mathbf{X}} + \dot{\mathbf{J}}_{wi} \dot{\mathbf{X}}, \quad (22)$$

where

$$\dot{\mathbf{J}}_{wi} = \frac{\tilde{\mathbf{s}}_i ((\dot{\mathbf{J}}_{vp} - \tilde{\mathbf{a}}_i \dot{\mathbf{J}}_{wp}) - [(\mathbf{J}_{wp} \dot{\mathbf{X}}) \times] \tilde{\mathbf{a}}_i \mathbf{J}_{wp}) - 2\mathbf{J}_{di} \mathbf{J}_0 \dot{\mathbf{X}} \mathbf{J}_{wi}}{\mathbf{d}_i}. \quad (23)$$

Finally, the acceleration of the mass centers of the i -th limb can be obtained by differentiating once again (18) and (19) with respect to time, respectively,

$$\dot{\mathbf{v}}_{1i} = e_1 \dot{\boldsymbol{\omega}}_i \times \mathbf{s}_i + e_1 \boldsymbol{\omega}_i \times (\boldsymbol{\omega}_i \times \mathbf{s}_i) = \mathbf{J}_{v1i} \ddot{\mathbf{X}} + \dot{\mathbf{J}}_{v1i} \dot{\mathbf{X}}, \quad (24)$$

where

$$\begin{aligned} \dot{\mathbf{J}}_{v1i} &= -e_1 \dot{\tilde{\mathbf{s}}}_i \dot{\mathbf{J}}_{wi} - e_1 \mathbf{s}_i \cdot (\mathbf{J}_{wi} \dot{\mathbf{X}})^T \dot{\mathbf{J}}_{wi}, \\ \dot{\mathbf{v}}_{2i} &= \dot{\mathbf{d}}_i \cdot \mathbf{s}_i + 2\dot{\mathbf{d}}_i (\boldsymbol{\omega}_i \times \mathbf{s}_i) + (\mathbf{d}_i - e_2) \dot{\boldsymbol{\omega}}_i \times \mathbf{s}_i + (\mathbf{d}_i - e_2) \boldsymbol{\omega}_i \times (\boldsymbol{\omega}_i \times \mathbf{s}_i) \\ &= \mathbf{J}_{v2i} \ddot{\mathbf{X}} + \dot{\mathbf{J}}_{v2i} \dot{\mathbf{X}}, \\ \dot{\mathbf{J}}_{v2i} &= \mathbf{s}_i \cdot \dot{\mathbf{J}}_{0i} - 2\mathbf{J}_{0i} \cdot \dot{\mathbf{X}} \cdot \tilde{\mathbf{s}}_i \cdot \mathbf{J}_{wi} + (e_2 - \mathbf{d}_i) [\tilde{\mathbf{s}}_i \cdot \dot{\mathbf{J}}_{wi} + [(\mathbf{J}_{wi} \dot{\mathbf{X}}) \times] \tilde{\mathbf{s}} \cdot \mathbf{J}_{wi}]. \end{aligned} \quad (25)$$

So far, the velocity and acceleration of the moving platform and sublimbs have been solved. In the next section, we will concentrate on the derivation of dynamics of the proposed manipulator.

4. Dynamics Analysis

The inverse dynamics problem of the parallel manipulator is to determine the required driving force under the

requirement generated a prescribed motion trajectory. For the 2RPU-2SPR parallel manipulator, the dynamic model in the Cartesian space can be deduced in the absence of friction and other disturbances by applying the principle of virtual work and d'Alembert formulation stated on the previous work [34], just only the key points are presented, the following dynamic equation can be obtained:

$$\begin{aligned} \mathbf{J}_0^T \boldsymbol{\tau}_a + \mathbf{J}_p \begin{bmatrix} \mathbf{f}_e + m_a \mathbf{g} - m_a \dot{\mathbf{v}}_p \\ \mathbf{n}_e - {}^B \mathbf{I}_p \dot{\boldsymbol{\omega}}_p - \boldsymbol{\omega}_p \times ({}^B \mathbf{I}_p \boldsymbol{\omega}_p) \end{bmatrix} \\ + \sum_i \mathbf{J}_{v\omega 1i}^T \begin{bmatrix} m_{1i} \mathbf{g} - m_{1i} \dot{\mathbf{v}}_{1i} \\ -{}^B \mathbf{I}_{1i} \dot{\boldsymbol{\omega}}_i - \boldsymbol{\omega}_i \times ({}^B \mathbf{I}_{1i} \boldsymbol{\omega}_i) \end{bmatrix} \\ + \sum_i \mathbf{J}_{v\omega 2i}^T \begin{bmatrix} m_{2i} \mathbf{g} - m_{2i} \dot{\mathbf{v}}_{2i} \\ -{}^B \mathbf{I}_{2i} \dot{\boldsymbol{\omega}}_i - \boldsymbol{\omega}_i \times ({}^B \mathbf{I}_{2i} \boldsymbol{\omega}_i) \end{bmatrix} = 0. \end{aligned} \quad (26)$$

By simplifying, the dynamics equation of the manipulator can be further deduced as

$$\begin{aligned} \mathbf{F}_X = - \left(\mathbf{J}_p \begin{bmatrix} \mathbf{f}_e + m_a \mathbf{g} - m_a \dot{\mathbf{v}}_p \\ \mathbf{n}_e - {}^B \mathbf{I}_p \dot{\boldsymbol{\omega}}_p - \boldsymbol{\omega}_p \times ({}^B \mathbf{I}_p \boldsymbol{\omega}_p) \end{bmatrix} \right. \\ \left. + \sum_i \mathbf{J}_{v\omega 1i}^T \begin{bmatrix} m_{1i} \mathbf{g} - m_{1i} \dot{\mathbf{v}}_{1i} \\ -{}^B \mathbf{I}_{1i} \dot{\boldsymbol{\omega}}_i - \boldsymbol{\omega}_i \times ({}^B \mathbf{I}_{1i} \boldsymbol{\omega}_i) \end{bmatrix} \right. \\ \left. + \sum_i \mathbf{J}_{v\omega 2i}^T \begin{bmatrix} m_{2i} \mathbf{g} - m_{2i} \dot{\mathbf{v}}_{2i} \\ -{}^B \mathbf{I}_{2i} \dot{\boldsymbol{\omega}}_i - \boldsymbol{\omega}_i \times ({}^B \mathbf{I}_{2i} \boldsymbol{\omega}_i) \end{bmatrix} \right), \end{aligned} \quad (27)$$

$$\begin{aligned} \mathbf{M}(\mathbf{X}) &= \left\{ \mathbf{J}_p^T \begin{bmatrix} m_a \mathbf{J}_{vp} \\ {}^B \mathbf{I}_p \mathbf{J}_{wp} \end{bmatrix} + \sum_i \mathbf{J}_{v\omega 1i}^T \begin{bmatrix} m_{1i} \mathbf{J}_{v1i} \\ {}^B \mathbf{I}_{1i} \mathbf{J}_{w1i} \end{bmatrix} + \sum_i \mathbf{J}_{v\omega 2i}^T \begin{bmatrix} m_{2i} \mathbf{J}_{v2i} \\ {}^B \mathbf{I}_{2i} \mathbf{J}_{w2i} \end{bmatrix} \right\}, \\ \mathbf{C}(\dot{\mathbf{X}}, \mathbf{X}) &= \left\{ \mathbf{J}_p^T \begin{bmatrix} m_a \dot{\mathbf{J}}_{vp} \\ {}^B \mathbf{I}_p \dot{\mathbf{J}}_{wp} + [(\mathbf{J}_{wp} \dot{\mathbf{X}}) \times] ({}^B \mathbf{I}_p \mathbf{J}_{wp}) \end{bmatrix} + \sum_i \mathbf{J}_{v\omega 1i}^T \begin{bmatrix} m_{1i} \dot{\mathbf{J}}_{v1i} \\ {}^B \mathbf{I}_{1i} \dot{\mathbf{J}}_{w1i} + [(\mathbf{J}_{v\omega 1i} \dot{\mathbf{X}}) \times] ({}^B \mathbf{I}_{1i} \mathbf{J}_{w1i}) \end{bmatrix} \right. \\ &\quad \left. + \sum_i \mathbf{J}_{v\omega 2i}^T \begin{bmatrix} m_{2i} \dot{\mathbf{J}}_{v2i} \\ {}^B \mathbf{I}_{2i} \dot{\mathbf{J}}_{w2i} + [(\mathbf{J}_{v\omega 2i} \dot{\mathbf{X}}) \times] ({}^B \mathbf{I}_{2i} \mathbf{J}_{w2i}) \end{bmatrix} \right\}, \\ \mathbf{N}(\mathbf{X}) &= \mathbf{J}_p^T \begin{bmatrix} m_a \mathbf{g} \\ \mathbf{0} \end{bmatrix} + \sum_i \mathbf{J}_{v\omega 1i}^T \begin{bmatrix} m_{1i} \mathbf{g} \\ \mathbf{0} \end{bmatrix} + \sum_i \mathbf{J}_{v\omega 2i}^T \begin{bmatrix} m_{2i} \mathbf{g} \\ \mathbf{0} \end{bmatrix} - \mathbf{J}_p^T \begin{bmatrix} \mathbf{f}_e \\ \mathbf{n}_e \end{bmatrix}, \end{aligned} \quad (29)$$

where $\mathbf{M}(\mathbf{X})$ is the positive definite inertia matrix, $\mathbf{C}(\dot{\mathbf{X}}, \mathbf{X})$ is the nonlinear matrix including the centrifugal and the Coriolis forces term, and $\mathbf{N}(\mathbf{X})$ is the gravitational force and external force term.

Actually, in order to consider the inertial parameter uncertainties and unknown disturbances, the dynamic equation of the parallel robotic manipulator should be written as

$$\mathbf{F}_X = \mathbf{M}(\mathbf{X})\ddot{\mathbf{X}} + \mathbf{C}(\dot{\mathbf{X}}, \mathbf{X})\dot{\mathbf{X}} + \mathbf{N}(\mathbf{X}) + \boldsymbol{\tau}'_d, \quad (30)$$

where $\boldsymbol{\tau}'_d$ is a lumped error vector containing unmodeled dynamics and external disturbances, such as frictions, clearances, wear, noises, and so on.

where \mathbf{F}_X denotes generalized force of the moving platform, ${}^B \mathbf{I}_{1i} = {}^B \mathbf{R}_i {}^i \mathbf{I}_{1i} ({}^B \mathbf{R}_i)^T$, and ${}^B \mathbf{I}_{2i} = {}^B \mathbf{R}_i {}^i \mathbf{I}_{2i} ({}^B \mathbf{R}_i)^T$.

In the mentioned above, ${}^i \mathbf{I}_{1i}$ and ${}^i \mathbf{I}_{2i}$ stand for the moment of inertia matrix of the lower limb and the upper limb expressed in their own local coordinate system, respectively.

Equation (27) is a dynamics equation of the parallel manipulator, which can be simplified into the general form

$$\mathbf{F}_X = \mathbf{M}(\mathbf{X})\ddot{\mathbf{X}} + \mathbf{C}(\dot{\mathbf{X}}, \mathbf{X})\dot{\mathbf{X}} + \mathbf{N}(\mathbf{X}), \quad (28)$$

where

In addition, the dynamic model has several properties that can be exploited to facilitate dynamic controller design, e.g.,

Property 1. The inertia matrix $\mathbf{M}(\mathbf{X})$ is symmetric and positive definite for any $\mathbf{X} \in R^n$.

Property 2. $\dot{\mathbf{M}}(\mathbf{X}) - 2\mathbf{C}(\mathbf{X}, \dot{\mathbf{X}})$ is skew symmetric for any \mathbf{X} , and the condition should be satisfied

$$\mathbf{X}^T [\dot{\mathbf{M}}(\mathbf{X}) - 2\mathbf{C}(\mathbf{X}, \dot{\mathbf{X}})]\mathbf{X} = 0. \quad (31)$$

Property 3. The dynamic model can be linearly expressed as

$$\mathbf{M}(\mathbf{X})\ddot{\mathbf{X}} + \mathbf{C}(\dot{\mathbf{X}}, \mathbf{X})\dot{\mathbf{X}} + \mathbf{N}(\mathbf{X}) = \mathbf{Y}(\ddot{\mathbf{X}}, \dot{\mathbf{X}}, \mathbf{X})\boldsymbol{\Theta}, \quad (32)$$

where \mathbf{Y} is a 3×36 known regressor matrix and Θ is a 36×1 unknown parameter vector formed by four parameters for the moving platform and four actuator limbs (upper and lower limbs) of the parallel manipulator. In general, there are four independent perturbation parameters, namely, the mass m_i of body and three independent inertia tensors $\mathbf{I}_{xx,i}$, $\mathbf{I}_{yy,i}$, $\mathbf{I}_{zz,i}$, i.e.,

$$\Theta_i = [m_i \ \mathbf{I}_{xx,i} \ \mathbf{I}_{yy,i} \ \mathbf{I}_{zz,i}]^T. \quad (33)$$

Actually, the regression matrix is very complex due to the coupling relationship [35, 36]; however, it is worth noting that the expressions can be achieved symbolically with the command function “*equationsToMatrix*” in MATLAB.

Although the dynamics formulation is very complex, the abovementioned three properties are very important to the controller design. Some detail proofs have been addressed in the literature [37].

5. Controller Design

With the consideration of the fact that the dynamic formulation of the redundantly actuated parallel manipulator meets the same properties as those of serial robots and nonredundant parallel manipulators, we can apply the control scheme utilized for serial robots and nonredundant parallel manipulators to parallel manipulators with redundant actuation [38, 39]. In order to achieve a good tracking performance of parallel manipulator in the Cartesian space, an effective advanced control strategy from nonlinear control theory is required. In this paper, we proposed three adaptive robust synchronous controllers to improve the tracking performance of the redundantly actuated parallel manipulator.

The position and orientation tracking error of the task space can be defined as

$$e_i(t) = X_i^d(t) - X_i(t), \quad i = 1, 2, 3, \quad (34)$$

where $X_i^d(t)$ and $X_i(t)$ denote the desired position and orientation and actual position and orientation, respectively. Besides $e_i(t) \rightarrow 0$, it is aimed to regulate the motion relationships among the mobility during the tracking process.

In order to further improve the tracking accuracy, the motion of moving platform needs to be coordinated to achieve synchronization. Therefore, it is essential to introduce the degree-of-freedom synchronization errors.

To guarantee the tracking error, then the synchronization error [40] can be defined by utilizing the differential error between the corresponding tracking error and the mean value of all the tracking errors:

$$\varepsilon_i = e_i - \frac{e_1 + e_2 + e_3}{N}, \quad N = 3. \quad (35)$$

Expanding equation (35), one can obtain

$$\begin{cases} \varepsilon_1 = \frac{N-1}{N}e_1 - \frac{1}{N}e_2 - \frac{1}{N}e_3, \\ \varepsilon_2 = -\frac{1}{N}e_1 + \frac{N-1}{N}e_2 - \frac{1}{N}e_3, \\ \varepsilon_3 = -\frac{1}{N}e_1 - \frac{1}{N}e_2 + \frac{N-1}{N}e_3. \end{cases} \quad (36)$$

Obviously, if $e_i(t)$ is given, then the synchronization error ε_i can be achieved. Furthermore, we can write equation (36) in the matrix form:

$$\boldsymbol{\varepsilon} = \mathbf{H}(t)\mathbf{e}, \quad (37)$$

where $\mathbf{e} = [e_1 \ e_2 \ e_3]^T$, and $\mathbf{H}(t)$ is the relationship matrix between trajectory tracking errors and synchronization errors.

$$\mathbf{H}(t) = \frac{1}{N} \begin{bmatrix} N-1 & -1 & -1 \\ -1 & N-1 & -1 \\ -1 & -1 & N-1 \end{bmatrix}. \quad (38)$$

The cross-coupling error is a compensation term which can reduce tracking error and improve the accuracy of tracking effectively by considering both the restriction and coordination between tracking error and synchronization error. It can be further defined as

$$\mathbf{e}^* = \mathbf{e} + \mathbf{P}\boldsymbol{\varepsilon} + \mathbf{Q} \int_0^t \boldsymbol{\varepsilon} dt, \quad (39)$$

where \mathbf{P} and \mathbf{Q} are the positive definite matrices.

From equation (39), the velocity of cross-coupling error can be obtained by derivative

$$\dot{\mathbf{e}}^* = \dot{\mathbf{e}} + \mathbf{P}\dot{\boldsymbol{\varepsilon}} + \mathbf{Q}\boldsymbol{\varepsilon}. \quad (40)$$

The reference velocity $\dot{\mathbf{X}}_r$ and acceleration $\ddot{\mathbf{X}}_r$ of the upper platform can be defined as

$$\begin{cases} \dot{\mathbf{X}}_r = \dot{\mathbf{X}}_d + \mathbf{P}\dot{\boldsymbol{\varepsilon}} + \mathbf{Q}\boldsymbol{\varepsilon} + \Lambda\mathbf{e}^*, \\ \ddot{\mathbf{X}}_r = \ddot{\mathbf{X}}_d + \mathbf{P}\ddot{\boldsymbol{\varepsilon}} + \mathbf{Q}\dot{\boldsymbol{\varepsilon}} + \Lambda\dot{\mathbf{e}}^*. \end{cases} \quad (41)$$

Obviously, the reference velocity $\dot{\mathbf{X}}_r$ is indeed very important for real-time modification to achieve the desired trajectory and guarantee the convergence of the tracking error.

Furthermore, the reference velocity error including aforementioned hybrid error (i.e., the switched function) can be defined as

$$\mathbf{S} = \dot{\mathbf{X}}_r - \dot{\mathbf{X}} = \dot{\mathbf{e}} + \mathbf{P}\dot{\boldsymbol{\varepsilon}} + \mathbf{Q}\boldsymbol{\varepsilon} + \Lambda\mathbf{e}^*. \quad (42)$$

The switched function, similar to a sliding surface, can be further simplified considering the relationship (39):

$$\mathbf{S} = \dot{\mathbf{e}}^* - \mathbf{P}\dot{\boldsymbol{\varepsilon}} - \mathbf{Q}\boldsymbol{\varepsilon} + \mathbf{P}\dot{\boldsymbol{\varepsilon}} + \mathbf{Q}\boldsymbol{\varepsilon} + \Lambda\mathbf{e}^* = \dot{\mathbf{e}}^* + \Lambda\mathbf{e}^*, \quad (43)$$

and its differentiation will be

$$\dot{\mathbf{S}} = \dot{\mathbf{e}}^{**} + \Lambda\dot{\mathbf{e}}^*. \quad (44)$$

The robust synchronization control law based on the dynamic feed-forward can be expressed by the following equation:

$$\mathbf{u} = \widehat{\mathbf{M}}\ddot{\mathbf{X}}_r + \widehat{\mathbf{C}}\dot{\mathbf{X}}_r + \widehat{\mathbf{G}} + \mathbf{K}\mathbf{S} + \mathbf{u}_{aux}. \quad (45)$$

In fact, the control law in abovementioned equation contains three terms, namely, the first term is the dynamic compensation term:

$$\mathbf{u}_1 = \widehat{\mathbf{M}}\ddot{\mathbf{X}}_r + \widehat{\mathbf{C}}\dot{\mathbf{X}}_r + \widehat{\mathbf{G}}, \quad (46)$$

where $\widehat{\mathbf{M}}$, $\widehat{\mathbf{C}}$, and $\widehat{\mathbf{G}}$ are the estimated matrices obtained from the matrices \mathbf{M} , \mathbf{C} , and \mathbf{G} , respectively.

The second term is the hybrid error compensation term:

$$\mathbf{u}_2 = \mathbf{K}\mathbf{S}, \quad (47)$$

and it is important to note that the second term can be expanded as

$$\begin{aligned} \mathbf{u}_2 &= \mathbf{K}\mathbf{S} = \mathbf{K} \left(\dot{\mathbf{e}} + \mathbf{P}\dot{\mathbf{e}} + \mathbf{Q}\mathbf{e} + \Lambda \left(\mathbf{e} + \mathbf{P}\mathbf{e} + \mathbf{Q} \int_0^t \mathbf{e} dt \right) \right) \\ &= \mathbf{K}\dot{\mathbf{e}} + \mathbf{K}\Lambda\mathbf{e} + \mathbf{K}\mathbf{P}\dot{\mathbf{e}} + (\mathbf{K}\mathbf{Q} + \mathbf{K}\Lambda\mathbf{P})\mathbf{e} + \mathbf{K}\Lambda\mathbf{Q} \int_0^t \mathbf{e} dt, \end{aligned} \quad (48)$$

where \mathbf{u}_2 contains PD control and PID control, and \mathbf{u}_2 is of crucial importance to improve tracking accuracy performance. In other words, PD control can eliminate the tracking errors, and PID control can eliminate the synchronization errors.

The third term is the robust compensation term that can improve the system stability in the presence of disturbance and uncertainties [41]:

$$\mathbf{u}_3 = \mathbf{u}_{aux}, \quad (49)$$

where \mathbf{u}_{aux} denotes the auxiliary robust control law, and \mathbf{u}_{aux} has three types of manner, as follows:

$$\mathbf{u}_{1aux} = \rho \frac{\mathbf{S}}{\|\mathbf{S}\|}, \quad (50)$$

where ρ is positive scalar, and $\mathbf{S}/\|\mathbf{S}\|$ is a symbolic function (i.e., sliding surface function) whose variation range is from -1 to 1 , so the system is also termed adaptive robust synchronous sliding mode control (AS-SMC).

$$\mathbf{u}_{2aux} = \frac{1}{\delta} \rho^2 \mathbf{S}, \quad (51)$$

where δ is positive scalar, and the smaller δ is, the bigger \mathbf{u}_{2aux} is, so it is called adaptive robust synchronous high gain control, or AS-High Gain for short.

$$\mathbf{u}_{3aux} = \frac{\rho^2 \mathbf{S}}{\rho \|\mathbf{S}\| + \delta}, \quad (52)$$

\mathbf{u}_{3aux} is compared with \mathbf{u}_{1aux} , if constant $\delta = 0$, then $\mathbf{u}_{3aux} = \mathbf{u}_{1aux}$. So \mathbf{u}_{1aux} is the special case of \mathbf{u}_{3aux} . If the constant $\delta > 0$, then \mathbf{u}_{3aux} compared with \mathbf{u}_{1aux} illustrates that the former has a small fluctuation range, and more

importantly its variation range is within -1 to 1 . Coincidentally, it also increases the frequency of vibration, so it is called adaptive robust synchronous high-frequency control or AS-High Frequency for short.

In a similar manner with (32), the following dynamic control equation can be written as a linear parameterization form with respect to these parameters:

$$\mathbf{M}\ddot{\mathbf{X}}_r + \mathbf{C}\dot{\mathbf{X}}_r + \mathbf{G} = \mathbf{Y}(\dot{\mathbf{X}}_r, \ddot{\mathbf{X}}_r, \dot{\mathbf{X}}, \mathbf{X})\Theta. \quad (53)$$

Then the linear parameterization of the dynamic equation enables us to derive

$$\widehat{\mathbf{M}}\ddot{\mathbf{X}}_r + \widehat{\mathbf{C}}\dot{\mathbf{X}}_r + \widehat{\mathbf{G}} = \mathbf{Y}(\dot{\mathbf{X}}_r, \ddot{\mathbf{X}}_r, \dot{\mathbf{X}}, \mathbf{X})\widehat{\Theta}, \quad (54)$$

where $\widehat{\Theta}$ denotes the estimated values (time-varying) for the parameter vector Θ , and the parameter estimation error $\widetilde{\Theta}$ can be described by

$$\widetilde{\Theta} = \widehat{\Theta} - \Theta. \quad (55)$$

Consequently, the control law can be also described with regression matrix, i.e.,

$$\mathbf{u} = \mathbf{Y}(\dot{\mathbf{X}}_r, \ddot{\mathbf{X}}_r, \dot{\mathbf{X}}, \mathbf{X})\widehat{\Theta} + \mathbf{K}\mathbf{S} + \mathbf{u}_{aux}. \quad (56)$$

We now turn our attention to analyzing the stability of the closed system with the Lyapunov function candidate

$$V(t) = \frac{1}{2} \mathbf{S}^T \mathbf{M} \mathbf{S} + \frac{1}{2} \widetilde{\Theta}^T \Gamma^{-1} \widetilde{\Theta}. \quad (57)$$

The differentiation of $V(t)$ with respect to time leads to

$$\dot{V}(t) = \mathbf{S}^T \left[\dot{\mathbf{M}} \mathbf{S} + \frac{1}{2} \dot{\mathbf{M}} \mathbf{S} \right] + \widetilde{\Theta}^T \Gamma^{-1} \dot{\widetilde{\Theta}}. \quad (58)$$

Considering the relation in equations (41), (43), (53), and (54) yields

$$\begin{aligned} \mathbf{M}\ddot{\mathbf{X}}_r + \mathbf{C}\dot{\mathbf{X}}_r - (\widehat{\mathbf{M}}\ddot{\mathbf{X}}_r + \widehat{\mathbf{C}}\dot{\mathbf{X}}_r) &= \mathbf{M}\dot{\mathbf{s}} + \mathbf{C}\mathbf{s} \\ &= \mathbf{Y}(\dot{\mathbf{X}}_r, \ddot{\mathbf{X}}_r, \dot{\mathbf{X}}, \mathbf{X})\Theta - \mathbf{F}_X. \end{aligned} \quad (59)$$

So the time derivative of $V(t)$ can be further expressed as

$$\begin{aligned} \dot{V}(t) &= \mathbf{S}^T \left[\dot{\mathbf{M}} \mathbf{S} + \frac{1}{2} \dot{\mathbf{M}} \mathbf{S} \right] + \widetilde{\Theta}^T \Gamma^{-1} \dot{\widetilde{\Theta}} \\ &= \mathbf{S}^T \left[\mathbf{Y}(\dot{\mathbf{X}}_r, \ddot{\mathbf{X}}_r, \dot{\mathbf{X}}, \mathbf{X})\Theta - \mathbf{F}_X \right] + \frac{1}{2} \mathbf{S}^T (\dot{\mathbf{M}} - 2\mathbf{C}) \mathbf{S} + \widetilde{\Theta}^T \Gamma^{-1} \dot{\widetilde{\Theta}} \\ &= \mathbf{S}^T \left[\mathbf{Y}(\dot{\mathbf{X}}_r, \ddot{\mathbf{X}}_r, \dot{\mathbf{X}}, \mathbf{X})\Theta - \mathbf{F}_X \right] + \widetilde{\Theta}^T \Gamma^{-1} \dot{\widetilde{\Theta}}, \end{aligned} \quad (60)$$

where the skew symmetry of $\dot{\mathbf{M}} - 2\mathbf{C}$ can be utilized to eliminate the term $(1/2)\mathbf{S}^T \dot{\mathbf{M}} \mathbf{S}$ which reflects the time-varying nature of the inertia matrix.

Substituting the control law (54) in the above equation, we obtain

$$\dot{V}(t) = -\mathbf{S}^T \mathbf{K} \mathbf{S} - \mathbf{S}^T \mathbf{u}_{aux} - \mathbf{S}^T \mathbf{Y}(\dot{\mathbf{X}}_r, \ddot{\mathbf{X}}_r, \dot{\mathbf{X}}, \mathbf{X})\widetilde{\Theta} + \widetilde{\Theta}^T \Gamma^{-1} \dot{\widetilde{\Theta}}. \quad (61)$$

It is worth noting that the following relation can be utilized:

$$[\mathbf{S}^T \mathbf{Y}(\dot{\mathbf{X}}_r, \ddot{\mathbf{X}}_r, \dot{\mathbf{X}}, \mathbf{X}) \tilde{\Theta}]^T = \mathbf{S}^T \mathbf{Y}(\dot{\mathbf{X}}_r, \ddot{\mathbf{X}}_r, \dot{\mathbf{X}}, \mathbf{X}) \tilde{\Theta}. \quad (62)$$

The result can be further derived as

$$\dot{V}(t) = -\mathbf{S}^T \mathbf{K} \mathbf{S} - \mathbf{S}^T \mathbf{u}_{aux} - \tilde{\Theta}^T [\mathbf{Y}(\dot{\mathbf{X}}_r, \ddot{\mathbf{X}}_r, \dot{\mathbf{X}}, \mathbf{X})^T \mathbf{s} - \Gamma^{-1} \dot{\tilde{\Theta}}]. \quad (63)$$

Let $\mathbf{Y}(\dot{\mathbf{X}}_r, \ddot{\mathbf{X}}_r, \dot{\mathbf{X}}, \mathbf{X})^T \mathbf{S} - \mathbf{S}^T \mathbf{u}_{aux} - \Gamma^{-1} \dot{\tilde{\Theta}} = 0$ satisfy.

Then, one can obtain

$$\dot{\tilde{\Theta}} = \Gamma \mathbf{Y}(\dot{\mathbf{X}}_r, \ddot{\mathbf{X}}_r, \dot{\mathbf{X}}, \mathbf{X})^T \mathbf{s}. \quad (64)$$

The adaptive law, i.e., the unknown dynamic parameters, can be estimated with

$$\dot{\hat{\Theta}} = \dot{\tilde{\Theta}} = \Gamma \mathbf{Y}(\dot{\mathbf{X}}_r, \ddot{\mathbf{X}}_r, \dot{\mathbf{X}}, \mathbf{X})^T \mathbf{s}. \quad (65)$$

Equation (63) is finally reduced to

$$\dot{V}(t) = -\mathbf{S}^T \mathbf{K} \mathbf{S} - \mathbf{S}^T \mathbf{u}_{aux} \leq 0. \quad (66)$$

As \mathbf{K} is a positive definite matrix, so $\dot{V}(\mathbf{0}) = 0$ and $\dot{V}(t) \leq 0$ which is proved to be a seminegative definite matrix. The sliding surface \mathbf{S} will asymptotically converge to zero, $t \rightarrow \infty$, and $\mathbf{S} = \mathbf{0}$. From equations (39) and (40), we can see that \mathbf{e}^* will be asymptotically zero, $\dot{\mathbf{e}}^*$ also converges to zero. Furthermore, from equation (37), $\boldsymbol{\varepsilon}$, $\dot{\boldsymbol{\varepsilon}}$, \mathbf{e} , and $\dot{\mathbf{e}}$ will converge to zero, and the upper platform can asymptotically track a desired trajectory in the Cartesian space, i.e., $\mathbf{X} \rightarrow \mathbf{X}_d$, the closed-loop system will be globally stable within finite time.

It is worth noting that the involved manipulator is a redundantly actuated parallel manipulator, so the driving force is redundant, which leads to multiple solutions of the input driving force. In order to reduce the internal force and improve the system control accuracy, the driving force is required to optimize and choose the optimal solution from multiple solutions. Herein, aiming at the minimum driving force value and reducing the internal force of the manipulator, the Euclidean norm of the driving force is selected to optimize the driving force. The optimized objective function can be expressed as

$$f = \boldsymbol{\tau}_a^T \mathbb{N} \boldsymbol{\tau}_a, \quad (67)$$

where $\boldsymbol{\tau}_a$ is the driving forces vector exerted on the actuated joints, and \mathbb{N} is the harmonious matrix of the actuator motors.

The optimization is constrained by the condition that linear mapping relationship between the actuated joint force and corresponding Cartesian space force, namely,

$$\mathbf{F}_X = \mathbf{J}_0^T \boldsymbol{\tau}_a. \quad (68)$$

The equation can be constructed by the Lagrange equation:

$$\bar{f} = \boldsymbol{\tau}_a^T \mathbb{N} \boldsymbol{\tau}_a + \lambda (\mathbf{F}_X - \mathbf{J}_0^T \boldsymbol{\tau}_a). \quad (69)$$

Partial derivative of the abovementioned equation (77) yields

$$\begin{cases} \frac{\partial \bar{f}}{\partial \boldsymbol{\tau}_a} = 2\boldsymbol{\tau}_a \mathbb{N} - \lambda \mathbf{J}_0^T, \\ \frac{\partial \bar{f}}{\partial \lambda} = \mathbf{F}_X - \mathbf{J}_0^T \boldsymbol{\tau}_a. \end{cases} \quad (70)$$

Let the partial derivative be equal to zero and find the extreme value

$$\begin{cases} \boldsymbol{\tau}_a = \frac{1}{2} \mathbb{N}^{-T} \mathbf{J}_0 \lambda^T, \\ \mathbf{F}_X = \mathbf{J}_0^T \boldsymbol{\tau}_a. \end{cases} \quad (71)$$

Combining the above two equations in (71) leads to

$$\mathbf{F}_X = \frac{1}{2} \mathbf{J}_0^T \mathbb{N}^{-T} \mathbf{J}_0 \lambda^T. \quad (72)$$

One can express with another form as well, namely,

$$\lambda^T = 2(\mathbf{J}_0^T \mathbb{N}^{-T} \mathbf{J}_0)^{-1} \mathbf{F}_X. \quad (73)$$

Substituting equation (73) in the first equation of (71), one can obtain the optimal driving force:

$$\boldsymbol{\tau}_a = \mathbb{N}^{-T} \mathbf{J}_0 (\mathbf{J}_0^T \mathbb{N}^{-T} \mathbf{J}_0)^{-1} \mathbf{F}_X = \mathbf{J}_0 (\mathbf{J}_0^T \mathbf{J}_0)^{-1} \mathbf{F}_X. \quad (74)$$

Therefore, the control law in actuated joints space can be described as

$$\boldsymbol{\tau}_a = \mathbf{J}_0 (\mathbf{J}_0^T \mathbf{J}_0)^{-1} \mathbf{F}_X = \mathbf{J}_0 (\mathbf{J}_0^T \mathbf{J}_0)^{-1} \mathbf{u}. \quad (75)$$

Finally, the overall diagram of the proposed control scheme is described in Figure 4, from which one can see that the control scheme consists of three main parts.

The desired trajectory parameter \mathbf{X}_d can be obtained once the trajectory function is given, while the actual operational task space parameter \mathbf{X} can be obtained with two methods. One is forward kinematics in which the position of the actuated joints are once known, then the position and orientations of the moving platform can be obtained by adopting the back propagation (BP) neural network optimization method or Newton-Raphson iteration, which converges rather quickly when the initial value is close to the desired solution [42]. However, the solving procedure of forward kinematics is very complicated and the computational efficiency is very low. The other efficient method to require the position and orientations of the moving platform is exactly what we want to introduce in this paper [43–45]. We know that the position z of the moving platform can be straightforwardly obtained by the position sensor, yet the rotational Euler angles cannot be required easily, maybe the angular velocity can be obtained by gyroscope sensor, but it is of no use in calculation. The rotation matrix \mathbf{R} defining the orientation of the moving platform with respect to the fixed coordinate system can be avaiably obtained by the camera sensor technique. We can obtain the rotational Euler angles α and β by interfacing with *MATLAB Stereo Camera*

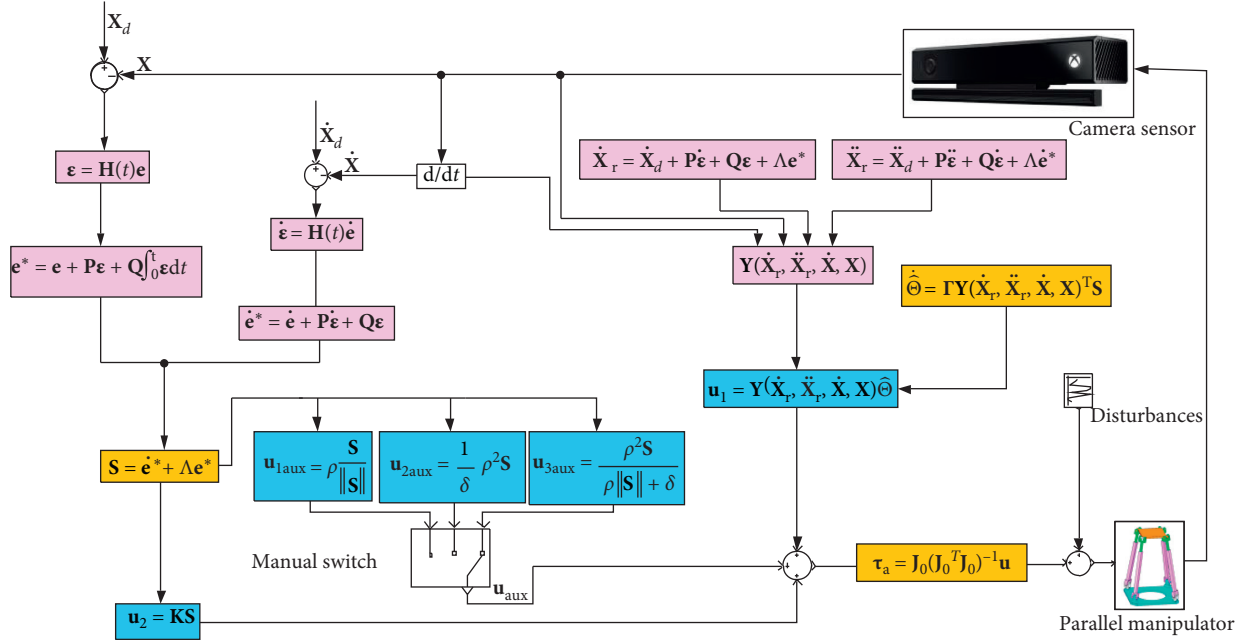


FIGURE 4: The proposed three adaptive robust synchronous control diagram of parallel manipulator.

Calibrator Toolbox [46] with equation (2), and the position distance can be figured out in real time on the personal computer. It is computationally simple, and it does not require measurement of the end-effector velocity and acceleration as well. The advantage of proposed simplified method can efficiently avoid the complex forward kinematics.

6. Simulation Analysis Tests

The parallel manipulator system in real environment is fabricated as shown in Figure 5, which mainly consists of a parallel manipulator, a U2D (or USB2Dynamixel, which is a small size USB communication converter that enables to control and to operate the Dynamixel with the personal computer) controller, a personal computer and a binocular camera (herein, binocular stereo vision technology are not discussed temporarily). The parallel manipulator can move by changing the rotation angles of four smart actuators (Dynamixel MX-12W, which is a high-performance actuator with a fully integrated DC motor, reduction gearhead, controller, driver, and network, all in one servo module actuator). The real position and velocity of the four actuators will be transmitted to the computer for data monitoring and implementing control in real time.

The Dynamixel actuator needs to be calibrated before the experiment and connected the personal computer through U2D (or USB2Dynamixel). The actuator information can be modified in terms of the software *RoboPlus*, and the information can be updated in *Dynamixel Wizard* modular, as shown in Figure 6. Some more information can be obtained on the *ROBOTIS e-Manual* [47]. In addition, the camera also needs to be calibrated with a square chessboard; when a sequence of different chessboard images are given, we can obtain the camera information (such as camera position and camera matrix) so as to detect the position and orientation of

the parallel manipulator. More information has been addressed in [48] where the authors proposed an automatic calibration algorithm by virtue of the two Hough transform, image corners, and invariant properties of the perspective transformation to determine the calibration points from a sequence of different images, and herein we do not discuss this issue in detail.

However, to validate the performance of the proposed controllers, first of all, the control schemes for the parallel manipulator are implemented within SimMechanics Toolbox environment, and the experimental tests will be executed in next paper. The simplified structural parameters of the 2RPU-2SPR parallel manipulator are listed in Table 1. Meanwhile, the constant parameters implemented in the three robust controllers are presented in Table 2.

To show the performance of the three robust controllers proposed in this paper, a challenging reference trajectory was developed. Specifically, the desired trajectory function of the moving platform generated by the following equations:

$$\begin{cases} \alpha(t) = \frac{\pi}{6} \sin(2t), \\ \beta(t) = \frac{\pi}{6} \cos(2t), \\ z(t) = 0.5 + 0.04t. \end{cases} \quad (76)$$

The initial position and orientation of the moving platform is $[z \ \alpha \ \beta]^T = [0.7 \ 0 \ 0]^T$, the simulation time is 8 seconds, the sampling time of the control system is 1 millisecond, and the solver is ode4 (Runge-Kutta) in Simulink, respectively.

The comparative experiments are carried out for the above three controllers. Figure 7 illustrates the desired

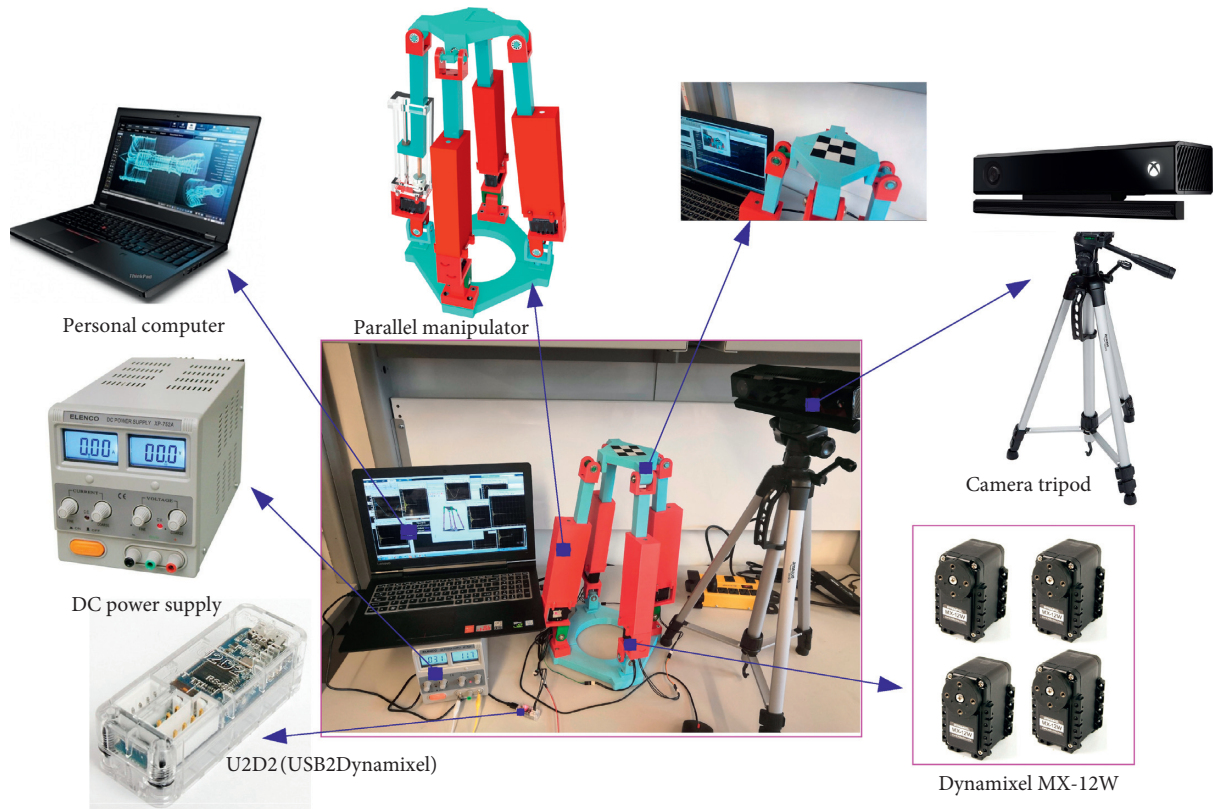


FIGURE 5: The simulation and experimental platform of the parallel manipulator.

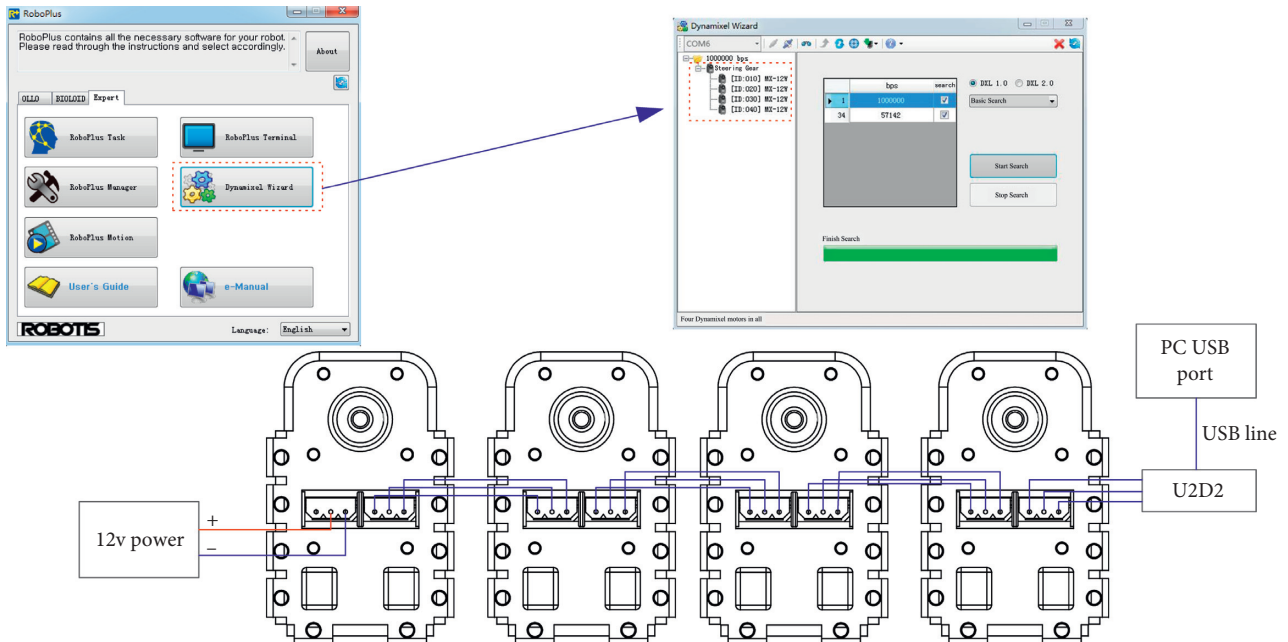


FIGURE 6: The schematic diagram of Dynamixel actuator calibration.

trajectory in the Cartesian space, the black dot indicates the starting point, and the desired trajectories of three degrees of freedom in the Cartesian space are depicted in Figure 8, respectively. From these results, it can be seen that the proposed three controllers can make the tracking error for

the desired trajectory globally asymptotically stable and achieve good trajectory tracking performance in the Cartesian space, since the unknown parameters can be accurately estimated by the adaptive law and then compensate with the PID and PD feed-forward linear control method.

TABLE 1: Structural parameters of the parallel manipulator.

Parameter	Description	Value
r_a	The radius of the moving platform	0.2 m
r_b	The radius of the fixed platform	0.339 m
m_a	The mass of the moving platform	12.75 kg
e_1	The distance between centroid and B_i joint	0.23 m
e_2	The distance between centroid and A_i joint	0.22 m
I_p	The inertia matrix of moving platform	$0.1 \times \text{diag}\{0.77, 1.07, 1.83\} \text{ kg}\cdot\text{m}^2$
m_1	The mass of the lower sublimb	0.95 kg
I_1	The inertia matrix of the lower sublimb	$0.01 \times \text{diag}\{2.88, 2.89, 0.05\} \text{ kg}\cdot\text{m}^2$
m_2	The mass of the upper sublimb	1.1 kg
I_2	The inertia matrix of the upper sublimb	$0.01 \times \text{diag}\{2.65, 2.67, 0.03\} \text{ kg}\cdot\text{m}^2$
g	The gravity acceleration	$[0, 0, -9.81]^T \text{ m/s}^2$

TABLE 2: Control gains of the utilized controllers.

Parameter	Value
P	$\text{diag}\{0.3, 0.3, 0.3\}$
Q	$\text{diag}\{0.5, 0.5, 0.5\}$
K	$\text{diag}\{600, 300, 300\}$
Λ	$\text{diag}\{100, 50, 50\}$
ρ	10
δ	0.5

The tracking errors in the Cartesian space of three controllers are presented in Figure 9. The position errors and orientation errors are drawn respectively, and the proposed controllers applied to the parallel manipulator for the prescribed trajectory tracking control are available. When the control system reaches a steady state, the errors will decrease gradually to zero, although the errors oscillated at the beginning or within some certain time. It is worth noting that AS-SMC and AS-High Frequency have better tracking performance than the AS-High Gain, especially on the z axis, i.e., the tracking error e_1 . Furthermore, AS-SMC has an equivalent or approximate equivalent tracking performance with AS-High Frequency.

In addition, the synchronous errors in the Cartesian space of three controllers are presented in Figure 10. By comparing the synchronous tracking performance ε_1 and ε_3 , we find that three controllers have approximate equivalent variation period and sustained time. But from the synchronous tracking error ε_2 , it can be seen that the AS-High Gain has great effect on the orientation tracking error in the Cartesian space but increase the synchronization error significantly. That is to say, AS-High Gain relies on high gain to adjust the error to achieve the goal of tracking.

The cross-coupling errors of three controllers are depicted in Figure 11. It is interesting to note that the influence laws are similar to trajectory tracking errors. In Figure 11, it is also clear that the change of the cross-coupling errors always causes a sharp increase before the cross-coupling errors converge to a very small value or less than a small value closer to zero. The developed AS-SMC and AS-High Frequency controllers show remarkable cross-coupling performances superior to AS-High Gain control scheme in three-degree-of-freedom directions.

The trajectory tracking errors are not only of importance in Cartesian space, but also important in joint space. The

tracking errors in joint space are illustrated in Figure 12, which shows the experimental trajectory tracking results in each prismatic joint for all the three controllers. We hope that all the actuated joints can be controlled to move in a synchronous way. Otherwise, a sudden impact may occur to damage the mechanical structures. In Figure 12, we can see that the errors of the actuated joints are very small, and the variation mainly appears within 0.5 seconds. In the next 7.5 seconds, the errors almost approach zero approximately, which demonstrates that the designed controllers have the advantage of quick response speed and excellent trajectory tracking results. In addition, the difference between AS-SMC and AS-High Frequency controllers is almost imperceptible, and the AS-High Gain controller is restricted to a large vicinity of the zero. All the tracking errors were limited to a small region with deviation from zero. The tracking errors are not leaving the zone as shown in Figure 12.

Similarly, the force tracking errors are very important to validate the controller performance and the simulation results including four actuators in joint space are illustrated in Figure 13. We should notice that the rand disturbances (for example, frictions, noises, clearances, wears, and so on.) are considered in the simulation process. Herein, we assume that the lumped uncertainty obeys discrete uniform random distribution, i.e.,

$$\tau'_d \in \text{unifrnd}(\mu, \sigma), \quad (77)$$

where unifrnd random obeys the discrete uniform distribution, μ is the minimum value, and σ is the maximum value. Herein, we define $\mu = -5$, $\sigma = 5$.

Further, we can see that the force tracking errors deviate from zero dramatically and they are driven back to the steady state fast after 0.5 seconds. However, the errors have a large fluctuation within 0.5 seconds, especially in the third picture with the AS-High Gain controller. The unexpected dash may destroy the structural components, so we should improve significantly and pay attention to this problem in the experimental process. In addition, it can be seen that the AS-High Frequency controller achieves the best force tracking performance from the experimental results. The tracking errors are relatively stable, since it introduces high-frequency robust technique into the controller design. The AS-High Frequency controller has better effectiveness compared with other controllers to guarantee stability in presence of unknown disturbance.

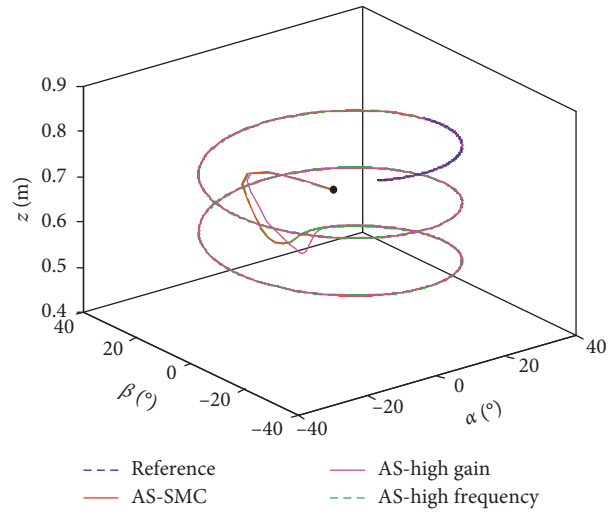
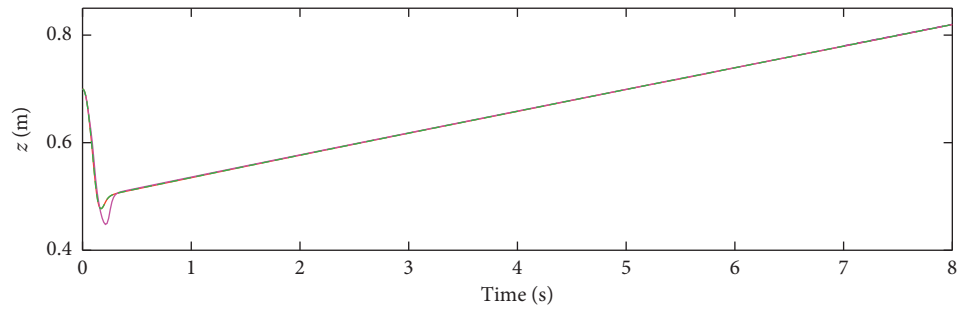
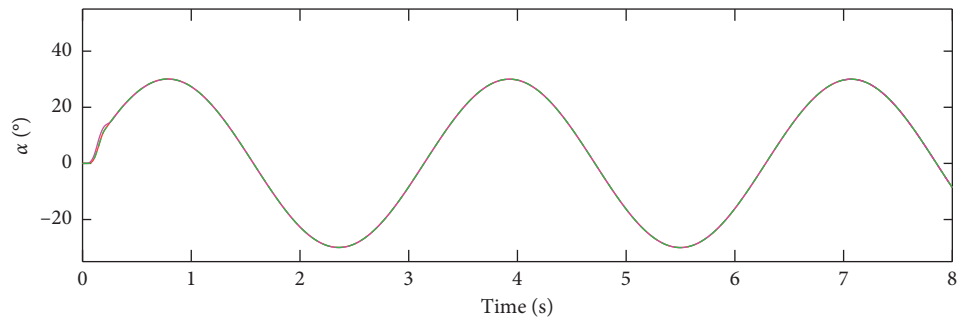


FIGURE 7: Desired trajectory in Cartesian space.



(a)



(b)

FIGURE 8: Continued.

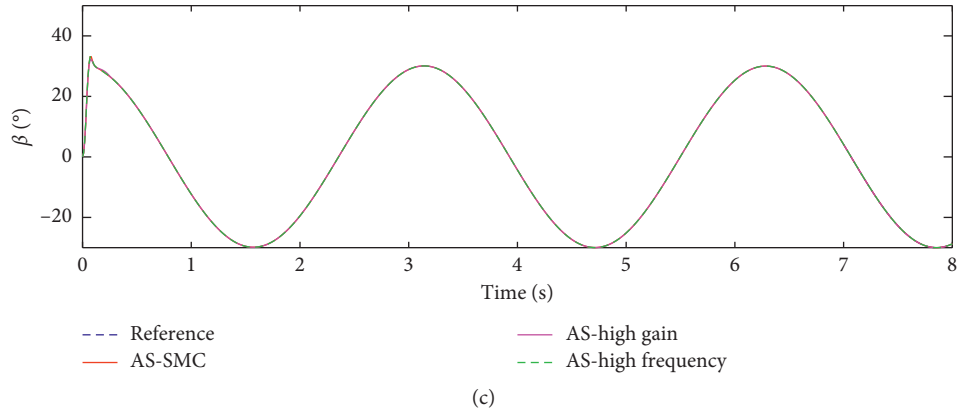


FIGURE 8: Desired trajectory of three degrees of freedom.

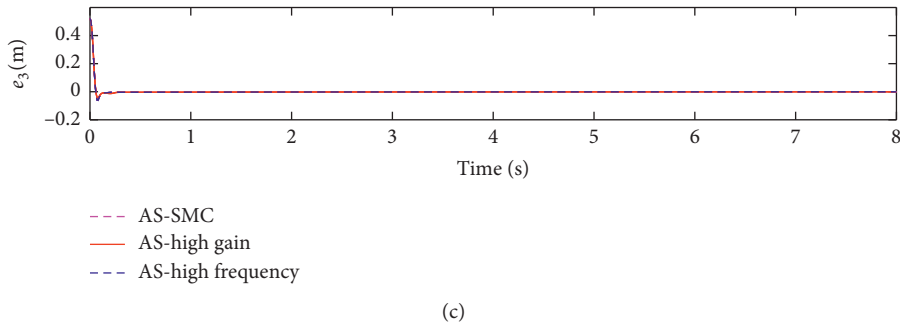
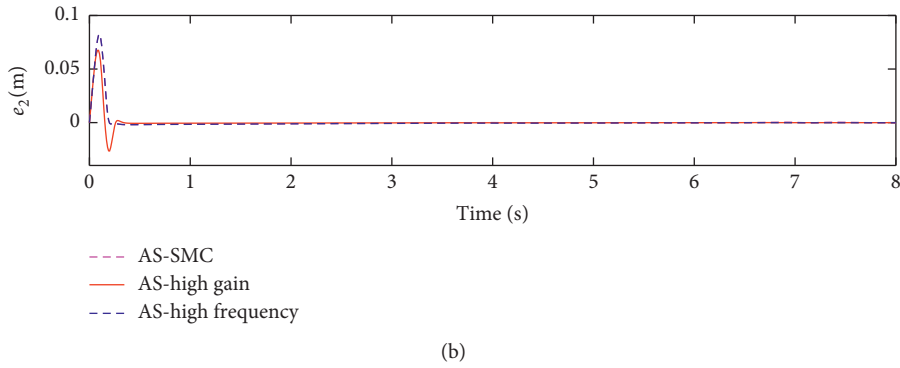
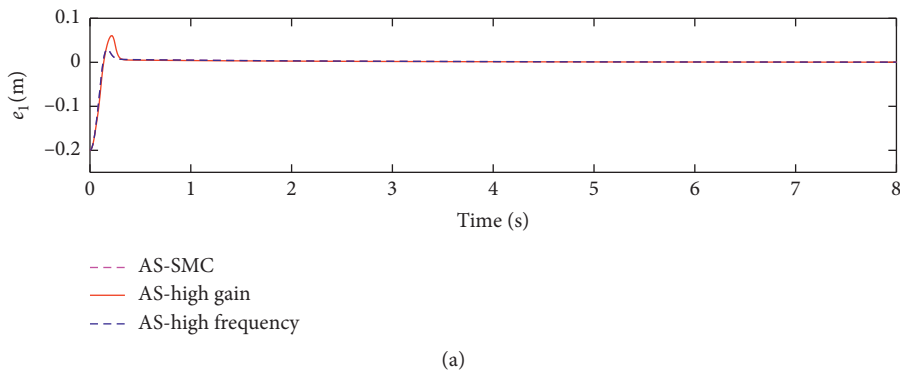


FIGURE 9: The trajectory tracking error.

A closer view to the force tracking errors in joint space is shown in Figure 14, which demonstrates that the AS-High Frequency controller approaches zero more accurately than the two other controllers, especially in the fourth picture. In

general, the steady state is relative, and the errors still display small chattering. Furthermore, the magnitude of the chattering in the error state is directly related to the disturbance terms. Moreover, the AS-High Gain controller has a high

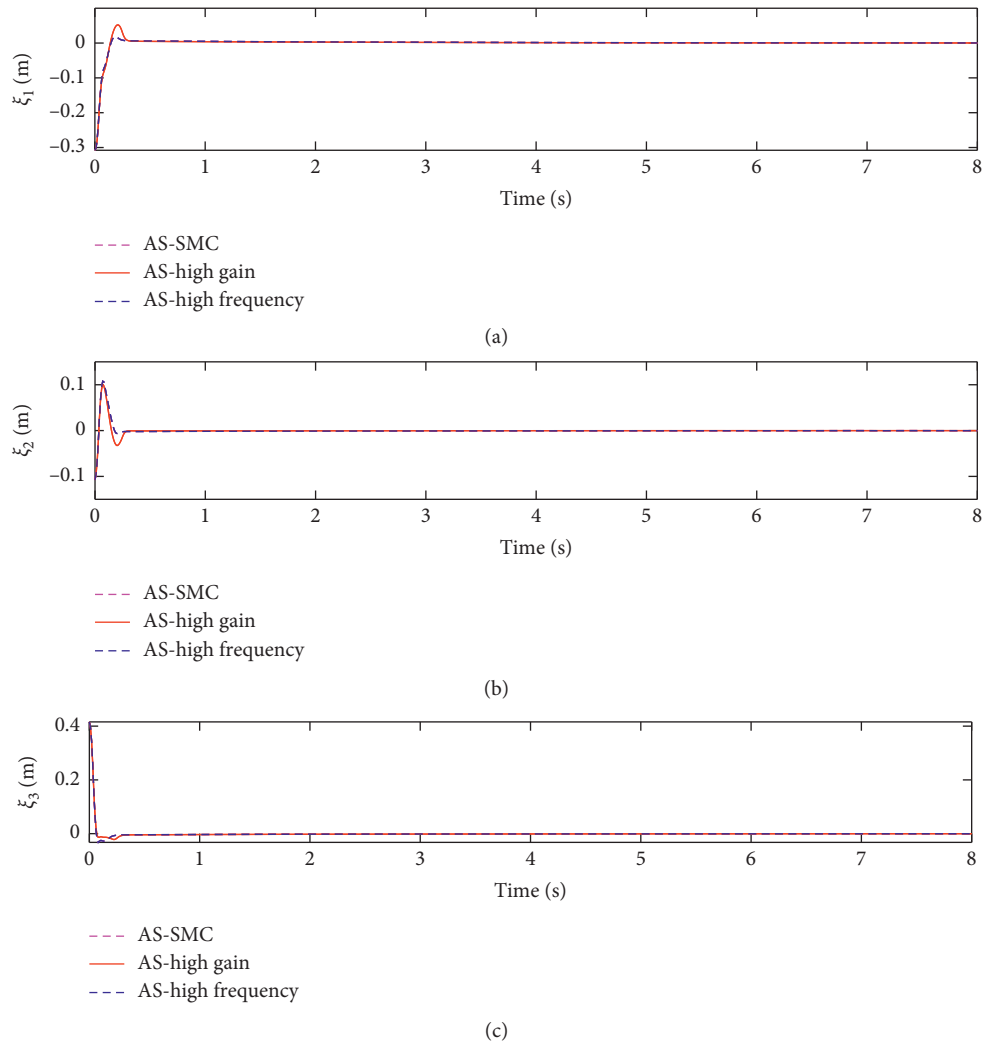


FIGURE 10: The synchronization errors.

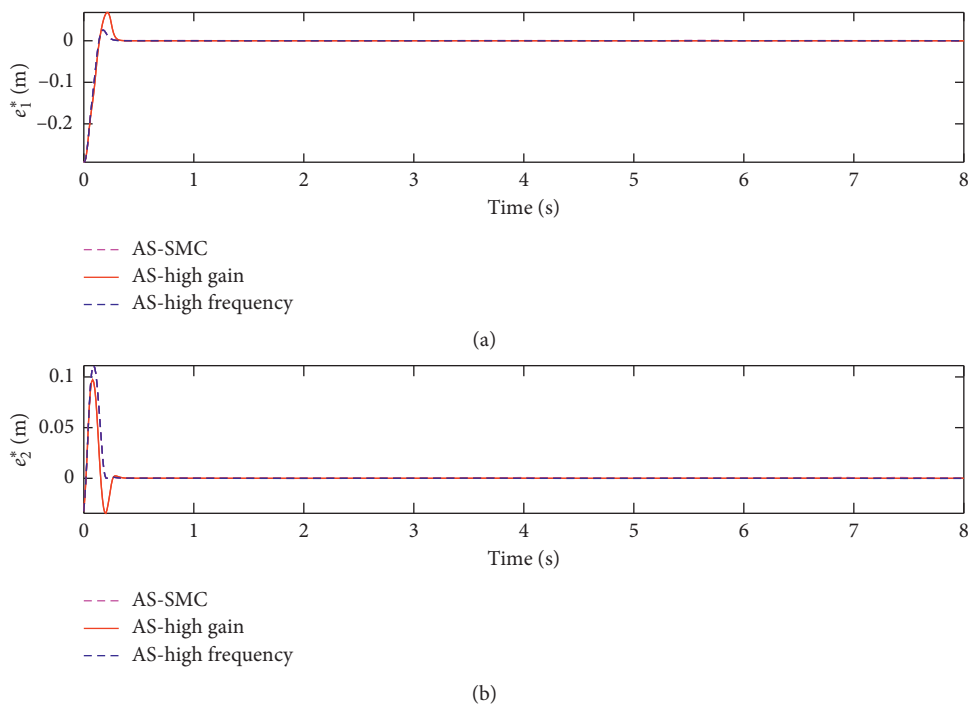


FIGURE 11: Continued.

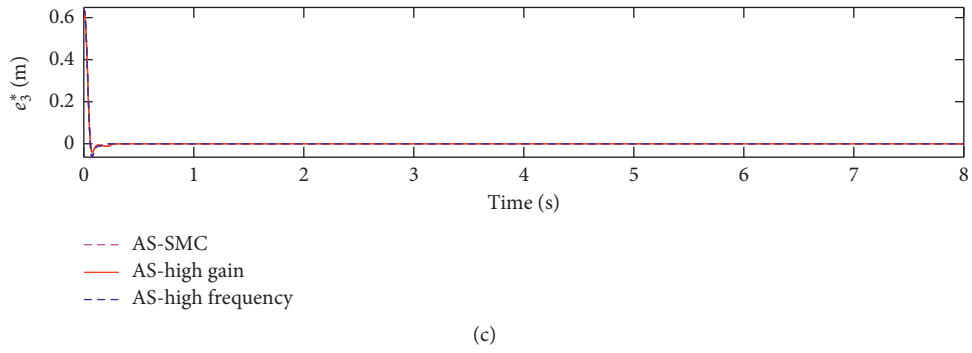


FIGURE 11: The cross-coupling errors.

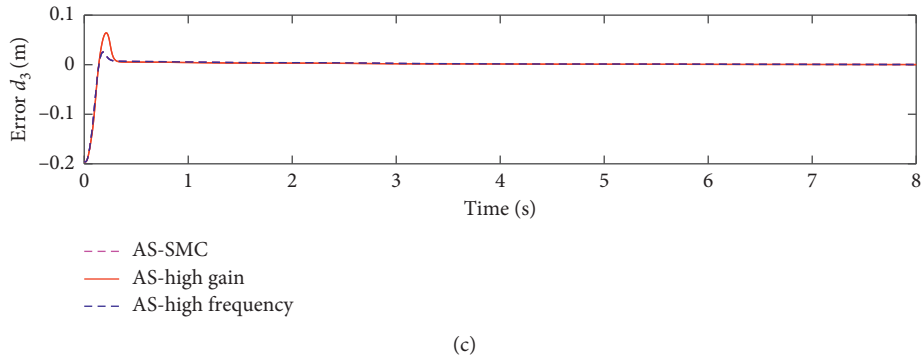
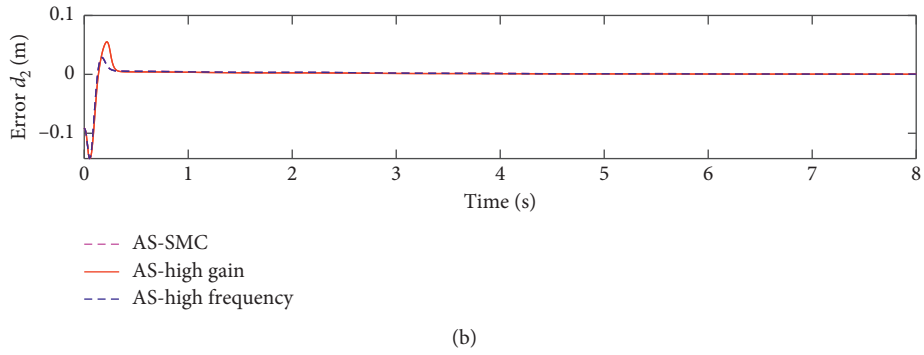
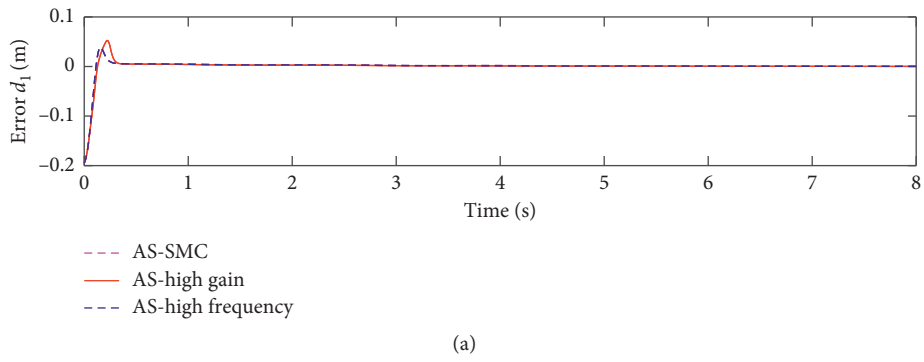
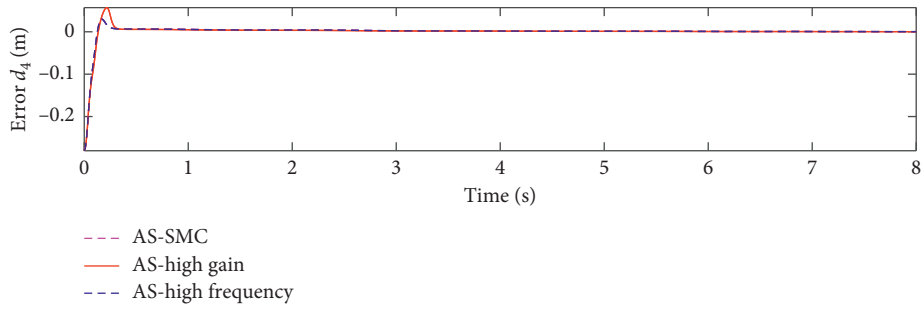
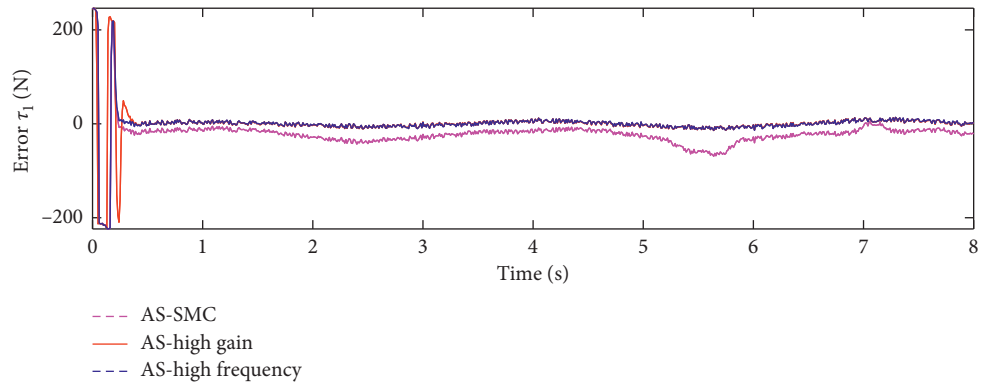


FIGURE 12: Continued.

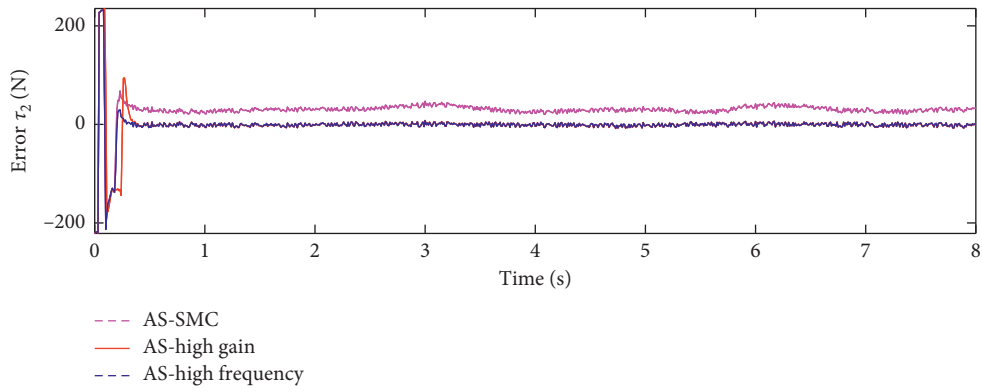


(d)

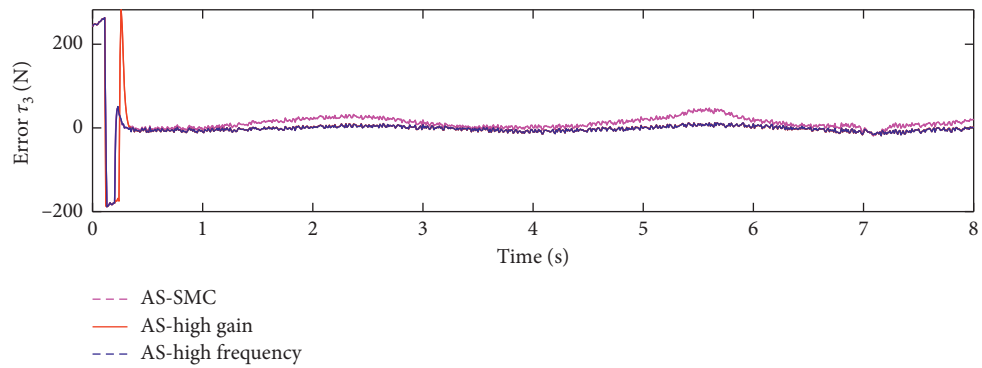
FIGURE 12: The position errors of actuator joints.



(a)



(b)



(c)

FIGURE 13: Continued.

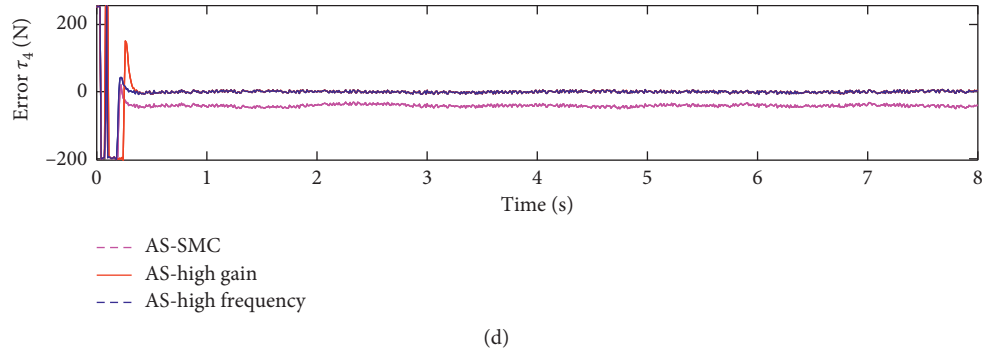


FIGURE 13: The force errors of actuator joints.

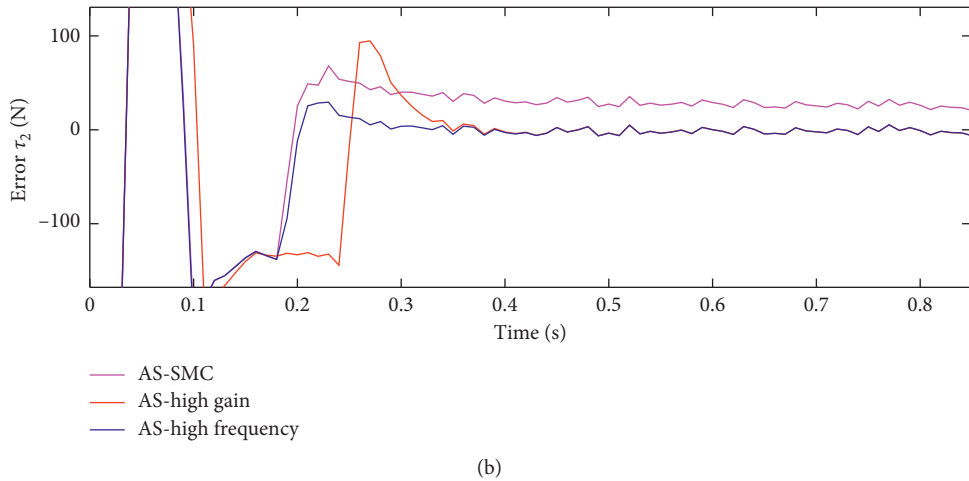
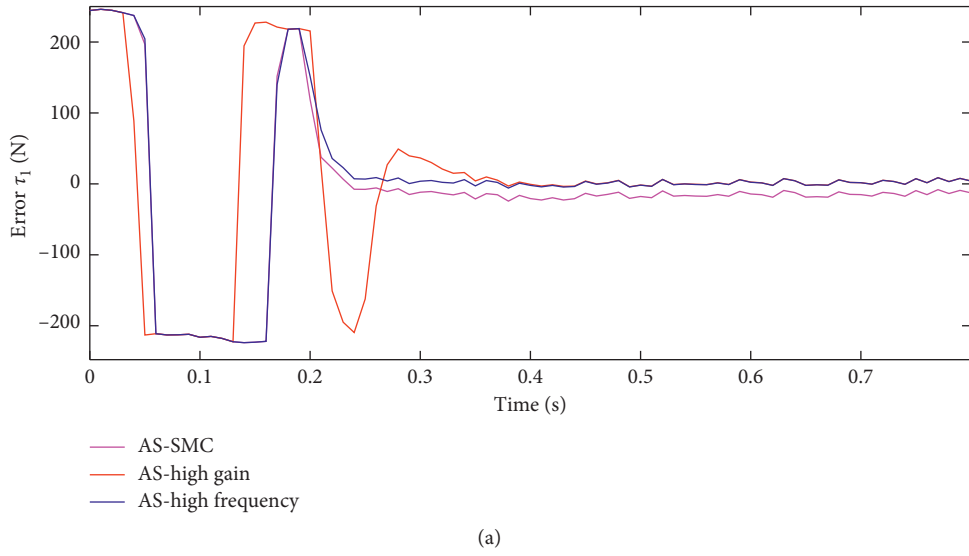
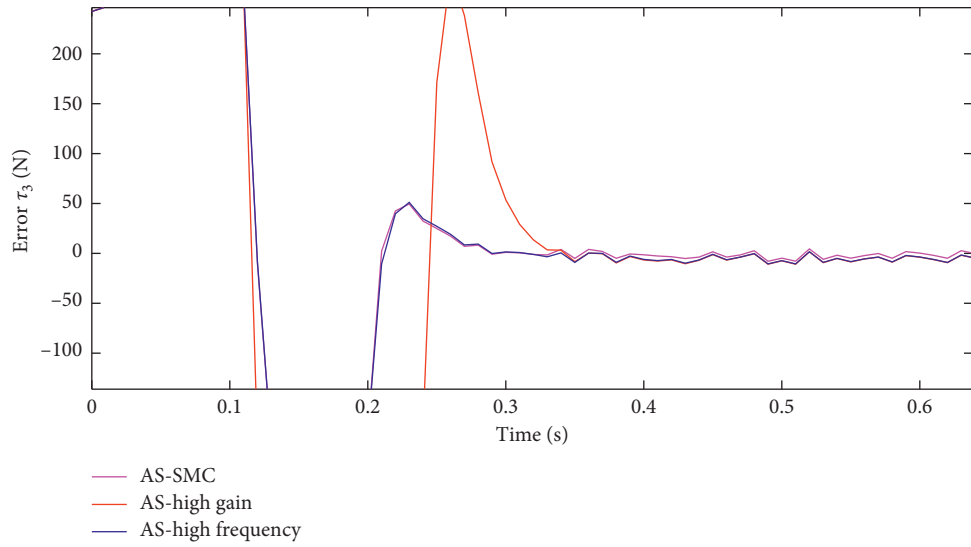
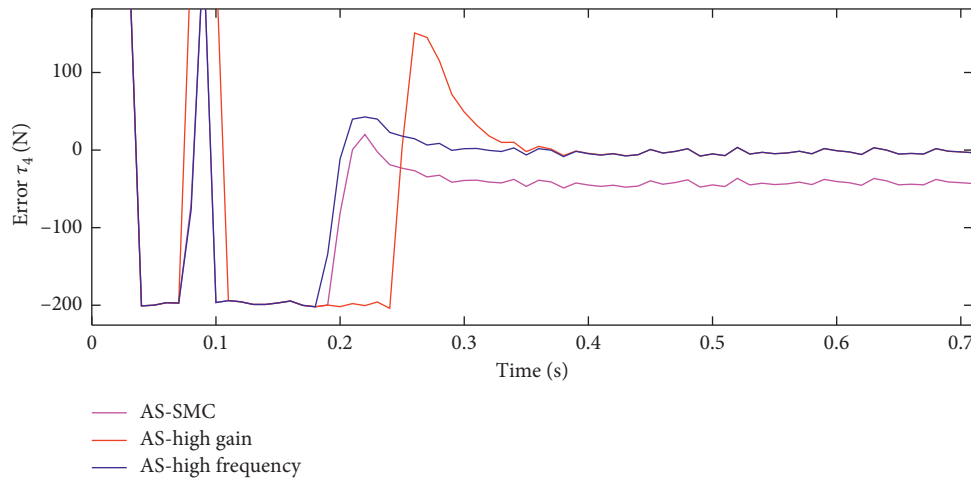


FIGURE 14: Continued.



(c)



(d)

FIGURE 14: The force errors of partial enlargement.

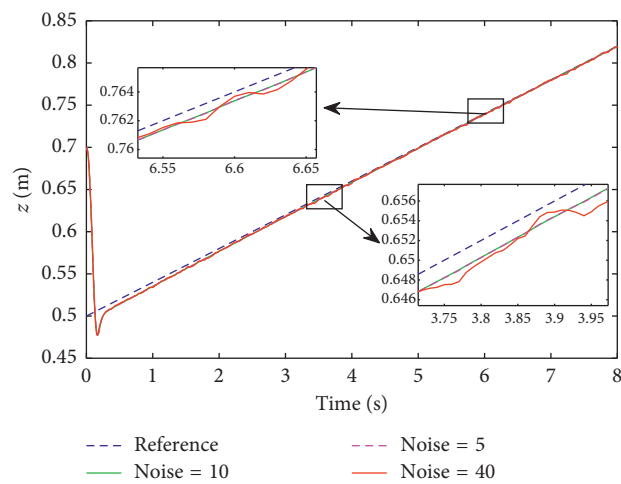


FIGURE 15: The influence of noise disturbances on robustness.

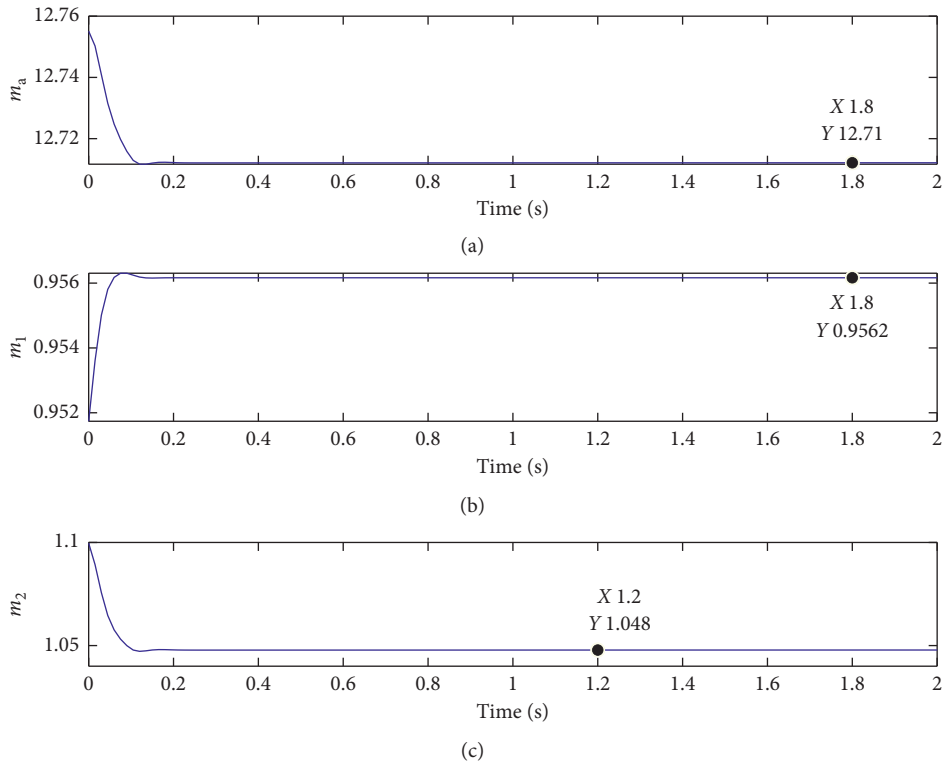


FIGURE 16: The estimated value of mass.

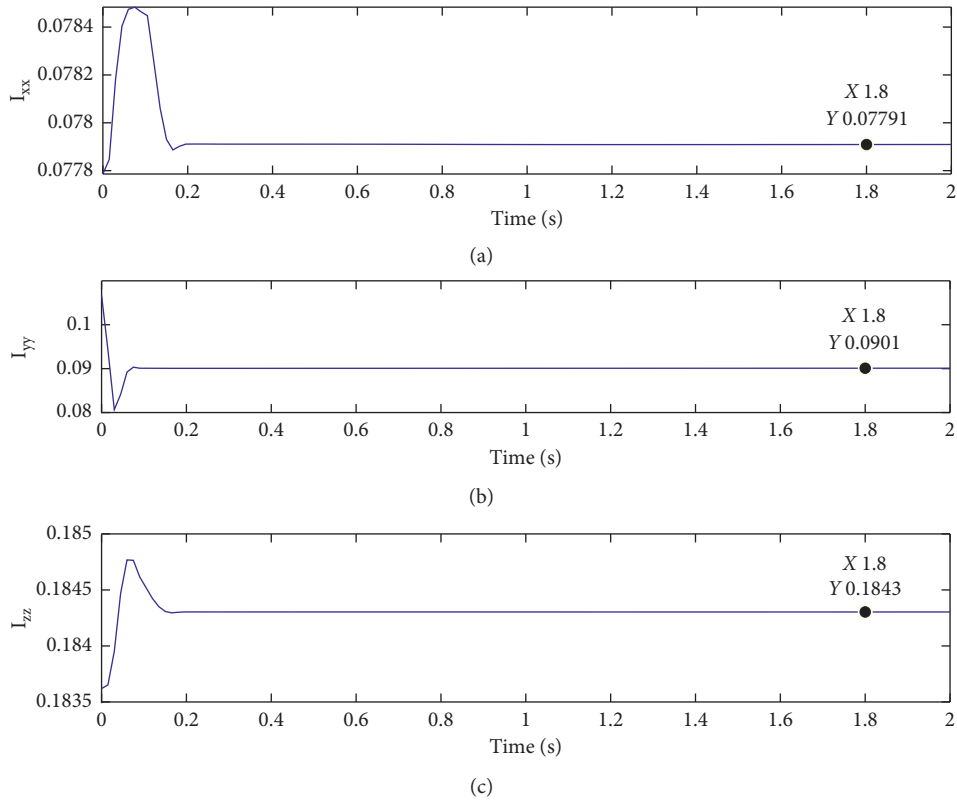


FIGURE 17: The estimated value of the moment of inertia of moving platform.

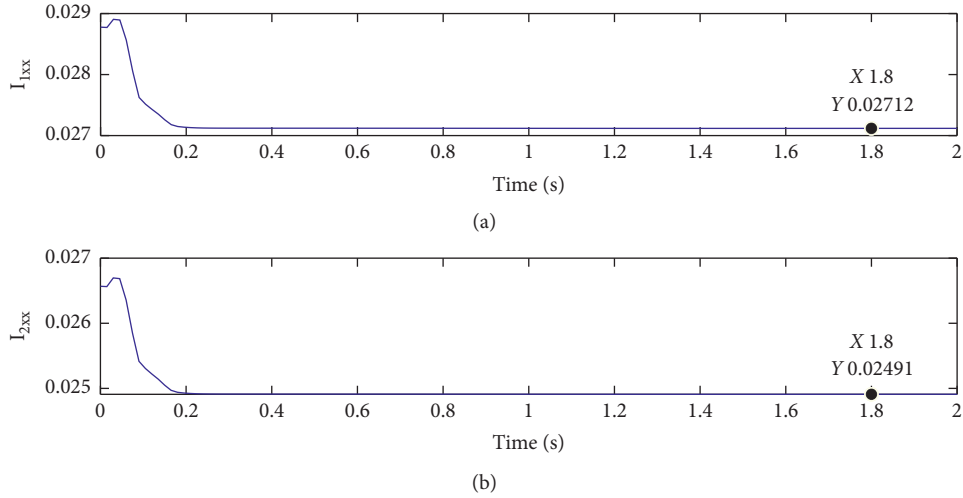


FIGURE 18: The moment of inertia of $I_{xx,1}$ and $I_{xx,2}$.

deviation before it reaches zero asymptotically. However, it is noticeable that the AS-SMC controller has a large variation nearby zero regions in the steady state compared with the AS-High Frequency controller, which illustrates that the AS-SMC controller has a much wider range from zero regions than the AS-High Frequency controller, and these results are actually in accordance with the theoretical analysis. Three controllers have no particular rules in response time, but they are generally compatible systematically. As a whole, the AS-SMC controller has much greater errors, while the AS-High Gain controller has much greater gain before the steady region, so the comparative analysis indicated that the AS-High Frequency controller has much better comprehensive performance.

In addition, the robustness simulation results depicted in Figure 15 demonstrate the reference trajectory tracking in z position direction under the different noise cases, i.e., noise = 5, noise = 10, and noise = 40. The local magnification illustrates that the high-frequency control system has approximate robust performance when the noise = 5 and the noise = 10, while the robust performance will be poor when the noise = 40, which is mainly because the parameter $\rho = 10$, and if the value of noise disturbances is greater than 10, then the robustness will decrease.

From theoretical analysis, we know that adaptive control law has the advantage that the unknown parameter values can be estimated and compensated for by real-time estimation, and the robust terms of the controller can guarantee the system to maintain a considerable state with the presence of unknown external disturbances. Herein, we utilized the AS-High Frequency control to estimate the unknown parameters online. The partial results are shown in Figures 16–18. In Figure 16, the estimated parameter (i.e., m_a m_1 m_2) converges to actual value $[12.71, 0.9562, 1.048]^T$, and the nominal value in Table 1 is $[12.75, 0.95, 1.1]^T$; then the two results are approximately equivalent. In Figure 17, the unknown parameter is the moment of inertia of the moving platform, the estimated values converge to the actual parameter values $[0.07791, 0.0901, 0.1843]^T$, and the nominal values are $[0.077, 0.107, 0.183]^T$. In

Figure 18, the estimated parameter (i.e., I_{1xx} and I_{2xx}) is the moment of inertia in the x direction of the upper limb and lower limb, and steady-state values of the unknown parameters converge to the estimation value $[0.02712, 0.02491]^T$, while the nominal value is $[0.0288, 0.0265]^T$. All the abovementioned estimated results illustrate that the actual values deviate from the nominal values within a small range due to ignoring manufacture tolerances, wear, friction, and so on. However, the proposed AS-High Frequency controller still can achieve satisfactory parameter estimation accuracy even without an accurate dynamic mathematic model, which greatly simplified the calculation process.

7. Conclusions

In this paper, we proposed three types of adaptive robust synchronous controllers for 2RPU-2SPR parallel manipulator with redundant actuation, the controllers are effective and stable when controlling the position and orientations of the platform, and the main contributions are following:

- (1) The inverse kinematic analysis of the parallel manipulator has been formulated firstly, the dynamics formulation is derived in terms of the principle of virtual work, and then the dynamics expression can be further linear parameterization with regression matrix form.
- (2) The three types of adaptive robust synchronous controllers are designed by incorporating the camera sensor technique into adaptive robust synchronous control architecture. Theoretical analysis implies the tracking errors, synchronization errors, and cross-coupling errors can converge to zero as were proved by utilizing the Lyapunov method.
- (3) The simulation tests are conducted to demonstrate that the proposed three controllers can substantially improve the tracking performance when the controllers were implemented in real time. By comparative analysis, the adaptive robust synchronous high-frequency controller showed a better tracking

performance among three controllers. In future works, to achieve higher accuracy for the parallel manipulator, the friction model should be further considered in the design of the controller, and the experiments will be executed on the prototype to verify the performance of the designed controller.

Data Availability

The data used to support the findings of this study are available from the corresponding author upon request.

Conflicts of Interest

The authors declare no conflicts of interest.

Acknowledgments

The authors would like to acknowledge the financial support of the Fundamental Research Funds for the Central Universities under grant nos. 2018JBZ007, 2018YJS136, and 2017YJS158, China Scholarship Council (CSC) under grant no. 201807090079. Meanwhile, Haiqiang Zhang is grateful to advanced robotics and mechatronics laboratory in York University and the science librarian John Dupuis.

References

- [1] D. Zhang, *Parallel Robotic Machine Tools*, Springer, Berlin, Germany, 2010.
- [2] M. D. Tafti, M. M. Moghaddam, and P. Torabi, "Kinematic analysis and mechatronic design of a 3-DOF parallel robot for craniotomy surgery," *Modares Mechanical Engineering*, vol. 17, no. 11, pp. 289–299, 2018.
- [3] L. A. Castaneda, A. Luviano-Juarez, and I. Chairea, "Robust trajectory tracking of a Delta robot through adaptive active disturbance rejection control," *IEEE Transactions on Control Systems Technology*, vol. 23, no. 4, pp. 1387–1398, 2015.
- [4] B. Hu, L. D. Zhang, and J. J. Yu, "Kinematics and dynamics analysis of a novel serial-parallel dynamic simulator," *Journal of Mechanical Science and Technology*, vol. 30, no. 11, pp. 5183–5195, 2016.
- [5] C. Gosselin and L.-T. Schreiber, "Kinematically redundant spatial parallel mechanisms for singularity avoidance and large orientational workspace," *IEEE Transactions on Robotics*, vol. 32, no. 2, pp. 286–300, 2016.
- [6] H. S. Kim, "Kinematically redundant parallel haptic device with large workspace," *International Journal of Advanced Robotics Systems*, vol. 9, no. 6, p. 260, 2012.
- [7] L. J. Puglisi, *Advanced control strategies for a 6 DOF hydraulic parallel robot based on the dynamic model*, Ph.D. thesis, Universidad Politecnica de Madrid, Madrid, Spain, 2016.
- [8] Y. Li and Q. Xu, "Dynamic modeling and robust control of a 3-PRC translational parallel kinematic machine," *Robotics and Computer-Integrated Manufacturing*, vol. 25, no. 3, pp. 630–640, 2009.
- [9] X. Liu, Y. Xu, J. Yao, J. Xu, S. Wen, and Y. Zhao, "Control-faceted dynamics with deformation compatibility for a 5-DOF active over-constrained spatial parallel manipulator 6PUS-UPU," *Mechatronics*, vol. 30, pp. 107–115, 2015.
- [10] S. H. Wen, J. H. Chen, G. Q. Qin, Q. Zhu, and H. Wang, "An improved fuzzy model predictive control algorithm based on the force/position control structure of the five-degree of freedom redundant actuation parallel robot," *International Journal of Advanced Robotic Systems*, vol. 15, no. 5, 2018.
- [11] M. Sharifzadeh, M. Tale Masouleh, A. Kalhor, and P. Shahverdi, "An experimental dynamic identification & control of an overconstrained 3-DOF parallel mechanism in presence of variable friction and feedback delay," *Robotics and Autonomous Systems*, vol. 102, pp. 27–43, 2018.
- [12] A. Muller, "Redundant actuation of parallel manipulators," in *Parallel manipulators, Towards New Applications*, vol. 4, London UK, IntechOpen, 2008.
- [13] H. Liu, T. Huang, A. Kecskeméthy, D. G. Chetwynd, and Q. Li, "Force/motion transmissibility analyses of redundantly actuated and overconstrained parallel manipulators," *Mechanism and Machine Theory*, vol. 109, pp. 126–138, 2017.
- [14] J. Yao, W. Gu, Z. Feng, L. Chen, Y. Xu, and Y. Zhao, "Dynamic analysis and driving force optimization of a 5-DOF parallel manipulator with redundant actuation," *Robotics and Computer-Integrated Manufacturing*, vol. 48, pp. 51–58, 2017.
- [15] R. Boudreau, J. Léger, H. Tinaou, and A. Gallant, "Dynamic analysis and optimization of a kinematically redundant planar parallel manipulator," *Transactions of the Canadian Society for Mechanical Engineering*, vol. 42, no. 1, pp. 20–29, 2018.
- [16] R. Boudreau and S. Nokleby, "Force optimization of kinematically-redundant planar parallel manipulators following a desired trajectory," *Mechanism and Machine Theory*, vol. 56, pp. 138–155, 2012.
- [17] X. Wang, S. Guo, H. B. Qu, and F. Q. Zhao, "Optimal allocation method of parallel mechanism and its application," *Journal of Mechanical Engineering*, vol. 55, no. 1, pp. 32–41, 2019.
- [18] L. Ren, J. K. Mills, and D. Sun, "Adaptive synchronized control for a planar parallel manipulator: theory and experiments," *Journal of Dynamic Systems, Measurement, and Control*, vol. 128, no. 4, pp. 976–979, 2006.
- [19] W. Shang and S. Cong, "Nonlinear adaptive task space control for a 2-DOF redundantly actuated parallel manipulator," *Nonlinear Dynamics*, vol. 59, no. 1-2, pp. 61–72, 2010.
- [20] R. Babaghasabha, M. A. Khosravi, and H. D. Taghirad, "Adaptive control of KNTU planar cable-driven parallel robot with uncertainties in dynamic and kinematic parameters," in *Proceedings of the Second International Conference on Cable-Driven Parallel Robots*, vol. 32, pp. 145–159, Cham, Switzerland, November 2015.
- [21] D. Zhang and B. Wei, "A review on model reference adaptive control of robotic manipulators," *Annual Reviews in Control*, vol. 43, pp. 188–198, 2017.
- [22] L. Wang, Z. Lu, X. P. Liu, K. Liu, and D. Zhang, "Adaptive control of a parallel robot via backstepping technique," *International Journal of Systems Control and Communications*, vol. 1, no. 3, pp. 312–324, 2005.
- [23] M. Honegger, A. Codourey, and E. Burdet, "Adaptive control of the hexaglide, a 6 DOF parallel manipulator," in *Proceedings of the 1997 IEEE international Conference on Robotics and Automation*, Albuquerque, NM, USA, April 1997.
- [24] D. Y. Zhao, S. Y. Li, and F. Gao, "Fully adaptive feedforward feedback synchronized tracking control for Stewart platform systems," *International Journal of Control, Automation, and System*, vol. 6, no. 5, pp. 689–701, 2008.
- [25] J. Shi, J. Yao, T. M. Li, and Y. S. Du, "Learning-based optimal desired compensation adaptive robust control for a flexure-based micromotion manipulator," *Applied Sciences*, vol. 7, no. 4, p. 406, 2017.
- [26] E. Yime, R. Saltaren, and J. Diaz, "Robust adaptive control of the Stewart-Gough robot in the task space," in *Proceedings of the 2010 American Control Conference*, pp. 5248–5253, Marriott Waterfront, Baltimore, MD, USA, June 2010.

- [27] X. C. Zhu, G. L. Tao, B. Yao, and J. Cao, "Adaptive robust posture control of parallel manipulator driven by pneumatic muscles with redundancy," *IEEE/ASME Transactions on Mechatronics*, vol. 13, no. 4, pp. 441–450, 2008.
- [28] S. Roy, S. B. Roy, and I. N. Kar, "Adaptive-robust control of Euler-Lagrange systems with linearly parametrizable uncertainty bound," *IEEE Transactions on Control Systems Technology*, vol. 26, no. 5, pp. 1842–1850, 2018.
- [29] M. Bennehar, *Some contributions to nonlinear adaptive control of PKMs: from design to real-time experiments*, Ph.D. thesis, Université de Montpellier, Montpellier, France, 2015.
- [30] W. W. Shang and S. Cong, "Dexterity and adaptive control of planar parallel manipulators with and without redundant actuation," *Journal of Computational and Nonlinear Dynamics*, vol. 10, no. 1, Article ID 011002, 2015.
- [31] A. T. Vo and H. J. Kang, "An adaptive neural non-singular fast-terminal sliding-mode control for industrial robotic manipulators," *Applied Sciences*, vol. 8, no. 12, p. 2562, 2018.
- [32] H. Zhang, H. Fang, D. Zhang, X. Luo, and Q. Zou, "Forward kinematics and workspace determination of a novel redundantly actuated parallel manipulator," *International Journal of Aerospace Engineering*, vol. 2019, Article ID 4769174, 14 pages, 2019.
- [33] G. Shen, Y. Tang, J. Zhao, H. Lu, X. Li, and G. Li, "Jacobian free monotonic descent algorithm for forward kinematics of spatial parallel manipulator," *Advances in Mechanical Engineering*, vol. 8, no. 4, 2016.
- [34] H.-Q. Zhang, H.-R. Fang, B.-S. Jiang, and S.-G. Wang, "Dynamic performance evaluation of a redundantly actuated and over-constrained parallel manipulator," *International Journal of Automation and Computing*, vol. 16, no. 3, pp. 274–285, 2019.
- [35] S. Roy and S. Baldi, "On reduced-complexity robust adaptive control of switched Euler-Lagrange systems," *Nonlinear Analysis: Hybrid Systems*, vol. 34, pp. 226–237, 2019.
- [36] S. Roy and S. Baldi, "A simultaneous adaptation law for a class of nonlinearly parametrized switched systems," *IEEE Control Systems Letters*, vol. 3, no. 3, pp. 487–492, 2019.
- [37] R. Ortega and M. W. Spong, "Adaptive motion control of rigid robots: a tutorial," in *Proceedings of the 27th IEEE Conference on Decision and Control*, pp. 1575–1584, Austin, TX, USA, December 1988.
- [38] T.-S. Zhan and C.-C. Kao, "Modified PSO method for robust control of 3RPS parallel manipulators," *Mathematical Problems in Engineering*, vol. 2010, Article ID 302430, 25 pages, 2010.
- [39] C. Yang, Q. Huang, H. Jiang, O. Ogbobe Peter, and J. Han, "PD control with gravity compensation for hydraulic 6-DOF parallel manipulator," *Mechanism and Machine Theory*, vol. 45, no. 4, pp. 666–677, 2010.
- [40] D. Shiferaw, A. Jain, and R. Mitra, "High performance control of Stewart platform manipulator using sliding mode control with synchronization error," *International Journal of Intelligent Mechatronics and Robotics*, vol. 1, no. 4, pp. 19–43, 2011.
- [41] P. K. Jamwal, S. Q. Xie, Y. H. Tsoi, and K. C. Aw, "Forward kinematics modelling of a parallel ankle rehabilitation robot using modified fuzzy inference," *Mechanism and Machine Theory*, vol. 45, no. 11, pp. 1537–1554, 2010.
- [42] F. Piltan, A. Taghizadegan, and N. B. Sulaiman, "Modeling and control of four degrees of freedom surgical robot manipulator using MATLAB/SIMULINK," *International Journal of Hybrid Information Technology*, vol. 8, no. 11, pp. 47–78, 2015.
- [43] S. Yao, H. Li, L. Zeng, and X. Zhang, "Vision-based adaptive control of a 3-RRR parallel positioning system," *Science China Technological Sciences*, vol. 61, no. 8, pp. 1253–1264, 2018.
- [44] A. Traslosheros, J. Sebastián, J. Torrijos, R. Carelli, and E. Castillo, "An inexpensive method for kinematic calibration of a parallel robot by using one hand-held camera as main sensor," *Sensors*, vol. 13, no. 8, pp. 9941–9965, 2013.
- [45] G. L. Wu, S. P. Bai, J. A. Kepler, and S. Caro, "Error modelling and experimental validation of a planar 3-PPR parallel manipulator with joint clearances," *Journal of Mechanisms and Robotics*, vol. 4, no. 4, Article ID 041008, 2012.
- [46] <https://www.mathworks.com/help/vision/ug/stereo-camera-calibrator-app.html>.
- [47] <http://manual.robotis.com/>.
- [48] A. Escalera and J. M. Armingol, "Automatic chessboard detection for intrinsic and extrinsic camera parameter calibration," *Sensors*, vol. 10, no. 3, pp. 2027–2044, 2010.

Research Article

Application of Supply-Demand-Based Optimization for Parameter Extraction of Solar Photovoltaic Models

Guojiang Xiong ¹, Jing Zhang,¹ Dongyuan Shi ² and Xufeng Yuan¹

¹Guizhou Key Laboratory of Intelligent Technology in Power System, College of Electrical Engineering, Guizhou University, Guiyang 550025, China

²State Key Laboratory of Advanced Electromagnetic Engineering and Technology, Huazhong University of Science and Technology, Wuhan 430074, China

Correspondence should be addressed to Guojiang Xiong; gjxiongee@foxmail.com

Received 12 September 2019; Accepted 30 October 2019; Published 16 November 2019

Guest Editor: Minchul Shin

Copyright © 2019 Guojiang Xiong et al. This is an open access article distributed under the Creative Commons Attribution License, which permits unrestricted use, distribution, and reproduction in any medium, provided the original work is properly cited.

Modeling solar photovoltaic (PV) systems accurately is based on optimal values of unknown model parameters of PV cells and modules. In recent years, the use of metaheuristics for parameter extraction of PV models gains more and more attentions thanks to their efficacy in solving highly nonlinear multimodal optimization problems. This work addresses a novel application of supply-demand-based optimization (SDO) to extract accurate and reliable parameters for PV models. SDO is a very young and efficient metaheuristic inspired by the supply and demand mechanism in economics. Its exploration and exploitation are balanced well by incorporating different dynamic modes of the cobweb model organically. To validate the feasibility and effectiveness of SDO, four PV models with diverse characteristics including RTC France silicon solar cell, PVM 752 GaAs thin film cell, STM6-40/36 monocrystalline module, and STP6-120/36 polycrystalline module are employed. The experimental results comparing with ten state-of-the-art algorithms demonstrate that SDO performs better or highly competitively in terms of accuracy, robustness, and convergence. In addition, the sensitivity of SDO to variation of population size is empirically investigated. The results indicate that SDO with a relatively small population size can extract accurate and reliable parameters for PV models.

1. Introduction

Rising energy costs, losses in the present-day electricity grid, risks from nuclear power generation, and global environmental changes highlight the increasing significance of renewable energy resources for electricity generation [1]. Among renewable energy resources, solar energy is the most abundant natural resource with many advantages such as easily exploitable, clean, discreet, inexhaustible, long lasting, and reliable [2, 3]. It has made a leap forward in recent years. According to the International Energy Agency (IEA) [4], renewable energy resources will have the fastest growth in the electricity sector, providing almost 30% of power demand in 2023, up from 24% in 2017. During this period, solar photovoltaic (PV) contributes the most with expected 575 GW of new installed capacity. Owing to the ever-growing capacity of PV in power systems, PV brings about great changes to power

system planning and operating. In such a context, optimal PV models appear especially important to analyze their dynamic conversion behaviors under diverse environmental conditions. Electrical equivalent circuit models are the most popular tools to describe the input-output characteristics of PV cells and modules. Among them, the single diode model (SDM) and the double diode model (DDM) are the most commonly used models [5]. The SDM and DDM have five and seven unknown model parameters, respectively. Extracting accurate values for these unknown parameters is the premise and promise of optimal PV models.

Up to now, a great number of parameter extraction methods for PV models have been elaborated. They can be broken down into two categories from solution principles: analytical methods and optimization methods. The analytical methods are a “taking a part for the whole” methodology. Namely, they mainly rely highly on several key data points

provided by the manufacturer. These data points such as short-circuit point, open-circuit point, and maximum power point of the current-voltage (I-V) characteristic curve are nameplate rating data measured under standard test condition (STC). They will change over time due to PV degradation [6]. In addition, some assumptions and approximations are introduced to simplify the established mathematical models. In such contexts, the analytical methods will result in inaccuracy in the involved model parameters.

Unlike the analytical methods, the optimization methods are a “taking all actual measured data for the whole” methodology. They are no longer confined to several key data points under the STC provided by the manufacturer but extended to depending on a large number of data points measured under actual operating conditions. These data points cover a wide range of the I-V characteristic curve and thereby can reflect the actual relationship between inputs and outputs of a PV model. The optimization methods firstly construct an objective function to reflect the difference between the measured data and the calculated data based on the idea of curve fitting and then minimize the resultant objective function to obtain values for the unknown model parameters. The optimization methods consist of deterministic methods and metaheuristic methods. The former, including Newton method [7], Newton–Raphson method [8], iterative curve fitting [9], and Levenberg–Marquardt algorithm [10], are considerably dependent on the gradient information and subjected to initial conditions. Therefore, they easily plunge into local minima leading to inaccurate and unreliable solutions especially for complicated multimodal problems such as the parameter extraction problem of PV models.

Different from the deterministic methods, the metaheuristic methods do not need the gradient information. They have no requirements on the specific search domain information or the continuity/convexity of objective functions and exhibit the merits of robustness, simplicity, ease of implementation, etc. [11–13]. Consequently, they are considered global optimization algorithms and have received increasing interests in recent years. The parameter extraction problem of PV models is highly nonlinear, nonconvex, and has many local minima. Under this circumstance, the use of metaheuristic methods for this problem seems to be a promising alternative. Up to now, many metaheuristic methods have been applied to solve this problem. For example, Ismail et al. [14] applied the genetic algorithm (GA) to compute the parameters of both SDM and DDM. Chellaswamy and Ramesh [15] proposed a differential evolution (DE) technique with adaptive mutation factor and crossover rate to different solar cell types. Biswas et al. [16] implemented a linear population size reduction technique of success history-based adaptive DE to estimate parameters for PV models. Jordehi [17] developed a five-staged successive mutation strategy to construct a high-quality leader to pull all particles in particle swarm optimization (PSO) and applied the resultant improved algorithm to three PV models. Merchaoui et al. [18] introduced an adaptive mutation to alleviate the premature convergence of PSO. Askarzadeh and Leandro [19] simplified the original bird mating optimizer (BMO) and used the improved algorithm to an amorphous silicon PV module at different operating conditions. Ali et al. [20] applied multiverse

optimization (MVO) to extract five parameters for the SDM. Oliva et al. [21] utilized the chaotic maps to improve the performance of the whale optimization algorithm (WOA) and applied the improved algorithm to different PV models. Chen et al. [22] employed generalized opposition-based learning to enhance teaching-learning-based optimization (TLBO) and applied the modified algorithm to two PV models. Yu et al. [23] obtained parameters for three PV models by an improved JAYA algorithm with three strategies including self-adaptive weight, experience-based learning strategy, and chaotic elite learning method. Xiong et al. solved the parameter extraction problem of different PV models by using several metaheuristics including symbiotic organisms search (SOS) algorithm [24], improved WOA based on two modified prey searching strategies [25], and hybrid DE with WOA [26]. In addition to the aforementioned metaheuristics, many more [27–40] have also been presented to solve the important problem.

The abovementioned metaheuristics have, to some extent, proven themselves promising methods for the parameter extraction problem of PV models. Their performances are largely attributed to their own well-tuned parameters and well-designed search strategies for balancing the exploration and exploitation. According to the famous no-free-lunch theorem [41], there is no “one size fits all” approach for solving all optimization problems. Similarly, there is no “one size fits all” metaheuristic for extracting accurate parameters for all PV models, which highly motivates the authors to attempt new ones for the purpose of achieving optimal or suboptimal solutions for the problem considered here.

In this paper, a very young and effective metaheuristic named supply-demand-based optimization (SDO) [42] developed in 2019 is first applied to the parameter extraction problem of PV models. SDO mathematically mimics both the demand relation of consumers and supply relation of producers described by the famous cobweb theory in economics. According to the cobweb model [43, 44], markets have three dynamic modes, i.e., convergent mode, divergent mode, and closed mode. They correspond to the exploitation, exploration, and demarcation between them in SDO, respectively. SDO can incorporate these three modes organically. It has shown high competition in solving some benchmark test functions and mechanical engineering optimization problems compared with some popular metaheuristics such as PSO, DE, GA, and TLBO. In this paper, the SDO is applied to four PV models with diverse characteristics, i.e., the RTC France silicon solar cell, PVM 752 GaAs thin film cell, STM6-40/36 monocrystalline module, and STP6-120/36 polycrystalline module. Ten state-of-the-art metaheuristics are employed to verify the feasibility and effectiveness of SDO. Besides, the sensitivity of SDO to variation of population size is also empirically investigated.

The rest of this paper is organized as follows. Section 2 describes the mathematical formulation of parameter extraction problem of PV models. Section 3 introduces the supply and demand mechanism of the cobweb model. The SDO is detailed in Section 4. Section 5 presents the experimental results and comparisons. Finally, the paper is concluded in Section 6.

2. Problem Formulation

2.1. Single Diode Model (SDM). The output current I_L of the SDM shown in Figure 1 is calculated as follows:

$$I_L = I_{ph} - I_d - I_{sh}, \quad (1)$$

where I_{ph} , I_{sh} , and I_d denote the photogenerated current, shunt resistor current, and diode current, respectively. I_d and I_{sh} are formulated as follows [5, 45–47]:

$$I_d = I_{sd} \cdot \left[\exp\left(\frac{V_L + R_s \cdot I_L}{nV_t}\right) - 1 \right], \quad (2)$$

$$V_t = \frac{kT}{q}, \quad (3)$$

$$I_{sh} = \frac{V_L + R_s \cdot I_L}{R_{sh}}, \quad (4)$$

where I_{sd} is the saturation current, V_L is the output voltage, R_s and R_{sh} are the series resistance and shunt resistance, respectively, n is the diode ideal factor, k is the Boltzmann constant ($1.3806503 \times 10^{-23}$ J/K), q is the electron charge ($1.60217646 \times 10^{-19}$ C), and T is the cell temperature (K).

By incorporating equations (2)–(4) into (1), the output current I_L can be yielded as follows:

$$I_L = I_{ph} - I_{sd} \cdot \left[\exp\left(\frac{V_L + R_s \cdot I_L}{nV_t}\right) - 1 \right] - \frac{V_L + R_s \cdot I_L}{R_{sh}}. \quad (5)$$

It is obvious that the SDM has five unknown parameters (i.e., I_{ph} , I_{sd} , R_s , R_{sh} , and n) that need to be extracted.

2.2. Double Diode Model (DDM). The DDM considers the effect of recombination current loss in the depletion region and therefore performs well in some applications especially for thin films at low irradiance [46]. The output current I_L of the DDM in Figure 2 is formulated as follows [5, 46]:

$$\begin{aligned} I_L &= I_{ph} - I_{d1} - I_{d2} - I_{sh} \\ &= I_{ph} - I_{sd1} \cdot \left[\exp\left(\frac{V_L + R_s \cdot I_L}{n_1 V_t}\right) - 1 \right] - I_{sd2} \\ &\quad \cdot \left[\exp\left(\frac{V_L + R_s \cdot I_L}{n_2 V_t}\right) - 1 \right] - \frac{V_L + R_s \cdot I_L}{R_{sh}}, \end{aligned} \quad (6)$$

where I_{sd1} and I_{sd2} are diode currents and n_1 and n_2 are diode ideal factors. The DDM has seven unknown parameters (i.e., I_{ph} , I_{sd1} , I_{sd2} , R_s , R_{sh} , n_1 , and n_2) that need to be extracted.

2.3. PV Module Model. The output current I_L of a PV module with $N_s \times N_p$ solar cells in series and/or in parallel can be calculated as follows.

For the SDM-based PV module,

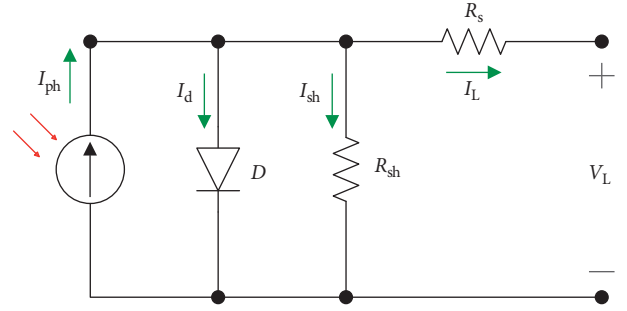


FIGURE 1: Equivalent circuit of the SDM.

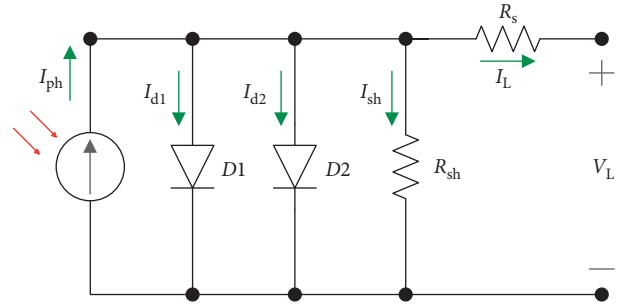


FIGURE 2: Equivalent circuit of the DDM.

$$I_L = N_p \left\{ I_{ph} - I_{sd} \cdot \left[\exp\left(\frac{V_L/N_s + R_s I_L/N_p}{nV_t}\right) - 1 \right] - \frac{V_L/N_s + R_s I_L/N_p}{R_{sh}} \right\}. \quad (7)$$

For the DDM-based PV module,

$$\begin{aligned} I_L &= N_p \left\{ I_{ph} - I_{sd1} \cdot \left[\exp\left(\frac{V_L/N_s + R_s I_L/N_p}{n_1 V_t}\right) - 1 \right] \right. \\ &\quad \left. - I_{sd2} \cdot \left[\exp\left(\frac{V_L/N_s + R_s I_L/N_p}{n_2 V_t}\right) - 1 \right] - \frac{V_L/N_s + R_s I_L/N_p}{R_{sh}} \right\}. \end{aligned} \quad (8)$$

2.4. Objective Function. In general, the root mean square error (RMSE) between the measured current $I_{L,measured}$ and the calculated current $I_{L,calculated}$ is used as the objective function [15, 17–19, 21–23]:

$$\min f(\mathbf{x}) = \text{RMSE}(\mathbf{x}) = \sqrt{\frac{1}{N} \sum_{k=1}^N [I_{L,calculated}^k(\mathbf{x}) - I_{L,measured}^k]^2}, \quad (9)$$

where N is the number of measured data and \mathbf{x} is the vector of unknown parameters.

3. Supply and Demand Mechanism of the Cobweb Model

The cobweb model [43, 44] is a famous economic theory used to study the fluctuation relationship between the price

and quantity of a commodity in a perfectly competitive market. It was apparently first named by Nicholas Kardor in 1934. The cobweb model is a dynamic equilibrium analysis theory based on elastic principle. According to this theory, for a given commodity, its quantity Q_{t+1} in the next time reacts to its current price P_t with an increasing supply function $Q_{t+1} = g(P_t)$ due to production lags, while its price P_{t+1} in the next time depends only on its corresponding quantity Q_{t+1} at the same time with a decreasing demand function $P_t = f(Q_t)$. Generally, both functions $f(\cdot)$ and $g(\cdot)$ are assumed to be linear as follows for the sake of simplification:

$$\text{Supply function } g(\cdot): Q_{t+1} - Q_e = K_g(P_t - P_e), \quad (10)$$

$$\text{Demand function } f(\cdot): P_{t+1} - P_e = K_f(Q_{t+1} - Q_e), \quad (11)$$

where $K_g > 0$ and $K_f < 0$ are the supply slop and demand slop, respectively, and $E_e(Q_e, P_e)^T$ is an equilibrium point.

By substituting equation (10) into equation (11), the following formulation is yielded:

$$P_{t+1} = K_f K_g P_t + (1 - K_f K_g) P_e. \quad (12)$$

Consequently, we can obtain the following equation (13) easily by using recursion:

$$P_{t+1} = (K_f K_g)^t P_1 + (1 - (K_f K_g)^t) P_e. \quad (13)$$

It can be seen from (13) that markets have the following three dynamic modes:

- (i) Convergent mode: If $|K_f K_g| < 1$, then $\lim_{t \rightarrow \infty} P_t \rightarrow P_e$; therefore, this market is stable and the price and quantity tend to spiral inwards with time as shown in Figure 3(a).
- (ii) Divergent mode: If $|K_f K_g| > 1$, then $\lim_{t \rightarrow \infty} P_t \rightarrow \infty$, which means that this market is divergent and the price and quantity tend to spiral outwards with time as shown in Figure 3(b).
- (iii) Closed mode: If $|K_f K_g| = 1$, when the time t is even, $\lim_{t \rightarrow \infty} P_t = P_1$; when t is odd, $\lim_{t \rightarrow \infty} P_t = 2P_e - P_1$. Hence, this market is oscillating and the price has the same impact on the supply and demand of the market as shown in Figure 3(c).

4. Supply-Demand-Based Optimization (SDO)

SDO [42] is a very young and effective metaheuristic algorithm inspired by the cobweb theory about the supply and demand mechanism. In SDO, there are ps markets and each market is considered a solution for a given optimization problem. Each market has D commodities corresponding to variables of the problem. Each commodity has a certain price and quantity at a given time. Therefore, each market actually has two solutions where one is a candidate solution $\mathbf{P}_i^t = [P_{i,1}^t, P_{i,2}^t, \dots, P_{i,D}^t]$ represented by the prices of commodities

and the other is a possible solution $\mathbf{Q}_i^t = [Q_{i,1}^t, Q_{i,2}^t, \dots, Q_{i,D}^t]$ composed by the quantities of commodities, where $i = 1, 2, \dots, ps$, $t = 1, 2, \dots, t_{\max}$, t_{\max} is the maximum number of iterations. Each price solution \mathbf{P}_i^t and quantity solution \mathbf{Q}_i^t are associated with the fitness values $f(\mathbf{P}_i^t)$ and $f(\mathbf{Q}_i^t)$, respectively. The fitness value $f(\mathbf{P}_i^t)$ is directly analogous to the rationality of a market. The price solution \mathbf{P}_i^t will be replaced by the quantity solution \mathbf{Q}_i^t if \mathbf{Q}_i^t is more rational, i.e., $f(\mathbf{Q}_i^t)$ is smaller than $f(\mathbf{P}_i^t)$ for a minimization optimization problem.

Although both the price solution \mathbf{P}_i^t and quantity solution \mathbf{Q}_i^t serve as solutions, they have different updating strategies. It can be seen from equations (10) and (11) that the prerequisite of obtaining the prices and quantities of a market is getting the position of the equilibrium point $\mathbf{E}_e^t = [E_{e,1}^t, E_{e,2}^t, \dots, E_{e,D}^t] = \begin{bmatrix} Q_{e,1}^t, Q_{e,2}^t, \dots, Q_{e,D}^t \\ P_{e,1}^t, P_{e,2}^t, \dots, P_{e,D}^t \end{bmatrix}$. However, the equilibrium point is not known *a priori* during the iterations. In this context, SDO adopts the following methods to determine the equilibrium point \mathbf{E}_e^t at each iteration. For the quantity, each market chooses a quantity solution $\mathbf{Q}_k^t = [Q_{k,1}^t, Q_{k,2}^t, \dots, Q_{k,D}^t]$ probabilistically as its quantity equilibrium vector $\mathbf{Q}_e^t = [Q_{e,1}^t, Q_{e,2}^t, \dots, Q_{e,D}^t]$ using fitness value-based roulette wheel selection as follows:

$$\lambda_i = \left| f(\mathbf{Q}_i^t) - \frac{1}{ps} \sum_{i=1}^{ps} f(\mathbf{Q}_i^t) \right|, \quad (14)$$

$$\mu_i = \frac{\lambda_i}{\sum_{i=1}^{ps} \lambda_i},$$

$$\mathbf{Q}_e^t = \mathbf{Q}_k^t, \quad k = \text{Roulette Wheel Selection}(\boldsymbol{\mu}),$$

where $\boldsymbol{\mu} = [\mu_1, \mu_2, \dots, \mu_{ps}]$.

Concerning the price, each market chooses either a price solution $\mathbf{P}_k^t = [P_{k,1}^t, P_{k,2}^t, \dots, P_{k,D}^t]$ probabilistically using fitness value-based roulette wheel selection or the average price vector $\mathbf{P}^t = [P_1^t, P_2^t, \dots, P_D^t]$ of all markets as its quantity equilibrium vector $\mathbf{P}_e^t = [P_{e,1}^t, P_{e,2}^t, \dots, P_{e,D}^t]$. \mathbf{P}_k^t and \mathbf{P}^t are chosen with the same probability:

$$\rho_i = \left| f(\mathbf{P}_i^t) - \frac{1}{ps} \sum_{i=1}^{ps} f(\mathbf{P}_i^t) \right|,$$

$$\sigma_i = \frac{\rho_i}{\sum_{i=1}^{ps} \rho_i}, \quad (15)$$

$$\mathbf{P}_e^t = \begin{cases} r_1 \cdot \mathbf{P}_k^t, & \text{if } r_2 \geq 0.5, \\ \mathbf{P}^t, & \text{if } r_2 < 0.5, \end{cases}$$

where $\overline{P}_d^t = (1/ps) \sum_{i=1}^{ps} P_{i,d}^t$, $d = 1, 2, \dots, D$, $k = \text{Roulette Wheel Selection}(\boldsymbol{\sigma})$, $\boldsymbol{\sigma} = [\sigma_1, \sigma_2, \dots, \sigma_{ps}]$, and r_1 and r_2 are random real numbers in $(0, 1)$.

After getting the position of the equilibrium point $\mathbf{E}_e^t = [E_{e,1}^t, E_{e,2}^t, \dots, E_{e,D}^t]$, the quantity and price adopt the following strategies to generate their corresponding trial vectors $\mathbf{TQ}_k^t = [TQ_{i,1}^t, TQ_{i,2}^t, \dots, TQ_{i,D}^t]$ and $\mathbf{TP}_k^t = [TP_{i,1}^t, TP_{i,2}^t, \dots, TP_{i,D}^t]$, respectively:

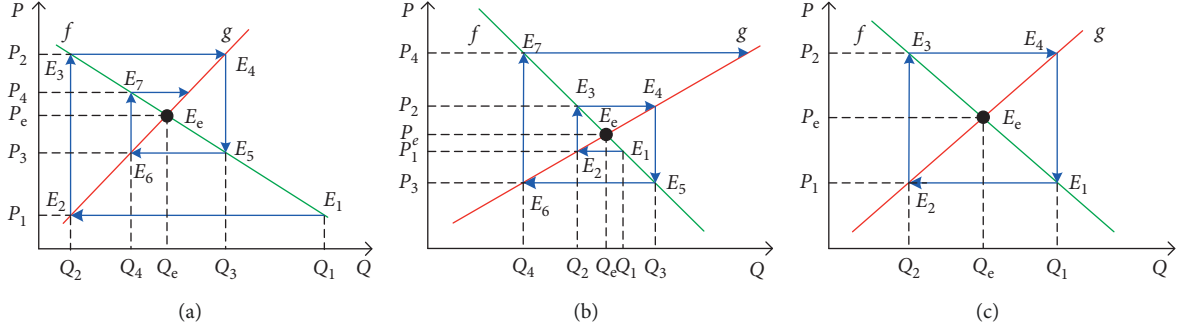


FIGURE 3: Dynamic modes of the cobweb model. (a) Convergent mode; (b) divergent mode; (c) closed mode.

$$\begin{aligned} TQ_{i,d}^t &= Q_{e,d}^t + \alpha \cdot (P_{i,d}^t - P_{e,d}^t), \\ TP_{i,d}^t &= P_{e,d}^t + \beta \cdot (TQ_{i,d}^t - Q_{e,d}^t), \end{aligned} \quad (16)$$

where $d = 1, 2, \dots, D$, and α and β denote the supply weight and demand weight, respectively. They are determined as follows:

$$\alpha = \frac{2 \cdot (t_{\max} - t + 1)}{t_{\max}} \cdot \sin(2\pi r_3), \quad (17)$$

$$\beta = 2 \cdot \cos(2\pi r_4), \quad (18)$$

where r_3 and r_4 are random real numbers in $(0, 1)$.

Thereafter, a selection is implemented to choose a fitter one as follows:

$$\begin{aligned} \mathbf{Q}_i^{t+1} &= \begin{cases} T\mathbf{Q}_i^t, & \text{if } f(T\mathbf{Q}_i^t) \leq f(\mathbf{Q}_i^t), \\ \mathbf{Q}_i^t, & \text{otherwise,} \end{cases} \\ \mathbf{P}_i^{t+1} &= \begin{cases} T\mathbf{P}_i^t, & \text{if } f(T\mathbf{P}_i^t) \text{ is the smallest one,} \\ \mathbf{Q}_i^{t+1}, & \text{if } f(\mathbf{Q}_i^{t+1}) \text{ is the smallest one,} \\ \mathbf{P}_i^t, & \text{otherwise.} \end{cases} \end{aligned} \quad (19)$$

It can be seen that if $|\alpha\beta| < 1$, then the corresponding market is stable or convergent, which means the supply and demand mechanism defines a search space in the neighborhood of the equilibrium point and allows the market to exploit its prices inside that domain. If $|\alpha\beta| > 1$, the corresponding market is divergent, indicating that the supply and demand mechanism defines a large search space far away from the equilibrium point and allows the market to explore its prices in new promising areas. $|\alpha\beta| = 1$ corresponds to the critical point between the exploration and exploitation. In addition, equations (17) and (18) enable SDO a smooth transition from exploration to exploitation as the iterations progress. Therefore, SDO exhibits exploration and exploitation and possesses an ability to balance them. The flowchart of SDO is shown in Figure 4.

5. Experimental Results

To validate the performance of SDO in solving the parameter extraction problem of PV models, SDO is applied to the following four different PV models with diverse characteristics:

- (i) RTC France silicon solar cell [48]: contains 26 pairs of I-V data points measured at 33°C under 1000 W/m² irradiance
- (ii) PVM 752 GaAs thin film cell [17]: contains 44 pairs of I-V data points measured at 25°C under 1000 W/m² irradiance
- (iii) STM6-40/36 monocrystalline module [30, 49]: composed of 36 cells in series with 20 pairs of I-V data points measured at 51°C
- (iv) STP6-120/36 polycrystalline module [30, 49]: composed of 36 cells in series with 24 pairs of I-V data points measured at 55°C

The search ranges for the involved parameters are presented in Table 1. In this work, both the SDM and DDM are used to model all of these four PV models. In addition, ten state-of-the-art algorithms including comprehensive learning particle swarm optimizer (CLPSO) [50], hybrid differential evolution with biogeography-based optimization (DE/BBO) [51], generalized oppositional teaching-learning-based optimization (GOTLBO) [22], improved JAYA optimization algorithm (IJAYA) [23], improved whale optimization algorithm (IWOA) [25], teaching-learning-based optimization with learning experience of other learners (LETLBO) [52], modified artificial bee colony algorithm (MABC) [53], opposition-based differential evolution (ODE) [54], teaching-learning-based artificial bee colony (TLABC) [55], and self-adaptive teaching-learning-based optimization (SATLBO) [56] are employed to verify SDO. The parameter settings for these ten compared algorithms are kept the same as those in their original literature and summarized in Table 2. The maximum number of fitness evaluations (Max_FEs) setting as 50000 [23, 24, 26, 30, 55, 56] serves as the stopping condition for fair comparison. In addition, for each algorithm, 50 independent runs are executed in MATLAB 2017a.

5.1. Results on the RTC France Silicon Solar Cell. The experimental results including the minimum (Min), maximum (Max), mean (Mean), and standard deviation (Std Dev) values of the RMSE values over 50 independent runs are recorded. Because the actual values for the involved parameters are not known *a priori*, so the RMSE values can be used as an index to weigh the extraction accuracy.

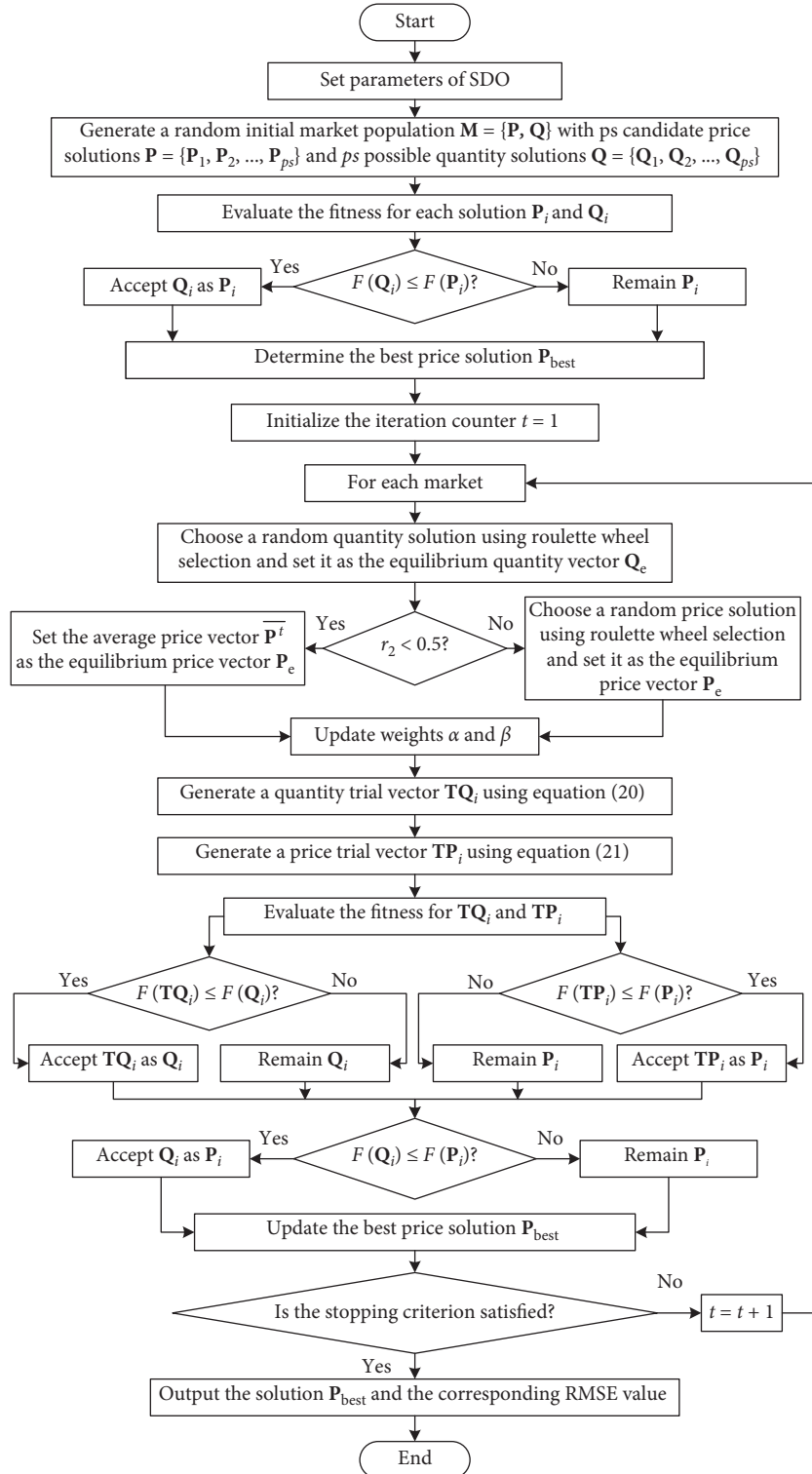


FIGURE 4: The flowchart of SDO.

For the RTC France silicon solar cell, the experimental results are summarized in Table 3. The best results are highlighted in **boldface**. It can be seen that, for the SDM, five algorithms including SDO, DE/BBO, ODE, SATLBO, and TLABC achieve the smallest RMSE value ($9.8602E-04$). Even so, SDO gets better results in terms of the maximum

RMSE, mean RMSE, and standard deviation values, indicating that it is more robust and can obtain more reliable and accurate values for the unknown parameters. For the DDM, SDO performs the best in all terms of RMSE values, demonstrating its robustness and accuracy again. In addition, Wilcoxon's rank sum test at confidence level 0.05 is

TABLE 1: Search ranges of parameters of PV models.

Parameter	RTC France cell		PVM 752 GaAs cell		STM6-40/36 module		STP6-120/36 module	
	LB	UB	LB	UB	LB	UB	LB	UB
I_{ph} (A)	0	1	0	1	0	2	0	8
I_{sd} (μA)	0	1	0	1	0	50	0	50
R_s (Ω)	0	0.5	0	1	0	0.36	0	0.36
R_{sh} (Ω)	0	100	0	1000	0	1000	0	1500
n, n_1, n_2	1	2	1	2	1	60	1	50

TABLE 2: Parameter settings for involved algorithms.

Algorithm	Parameter settings
CLPSO	ps = 40, $w = 0.9 \rightarrow 0.4$, $c = 1.49445$, $m = 7$
DE/BBO	ps = 100, $F = \text{rand}(0.1, 0.9)$, CR = 0.9, $E = I = 1$
GOTLBO	ps = 50, Jr = 0.4
IJAYA	ps = 20
IWOA	ps = 50, $a = 2 \rightarrow 0$
LETLBO	ps = 50
MABC	ps = 150, limit = 100, $P = 0.7$
ODE	ps = 100, $F = 0.5$, CR = 0.9, Jr = 0.3
SATLBO	ps = 40
TLABC	ps = 50, limit = 200, $F = \text{rand}(0, 1)$
SDO	ps = 20

TABLE 3: Experimental results on the RTC France solar cell.

Model	Algorithm	Min	Max	Mean	Std. dev.	Significance
SDM	CLPSO	1.0016E-03	1.4520E-03	1.1329E-03	1.0917E-04	†
	DE/BBO	9.8602E-04	1.2373E-03	1.0533E-03	5.0412E-05	†
	GOTLBO	9.8627E-04	1.4071E-03	1.0796E-03	9.8773E-05	†
	IJAYA	9.8603E-04	1.0019E-03	9.8934E-04	3.5283E-06	†
	IWOA	9.8829E-04	3.2095E-03	1.4633E-03	3.7745E-04	†
	LETLBO	9.8604E-04	1.1558E-03	1.0145E-03	3.7825E-05	†
	MABC	1.0154E-03	1.8145E-03	1.1980E-03	1.6722E-04	†
	ODE	9.8602E-04	1.4627E-03	1.0628E-03	1.1279E-04	†
	SATLBO	9.8602E-04	1.0416E-03	9.9082E-04	9.3056E-06	†
	TLABC	9.8602E-04	1.0311E-03	9.9051E-04	9.3740E-06	†
	SDO	9.8602E-04	9.8616E-04	9.8603E-04	2.5141E-08	
DDM	CLPSO	1.0084E-03	1.7444E-03	1.2000E-03	1.4938E-04	†
	DE/BBO	9.8589E-04	1.7089E-03	1.1715E-03	1.8756E-04	†
	GOTLBO	9.8736E-04	1.4216E-03	1.1419E-03	1.2637E-04	†
	IJAYA	9.8439E-04	1.1977E-03	1.0045E-03	3.6754E-05	†
	IWOA	9.8629E-04	2.1982E-03	1.3907E-03	3.0524E-04	†
	LETLBO	9.8270E-04	1.3936E-03	1.0648E-03	1.0259E-04	†
	MABC	9.8707E-04	1.2597E-03	1.0740E-03	5.8610E-05	†
	ODE	9.8271E-04	1.1779E-03	9.9590E-04	3.1806E-05	≈
	SATLBO	9.8301E-04	1.1634E-03	1.0024E-03	3.5296E-05	†
	TLABC	9.8349E-04	1.2529E-03	1.0247E-03	6.0243E-05	†
	SDO	9.8250E-04	1.0271E-03	9.8822E-04	8.8518E-06	

used to compare the significance between SDO and other algorithms. The marks “†,” “≈,” and “≈” denote that SDO is better than, worse than, and similar to the compared algorithm, respectively. It is clear that SDO is significantly better than all of the other ten compared algorithms on the SDM. With regards to the DDM, SDO wins other nine algorithms except ODE while both SDO and ODE get the

similar results statistically. Moreover, the convergence curves illustrated in Figure 5 are provided to study the convergence property of SDO. It shows that IJAYA converges the fastest at the large part of evolutionary process. Nevertheless, it is gradually overtaken and finally surpassed by SDO after about 35000 and 34000 fitness evaluations for the SDM and DDM, respectively, indicating that SDO has a

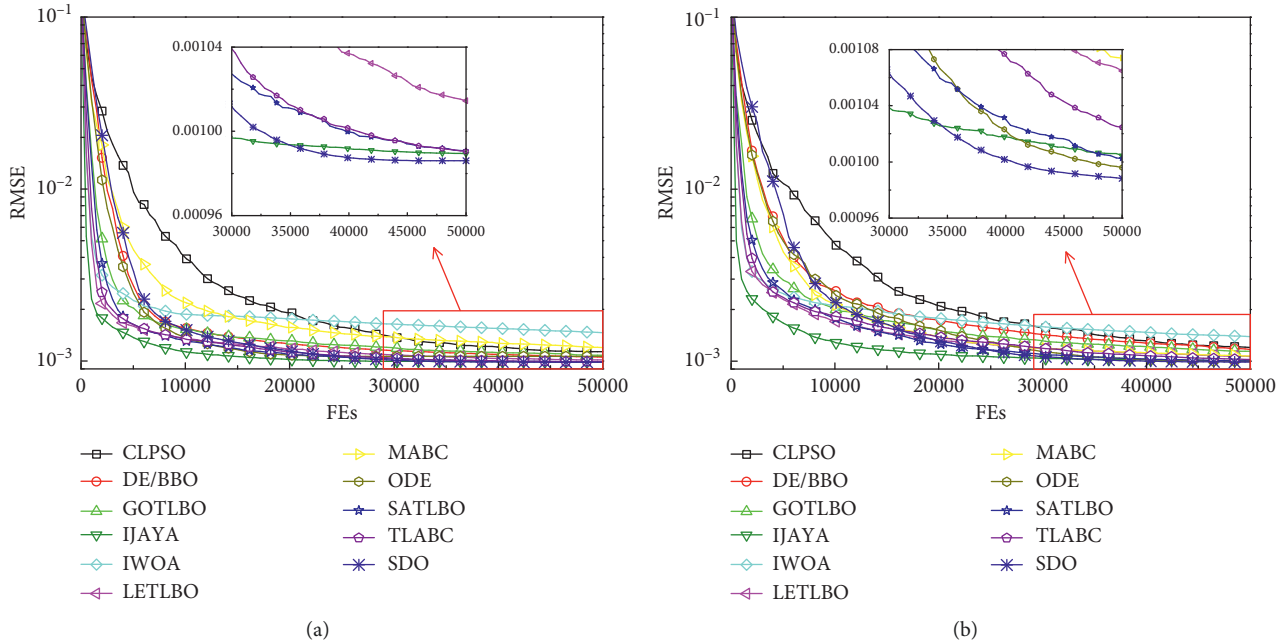


FIGURE 5: Convergence curves for the RTC France silicon solar cell. (a) SDM; (b) DDM.

relatively fast convergence speed throughout the evolutionary process.

The extracted values obtained by SDO for the involved unknown parameters corresponding to the minimum RMSE are listed in Table 4. With these extracted parameters, the I-V and P-V characteristic curves can be reconstructed easily as shown in Figure 6. It is obvious that the calculated data achieved by SDO agree with the measured data well throughout the entire voltage range. In addition, the individual absolute error (IAE) between the calculated current and measured current is recorded in Table 5. All of the IAE values are smaller than 0.0016, meaning that the values extracted by SDO for the involved parameters of both the SDM and DDM are very accurate.

Additionally, comparing the results of the SDM and DDM, we can find that the minimum RMSE value provided by the DDM is lower than that given by the SDM. The sum of IAE obtained by the DDM is 0.01730620 which is smaller than that (0.1770381) given by SDM, indicating that the DDM may be more suitable for the RTC France silicon solar cell. On the other side, we also observe that the SDM is better than the DDM in terms of the maximum RMSE, mean RMSE, and standard deviation values. This is mainly because the DDM has seven unknown parameters that need to be extracted while the SDM only has five. Therefore, the DDM is more complex with more local minima and the solution algorithms are more likely to get into them.

5.2. Results on PVM 752 GaAs Thin Film Cell. For the PVM 752 GaAs thin film cell, the RMSE values are presented in Table 6. It is clear that IJAYA achieves the best values in all terms of RMSE for the SDM while SDO gets the second best minimum RMSE value. Considering the maximum RMSE and mean RMSE, besides IJAYA, both SATLBO and TLABC are also better than SDO while SDO performs better than the rest

seven algorithms, which is also verified by Wilcoxon's rank sum test results. For the DDM, IJAYA still performs well but it is worse than SDO in terms of minimum RMSE where IWOA gets the least value. In addition, SDO beats both SATLBO and TLABC for the DDM, indicating SDO is more effective in solving this complex model. The test results show SDO is better than the nine algorithms except IJAYA. The convergence curves in Figure 7 show that IJAYA is the fastest while SDO maintains a relatively fast speed even at the later stage.

The extracted optimal parameters obtained by SDO are tabulated in Table 7, and the reconstructed I-V and P-V characteristic curves corresponding to these optimal parameters are presented in Figure 8. Figure 8 shows that the calculated data achieved by SDO with both the SDM and DDM are in good coincidence with the measured data. The IAE values in Table 8 are all smaller than 0.0004, which demonstrates the good accuracy of SDO again. Table 8 also reveals that the DDM provides a smaller value of the sum of IAE than the SDM, which results in an inference of good adaptability of the DDM for the PVM 752 GaAs thin film cell.

5.3. Results on the STM6-40/36 Monocrystalline Module. Table 9 presents the experimental results on the STM6-40/36 monocrystalline module. It clearly shows that SDO provides the least values in all terms of RMSE for both the SDM and DDM. In addition, the standard deviation values of SDO for both the SDM and DDM are at least one order of magnitude lower than those of the other compared algorithms, indicating its good robustness on this PV module. Wilcoxon's rank sum test results demonstrate that SDO is significantly better than ten and nine algorithms for the SDM and DDM, respectively. Both IJAYA and SDO get the similar result for the DDM statistically. The convergence curves in Figure 9 manifest that IJAYA still performs well but it is surpassed by

TABLE 4: Extracted value for the parameters of the RTC France solar cell by SDO.

Model	I_{ph} (A)	I_{sd1} (μ A)	R_s (Ω)	R_{sh} (Ω)	n_1	I_{sd2} (μ A)	n_2	RMSE
SDM	0.7608	0.3230	0.0364	53.7185	1.4812	—	—	$9.8602E-04$
DDM	0.7608	0.7879	0.0368	55.5705	2.0000	0.2214	1.4493	$9.8250E-04$

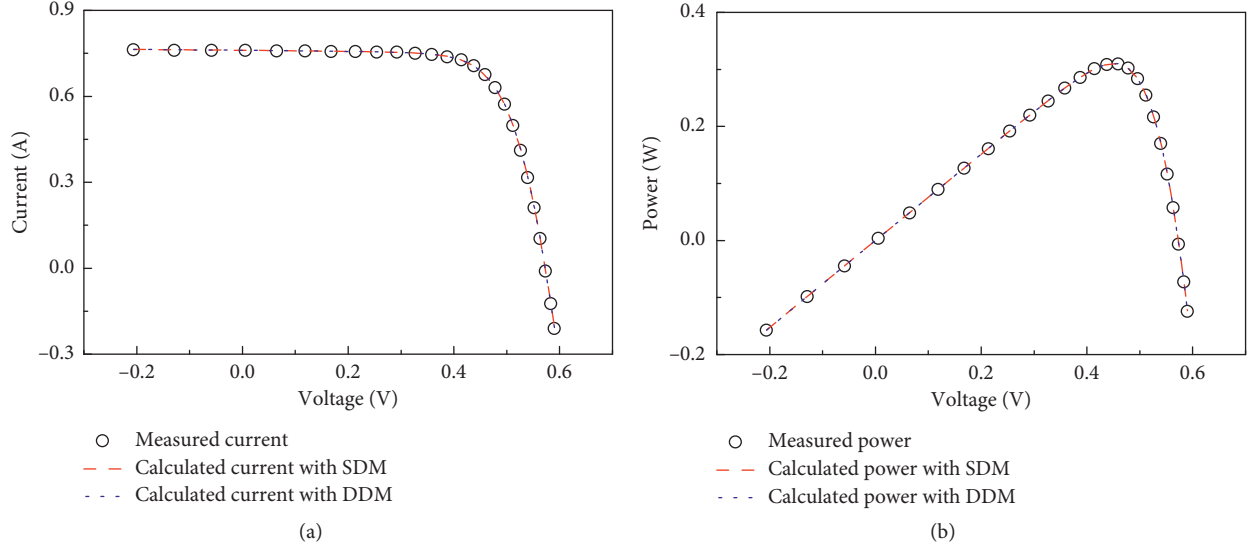


FIGURE 6: Comparison between the measured and calculated data achieved by SDO for the RTC France silicon solar cell. (a) I-V characteristic; (b) P-V characteristic.

TABLE 5: Calculated results for the RTC France solar cell by SDO.

Item	V_L (V)	I_L measured (A)	SDM		DDM	
			I_L calculated (A)	IAE (A)	I_L calculated (A)	IAE (A)
1	-0.2057	0.7640	0.76408765	0.00008765	0.76397865	0.00002135
2	-0.1291	0.7620	0.76266264	0.00066264	0.76260103	0.00060103
3	-0.0588	0.7605	0.76135473	0.00085473	0.76133641	0.00083641
4	0.0057	0.7605	0.76015424	0.00034576	0.76017502	0.00032498
5	0.0646	0.7600	0.75905593	0.00094407	0.75911090	0.00088910
6	0.1185	0.7590	0.75804334	0.00095666	0.75812616	0.00087384
7	0.1678	0.7570	0.75709159	0.00009159	0.75719293	0.00019293
8	0.2132	0.7570	0.75614207	0.00085793	0.75624879	0.00075121
9	0.2545	0.7555	0.75508732	0.00041268	0.75518142	0.00031858
10	0.2924	0.7540	0.75366447	0.00033553	0.75372478	0.00027522
11	0.3269	0.7505	0.75138806	0.00088806	0.75139526	0.00089526
12	0.3585	0.7465	0.74734834	0.00084834	0.74729210	0.00079210
13	0.3873	0.7385	0.74009688	0.00159688	0.73998463	0.00148463
14	0.4137	0.7280	0.72739678	0.00060322	0.72725709	0.00074291
15	0.4373	0.7065	0.70695328	0.00045328	0.70682936	0.00032936
16	0.4590	0.6755	0.67529492	0.00020508	0.67522713	0.00027287
17	0.4784	0.6320	0.63088433	0.00111567	0.63088881	0.00111119
18	0.4960	0.5730	0.57208207	0.00091793	0.57214459	0.00085541
19	0.5119	0.4990	0.49949167	0.00049167	0.49957588	0.00057588
20	0.5265	0.4130	0.41349364	0.00049364	0.41356039	0.00056039
21	0.5398	0.3165	0.31721950	0.00071950	0.31724334	0.00074334
22	0.5521	0.2120	0.21210317	0.00010317	0.21207988	0.00007988
23	0.5633	0.1035	0.10272136	0.00077864	0.10266820	0.000683180
24	0.5736	-0.0100	-0.00924878	0.00075122	-0.00930040	0.00069960
25	0.5833	-0.1230	-0.12438136	0.00138136	-0.12439113	0.00139113
26	0.5900	-0.2100	-0.20919308	0.00080692	-0.20914419	0.00085581
Sum of IAE				0.01770381		0.01730620

TABLE 6: Experimental results on the PVM 752 GaAs thin film cell.

Model	Algorithm	Min	Max	Mean	Std. dev.	Significance
SDM	CLPSO	2.3769E-04	6.2527E-04	5.2031E-04	7.0536E-05	†
	DE/BBO	4.4257E-04	5.4430E-04	4.9571E-04	2.2319E-05	†
	GOTLBO	2.9492E-04	4.9484E-04	4.0204E-04	4.7484E-05	†
	IJAYA	2.2880E-04	2.7167E-04	2.5378E-04	1.1645E-05	‡
	IWOA	2.4740E-04	5.7399E-04	4.5156E-04	8.9898E-05	†
	LETLBO	2.7261E-04	3.9623E-04	3.3354E-04	3.1904E-05	†
	MABC	2.8780E-04	6.2992E-04	4.9864E-04	8.6429E-05	†
	ODE	3.3079E-04	5.1531E-04	4.5800E-04	3.7762E-05	†
	SATLBO	2.3507E-04	3.1341E-04	2.7396E-04	1.6165E-05	‡
	TLABC	2.5814E-04	3.4267E-04	2.8923E-04	2.0936E-05	‡
SDO	2.3487E-04	3.7700E-04	3.1727E-04	2.7687E-05		
DDM	CLPSO	3.6535E-04	8.0492E-04	6.3929E-04	9.0095E-05	†
	DE/BBO	4.0709E-04	5.8587E-04	5.2992E-04	3.5679E-05	†
	GOTLBO	3.0186E-04	5.5029E-04	4.1337E-04	6.0833E-05	†
	IJAYA	2.1537E-04	3.5937E-04	2.5929E-04	2.2873E-05	‡
	IWOA	2.0527E-04	5.7609E-04	3.8642E-04	9.3900E-05	†
	LETLBO	2.7139E-04	4.9192E-04	3.4188E-04	4.6623E-05	†
	MABC	3.8852E-04	6.7013E-04	5.6206E-04	6.1736E-05	†
	ODE	3.4568E-04	5.0415E-04	4.2829E-04	3.7022E-05	†
	SATLBO	2.3785E-04	5.4593E-04	3.2119E-04	6.7473E-05	†
	TLABC	2.3397E-04	5.8888E-04	3.4127E-04	5.9141E-05	†
SDO	2.1318E-04	4.7178E-04	2.8703E-04	5.1523E-05		

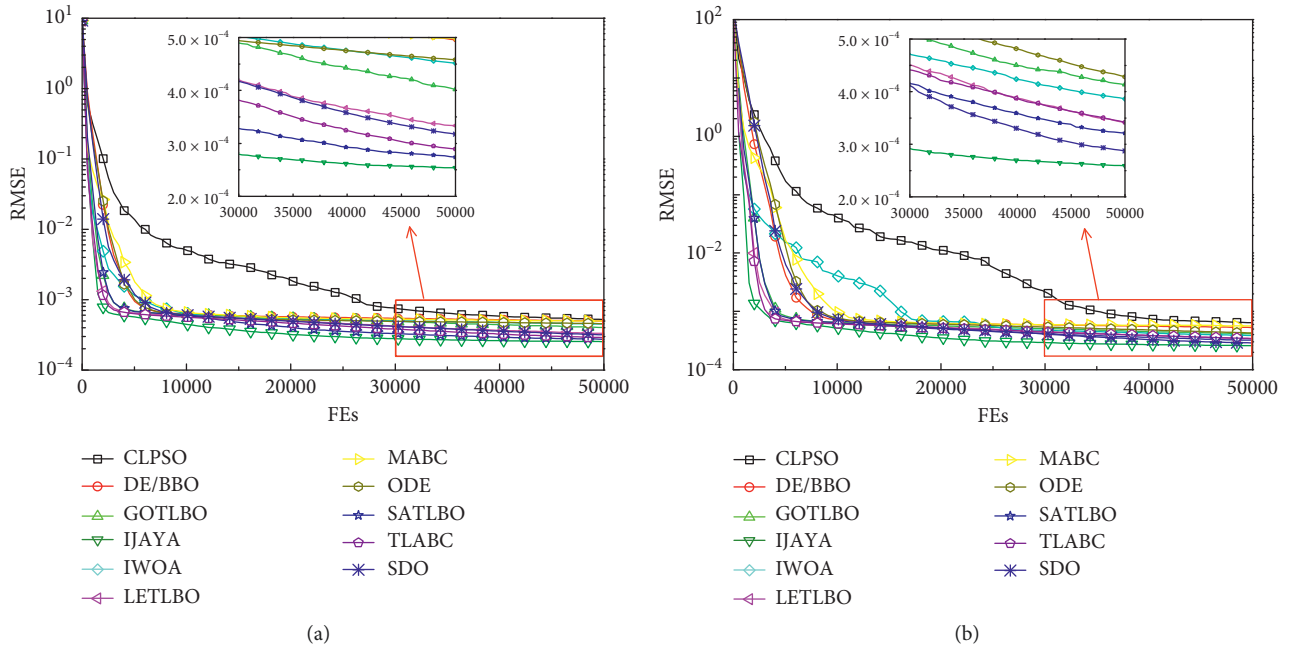


FIGURE 7: Convergence curves for the PVM 752 GaAs thin film cell. (a) SDM; (b) DDM.

TABLE 7: Extracted value for the parameters of PVM 752 GaAs thin film cell by SDO.

Model	I_{ph} (A)	I_{sd1} (μA)	R_s (Ω)	R_{sh} (Ω)	n_1	I_{sd2} (μA)	n_2	RMSE
SDM	0.1000	5.9440E-06	0.6499	668.5946	1.6467	—	—	2.3487E-04
DDM	0.1001	7.2313E-04	0.6684	637.3026	2.0000	6.2352E-05	1.5152	2.1318E-04

SDO after about 43000 and 31000 fitness evaluations for the SDM and DDM, respectively, indicating that SDO performs highly competitively at the later stage.

Table 10 reports the extracted optimal parameters yielded by SDO, and Figure 10 illustrates the reconstructed I-V and P-V characteristic curves. We can see that the

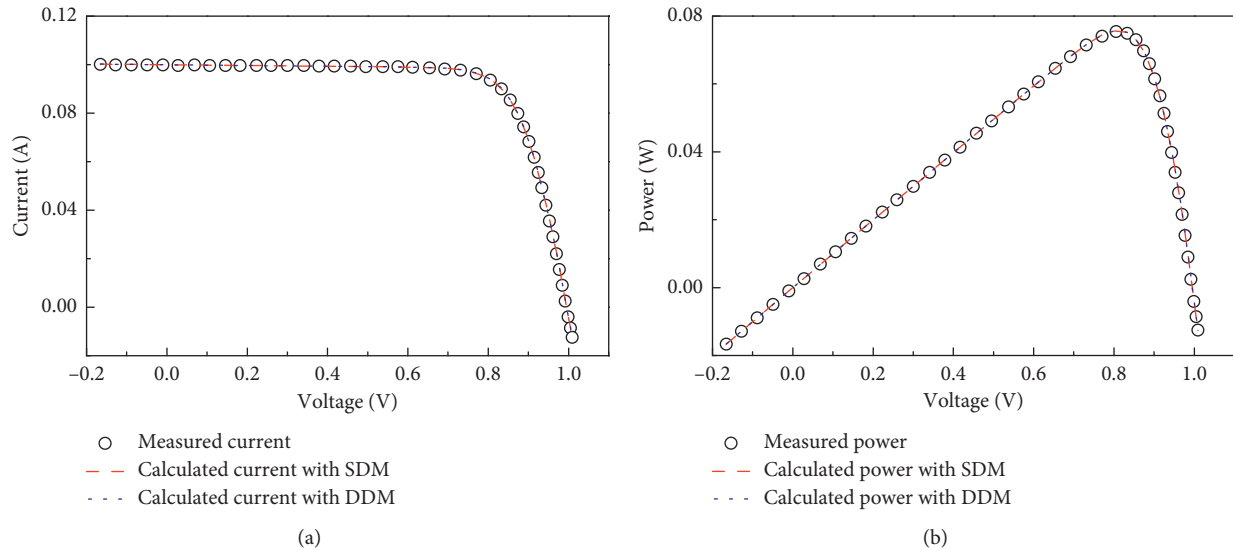


FIGURE 8: Comparison between the measured and calculated data achieved by SDO for the PVM 752 GaAs thin film cell. (a) I-V characteristic; (b) P-V characteristic.

calculated data achieved by SDO are in good agreement with the measured data over the entire voltage range. Besides, Table 11 shows that all of the IAE values are less than 0.00607. Table 11 also testifies to that both the SDM and DDM obtain a comparable sum of IAE value, indicating that the DDM brings no benefit in terms of accuracy for the STM6-40/36 monocrystalline module. Moreover, Table 9 shows that the DDM gives larger values in all terms of RMSE except the minimum RMSE, meaning that the DDM is more complex and the solution algorithms are harder to get comparable results as those given by the SDM under the same considered condition (i.e., with the same Max_FEs).

5.4. Results on the STP6-120/36 Polycrystalline Module.

With regards to the STP6-120/36 polycrystalline module, the experimental results tabulated in Table 12 show that ODE and SDO achieve the same least values ($1.6601E-02$) for both the SDM and DDM. However, SDO beats ODE in the rest terms of RMSE. Actually, Wilcoxon's rank sum test results also declare that SDO is significantly better than all of the other algorithms including ODE. The convergence curves in Figure 11 demonstrate that although SDO is relatively slow at the first stage, it has the ability of jumping out of local optima and keeping a relatively fast speed to search more promising areas at the later stage. Finally, it surpasses all compared algorithms after about 43000 and 46000 fitness evaluations for the SDM and DDM, respectively.

The extracted optimal parameters obtained by SDO are provided in Table 13. Using these parameters, the output currents and powers corresponding to the measured voltages can be calculated easily and they are summarized in Table 14. It can be seen that all IAE values are less than 0.0375. The reconstructed I-V and P-V characteristic curves presented in Figure 12 show again that the calculated data acquired by SDO with both the SDM and DDM all fit with the measured

data well. Besides, although the value of sum of IAE given by the DDM in Table 14 is slightly smaller than that of the SDM, the difference (0.00000089) is in practice very small, which concludes that both the SDM and DDM provide a similar accuracy for the STP6-120/36 polycrystalline module. Furthermore, Table 12 also proves that optimizing the DDM is more difficult than optimizing the SDM.

5.5. Overall Performance. In the above four sections, only the single-model statistical analysis by Wilcoxon's rank sum test is implemented to compare SDO with the other algorithms. As recommended in [57], the multiple-model statistical analysis that considers all the involved models simultaneously is also very momentous to verify the performance of SDO. In this section, the popular Friedman test at confidence level 0.05 is used to check the overall behavior of SDO in solving the problem concerned here. The test result is given in Figure 13. Clearly, SDO obtains the first overall best ranking, followed by IJAYA, TLABC, SATLBO, LETLBO, ODE, GOTLBO, DE/BBO, IWOA, CLPSO, and MABC. In conclusion, it can be confirmed by combining the single-model statistical analysis results in Tables 3, 6, 9, and 12 with the multiple-model statistical analysis result in Figure 13 that the overall performance of SDO is the best among all of involved algorithms in terms of the final solution quality, i.e., extraction accuracy.

5.6. Influence of Population Size on SDO. Population size is always a key parameter in metaheuristics and choosing an appropriate value is very important in solving different problems [58, 59]. In this section, the influence of ps on SDO in solving the parameter extraction problem of PV models is investigated. Five values of ps from 10 to 50 with an interval of 10 are tested. The value of Max_FEs is kept the same as that in

TABLE 8: Calculated results for the PVM 752 GaAs thin film cell by SDO.

Item	V_L (V)	I_L measured (A)	SDM		DDM	
			I_L calculated (A)	IAE (A)	I_L calculated (A)	IAE (A)
1	-0.1659	0.1001	0.10018154	0.00008154	0.10021151	0.00011151
2	-0.1281	0.1000	0.10012506	0.00012506	0.10015227	0.00015227
3	-0.0888	0.0999	0.10006634	0.00016634	0.10009069	0.00019069
4	-0.0490	0.0999	0.10000688	0.00010688	0.10002834	0.00012834
5	-0.0102	0.0999	0.09994894	0.00004894	0.09996763	0.00006763
6	0.0275	0.0998	0.09989268	0.00009268	0.09990874	0.00010874
7	0.0695	0.0999	0.09983014	0.00006986	0.09984342	0.00005658
8	0.1061	0.0998	0.09977592	0.00002408	0.09978514	0.00001486
9	0.1460	0.0998	0.09971549	0.00008451	0.09972260	0.00007740
10	0.1828	0.0997	0.09966050	0.00003950	0.09966491	0.00003509
11	0.2230	0.0997	0.09960043	0.00009957	0.09960189	0.00009811
12	0.2600	0.0996	0.09954514	0.00005486	0.09954387	0.00005613
13	0.3001	0.0997	0.09948520	0.00021480	0.09948096	0.00021904
14	0.3406	0.0996	0.09942463	0.00017537	0.09941735	0.00018265
15	0.3789	0.0995	0.09936727	0.00013273	0.09935706	0.00014294
16	0.4168	0.0994	0.09931034	0.00008966	0.09929711	0.00010289
17	0.4583	0.0994	0.09924747	0.00015253	0.09923068	0.00016932
18	0.4949	0.0993	0.09919090	0.00010910	0.09917063	0.00012937
19	0.5370	0.0993	0.09912292	0.00017708	0.09909827	0.00020173
20	0.5753	0.0992	0.09905215	0.00014785	0.09902168	0.00017832
21	0.6123	0.0990	0.09896636	0.00003364	0.09892948	0.00007052
22	0.6546	0.0988	0.09881370	0.00001370	0.09876896	0.00003104
23	0.6918	0.0983	0.09855916	0.00025916	0.09850763	0.00020763
24	0.7318	0.0977	0.09797091	0.00027091	0.09792068	0.00022068
25	0.7702	0.0963	0.09667172	0.00037172	0.09664210	0.00034210
26	0.8053	0.0937	0.09407833	0.00037833	0.09409539	0.00039539
27	0.8329	0.0900	0.09026480	0.00026480	0.09032920	0.00032920
28	0.8550	0.0855	0.08546271	0.00003729	0.08555594	0.00005594
29	0.8738	0.0799	0.07977453	0.00012547	0.07987373	0.00002627
30	0.8887	0.0743	0.07405040	0.00024960	0.07413798	0.00016202
31	0.9016	0.0683	0.06815879	0.00014121	0.06822618	0.00007382
32	0.9141	0.0618	0.06159982	0.00020018	0.06164026	0.00015974
33	0.9248	0.0555	0.05532216	0.00017784	0.05533722	0.00016278
34	0.9344	0.0493	0.04918034	0.00011966	0.04917310	0.00012690
35	0.9445	0.0422	0.04221514	0.00001514	0.04218800	0.00001200
36	0.9533	0.0357	0.03574346	0.00004346	0.03570303	0.00000303
37	0.9618	0.0291	0.02915271	0.00005271	0.02910474	0.00000474
38	0.9702	0.0222	0.02232790	0.00012790	0.02227858	0.00007858
39	0.9778	0.0157	0.01589993	0.00019993	0.01585531	0.00015531
40	0.9852	0.0092	0.00942200	0.00022200	0.00938796	0.00018796
41	0.9926	0.0026	0.00273929	0.00013929	0.00272204	0.00012204
42	0.9999	-0.0040	-0.00404317	0.00004317	-0.00403767	0.00003767
43	1.0046	-0.0085	-0.00850506	0.00000506	-0.00848146	0.00001854
44	1.0089	-0.0124	-0.01264980	0.00024980	-0.01260726	0.00020726
Sum of IAE				0.00593491		0.00561477

Section 5.1. The experimental results over 50 independent runs are illustrated in Figure 14. It is obvious that ps does affect the performance of SDO. Specifically, a smaller value (e.g. ≤ 20) is beneficial to SDO. When the value of ps exceeds 20, the larger the value of ps , the worse the performance of SDO. In addition, SDO obtains the best mean RMSE values with $ps = 20$ on three PV models including the RTC France silicon solar cell, STM6-40/36 monocrystalline module, and STP6-120/36 polycrystalline module. While on the PVM 752 GaAs thin film cell, SDO with $ps = 10$ is slightly better than that with $ps = 20$. The main reasons are as follows:

- (i) The parameter extraction problem of PV models belongs to a low-dimensional optimization problem. There is no need to set a relatively large population. Notwithstanding enriching the population diversity with a large population, all markets (i.e., individuals) scatter in the whole search domain, which is not good for the convergence. Additionally, a large population means that a considerable number of fitness evaluations will be expended, especially that SDO expends $2 \times ps$ fitness evaluations at each iteration. In this context, the number of iterations will

TABLE 9: Experimental results on the STM6-40/36 module.

Model	Algorithm	Min	Max	Mean	Std. dev.	Significance
SDM	CLPSO	2.3723E-03	1.1682E-02	4.4191E-03	1.5097E-03	†
	DE/BBO	2.3456E-03	3.0233E-03	2.6869E-03	1.6177E-04	†
	GOTLBO	1.9424E-03	3.3244E-03	2.7496E-03	2.9176E-04	†
	IJAYA	1.7344E-03	2.4448E-03	1.8070E-03	1.1705E-04	†
	IWOA	1.7326E-03	3.9651E-03	2.7463E-03	5.1334E-04	†
	LETLBO	1.7385E-03	3.3171E-03	2.4289E-03	4.2059E-04	†
	MABC	3.0221E-03	3.0890E-02	1.0045E-02	6.7529E-03	†
	ODE	2.1744E-03	3.2718E-03	2.7751E-03	2.4512E-04	†
	SATLBO	1.7469E-03	2.4915E-03	1.9018E-03	1.2036E-04	†
	TLABC	1.7338E-03	2.1368E-03	1.8602E-03	1.0641E-04	†
	SDO	1.7298E-03	1.9500E-03	1.7703E-03	4.5108E-05	
DDM	CLPSO	2.7951E-03	1.0415E-02	4.3612E-03	1.2092E-03	†
	DE/BBO	2.3524E-03	3.0713E-03	2.7546E-03	1.7561E-04	†
	GOTLBO	2.3605E-03	4.7391E-03	3.4289E-03	6.0545E-04	†
	IJAYA	1.7310E-03	2.7828E-03	1.8875E-03	2.2946E-04	≈
	IWOA	1.7305E-03	3.7688E-03	2.8740E-03	5.2943E-04	†
	LETLBO	1.7646E-03	3.6799E-03	2.7820E-03	4.4982E-04	†
	MABC	3.1313E-03	2.5346E-02	1.0901E-02	6.7349E-03	†
	ODE	2.4339E-03	3.2422E-03	2.8297E-03	2.0219E-04	†
	SATLBO	1.7556E-03	4.2588E-03	1.9882E-03	3.4909E-04	†
	TLABC	1.7348E-03	2.1727E-03	1.8917E-03	1.0598E-04	†
	SDO	1.7298E-03	2.0288E-03	1.8118E-03	7.2421E-05	

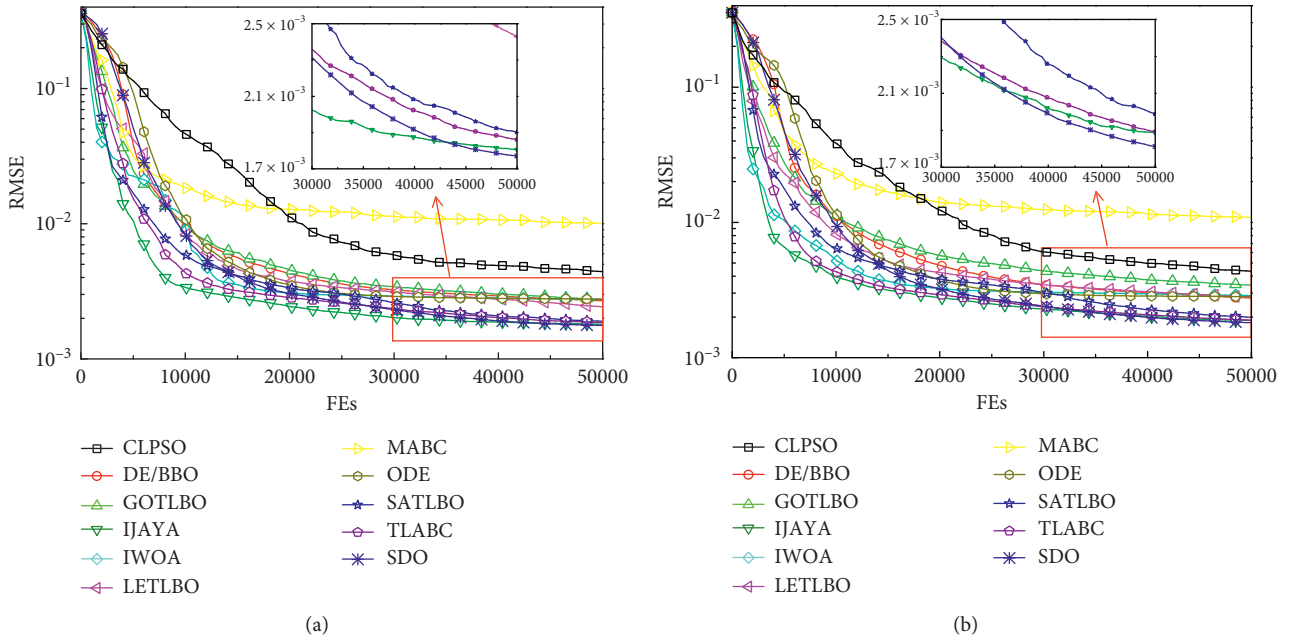


FIGURE 9: Convergence curves for the STM6-40/36 monocrystalline module. (a) SDM; (b) DDM.

be decreased significantly under a given Max_FEs, which is not conducive to low-dimensional optimization problems.

- (ii) The problem considered here is a typical multimodal optimization problem with many local minima. Although a very small population size can increase the number of iterations, the population diversity is low, resulting in poor possible movements of individuals. All individuals are easy to swarm towards

a certain local optima and thereby suffer from premature convergence. For example, we can see from Figure 14 that SDO with $ps = 10$ suffers from premature convergence frequently leading to relatively large values of RMSE over 50 runs on many cases such as Figures 14(a), 14(b), 14(f), and 14(g).

In fact, there is no axiom or rule that can be used to determine a proper population size for different optimization problems so far. With regards to the problem

TABLE 10: Extracted value for the parameters of the STM6-40/36 module by SDO.

Model	I_{ph} (A)	I_{sd1} (μ A)	R_s (Ω)	R_{sh} (Ω)	n_1	I_{sd2} (μ A)	n_2	RMSE
SDM	1.6639	1.7387	0.0043	15.9283	1.5203	—	—	$1.7298E-03$
DDM	1.6639	1.7385	0.0043	15.9372	1.5203	49.9985	54.5816	$1.7298E-03$

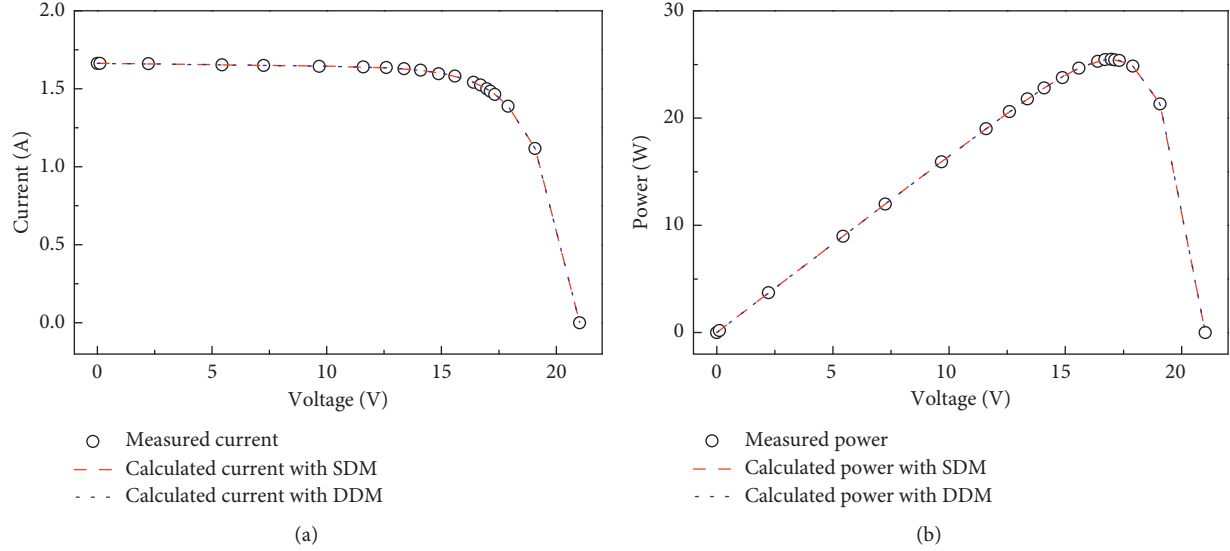


FIGURE 10: Comparison between the measured and calculated data achieved by SDO for the STM6-40/36 monocrystalline module. (a) I-V characteristic; (b) P-V characteristic.

TABLE 11: Calculated results for the STM6-40/36 module by SDO.

Item	V_L (V)	I_L measured (A)	SDM			DDM	
			I_L calculated (A)	IAE (A)	I_L calculated (A)	IAE (A)	
1	0.0000	1.6630	1.66345813	0.00045813	1.66345837	0.00045837	
2	0.1180	1.6630	1.66325224	0.00025224	1.66325248	0.00025248	
3	2.2370	1.6610	1.65955120	0.00144880	1.65955152	0.00144848	
4	5.4340	1.6530	1.65391445	0.00091445	1.65391477	0.00091477	
5	7.2600	1.6500	1.65056577	0.00056577	1.65056600	0.00056600	
6	9.6800	1.6450	1.64543056	0.00043056	1.64543061	0.00043061	
7	11.5900	1.6400	1.63923444	0.00076556	1.63923432	0.00076568	
8	12.6000	1.6360	1.63371579	0.00228421	1.63371559	0.00228441	
9	13.3700	1.6290	1.62728848	0.00171152	1.62728824	0.00171176	
10	14.0900	1.6190	1.61831518	0.00068482	1.61831493	0.00068507	
11	14.8800	1.5970	1.60306738	0.00606738	1.60306715	0.00606715	
12	15.5900	1.5810	1.58158500	0.00058500	1.58158482	0.00058482	
13	16.4000	1.5420	1.54232828	0.00032828	1.54232820	0.00032820	
14	16.7100	1.5240	1.52122523	0.00277477	1.52122518	0.00277482	
15	16.9800	1.5000	1.49920572	0.00079428	1.49920570	0.00079430	
16	17.1300	1.4850	1.48527115	0.00027115	1.48527114	0.00027114	
17	17.3200	1.4650	1.46564321	0.00064321	1.46564322	0.00064322	
18	17.9100	1.3880	1.38759934	0.00040066	1.38759934	0.00040066	
19	19.0800	1.1180	1.11837210	0.00037210	1.11837178	0.00037178	
20	21.0200	0.0000	-0.00002129	0.00002129	-0.00002130	0.00002130	
Sum of IAE				0.02177419		0.02177500	

considered in this work, it is recommended to set a moderate value with $ps = 20$ for SDO.

5.7. Comparison with Reported Results. In order to further verify the performance of SDO in solving the parameter

extraction problem of PV models, its results are compared with the reported results of some well-designed parameter extraction algorithms on the RTC France silicon solar cell. The comparison results are presented in Table 15. It shows that SDO is highly competitive. For the SDM, although it is worse than RF, RSS, and TSLLS, it is better than or similar

TABLE 12: Experimental results on the STP6-120/36 module.

Model	Algorithm	Min	Max	Mean	Std. dev.	Significance
SDM	CLPSO	1.6963E-02	4.1099E-02	2.3735E-02	5.8696E-03	†
	DE/BBO	2.4232E-02	3.5363E-02	2.8826E-02	2.6045E-03	†
	GOTLBO	1.7125E-02	3.4055E-02	2.1265E-02	3.3083E-03	†
	IJAYA	1.6622E-02	1.6953E-02	1.6799E-02	7.3789E-05	†
	IWOA	1.6607E-02	1.2215E-01	2.7637E-02	1.4981E-02	†
	LETLBO	1.6780E-02	4.6301E-02	1.9915E-02	4.9607E-03	†
	MABC	1.7238E-02	5.4369E-02	4.0777E-02	8.9788E-03	†
	ODE	1.6601E-02	3.9657E-02	2.5704E-02	6.4560E-03	†
	SATLBO	1.6652E-02	1.8713E-02	1.7042E-02	3.9219E-04	†
	TLABC	1.6605E-02	1.7300E-02	1.6784E-02	1.6458E-04	†
SDO	1.6601E-02	1.6866E-02	1.6683E-02	7.1751E-05		
DDM	CLPSO	1.6879E-02	4.7602E-02	2.5034E-02	6.7086E-03	†
	DE/BBO	2.1421E-02	3.6806E-02	2.9386E-02	2.9562E-03	†
	GOTLBO	1.7208E-02	4.3479E-02	2.6040E-02	7.2481E-03	†
	IJAYA	1.6632E-02	1.7935E-02	1.6823E-02	1.7512E-04	†
	IWOA	1.6629E-02	4.0750E-02	2.2580E-02	5.2119E-03	†
	LETLBO	1.6828E-02	3.1588E-02	1.9795E-02	3.0745E-03	†
	MABC	1.8634E-02	5.5329E-02	4.2947E-02	9.3427E-03	†
	ODE	1.6601E-02	3.8352E-02	2.5832E-02	6.3294E-03	†
	SATLBO	1.6678E-02	1.9395E-02	1.7107E-02	4.8711E-04	†
	TLABC	1.6633E-02	1.8324E-02	1.6836E-02	2.5365E-04	†
SDO	1.6601E-02	1.7268E-02	1.6741E-02	1.2362E-04		

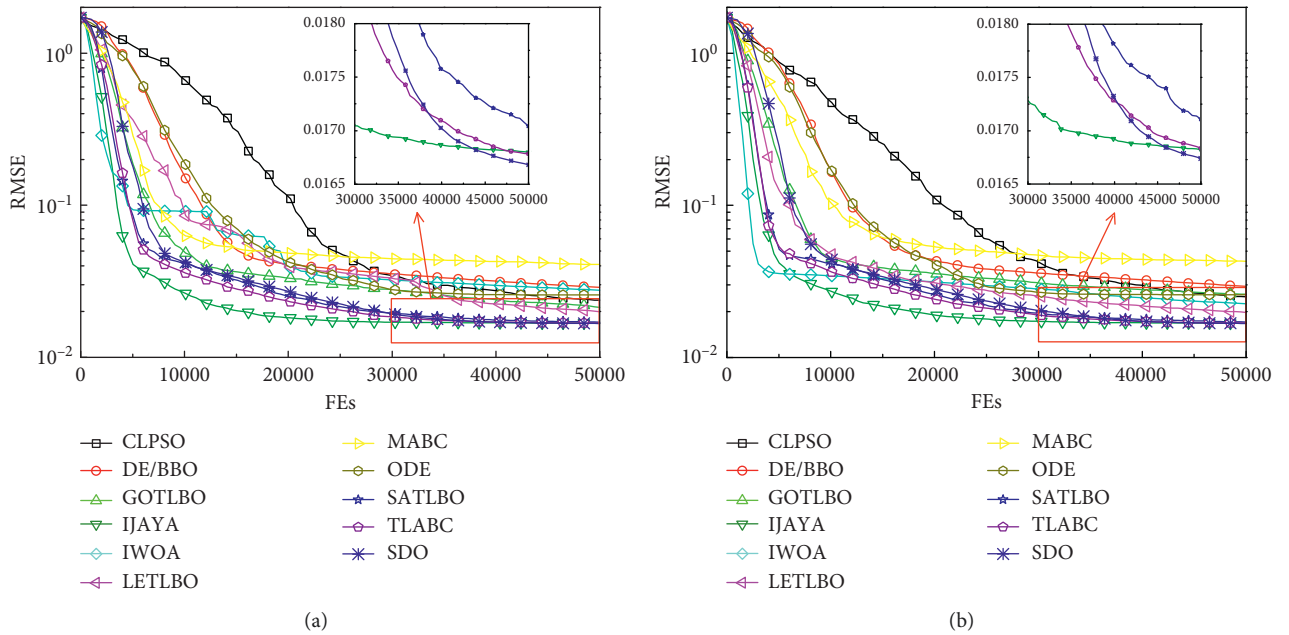


FIGURE 11: Convergence curves for the STP6-120/36 polycrystalline module. (a) SDM; (b) DDM.

TABLE 13: Extracted value for the parameters of STP6-120/36 module by SDO.

Model	I_{ph} (A)	I_{sd1} (μA)	R_s (Ω)	R_{sh} (Ω)	n_1	I_{sd2} (μA)	n_2	RMSE
SDM	7.4725	2.3350	0.0046	22.2199	1.2601	—	—	1.6601E-02
DDM	7.4725	6.1168E-02	0.0046	22.2350	48.2465	2.3354	1.2601	1.6601E-02

to other algorithms in terms of the minimum RMSE value. For the DDM, SDO achieves a very competitive minimum RMSE value that is only slightly larger than that of ABC-TRR.

Additionally, in terms of other RMSE values, SDO also yields comparable performance. In summary, the comparison demonstrates the good performance of SDO once again.

TABLE 14: Calculated results for the STP6-120/36 module by SDO.

Item	V_L (V)	I_L measured (A)	SDM		DDM	
			I_L calculated (A)	IAE (A)	I_L calculated (A)	IAE (A)
1	19.2100	0.0000	0.00116434	0.00116434	0.00115600	0.00115600
2	17.6500	3.8300	3.83228233	0.00228233	3.83228460	0.00228460
3	17.4100	4.2900	4.27392911	0.01607089	4.27393114	0.01606886
4	17.2500	4.5600	4.54628987	0.01371013	4.54629162	0.01370838
5	17.1000	4.7900	4.78583302	0.00416698	4.78583443	0.00416557
6	16.9000	5.0700	5.08193389	0.01193389	5.08193481	0.01193481
7	16.7600	5.2700	5.27376516	0.00376516	5.27376571	0.00376571
8	16.3400	5.7500	5.77681381	0.02681381	5.77681335	0.02681335
9	16.0800	6.0000	6.03749239	0.03749239	6.03749146	0.03749146
10	15.7100	6.3600	6.34872743	0.01127257	6.34872610	0.01127390
11	15.3900	6.5800	6.56792937	0.01207063	6.56792798	0.01207202
12	14.9300	6.8300	6.81486011	0.01513989	6.81485901	0.01514099
13	14.5800	6.9700	6.95844905	0.01155095	6.95844839	0.01155161
14	14.1700	7.1000	7.08813731	0.01186269	7.08813732	0.01186268
15	13.5900	7.2300	7.21776104	0.01223896	7.21776204	0.01223796
16	13.1600	7.2900	7.28413003	0.00586997	7.28413171	0.00586829
17	12.7400	7.3400	7.33148314	0.00851686	7.33148538	0.00851462
18	12.3600	7.3700	7.36326482	0.00673518	7.36326746	0.00673254
19	11.8100	7.3800	7.39587315	0.01587315	7.39587620	0.01587620
20	11.1700	7.4100	7.42026500	0.01026500	7.42026828	0.01026828
21	10.3200	7.4400	7.43909223	0.00090777	7.43909549	0.00090451
22	9.7400	7.4200	7.44671497	0.02671497	7.44671805	0.02671805
23	9.0600	7.4500	7.45253755	0.00253755	7.45254032	0.00254032
24	0.0000	7.4800	7.47098178	0.00901822	7.47097731	0.00902269
Sum of IAE				0.27797428		0.27797339

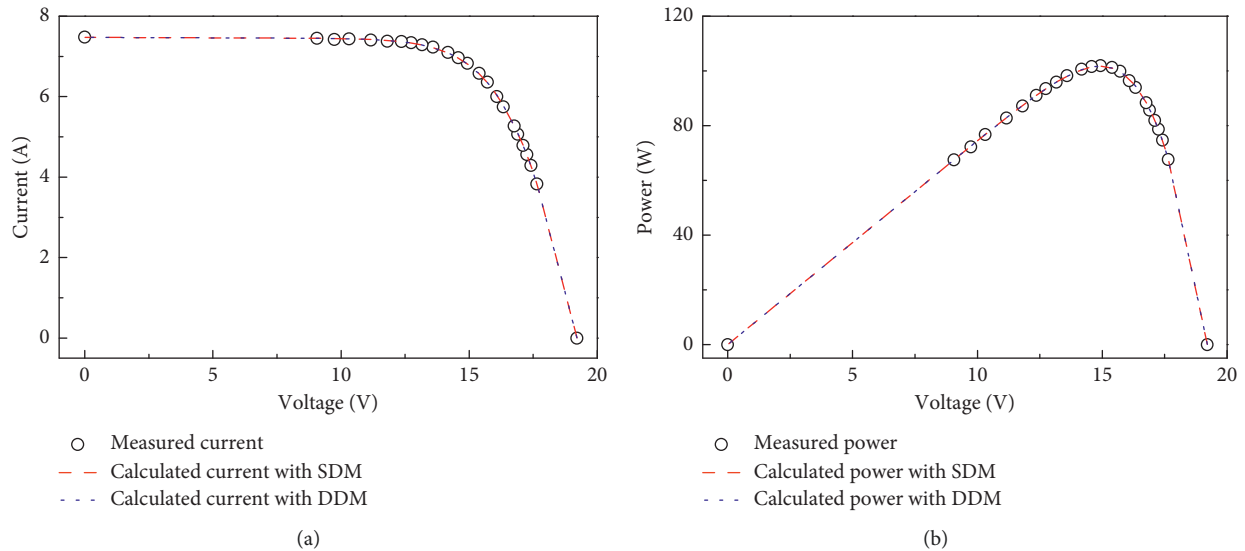


FIGURE 12: Comparison between the measured and calculated data achieved by SDO for the STP6-120/36 polycrystalline module. (a) I-V characteristic; (b) P-V characteristic.

6. Conclusions and Future Work

SDO is a very new and effective metaheuristic. In this paper, SDO is first applied to the parameter extraction problem of PV models. Its feasibility and effectiveness are experimentally verified via four PV models including cells and modules with different characteristics. The experimental results summarize that

- (i) SDO performs better or competitively compared with other well-designed algorithms according to both simulation results and Wilcoxon's rank sum test results. It, overall, obtains the first ranking according to the Friedman test.
- (ii) SDO exhibits good convergence property especially at the later stage of evolutionary process, indicating

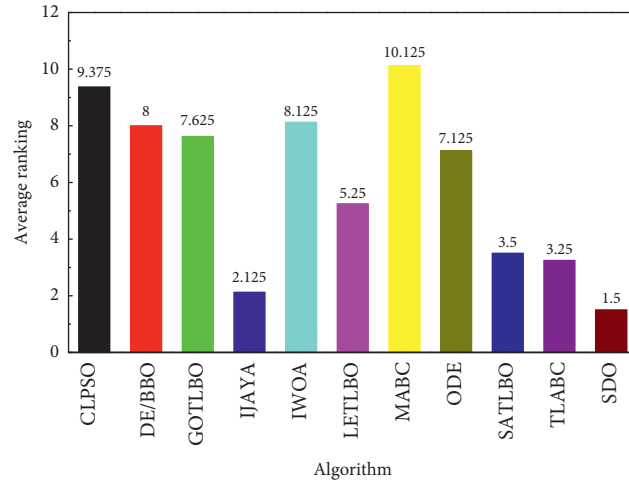


FIGURE 13: Friedman test result.

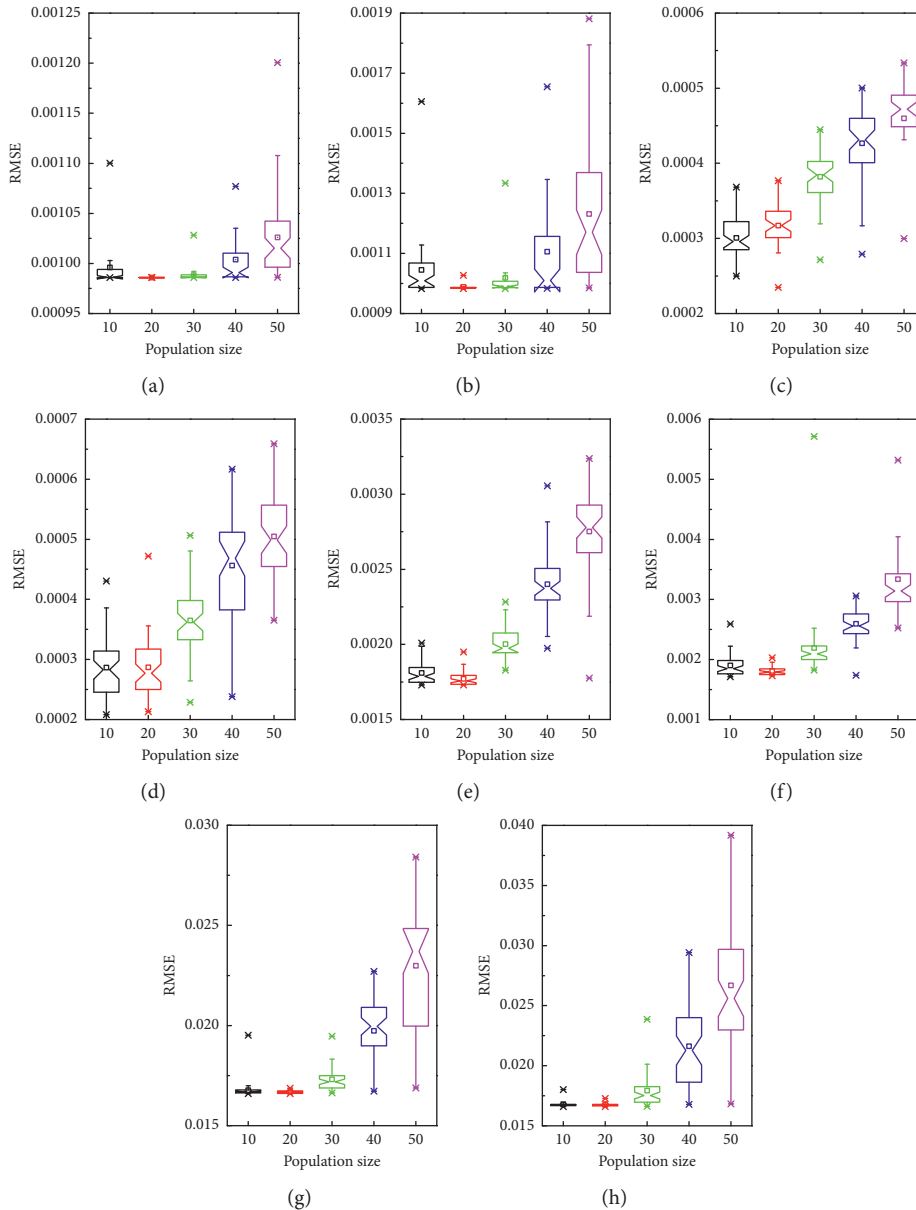


FIGURE 14: Influence of population size on SDO. (a) RTC France silicon solar cell with the SDM; (b) RTC France silicon solar cell with DDM; (c) PVM 752 GaAs thin film cell with the SDM; (d) PVM 752 GaAs thin film cell with the DDM; (e) STM6-40/36 monocrystalline module with the SDM; (f) STM6-40/36 monocrystalline module with the DDM; (g) STP6-120/36 polycrystalline module with the SDM; (h) STP6-120/36 polycrystalline module with the DDM.

TABLE 15: Comparison with reported results on the RTC France solar cell.

Model	Algorithm	Min	Max	Mean	Std. dev.
SDM	RF [60]	$7.7301E-04$	NA	NA	NA
	RSS [61]	$7.7301E-04$	NA	NA	NA
	LI [62]	$1.0548E-03$	NA	NA	NA
	TSLLS [63]	$7.7301E-04$	NA	NA	NA
	Tong and Pora [49]	$1.5051E-03$	NA	NA	NA
	Tayyan [64]	$2.9117E-03$	NA	NA	NA
	MABC [65]	$9.862E-04$	NA	NA	NA
	ABSO [66]	$9.9124E-04$	NA	NA	NA
	BBO-M [67]	$9.8634E-04$	NA	NA	NA
	GGHS [68]	$9.9078E-04$	NA	NA	NA
	CARO [69]	$9.8665E-04$	NA	NA	NA
	SOS [24]	$9.8609E-04$	$1.1982E-03$	$1.0245E-03$	$5.2184E-05$
	MSSO [70]	$9.8607E-04$	NA	NA	NA
	CWOA [21]	$9.8604E-04$	NA	NA	$1.0216E-08$
	CSO [71]	$9.8602E-04$	NA	$9.8602E-04$	$5.4941E-09$
	MADE [72]	$9.8602E-04$	$9.8602E-04$	$9.8602E-04$	$2.74E-15$
	EO-Jaya [73]	$9.8603E-04$	NA	NA	NA
	ILCOA [74]	$9.8602E-04$	NA	NA	NA
	FPSO [75]	$9.8602E-04$	NA	NA	$2.0142E-08$
	PGJAYA [76]	$9.8602E-04$	$9.8602E-04$	$9.8602E-04$	$1.4485E-09$
	OBWOA [77]	$9.8602E-04$	NA	NA	NA
	ABC-TRR [78]	$9.8602E-04$	$9.8602E-04$	$9.8602E-04$	$6.15E-17$
	NM-MPSO [79]	$9.8602E-04$	NA	NA	NA
SDO	$9.8602E-04$	$9.8616E-04$	$9.8603E-04$	$2.5141E-08$	
DDM	MABC [65]	$9.8276E-04$	NA	NA	NA
	ABSO [66]	$9.8344E-04$	NA	NA	NA
	BBO-M [67]	$9.8272E-04$	NA	NA	NA
	IGHS [68]	$9.8635E-04$	NA	NA	NA
	CARO [69]	$9.8260E-04$	NA	NA	NA
	SOS [24]	$9.8518E-04$	$1.3498E-03$	$1.0627E-03$	$9.6141E-05$
	MSSO [70]	$9.8281E-04$	NA	NA	NA
	CWOA [21]	$9.8279E-04$	NA	NA	$1.1333E-07$
	CSO [71]	$9.8252E-04$	NA	$9.9619E-04$	$3.4681E-05$
	MADE [72]	$9.8261E-04$	$9.8786E-04$	$9.8608E-04$	$8.02E-05$
	EO-Jaya [73]	$9.8262E-04$	NA	NA	NA
	ILCOA [74]	$9.8257E-04$	NA	NA	NA
	FPSO [75]	$9.8253E-04$	NA	NA	$3.1469E-08$
	PGJAYA [76]	$9.8263E-04$	$9.9499E-04$	$9.8582E-04$	$2.5375E-05$
	OBWOA [77]	$9.8251E-04$	NA	NA	NA
	ABC-TRR [78]	$9.8249E-04$	$9.8602E-03$	$9.8256E-03$	$4.95E-07$
	NM-MPSO [79]	$9.8250E-04$	NA	NA	NA
	EVPS [80]	$9.8510E-04$	$1.1190E-03$	$1.0083E-03$	$2.5375E-05$
SDO	$9.8250E-04$	$1.0271E-03$	$9.8822E-04$	$8.8518E-06$	

NA: not available in the literature.

it is with the capability of jumping out of local optima and exploring more promising regions.

- (iii) The population size affects the performance of SDO significantly. In general, a small size is relatively safe for low-dimensional optimization problems. For the problem considered in this work, the size setting as 20 is recommended for SDO.

The experimental results and comparisons demonstrate that SDO can serve as a promising alternative to extract accurate and reliable parameters for PV models. In future work, on one hand, local search methods and adaptive learning strategies will be employed to accelerate SDO's convergence rate especially at the early stage and to choose appropriate population sizes for SDO in solving different optimization

problems, respectively. On the other hand, attempts will be made to apply SDO to other electrical engineering problems such as MPPT, economic dispatch, and optimal power flow.

Nomenclature

I_d :	Diode current (A)
I_L :	Output current (A)
I_{ph} :	Photogenerated current (A)
I_{sd} , I_{sd1} , and I_{sd2} :	Saturation currents (A)
I_{sh} :	Shunt resistor current (A)
k :	Boltzmann constant
n , n_1 , and n_2 :	Diode ideality factors
N_p :	Number of cells in parallel

N_s :	Number of cells in series	ILCOA:	Improved Lozi map-based chaotic optimization
q :	Electron charge	IWOA:	Improved whale optimization algorithm
R_s :	Series resistance (Ω)	LETLBO:	Teaching-learning-based optimization with learning experience of other learners
R_{sh} :	Shunt resistance (Ω)	LI:	Linear identification method
T :	Cell temperature (K)	MABC:	Modified artificial bee colony algorithm
V_L :	Output voltage (V)	MADE:	Memetic adaptive differential evolution
V_t :	Diode thermal voltage (V)	MSSO:	Modified simplified swarm optimization
$I-V$:	Current-voltage	NM-MPSO:	Hybrid nelder–mead and modified particle swarm optimization
$P-V$:	Power-voltage	OBWOA:	Improved opposition-based whale optimization algorithm
PV:	Photovoltaic	ODE:	Opposition-based differential evolution
N :	Number of experimental data	PGJAYA:	Performance-guided Jaya algorithm
x :	Extracted parameters vector	RF:	Reduced form method
SDM:	Single diode model	RSS:	Reduced-space search
DDM:	Double diode model	SATLBO:	Self-adaptive teaching-learning-based optimization
IAE:	Individual absolute error	SDO:	Supply-demand-based optimization
RMSE:	Root mean square error	SOS:	Symbiotic organisms search
Min:	Minimum RMSE	Tayyan:	Tayyan’s method
Max:	Maximum RMSE	TLABC:	Teaching-learning-based artificial bee colony
Mean:	Mean RMSE	Tong and Pora:	Tong and Pora’s method
Std. Dev:	Standard deviation	TSLLS:	Two-step linear least-squares method.
D :	Dimension of extracted parameters vector		
ps:	Size of population		
t :	Current iteration		
t_{max} :	Maximum number of iterations		
Max_FEs:	Maximum number of fitness evaluations		
E_e :	Equilibrium point		
P_i :	i th price solution		
P_{best} :	Best price solution found so far		
Q_i :	i th quantity solution		
TP_i :	i th trial price solution		
TQ_i :	i th trial quantity solution		
K_g :	Supply slop		
K_f :	Demand slop		
α :	Supply weight		
β :	Demand weight		
$r_1, r_2, r_3,$ and r_4 :	Random real numbers in (0, 1)		
ABSO:	Artificial bee swarm optimization		
ABC-TRR:	Hybrid trust-region reflective algorithm		
BBO-M:	Biogeography-based optimization with mutation strategies		
CARO:	Chaotic asexual reproduction optimization		
CLPSO:	Comprehensive learning particle swarm optimizer		
CSO:	Cat swarm optimization		
CWOA:	Improved chaotic whale optimization algorithm		
DE/BBO:	Hybrid differential evolution with biogeography-based optimization		
EO-Jaya:	Elite opposition-based Jaya algorithm		
EVPS:	Enhanced vibrating particles system		
FPSO:	Flexible particle swarm optimization		
GGHS:	Grouping-based global harmony search		
GOTLBO:	Generalized oppositional teaching-learning-based optimization		
IGHS:	Innovative global harmony search		
IJAYA:	Improved Jaya optimization algorithm		

Data Availability

The data used to support the findings of this study are available from the corresponding author upon request.

Conflicts of Interest

The authors declare that they have no conflicts of interest.

Acknowledgments

The authors would like to thank Dr. Weiguo Zhao for providing the original code of SDO. This work was supported by the National Natural Science Foundation of China (Grant nos. 51907035, 51867005, and 51667007), the Scientific Research Foundation for the Introduction of Talent of Guizhou University (Grant no. [2017]16), the Guizhou Province Science and Technology Innovation Talent Team Project (Grant no. [2018]5615), the Guizhou Education Department Growth Foundation for Youth Scientific and Technological Talents (Grant no. QianJiaoHe KY Zi [2018] 108), and the Science and Technology Foundation of Guizhou Province (Grant no. QianKeHe Platform Talents [2018]5781).

References

- [1] M. H. Rehmani, M. Reisslein, A. Rachedi, M. Erol-Kantarci, and M. Radenkovic, “Integrating renewable energy resources into the smart grid: recent developments in information and

- communication technologies,” *IEEE Transactions on Industrial Informatics*, vol. 14, no. 7, pp. 2814–2825, 2018.
- [2] N. A. Ludin, N. I. Mustafa, M. M. Hanafiah et al., “Prospects of life cycle assessment of renewable energy from solar photovoltaic technologies: a review,” *Renewable and Sustainable Energy Reviews*, vol. 96, pp. 11–28, 2018.
 - [3] P. Li, W. Gu, L. Wang, B. Xu, M. Wu, and W. Shen, “Dynamic equivalent modeling of two-staged photovoltaic power station clusters based on dynamic affinity propagation clustering algorithm,” *International Journal of Electrical Power & Energy Systems*, vol. 95, pp. 463–475, 2018.
 - [4] International Energy Agency, *Renewables 2018*, International Energy Agency, Paris, France, 2018.
 - [5] A. M. Humada, M. Hojabri, S. Mekhilef, and H. M. Hamada, “Solar cell parameters extraction based on single and double-diode models: a review,” *Renewable and Sustainable Energy Reviews*, vol. 56, pp. 494–509, 2016.
 - [6] R. C. M. Gomes, M. A. Vitorino, D. A. Fernandes, and R. Wang, “Shuffled complex evolution on photovoltaic parameter extraction: a comparative analysis,” *IEEE Transactions on Sustainable Energy*, vol. 8, no. 2, pp. 805–815, 2016.
 - [7] W. Li, M. C. Paul, M. Rolley et al., “A scaling law for monocrystalline PV/T modules with CCPC and comparison with triple junction PV cells,” *Applied Energy*, vol. 202, pp. 755–771, 2017.
 - [8] S. Raj, A. Kumar Sinha, and A. K. Panchal, “Solar cell parameters estimation from illuminated I-V characteristic using linear slope equations and Newton-Raphson technique,” *Journal of Renewable and Sustainable Energy*, vol. 5, no. 3, Article ID 033105, 2013.
 - [9] M. G. Villalva, J. R. Gazoli, and E. R. Filho, “Comprehensive approach to modeling and simulation of photovoltaic arrays,” *IEEE Transactions on Power Electronics*, vol. 24, no. 5, pp. 1198–1208, 2009.
 - [10] Y. Xu, X. Kong, Y. Zeng, S. Tao, and X. Xiao, “A modeling method for photovoltaic cells using explicit equations and optimization algorithm,” *International Journal of Electrical Power & Energy Systems*, vol. 59, pp. 23–28, 2014.
 - [11] G. Xiong, D. Shi, and X. Duan, “Multi-strategy ensemble biogeography-based optimization for economic dispatch problems,” *Applied Energy*, vol. 111, pp. 801–811, 2013.
 - [12] G. Xiong, J. Zhang, D. Shi, and Y. He, “Parameter identification of solid oxide fuel cells with ranking teaching-learning based algorithm,” *Energy Conversion and Management*, vol. 174, pp. 126–137, 2018.
 - [13] G. Xiong, D. Shi, J. Zhang, and Y. Zhang, “A binary coded brain storm optimization for fault section diagnosis of power systems,” *Electric Power Systems Research*, vol. 163, pp. 441–451, 2018.
 - [14] M. S. Ismail, M. Moghavvemi, and T. M. I. Mahlia, “Characterization of PV panel and global optimization of its model parameters using genetic algorithm,” *Energy Conversion and Management*, vol. 73, pp. 10–25, 2013.
 - [15] C. Chellaswamy and R. Ramesh, “Parameter extraction of solar cell models based on adaptive differential evolution algorithm,” *Renewable Energy*, vol. 97, pp. 823–837, 2016.
 - [16] P. P. Biswas, P. N. Suganthan, G. Wu, and G. A. J. Amaratunga, “Parameter estimation of solar cells using datasheet information with the application of an adaptive differential evolution algorithm,” *Renewable Energy*, vol. 132, pp. 425–438, 2019.
 - [17] A. R. Jordehi, “Enhanced leader particle swarm optimisation (ELPSO): an efficient algorithm for parameter estimation of photovoltaic (PV) cells and modules,” *Solar Energy*, vol. 159, pp. 78–87, 2018.
 - [18] M. Merchaoui, A. Sakly, and M. F. Mimouni, “Particle swarm optimisation with adaptive mutation strategy for photovoltaic solar cell/module parameter extraction,” *Energy Conversion and Management*, vol. 175, pp. 151–163, 2018.
 - [19] A. Askarzadeh and L. D. S. Coelho, “Determination of photovoltaic modules parameters at different operating conditions using a novel bird mating optimizer approach,” *Energy Conversion and Management*, vol. 89, pp. 608–614, 2015.
 - [20] E. E. Ali, M. A. El-Hameed, A. A. El-Fergany, and M. M. El-Arini, “Parameter extraction of photovoltaic generating units using multi-verse optimizer,” *Sustainable Energy Technologies and Assessments*, vol. 17, pp. 68–76, 2016.
 - [21] D. Oliva, M. Abd El Aziz, and A. Ella Hassanien, “Parameter estimation of photovoltaic cells using an improved chaotic whale optimization algorithm,” *Applied Energy*, vol. 200, pp. 141–154, 2017.
 - [22] X. Chen, K. Yu, W. Du, W. Zhao, and G. Liu, “Parameters identification of solar cell models using generalized oppositional teaching learning based optimization,” *Energy*, vol. 99, pp. 170–180, 2016.
 - [23] K. Yu, J. J. Liang, B. Y. Qu, X. Chen, and H. Wang, “Parameters identification of photovoltaic models using an improved JAYA optimization algorithm,” *Energy Conversion and Management*, vol. 150, pp. 742–753, 2017.
 - [24] G. Xiong, J. Zhang, X. Yuan, D. Shi, and Y. He, “Application of symbiotic organisms search algorithm for parameter extraction of solar cell models,” *Applied Sciences*, vol. 8, no. 11, p. 2155, 2018.
 - [25] G. Xiong, J. Zhang, D. Shi, and Y. He, “Parameter extraction of solar photovoltaic models using an improved whale optimization algorithm,” *Energy Conversion and Management*, vol. 174, pp. 388–405, 2018.
 - [26] G. Xiong, J. Zhang, X. Yuan, D. Shi, Y. He, and G. Yao, “Parameter extraction of solar photovoltaic models by means of a hybrid differential evolution with whale optimization algorithm,” *Solar Energy*, vol. 176, pp. 742–761, 2018.
 - [27] R. Abbassi, A. Abbassi, A. A. Heidari, and S. Mirjalili, “An efficient salp swarm-inspired algorithm for parameters identification of photovoltaic cell models,” *Energy Conversion and Management*, vol. 179, pp. 362–372, 2019.
 - [28] H. G. G. Nunes, J. A. N. Pombo, P. M. R. Bento, S. J. P. S. Mariano, and M. R. A. Calado, “Collaborative swarm intelligence to estimate PV parameters,” *Energy Conversion and Management*, vol. 185, pp. 866–890, 2019.
 - [29] B. Subudhi and R. Pradhan, “Bacterial foraging optimization approach to parameter extraction of a photovoltaic module,” *IEEE Transactions on Sustainable Energy*, vol. 9, no. 1, pp. 381–389, 2018.
 - [30] S. Li, W. Gong, X. Yan et al., “Parameter extraction of photovoltaic models using an improved teaching-learning-based optimization,” *Energy Conversion and Management*, vol. 186, pp. 293–305, 2019.
 - [31] X. Gao, Y. Cui, J. Hu et al., “Parameter extraction of solar cell models using improved shuffled complex evolution algorithm,” *Energy Conversion and Management*, vol. 157, pp. 460–479, 2018.
 - [32] A. Valdivia-González, D. Zaldívar, E. Cuevas, M. Pérez-Cisneros, F. Fausto, and A. González, “A chaos-embedded gravitational search algorithm for the identification of electrical parameters of photovoltaic cells,” *Energies*, vol. 1052, 2017.

- [33] J. P. Ram, T. S. Babu, T. Dragicevic, and N. Rajasekar, "A new hybrid bee pollinator flower pollination algorithm for solar PV parameter estimation," *Energy Conversion and Management*, vol. 135, pp. 463–476, 2017.
- [34] H. Rezk and A. Fathy, "A novel optimal parameters identification of triple-junction solar cell based on a recently meta-heuristic water cycle algorithm," *Solar Energy*, vol. 157, pp. 778–791, 2017.
- [35] S. Bana and R. P. Saini, "Identification of unknown parameters of a single diode photovoltaic model using particle swarm optimization with binary constraints," *Renewable Energy*, vol. 101, pp. 1299–1310, 2017.
- [36] A. Fathy and H. Rezk, "Parameter estimation of photovoltaic system using imperialist competitive algorithm," *Renewable Energy*, vol. 111, pp. 307–320, 2017.
- [37] D. Kler, P. Sharma, A. Banerjee, K. P. S. Rana, and V. Kumar, "PV cell and module efficient parameters estimation using evaporation rate based water cycle algorithm," *Swarm and Evolutionary Computation*, vol. 35, pp. 93–110, 2017.
- [38] D. H. Muhsen, A. B. Ghazali, T. Khatib, and I. A. Abed, "A comparative study of evolutionary algorithms and adapting control parameters for estimating the parameters of a single-diode photovoltaic module's model," *Renewable Energy*, vol. 96, pp. 377–389, 2016.
- [39] K. Ishaque, Z. Salam, S. Mekhilef, and A. Shamsudin, "Parameter extraction of solar photovoltaic modules using penalty-based differential evolution," *Applied Energy*, vol. 99, pp. 297–308, 2012.
- [40] V. J. Chin, Z. Salam, and K. Ishaque, "An accurate and fast computational algorithm for the two-diode model of PV module based on a hybrid method," *IEEE Transactions on Industrial Electronics*, vol. 64, no. 8, pp. 6212–6222, 2017.
- [41] D. H. Wolpert and W. G. Macready, "No free lunch theorems for optimization," *IEEE Transactions on Evolutionary Computation*, vol. 1, no. 1, pp. 67–82, 1997.
- [42] W. Zhao, L. Wang, and Z. Zhang, "Supply-demand-based optimization: a novel economics-inspired algorithm for global optimization," *IEEE Access*, vol. 7, pp. 73182–73206, 2019.
- [43] F. V. Waugh, "Cobweb models," *American Journal of Agricultural Economics*, vol. 46, no. 5, pp. 732–750, 1964.
- [44] C. Chiarella, "The cobweb model," *Economic Modelling*, vol. 5, no. 4, pp. 377–384, 1988.
- [45] A. Ashouri-Zadeh, M. Toulabi, A. S. Dobakhshari, S. Taghipour-Broujeni, and A. M. Ranjbar, "A novel technique to extract the maximum power of photovoltaic array in partial shading conditions," *International Journal of Electrical Power & Energy Systems*, vol. 101, pp. 500–512, 2018.
- [46] V. J. Chin, Z. Salam, and K. Ishaque, "Cell modelling and model parameters estimation techniques for photovoltaic simulator application: a review," *Applied Energy*, vol. 154, pp. 500–519, 2015.
- [47] R. Gammoudi, H. Brahmi, and R. Dhifaoui, "Estimation of climatic parameters of a PV system based on gradient method," *Complexity*, vol. 2019, Article ID 7385927, 10 pages, 2019.
- [48] T. Easwarakhanthan, J. Bottin, I. Bouhouch, and C. Boutrit, "Nonlinear minimization algorithm for determining the solar cell parameters with microcomputers," *International Journal of Solar Energy*, vol. 4, no. 1, pp. 1–12, 1986.
- [49] N. T. Tong and W. Pora, "A parameter extraction technique exploiting intrinsic properties of solar cells," *Applied Energy*, vol. 176, pp. 104–115, 2016.
- [50] J. J. Liang, A. K. Qin, P. N. Suganthan, and S. Baskar, "Comprehensive learning particle swarm optimizer for global optimization of multimodal functions," *IEEE Transactions on Evolutionary Computation*, vol. 10, no. 3, pp. 281–295, 2006.
- [51] W. Gong, Z. Cai, and C. X. Ling, "DE/BBO: a hybrid differential evolution with biogeography-based optimization for global numerical optimization," *Soft Computing*, vol. 15, no. 4, pp. 645–665, 2010.
- [52] F. Zou, L. Wang, X. Hei, and D. Chen, "Teaching-learning-based optimization with learning experience of other learners and its application," *Applied Soft Computing*, vol. 37, pp. 725–736, 2015.
- [53] W.-F. Gao and S.-Y. Liu, "A modified artificial bee colony algorithm," *Computers & Operations Research*, vol. 39, no. 3, pp. 687–697, 2012.
- [54] S. Rahnamayan, H. R. Tizhoosh, and M. M. A. Salama, "Opposition-based differential evolution," *IEEE Transactions on Evolutionary Computation*, vol. 12, no. 1, pp. 64–79, 2008.
- [55] X. Chen, B. Xu, C. Mei, Y. Ding, and K. Li, "Teaching-learning-based artificial bee colony for solar photovoltaic parameter estimation," *Applied Energy*, vol. 212, pp. 1578–1588, 2018.
- [56] K. Yu, X. Chen, X. Wang, and Z. Wang, "Parameters identification of photovoltaic models using self-adaptive teaching-learning-based optimization," *Energy Conversion and Management*, vol. 145, pp. 233–246, 2017.
- [57] S. García, D. Molina, M. Lozano, and F. Herrera, "A study on the use of non-parametric tests for analyzing the evolutionary algorithms' behaviour: a case study on the CEC'2005 special session on real parameter optimization," *Journal of Heuristics*, vol. 15, no. 6, pp. 617–644, 2009.
- [58] G. Xiong, J. Zhang, X. Yuan et al., "A novel method for economic dispatch with across neighborhood search: a case study in a provincial power grid, China," *Complexity*, vol. 2018, Article ID 2591341, 18 pages, 2018.
- [59] G. Xiong and D. Shi, "Hybrid biogeography-based optimization with brain storm optimization for non-convex dynamic economic dispatch with valve-point effects," *Energy*, vol. 157, pp. 424–435, 2018.
- [60] A. Laudani, F. Riganti Fulginei, and A. Salvini, "High performing extraction procedure for the one-diode model of a photovoltaic panel from experimental I-V curves by using reduced forms," *Solar Energy*, vol. 103, no. 103, pp. 316–326, 2014.
- [61] A. A. Cardenas, M. Carrasco, F. Mancilla-David, A. Street, and R. Cardenas, "Experimental parameter extraction in the single-diode photovoltaic model via a reduced-space search," *IEEE Transactions on Industrial Electronics*, vol. 64, no. 2, pp. 1468–1476, 2017.
- [62] H. I. L. Li, Z. Ye, J. Ye, D. Yang, and H. Du, "A linear identification of diode models from single I-V characteristics of PV panels," *IEEE Transactions on Industrial Electronics*, vol. 62, no. 7, pp. 4181–4193, 2015.
- [63] F. J. Toledo, J. M. Blanes, and V. Galiano, "Two-step linear least-squares method for photovoltaic single-diode model parameters extraction," *IEEE Transactions on Industrial Electronics*, vol. 65, no. 8, pp. 6301–6308, 2018.
- [64] A. A. E. Tayyan, "An approach to extract the parameters of solar cells from their illuminated I-V curves using the Lambert W function," *Sudan University of Science & Technology*, vol. 39, pp. 1–15, 2015.
- [65] M. Jamadi, F. Merrikh-Bayat, and M. Bigdeli, "Very accurate parameter estimation of single- and double-diode solar cell models using a modified artificial bee colony algorithm," *International Journal of Energy and Environmental Engineering*, vol. 7, no. 1, pp. 13–25, 2016.

- [66] A. Askarzadeh and A. Rezaadeh, "Artificial bee swarm optimization algorithm for parameters identification of solar cell models," *Applied Energy*, vol. 102, no. 2, pp. 943–949, 2013.
- [67] Q. Niu, L. Zhang, and K. Li, "A biogeography-based optimization algorithm with mutation strategies for model parameter estimation of solar and fuel cells," *Energy Conversion and Management*, vol. 86, pp. 1173–1185, 2014.
- [68] A. Askarzadeh and A. Rezaadeh, "Parameter identification for solar cell models using harmony search-based algorithms," *Solar Energy*, vol. 86, no. 11, pp. 3241–3249, 2012.
- [69] X. Yuan, Y. He, and L. Liu, "Parameter extraction of solar cell models using chaotic asexual reproduction optimization," *Neural Computing and Applications*, vol. 26, no. 5, pp. 1227–1239, 2015.
- [70] P. Lin, S. Cheng, W. Yeh, Z. Chen, and L. Wu, "Parameters extraction of solar cell models using a modified simplified swarm optimization algorithm," *Solar Energy*, vol. 144, pp. 594–603, 2017.
- [71] L. Guo, Z. Meng, Y. Sun, and L. Wang, "Parameter identification and sensitivity analysis of solar cell models with cat swarm optimization algorithm," *Energy Conversion and Management*, vol. 108, pp. 520–528, 2016.
- [72] S. Li, W. Gong, X. Yan, C. Hu, D. Bai, and L. Wang, "Parameter estimation of photovoltaic models with memetic adaptive differential evolution," *Solar Energy*, vol. 190, pp. 465–474, 2019.
- [73] L. Wang and C. Huang, "A novel elite opposition-based Jaya algorithm for parameter estimation of photovoltaic cell models," *Optik*, vol. 155, pp. 351–356, 2018.
- [74] N. Pourmousa, S. M. Ebrahimi, M. Malekzadeh, and M. Alizadeh, "Parameter estimation of photovoltaic cells using improved Lozi map based chaotic optimization algorithm," *Solar Energy*, vol. 180, pp. 180–191, 2019.
- [75] S. M. Ebrahimi, E. Salahshour, M. Malekzadeh, and F. Francisco Gordillo, "Parameters identification of PV solar cells and modules using flexible particle swarm optimization algorithm," *Energy*, vol. 179, pp. 358–372, 2019.
- [76] K. Yu, B. Qu, C. Yue, S. Ge, X. Chen, and J. Liang, "A performance-guided JAYA algorithm for parameters identification of photovoltaic cell and module," *Applied Energy*, vol. 237, pp. 241–257, 2019.
- [77] M. Abd Elaziz and D. Oliva, "Parameter estimation of solar cells diode models by an improved opposition-based whale optimization algorithm," *Energy Conversion and Management*, vol. 171, pp. 1843–1859, 2018.
- [78] L. Wu, Z. Chen, C. Long et al., "Parameter extraction of photovoltaic models from measured I-V characteristics curves using a hybrid trust-region reflective algorithm," *Applied Energy*, vol. 232, pp. 36–53, 2018.
- [79] N. F. A. Hamid, N. A. Rahim, and J. Selvaraj, "Solar cell parameters identification using hybrid Nelder-Mead and modified particle swarm optimization," *Journal of Renewable and Sustainable Energy*, vol. 8, no. 1, p. 015502, 2016.
- [80] P. J. Gnetchejo, S. N. Essiane, P. Ele, R. Wamkeue, D. M. Wapet, and S. P. Ngoffe, "Enhanced vibrating particles system Algorithm for parameters estimation of photovoltaic system," *Journal of Power and Energy Engineering*, vol. 7, no. 8, pp. 1–26, 2019.

Research Article

A New Design Method for PI-PD Control of Unstable Fractional-Order System with Time Delay

Min Zheng ^{1,2} Tao Huang ² and Guangfeng Zhang ²

¹School of Mechatronic Engineering and Automation, Shanghai University, Shanghai Key Laboratory of Power Station Automation Technology, 200072 Shanghai, China

²School of Mechatronic Engineering and Automation, Shanghai University, 200072 Shanghai, China

Correspondence should be addressed to Min Zheng; zhengmin203@163.com

Received 25 July 2019; Accepted 4 October 2019; Published 30 October 2019

Guest Editor: Wonhee Kim

Copyright © 2019 Min Zheng et al. This is an open access article distributed under the Creative Commons Attribution License, which permits unrestricted use, distribution, and reproduction in any medium, provided the original work is properly cited.

In this paper, a practical PI-PD controller parameter tuning method is proposed, which uses the incenter of the triangle and the Fermat point of the convex polygon to optimize the PI-PD controller. Combined with the stability boundary locus method, the PI-PD controller parameters that can ensure stability for the unstable fractional-order system with time delay are obtained. Firstly, the parameters of the inner-loop PD controller are determined by the centre coordinates of the CSR in the $k_d - k_f$ plane. Secondly, a new graphical method is used to calculate the parameters of the PI controller, in which Fermat points in the CSR of $(k_p - k_i)$ plane are selected. Furthermore, the method is extended to uncertain systems, and the PI-PD controller parameters are obtained by using the proposed method through common stable region of all stable regions. The proposed graphical method not only ensures the stability of the closed-loop system but also avoids the complicated optimization calculations. The superior control performance of this method is illustrated by simulation.

1. Introduction

Proportional-integral-derivative (PID) controller has been widely used in industrial control systems for decades because of its simple structure and convenient implementation [1–6]. As the control plant becomes more and more complex, the performance of the controller is required to be higher and higher and the controllability of the system becomes difficult to solve. By using Schade's fixed point theorem, the controllability problem of nonlinear fractional integro-differential dynamical systems is transformed into the fixed point problem in [7]. The integral-order PID (IOPID) controller has limitations in control integration, instability, and delay process, and it often leads to large step response, large overshoot, and large impact, especially for unstable complex systems with time delay, and it is difficult to obtain good closed-loop performance [8–12]. Researchers have proposed a series of controller design schemes, including integer-order PID (IOPID) controller, sliding mode controller (SMC) to fractional-order PID (FOPID) controller,

fractional-order sliding mode controller and other complex controllers, and so on [12–19]. The computational cost of these controllers increases geometrically with the change of controller structure complexity, but the performance improvement is not satisfactory. For this reason, researchers put forward a PI-PD controller structure by changing the structure of PID controllers in [8, 9, 20]. The controller converts the unstable open-loop plant into the stable open-loop plant through the PD controller of the internal loop circuit, ensuring that the open-loop poles of the resonance and integration processes are in the proper position. The PI controller of the outer loop controls the inner loop of the system as a whole. Many studies have shown that the PI-PD structure has superior closed-loop performance for an unstable system with time delay [20]. The IOPID controller has three adjustable parameters, while the PI-PD controller has four adjustable parameters. Therefore, the PI-PD controller has advantages over the IOPID controller in terms of control structure and control freedom [21, 22]. The traditional controller has a good control effect on the precise model

with certain parameters. However, in most cases, the exact model of the actual system could not be obtained [23]. Therefore, an excellent controller design must meet the requirements of robustness, stability, control performance, and the ability to overcome the uncertainty of model parameters [24, 25].

In practical applications, PID controller parameter tuning methods are divided into three categories: the iterative optimization method based on intelligent optimization [26, 27]; the setting formula method for specific system [3, 4, 28]; and a parameter selection method [29–34] based on the stable region. The stable boundary locus (SBL) method has been widely studied, which provides an effective solution for some specific systems.

In recent years, PI-PD controllers have been used extensively in systems with unstable processes and time delay. Kaya and Atherton [28] studied the first-order time-delay unstable system of a PI-PD controller by using a simple regulation formula tuning method, taking integral of squared error (ISE) and integral of squared time weighted error (ISTE) as performance indicators. Tan [29] and Srivastava and Pandit [30] proposed a graphic method based on SBL by using gain phase tester to achieve the specified gain and phase margin and extended this method to the systems with parameter uncertainty by Kharitonov theorem. For the systems with uncertain time-varying delays, Shariati proposed a neutral system approach to stabilize and synthesize H_∞ PI-PD controllers. A new bounded real lemma was given for neutral systems with efficiency in designing the H_∞ controllers with both state delay and state derivative delay coefficients depending on the controller parameters [35]. Onat et al. [31, 32] proposed the concept of the weight geometric centre (WGC) method based on stable domain, which was applied to the parameter design of a PI controller. Ozyetkin [36] extended the WGC method to the fractional-order PI-PD. All the sample points that make up the stable locus boundary would be used to calculate the coordinate of WGC point. However, it has the large calculation cost which is not conducive to the application of real-time system control. In addition, under fractional-order control, WGC points do not always fall into the stable region. Onat [34] simplified the WGC method and constructed a convex stabilization region with only three points to ensure that the WGC is in the stable region.

However, the above literature only considered integer-order systems. On the other hand, there is little research on the PI-PD controller design through these graphical parameter selection methods. Inspired by the above analysis, the main contribution of this paper is to solve the parameters of the general fractional-order time-delay system PI-PD controller by the graphical method and generalize it to the parameter uncertainty system. In this paper, a new method to tune the parameters of PI-PD is proposed by using the incenter point, Fermat point, and geometry method in convex stable region (CSR). The main design process includes the following steps: firstly, for the open-loop uncertain system, the internal loop PD controller is designed. The stability boundary locus on the

$k_d - k_f$ plane is obtained by using the internal loop closed-loop characteristic polynomial. Then, the incenter coordinates of the CSR are computed. Secondly, embedding PD controller parameters into transfer function, desired stability boundary locus of PI controller is computed by the same procedure. Then, a quadrilateral Fermat point in CSR of the outer loop is obtained which is the parameter of the PI controller. This method only needs simple geometric calculation to obtain the parameters of the PI-PD controller, which is solved in the stable region to ensure the closed-loop stability. It uses several special points of the stable region and fewer points describing the coordinates than the WGC method, ensuring that the calculated points are situated in the stable region and the PI-PD controller has superior robustness. The simulation example shows that the method presented in this paper has a satisfactory control effect.

The structure of this paper is organized as follows. In Section 2, the problem statements of the controlled plant and controller are given, and then the proposed method is presented and extended to uncertain systems. Simulative and experimental application examples are considered to illustrate the effectiveness of the proposed method in Section 3. Section 4 gives conclusion.

2. Main Results

2.1. Problem Statement. The generalized PI-PD negative feedback system shown in Figure 1, where r is the set point and y is the negative feedback output. The generalized fractional transfer function $G_p(s)$ is written as follows:

$$G_p(s) = \frac{N_p(s)}{D_p(s)} e^{-\tau s}, \quad (1)$$

where τ is the time delay and $N_p(s)$ and $D_p(s)$ are the numerator and the denominator of the transfer function, respectively. They are defined with the forms:

$$\begin{aligned} N_p(s) &= b_0 s^{\beta_0} + b_1 s^{\beta_1} + \dots + b_{n-1} s^{\beta_{n-1}} + b_n s^{\beta_n} = \sum_{i=0}^n b_i s^{\beta_i}, \\ D_p(s) &= a_0 s^{\alpha_0} + a_1 s^{\alpha_1} + \dots + a_{n-1} s^{\alpha_{n-1}} + a_n s^{\alpha_n} = \sum_{i=0}^n a_i s^{\alpha_i}, \end{aligned} \quad (2)$$

where $a_j, b_j, \alpha_j, \beta_j, i, j = 0, 1, \dots, n$ are real numbers and $\alpha_n > \alpha_{n-1} > \dots > \alpha_2 > \alpha_1 > \alpha_0 \geq 0, \beta_n > \beta_{n-1} > \dots > \beta_2 > \beta_1 > \beta_0 \geq 0, \alpha_n > \beta_n$. The internal loop PD controller $C_{PD}(s)$ and external loop PI controller $C_{PI}(s)$ are defined as

$$C_{PD}(s) = \frac{N_{PD}(s)}{D_{PD}(s)} = k_f + \frac{k_d s}{T s + 1}, \quad (3)$$

$$C_{PI}(s) = \frac{N_{PI}(s)}{D_{PI}(s)} = k_p + \frac{k_i}{s}, \quad (4)$$

where $T = 0.01$, k_f and k_d are proportional and differential gains of the internal loop PD controller, and k_p and k_i are proportional and integral gains of the outer-loop PI controller, respectively.

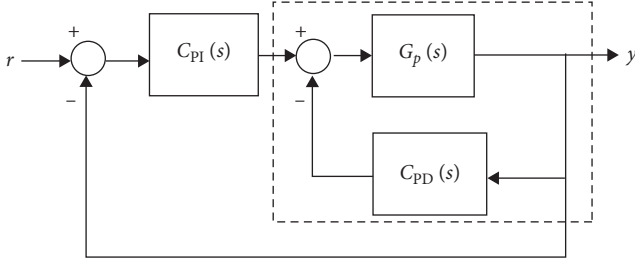


FIGURE 1: The PI-PD control system for generalized fractional plant.

The main purpose is to solve the parameters of the generalized fractional-order time-delay system (1) with PI-PD controller (3) and (4) by the graphical method.

2.2. The Proposed Method. The PI-PD controller has four adjustable parameters (k_f, k_d, k_p, k_i) that need to be determined. The internal PD controller is used to change the poles of the plant transfer function $G_p(s)$ to more desirable locations for control by the outer-loop PI controller.

Substituting $s^\alpha = \omega^\alpha (\cos(\alpha\pi/2) + j \sin(\alpha\pi/2))$ into (1) and dividing the numerator and denominator into a real part and an imaginary part, one can write

$$\frac{N_p(j\omega)}{D_p(j\omega)} = \frac{N_{PE}(j\omega) + jN_{PO}(j\omega)}{D_{PE}(j\omega) + jD_{PO}(j\omega)}. \quad (5)$$

Simplify $N_{PE}(j\omega), N_{PO}(j\omega), D_{PE}(j\omega)$, and $D_{PO}(j\omega)$ as N_{PE}, N_{PO}, D_{PE} , and D_{PO} , where N_{PE}, N_{PO} are the real part and the imaginary part and D_{PE}, D_{PO} are the real part and the imaginary part, respectively. The expressions are given as

$$\begin{aligned} N_{PE} &= \sum_{i=0}^n b_i \omega^{\beta_i} \cos\left(\frac{\beta_i}{2} \pi\right); \\ N_{PO} &= \sum_{i=0}^n b_i \omega^{\beta_i} \sin\left(\frac{\beta_i}{2} \pi\right); \\ D_{PE} &= \sum_{i=0}^n a_i \omega^{\alpha_i} \cos\left(\frac{\alpha_i}{2} \pi\right); \\ D_{PO} &= \sum_{i=0}^n a_i \omega^{\alpha_i} \sin\left(\frac{\alpha_i}{2} \pi\right). \end{aligned} \quad (6)$$

As shown in Figure 1, the internal loop negative feedback transfer function is

$$\phi_1(s) = \frac{G_p(s)}{1 + C_{PD}(s)G_p(s)}. \quad (7)$$

The closed-loop characteristic polynomial of the internal loop negative feedback transfer function is written as

$$\begin{aligned} \Delta_{PD}(s; k_f, k_d) &= 1 + C_{PD}(s)G_p(s) \\ &= (s + 100)D_p(s) + ((k_f + 100k_d)s + 100k_f) \\ &\quad \cdot N_p(s)e^{-\tau s}. \end{aligned} \quad (8)$$

Substitute $s = j\omega$ and $e^{-j\tau\omega} = \cos(\tau\omega) - j \sin(\tau\omega)$ into inner-loop transfer function (8) and divide it into real part and imaginary part as follows:

$$\begin{aligned} \Delta_{PD}(j\omega; k_f, k_d) &= 100(D_{PE} + jD_{PO}) + \omega(jD_{PE} - D_{PO}) \\ &\quad + ((m_1N_{PE} + m_2N_{PO}) + j(m_1N_{PO} \\ &\quad + m_2N_{PE}))\cos(\tau\omega) \\ &\quad + ((m_1N_{PO} + m_2N_{PE}) - j(m_1N_{PE} \\ &\quad + m_2N_{PO}))\sin(\tau\omega) \\ &= \text{Re}_{\Delta,PD} + j\text{Im}_{\Delta,PD} = 0, \end{aligned} \quad (9)$$

where $m_1 = 100k_f$ and $m_2 = (k_f + 100k_d)\omega$.

Taking the real part and the imaginary part of the characteristic polynomial as zero, they can be simplified into the following form:

$$\begin{cases} \text{Re}_{\Delta,PD} = A_1k_f + B_1k_d + C_1 = 0, \\ \text{Im}_{\Delta,PD} = A_2k_f + B_2k_d + C_2 = 0, \end{cases} \quad (10)$$

where $A_1 = (100N_{PE} + \omega N_{PO})\cos(\tau\omega) + (100N_{PO} + \omega N_{PE})\sin(\tau\omega)$; $A_2 = (100N_{PO} + \omega N_{PE})\cos(\tau\omega) - (100N_{PE} + \omega N_{PO})\sin(\tau\omega)$; $B_1 = 100\omega N_{PO} \cos(\tau\omega) + 100\omega N_{PE} \sin(\tau\omega)$; $B_2 = 100\omega N_{PE} \cos(\tau\omega) - 100\omega N_{PO} \sin(\tau\omega)$; $C_1 = 100D_{PE} - \omega D_{PO}$; and $C_2 = 100D_{PO} - \omega D_{PE}$.

Solving equation (10), we can get the expression of k_f and k_d and draw the stable boundary curve on the $k_d - k_f$ plane when $\omega \in (0, \infty)$. The expressions k_f and k_d are given

$$\begin{cases} k_d = \frac{A_1C_2 - A_2C_1}{B_1A_2 - A_1B_2}, \\ k_f = \frac{B_2C_1 - B_1C_2}{B_1A_2 - A_1B_2}. \end{cases} \quad (11)$$

According to the obtained SBL, the vertices and corner points of the stable region are devoted to describe the CSR. In a general $k_d - k_f$ plane, the CSR is designed as a triangle with one vertex and two corner points, whose coordinates are (k_{d1}, k_{f1}) , (k_{d2}, k_{f2}) , and (k_{d3}, k_{f3}) . In order to ensure that the obtained point is in the stable region, here we propose the concept of the incenter of the CSR, whose coordinate expression is as follows:

$$H = \frac{\begin{bmatrix} k_{d1} & k_{d2} & k_{d3} \\ k_{f1} & k_{f2} & k_{f3} \end{bmatrix} \begin{bmatrix} a \\ b \\ c \end{bmatrix}}{a + b + c}, \quad (12)$$

where a, b , and c are the modules of the three-sided vectors. The vector H obtained in (12) is the inner-loop PD controller parameter $(k_d; k_f)$.

Then, the inner-loop negative feedback system has the following form:

$$\begin{aligned} \phi_1(s) &= \frac{N(s)}{D(s)} = \frac{G_p(s)}{1 + C_{PD}(s)G_p(s)} \\ &= \frac{(s + 100)N_p(s)e^{-\tau s}}{(s + 100)D_p(s) + N_p(s)e^{-\tau s}((k_f + 100k_d)s + 100k_f)}. \end{aligned} \quad (13)$$

Simplify the inner-loop transfer function (13) and split the numerator and denominator into real parts and imaginary parts, respectively:

$$\frac{N(j\omega)}{D(j\omega)} = \frac{N_E(j\omega) + jN_O(j\omega)}{D_E(j\omega) + jD_O(j\omega)}. \quad (14)$$

Simplify $N_E(j\omega)$, $N_O(j\omega)$, $D_E(j\omega)$, and $D_O(j\omega)$ as N_E , N_O , D_E , and D_O , where N_E, N_O are the real part and imaginary part of numerator and D_E, D_O are the real part and imaginary part of the denominator, respectively. Their expressions are as follows:

$$\begin{aligned} N_E &= (N_{PE} \cos(\tau\omega) + N_{PO} \sin(\tau\omega))(n_1 + 100) + (N_{PE} \sin(\tau\omega) \\ &\quad - N_{PO} \cos(\tau\omega))n_2, \\ N_O &= (N_{PE} \cos(\tau\omega) + N_{PO} \sin(\tau\omega))n_2 + (N_{PO} \cos(\tau\omega) \\ &\quad - N_{PE} \sin(\tau\omega))(n_1 + 100), \\ D_E &= A_1 k_f + B_1 k_d + C_1; \\ D_O &= A_2 k_f + B_2 k_d + C_2. \end{aligned} \quad (15)$$

Regarding the inner loop as a whole, the transfer function of the system is written as

$$\phi_2(s) = \frac{C_{PI}(s)\phi_1(s)}{1 + C_{PI}(s)\phi_1(s)}. \quad (16)$$

Therefore, the closed-loop characteristic equation of the outer loop is determined as follows:

$$\begin{aligned} \Delta_{PI}(s; k_p, k_i) &= 1 + C_{PI}(s)G_p(s) \\ &= sD(s) + ((k_p s + k_d)N(s)). \end{aligned} \quad (17)$$

Substitute (4) and (12) into the closed-loop characteristic equation (16) and divide it into real part and imaginary parts:

$$\Delta_{PI}(j\omega; k_p, k_i) = \text{Re}_{\Delta, PI} + j\text{Im}_{\Delta, PI} = 0. \quad (18)$$

Simplify the characteristic equation into a binary equations with unknown parameters k_p, k_i :

$$\begin{cases} \text{Re}_{\Delta, PI} = \overline{A_1}k_p + \overline{B_1}k_i + \overline{C_1} = 0, \\ \text{Im}_{\Delta, PI} = \overline{A_2}k_p + \overline{B_2}k_i + \overline{C_2} = 0, \end{cases} \quad (19)$$

where $\overline{A_1} = -\omega N_O$; $\overline{A_2} = \omega N_E$; $\overline{B_1} = N_E$; $\overline{B_2} = N_O$; $\overline{C_1} = -\omega D_O$; and $\overline{C_2} = \omega D_E$.

The parameters of SBL and the stability region of the outer-loop PI controller on the $k_p - k_i$ plane are obtained by solving equation (19). And a SBL is drawn on the $k_p - k_i$ plane:

$$\begin{cases} k_p = \frac{\overline{B_2}\overline{C_1} - \overline{B_1}\overline{C_2}}{\overline{B_1}\overline{A_2} - \overline{A_1}\overline{B_2}}, \\ k_i = \frac{\overline{A_1}\overline{C_2} - \overline{A_2}\overline{C_1}}{\overline{B_1}\overline{A_2} - \overline{A_1}\overline{B_2}}. \end{cases} \quad (20)$$

For obtaining the outer-loop PI controller parameters, this paper introduces a Fermat point concept that has the smallest sum of distances to the vertices of the polygon. In

order to optimize calculation of Fermat point, a trapezoid is designed at first. The four vertices include two corner points and two points on the SBL which are 1/2 of the longitudinal distance between the cusp and corner point. Fermat point is the diagonal intersection point.

The proposed method includes the following five steps:

Step 1: according to equation (11), the relationship between the parameters k_d, k_f of the inner-loop PD controller could be obtained. And the SBL could be drawn on the $k_d - k_f$ plane.

Step 2: by selecting the vertices and corner points of the CSR, the incenter of the convex CSR is computed according to equation (12). Its coordinates $H(k_d, k_f)$ are the parameters of the inner-loop PD controller.

Step 3: calculating the transfer function of the inner loop based on the obtained parameters (k_d, k_f).

Step 4: according to equation (20), the relation of the outer-loop PI controller parameters k_p, k_i could be obtained. The SBL is drawn on the $k_p - k_i$ plane.

Step 5: determining the corner point and the boundary point of the SBL; the intersection point of the trapezoid diagonal is the parameter of the outer-loop PI controller.

Remark 1. For fractional-order time-delay systems, the traditional method of selecting stable regions is usually determined by manually selecting a large number of test points in all the regions divided by the stable boundary trajectories, which will lead to time consumption. Inspired by [37], this paper gives a simple parameter tuning method of FOPID controller, which avoids time-consuming stability test.

2.3. Method Extension of Uncertain Systems. Due to modelling errors and other factors, it is an important issue for the analysis and design of the uncertain parameter control systems with time delay in control theory. In this article, the design method is extended to the fractional-order system with time delay and parameter uncertainty. Multiple transfer functions are attained in the condition of uncertain parameters. Consider the transfer function with parameter uncertainty for the control system shown in Figure 1. It is defined as follows:

$$G_p(s) = \frac{\sum_{j=0}^n b_j s^{\beta_j}}{\sum_{i=0}^m a_i s^{\alpha_i}} e^{-\tau s}, \quad (21)$$

where $a_i \in [\underline{a}_i, \overline{a}_i]$, $b_j \in [\underline{b}_j, \overline{b}_j]$, $\alpha_i \in [\underline{\alpha}_i, \overline{\alpha}_i]$, $\beta_j \in [\underline{\beta}_j, \overline{\beta}_j]$, $i = 0, 1, \dots, m$ and $j = 0, 1, \dots, n$. According to the number of uncertain parameters in the general transfer function, there are $m^2 \times n^2$ Kharitonov plants in total.

For the uncertain parameter system with time delay, all steps of the method put forward in paper are individually processed for each transfer function in terms of the Kharitonov theorem. Then, the common stable domain of all transfer functions and its convex stable domain are obtained.

Finally, the incenter of the inner loop and the Fermat points of outer loop of the common convex stability region are obtained, and then a robust PI-PD controller is designed.

The proposed method extension of the time-delay uncertain system could be classified into the following steps:

Step 1: for all submodels, the inner-loop stable boundary loci are calculated separately, and the common stable region is determined graphically on the $k_d - k_f$ plane.

Step 2: then, the CCSR is determined according to the corner points, intersection points, and individual tip points. The incenter of the CCSR is computed by applying (12). The coordinate of the incenter is the parameter (k_d, k_f) of the PD controller in the internal loop.

Step 3: by substituting the values k_d and k_f into the inner-loop system, the transfer functions of the outer loop are obtained for all the submodels simplified based on the Kharitonov theorem.

Step 4: the common stable region of the outer-loop PI controller on the $k_p - k_i$ plane is determined based on all closed-loop transfer functions.

Step 5: looking for corner points, tip points, and bipartite points of the common stable area, the CCSR based on these points is obtained. The Fermat point of the CCSR is given by the graphical method, which is parameter (k_p, k_i) of the outer-loop PI controller.

Remark 2. The method proposed in this paper is an empirical parameter adjustment method, which is only suitable for systems that can clearly distinguish stable regions in images. For uncertain systems, it is only applicable to the case with common stable region. Otherwise, further research is needed to find other control methods.

3. Simulation

Several simulation examples show the effectiveness of the proposed method. It includes the following plants: two unstable time-delay systems of order 1 and order 2, respectively, the time-delay unstable fractional plant with uncertain parameters, and the two fractional-order plants.

3.1. Example A. Consider a first-order unstable transfer function with time delay which was studied by Tan [29], Onat [34], Kaya [38], and Visioli [39]. It has the following form:

$$G_p(s) = \frac{4}{4s - 1} e^{-2s}. \quad (22)$$

According to the proposed steps, the stable region of the inner-loop system is obtained. The SBL is drawn in the $k_d - k_f$ plane. And the convex region of the stable region is demonstrated in Figure 2. It shows that the convex

stability region consists of one vertex V and two corner points C_1 and C_2 . The convex stability region of the PD controller can be described as a triangle by these points. According to the coordinates of the above points, the incenter (Inc) of the PD controller can be calculated by applying equation (12), and its coordinate is (0.461, 0.469). The inner-loop PD controller parameters are $k_d = 0.461$ and $k_f = 0.499$.

Substituting the PD controller parameters into the inner loop, the system transfer function is obtained by using (20). For the outer loop, PI controller parameters' stability region is drawn in the $k_p - k_i$ plane in Figure 3. Figure 3 also demonstrates the CSR. In this step, two corner points C_3 and C_4 and two points E_1 and E_2 on the SBL with a longitudinal distance of 1/2 from the corner point to the cusp point are given as shown in Figure 3. These points describe the convex region as a trapezoid. Then, the coordinates of Fermat points (Fps) are obtained as (0.06475, 0.04573), and the parameters of the inner-loop PI controller are $k_p = 0.06459$ and $k_i = 0.04564$. Thus, parameters of the PI-PD controller are $k_d = 0.461$, $k_f = 0.499$, $k_p = 0.06459$, and $k_i = 0.04564$.

In Figure 4, the unit step response of the method put forward in this paper is compared with the methods put forward by Onat [34], Tan [29], Kaya [38], and Visioli [39]. Table 1 gives the parameters of the various methods. The settling time, overshoot, rise time, peak time, and IAE values are used as evaluation index. Table 2 gives the evaluation values of this proposed method, other controller designs, and optimization methods. In light of the evaluation criteria, the tuning method proposed in this paper exhibits the superior performance. This method has the lowest settling time and the smallest overshoot. The response speed of the PID controller is fast, but other performances are not ideal. In this example, the PI-PD controller proved to be superior to PID controller, and the parameter tuning method is the best in comparison.

3.2. Example B. View a second-order unstable transfer function which was studied by Kaya and Atherton [28]:

$$G_p(s) = \frac{1}{2s^2 + s - 1} e^{-0.3s}. \quad (23)$$

The stability region of the inner-loop PD controller is shown in Figure 5. A vertex V and two corner points C_1 and C_2 in Figure 5 construct a CSR. Inc stands for convex stable region, and Inc can be calculated as (5.51, 4.8667), and then the inner-loop PD controller parameters are $k_d = 5.51$ and $k_f = 4.8667$.

By substituting the PD controller parameters ($k_d = 5.51$, $k_f = 4.8667$) into the inner loop, the transfer function can be obtained by using (12). Figure 6 gives the stable region and its convex region of the outer ring PI controller in the $k_p - k_i$ plane. C_3 and C_4 are the corner points and E_1 and E_2 are the bisection points. The diagonal intersection coordinate of the quadrilateral is obtained by the graphic method, and the coordinate values of Fp are $k_p = 3.77$ and $k_i = 4.75$. Through the above analysis and calculation, the PI-PD controller parameters calculated by

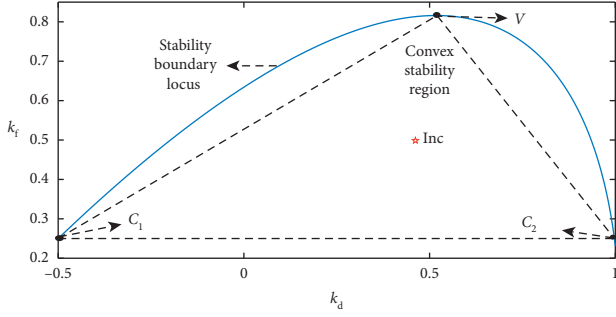


FIGURE 2: Convex stability region and incenter of PD controller in example A.

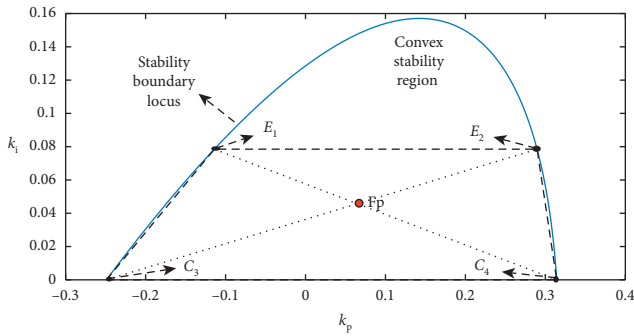


FIGURE 3: Convex stability region and Fermat point of PI controller in example A.

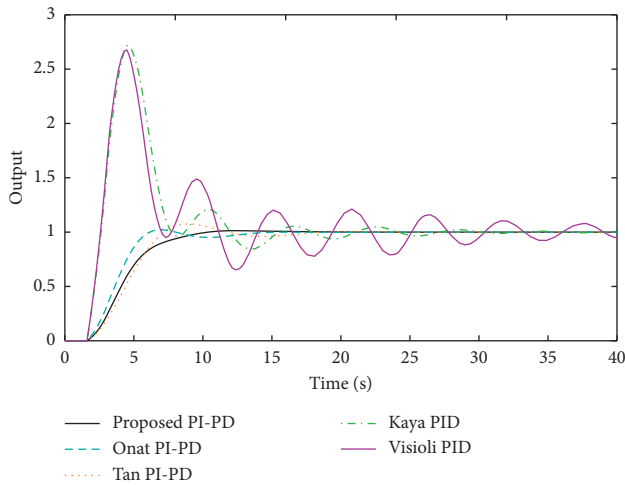


FIGURE 4: Unit step responses comparison of various methods for example A.

the proposed method are determined. They are $k_d = 5.51$, $k_f = 4.8667$, $k_p = 3.77$, and $k_i = 4.75$.

Figure 7 gives the comparison between the PI-PD controller optimized by the parameter tuning method put forward in this paper and the controller put forward by Kaya and Atherton [28]. The unit step responses of these controllers are illustrated in Figure 7. Controller parameters are shown in Table 3. Table 4 gives the

performance indexes of the several studies in this example. Obviously, the proposed method has lowest overshoot and peak time. And it also has a small IAE in this example. It is obvious that the tuning method put forward in this paper is better than the others.

3.3. *Example C.* This example considers a time-delay unstable transfer function with uncertain parameters. The transfer function is written as

$$G_p(s) = \frac{1}{s^a - b} e^{-0.2s}, \quad (24)$$

where $a \in [0.8, 1.2]$ and $b \in [0.5, 1.5]$. Four boundary transfer functions are taken into account based on Kharitonov's theorem which are $G_{p1}(s)$, $G_{p2}(s)$, $G_{p3}(s)$, and $G_{p4}(s)$. The plants are given in (25)–(28), respectively:

$$G_{p1}(s) = \frac{1}{s^{1.2} - 0.5} e^{-0.2s}, \quad (25)$$

$$G_{p2}(s) = \frac{1}{s^{1.2} - 1.5} e^{-0.2s}, \quad (26)$$

$$G_{p3}(s) = \frac{1}{s^{0.8} - 1.5} e^{-0.2s}, \quad (27)$$

$$G_{p4}(s) = \frac{1}{s^{0.8} - 0.5} e^{-0.2s}. \quad (28)$$

Above all, stability boundary loci of edge plants in the inner loop are drawn in the $k_d - k_f$ plane in Figure 8. According to the stable boundary loci obtained above, the common stability region is obtained as shown as the shadow in Figure 8. Figure 9 enlarges CSR in Figure 8 and gives CCSR composed of corner points C_1 and C_2 and vertex V . C_1 is the intersection of two stable boundary loci. The parameters of the inner-loop PD controller are the values of Inc coordinates with $k_d = 0.0314$ and $k_f = 2.205$.

Furthermore, for outer loop, stability boundary loci of edge plants are drawn in Figure 10, and the shadow is the CSR. Figure 11 enlarges CSR in Figure 10 and gives CCSR as a trapezoid composed of corner points C_3 and C_4 and the bisection points E_1 and E_2 of the common stable region. Applying the method proposed in the paper, the common convex region is designed as a trapezoid and Fermat point is the diagonal intersection of the trapezoid. Therefore, the values of Fp coordinate in Figure 11 are the parameters of the outer-loop PI controller with $k_p = 1.518$ and $k_f = 1.644$. Through the above two steps, the PI-PD controller of the system is obtained, and its parameters are $k_d = 0.0314$, $k_f = 2.205$, $k_p = 1.518$, and $k_i = 1.644$.

Finally, for the parameters of the uncertain system, the cell step responses of the four boundary plants are obtained in Figure 12. For the uncertain system, the controller has strong robustness.

3.4. *Example D.* Consider the following transfer function, which has an order of 0.8:

TABLE 1: Controller parameters comparison of various methods in example A (other data cited from [34]).

Controller	Proposed PI-PD	Onat PI-PD	Tan PI-PD	Kaya PI-PD	Visioli PID
Parameters	$k_d = 0.461$	$k_d = 0.3412$	$k_d = 0.20$	$k_p = 0.6217$	$k_p = 0.652$
	$k_f = 0.499$	$k_f = 0.439$	$k_f = 0.413$	$k_i = 0.0722$	$k_i = 0.0789$
	$k_p = 0.06459$	$k_p = 0.107$	$k_p = 0.07$	$k_d = 0.5352$	$k_d = 0.6309$
	$k_i = 0.04564$	$k_i = 0.0393$	$k_i = 0.03$		

TABLE 2: Performance metrics comparison of various methods in example A (other data cited from [34]).

Controller	Settling time (s)	Overshoot (%)	Rise time (s)	Peak time (s)	IAE
Proposed PI-PD	11.81	1.35	5.80	15.68	5.63
Onat PI-PD	16.04	2.13	3.77	8.63	4.87
Tan PI-PD	20.26	6.24	4.64	10.62	5.89
Kaya PI-PD	17.70	174.16	0.45	5.01	8.57
Visioli PID	24.15	191.65	0.32	4.00	9.18

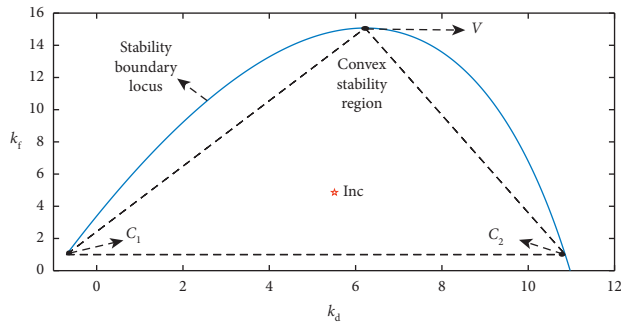


FIGURE 5: Convex stability region and incenter of PD controller in example B.

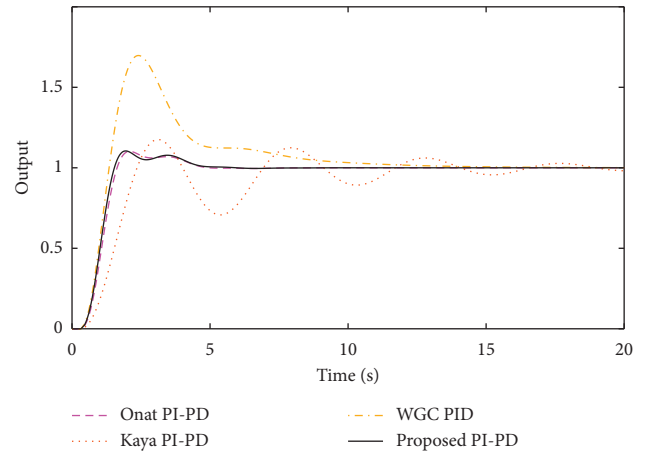


FIGURE 7: Step responses comparison of various methods for example B.

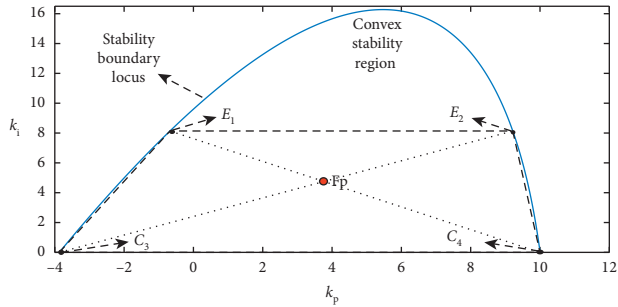


FIGURE 6: Convex stability region and Fermat point of PI controller in example B.

$$G_p(s) = \frac{1}{s^{0.8} - 1} e^{-0.2s}. \quad (29)$$

In this example, if the point at $\omega = 0$ is used as a corner point, the CSR is as shown in Figure 13. The convex region contains a lot of unstable regions, and the WGC point and the incenter of the convex region are outside of the stable region. Therefore, as shown in Figure 14, a new point C_1 is defined as the left corner point. The height of C_1 is equal to the original corner point. And C_1 is closer to the stable region. C_2 is another corner point of the new convex stable region, and V is the vertex of the stable region.

For inner loop, Inc coordinates are obtained as $k_d = -0.041$ and $k_f = 1.55$ and centroid coordinates are obtained as $k_d = 0.00947$ and $k_f = 2.5633$.

And for the outer loop, using the WGC method, the convex stability region is given as Figure 15. C_3 , C_4 , and C_5 are the corner points of the stable region, and V is the vertex of the stable region. The centroid PI controller parameters are obtained as $k_p = 0.1072$ and $k_i = 2.805$. Applying the method put forward in this paper, the convex stability region of PI controller is given in Figure 16. The convex stable region is a trapezoid composed of the corner points C_6 and C_7 and the bisection points E_1 and E_2 of the common stable region. The outer-loop PI controller parameters are computed as Fp with $k_p = 1.527$ and $k_i = 2.515$. Accordingly, the PI-PD controller optimized by using the WGC method and the method proposed in this paper is determined. The parameters of the WGC method are $k_d = 0.00947$, $k_f = 2.5633$, and $k_p = 0.1072$, $k_i = 2.805$, and the parameters of the proposed method are $k_d = -0.041$, $k_f = 1.55$, and $k_p = 1.527$, $k_i = 2.515$. The unit step responses are given in Figure 17. Compared with Onat's method, the method proposed in this paper can achieve faster response.

TABLE 3: Controller parameters comparison of various methods in example B (other data cited from [34]).

Controller	Proposed PI-PD	Onat PI-PD	Kaya PI-PD	Atherton PID
Parameters	$k_d = 5.51$	$k_d = 5.46$	$k_d = 0.535$	$k_p = 1.398$
	$k_f = 4.8667$	$k_f = 5.69$	$k_f = 3$	$k_i = 0.793$
	$k_p = 3.77$	$k_p = 3$	$k_p = 1.398$	$k_d = 0.535$
	$k_i = 4.75$	$k_i = 5.3$	$k_i = 0.793$	

TABLE 4: Performance metrics comparison of various methods in example B (other data cited from [34]).

Controller	Settling time (s)	Overshoot (%)	Rise time (s)	Peak time (s)	IAE
Proposed PI-PD	11.81	1.35	5.80	15.68	5.63
Onat PI-PD	16.04	2.13	3.77	8.63	4.87
Tan PI-PD	20.26	6.24	4.64	10.62	5.89
Kaya PI-PD	17.70	174.16	0.45	5.01	8.57
Visioli PID	24.15	191.65	0.32	4.00	9.18

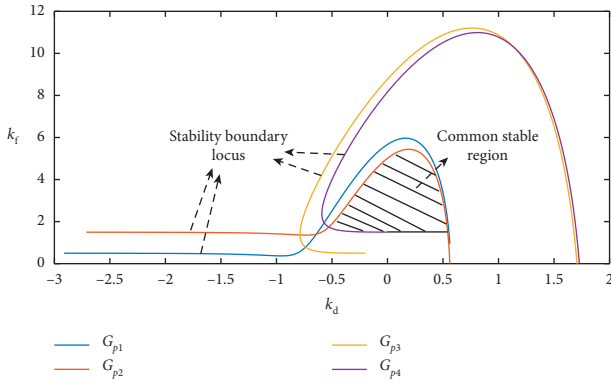


FIGURE 8: Stability boundary loci of inner-loop PD controller for uncertain systems in example C.

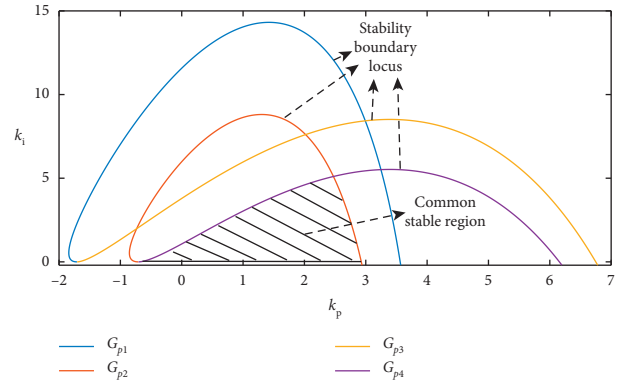


FIGURE 10: Stability boundary loci of outer-loop PI controller for uncertain systems in example C.

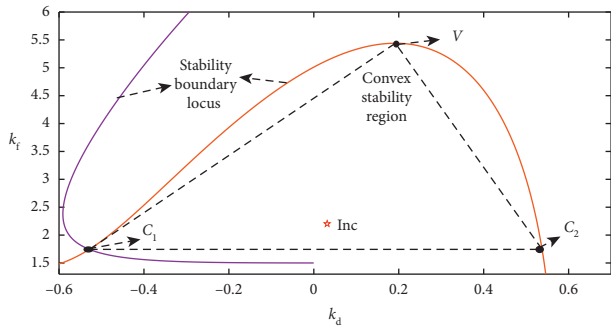


FIGURE 9: Common convex stable region and incenter of PD controller in example C.

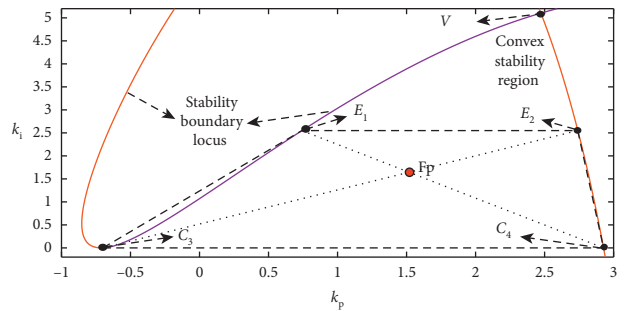


FIGURE 11: Common convex stable region and Fermat point of the PI controller in example C.

3.5. *Example E.* Consider the case of order 1.2 of fractional transfer function in example 3:

$$G_p(s) = \frac{1}{s^{1.2} - 1} e^{-0.2s}. \quad (30)$$

According to the method proposed in this paper, the corner points are selected. The stable region and its regular convex stability region of the inner loop and outer loop are shown in Figures 18 and 19, respectively. C_1 , C_2 , C_3 , and C_4

are the corner points, V is the vertex point, and E_1 and E_2 are the bisection points. The inner PD controller parameters are the coordinates of Inc with $k_d = 0.799$ and $k_f = 1.823$, and the outer PI controller parameters are the coordinates of Fp with $k_p = 4.976$ and $k_i = 7.75$.

Due to the inward extension of corner points, the following attempts were made in this paper to select inflection points on the boundary to replace corner points. The stable region and the convex region are as shown in Figures 20 and

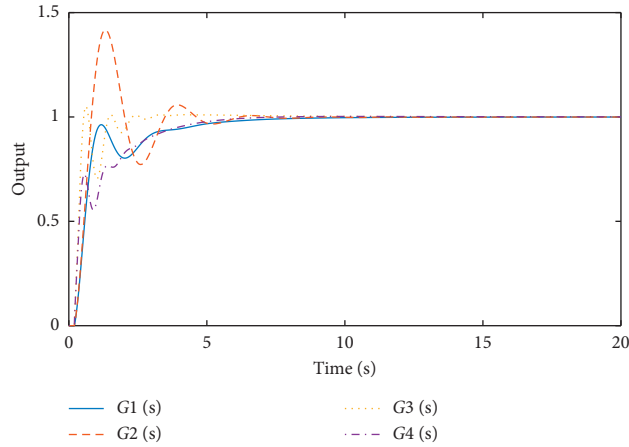


FIGURE 12: Step response comparison of various methods for example C.

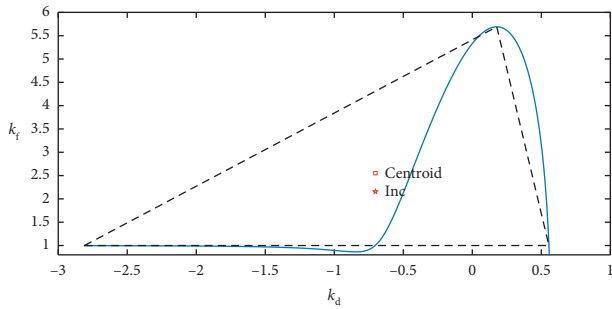


FIGURE 13: General corner point of inner-loop PD controller in example D.

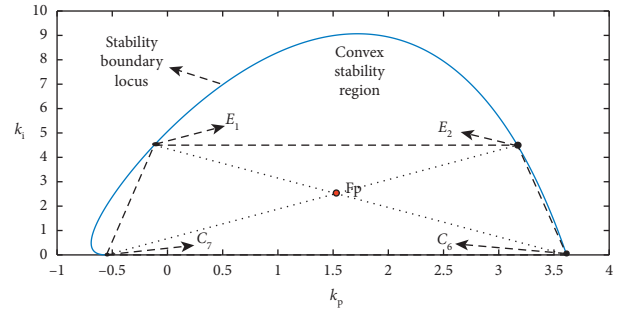


FIGURE 16: Convex stability region and Fermat point of PI controller in example D.

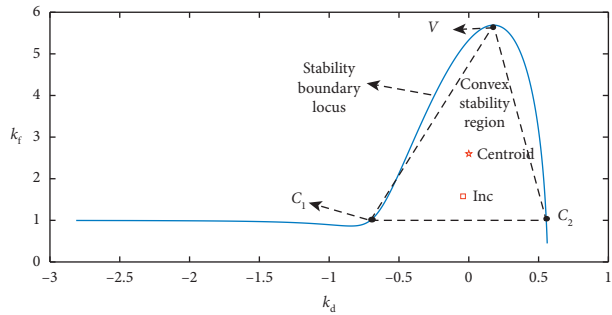


FIGURE 14: New corner point of inner-loop PD controller in example D.

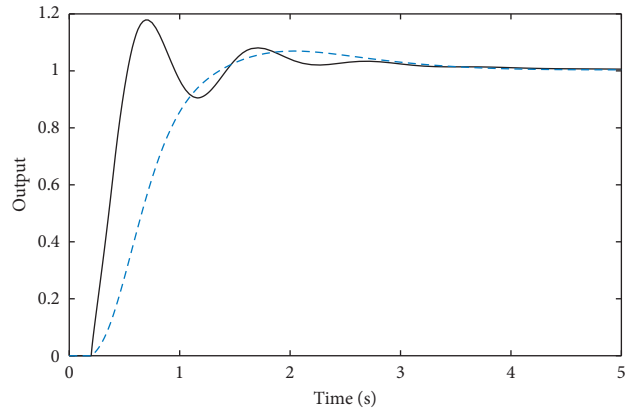


FIGURE 17: Step responses in example D.

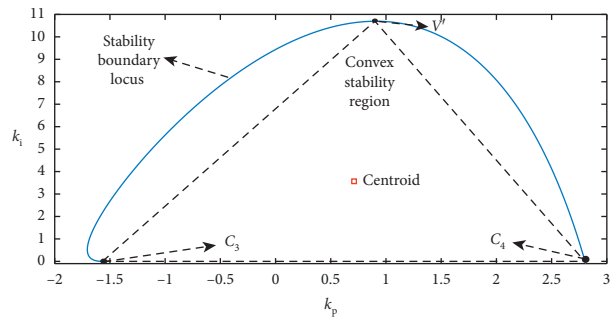


FIGURE 15: Convex stability region and centroid of the PI controller in example D.

21. $C_5, C_6, C_7,$ and C_8 are the corner points, V is the vertex point, and E_3 and E_4 are the bisection points. (k_d, k_f) and (k_p, k_i) are the coordinates of Inc and Fp, respectively. The parameters of this improved PI-PD controller are $k_d = 0.533, k_f = 2.941, k_p = 3.488,$ and $k_i = 5.363$. The unit step responses are compared as shown in Figure 22. The two methods show the same settling time. However, the improved method is better than the former one in the field of overshoot and IAE capabilities.

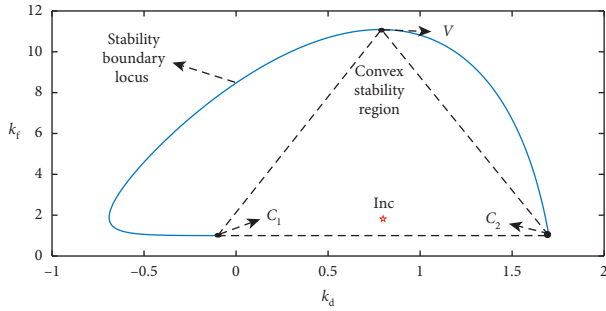


FIGURE 18: Convex stability region designed by regular point in example E.

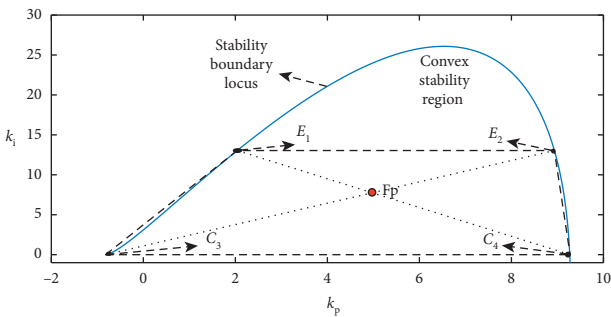


FIGURE 19: Regular convex stability region and Fermat point of PI controller in example E.

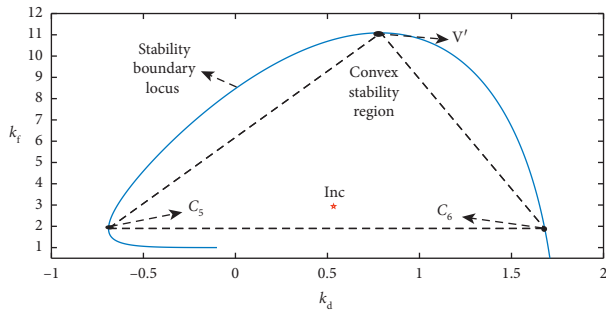


FIGURE 20: Changed convex stability region and incenter of PD controller in example E.

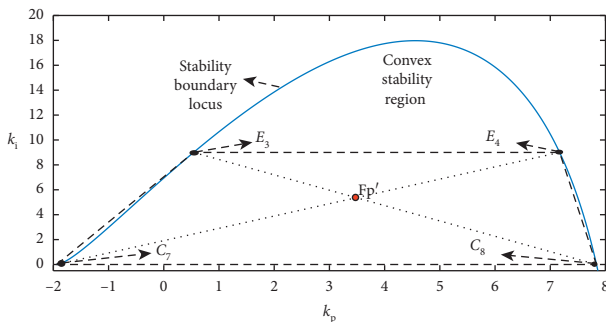


FIGURE 21: Changed convex stability region and Fermat point of PI controller in example E.

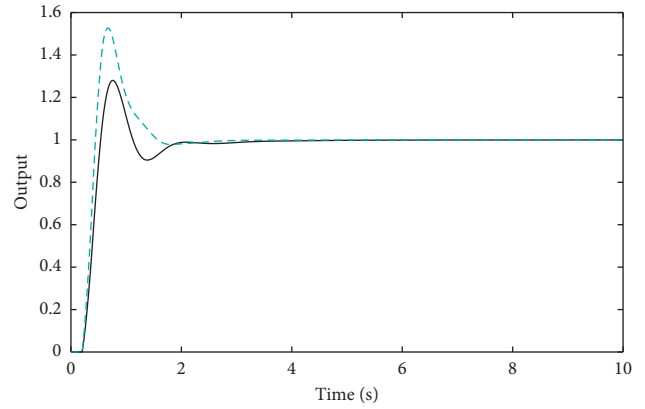


FIGURE 22: Step response for example E.

4. Conclusions

In this paper, a PI-PD control parameter graphical tuning method for unstable fractional time-delay systems is proposed by using the concept of incenter and Fermat points of CSRs. The method obtains the inner-loop stable boundary locus and the outer-loop stable boundary locus by establishing the characteristic equations. CSR is designed, and the incenter of the inner-loop CSR and Fermat point of outer-loop convex stable region are obtained, respectively. This method uses several special points on the stable boundary locus to determine the convex stable region. The method has the advantages of convenient calculation and easy implementation in engineering. This method is popularized to the uncertain system by applying Kharitonov's theorem. Simulation examples verify the effectiveness of the method put forward in the paper. In future studies, the proposed method can also be extended to the $PI^\lambda-PD^\mu$ controller.

Nomenclature

- SBL: Stable boundary locus
- ISE: Integral of squared error
- ISTE: Integral of squared time weighted error
- WGC: Weight geometric centre
- CSR: Convex stable region
- CCSR: Common convex stable region
- k_d : Derivative gain of the PD controller
- k_f : Proportional gain of the PD controller
- k_p : Proportional gain of the PI controller
- k_i : Integral gain of the PI controller
- C_{PI} : Transfer function of the PI controller
- C_{PD} : Transfer function of the PD controller
- s : Laplace variable
- j : Imaginary $\sqrt{-1}$
- ω : Frequency
- Δ : Characteristic equation
- N : Numerator of the transfer function
- D : Denominator of the transfer function
- Inc: Incenter of the convex stable region

Fp: Fermat point
 C_1, C_2, \dots : Corner of the stable region
 V: Vertex of the stable region

Data Availability

Processing data applied to support the results of this study are included within the article.

Conflicts of Interest

The authors declare that they have no conflicts of interest.

Acknowledgments

This study was supported in part by Shanghai Key Laboratory of Power Station Technology and National Natural Science Foundation under grant no. 61873335.

References

- [1] S. Bouabdallah, A. Noth, and R. Siegwart, "PID vs. LQ control techniques applied to an indoor micro quadrotor," in *Proceedings of the 2004 IEEE/RSJ International Conference on Intelligent Robots and Systems*, vol. 3, pp. 2451–2456, IEEE, Sendai, Japan, September 2004.
- [2] K. S. Tang, K. F. Man, G. R. Chen, and S. Kwong, "An optimal fuzzy PID controller," *IEEE Transactions on Industrial Electronics*, vol. 48, no. 4, pp. 757–765, 2001.
- [3] S. Skogestad, "Simple analytic rules for model reduction and PID controller tuning," *Modelling Identification & Control*, vol. 13, no. 4, pp. 291–309, 2004.
- [4] K. J. Åström and T. Hägglund, "Revisiting the Ziegler-Nichols step response method for PID control," *Journal of Process Control*, vol. 14, no. 6, pp. 635–650, 2004.
- [5] Y. Lee, S. Park, M. Lee, and C. Brosilow, "PID controller tuning for desired closed-loop responses for SI/SO systems," *AIChE Journal*, vol. 44, no. 1, pp. 106–115, 1998.
- [6] K. H. Ang, G. Chong, and L. Yun, "PID control system analysis, design, and technology," *IEEE Transactions on Control Systems Technology*, vol. 13, no. 4, pp. 559–576, 2005.
- [7] Y. Yi, D. Chen, and Q. Xie, "Controllability of nonlinear fractional order integrodifferential system with input delay," *Mathematical Methods in the Applied Sciences*, vol. 42, no. 11, pp. 3799–3817, 2019.
- [8] I. Kaya, "A PI-PD controller design for control of unstable and integrating processes," *ISA Transactions*, vol. 42, no. 1, pp. 111–121, 2003.
- [9] I. Kaya, "PI-PD controllers for controlling stable processes with inverse response and dead time," *Electrical Engineering*, vol. 98, no. 1, pp. 55–65, 2016.
- [10] E. E. Ezema, I. I. Eneh, and O. L. Daniya, "Improving structural limitations of PID controller for unstable processes," *International Journal of Engineering Research & Applications*, vol. 4, no. 9, pp. 87–90, 2014.
- [11] Z. Yan, "Research on application of fuzzy PID controller in two-container water tank system control," in *Proceedings of the International Conference on Machine Vision & Human-Machine Interface*, April 2010.
- [12] K. J. Åström and T. Hägglund, "The future of PID control," *Control Engineering Practice*, vol. 9, no. 11, pp. 1163–1175, 2001.
- [13] S. M. Asyraf, P. M. Heerwan, and I. M. Izhar, "The comparison respond of braking torque control between PID and SMC controller for electric powered wheelchair descending on slope condition," *IOP Conference Series: Materials Science & Engineering Conference Series*, vol. 342, Article ID 012088, 2018.
- [14] C. Zeng, *Develop a Robust Nonlinear Controller for Large Aircraft by Applying NDI, SMC and Adaptive Control*, Cranfield University, Cranfield, UK, 2012.
- [15] M. Zamani, M. Karimi-Ghartemani, N. Sadati, and M. Parniani, "Design of a fractional order PID controller for an AVR using particle swarm optimization," *Control Engineering Practice*, vol. 17, no. 12, pp. 1380–1387, 2009.
- [16] C. Qin, N. Qi, and Z. Song, "Fractional PID controller design of hypersonic flight vehicle," in *Proceedings of the 2010 International Conference on Computer, Mechatronics, Control and Electronic Engineering*, August 2010.
- [17] P. Roy, S. Sarkar, B. K. Roy, and N. Singh, "A comparative study between fractional order SMC and SMC applied to magnetic levitation system," in *Proceedings of the 2017 Indian Control Conference*, pp. 473–478, IEEE, Guwahati, India, January 2017.
- [18] Z. Jia, X. Sun, and N. Zhang, "A new type of nonlinear controller-nine-point controller," in *Proceedings of the 2002 International Conference on Control and Automation (ICCA)*, Xiamen, China, June 2002.
- [19] A. Kumar and V. Kumar, "Evolving an interval type-2 fuzzy PID controller for the redundant robotic manipulator," *Expert Systems with Applications*, vol. 73, pp. 161–177, 2017.
- [20] S. Nema and P. K. Padhy, "PI-PD controller for stable and unstable processes," *International Journal of Systems, Control and Communications*, vol. 5, no. 2, pp. 156–165, 2013.
- [21] N. K. Vastrakar and P. K. Padhy, "Simplified PSO PI-PD controller for unstable processes," in *Proceedings of the 2013 International Conference on Intelligent Systems Modelling & Simulation*, January 2013.
- [22] G. A. Hassaan, "Robustness of I-PD, PD-PI and PI-PD controllers used with second-order processes," *International Journal of Scientific & Technical Research*, vol. 3, no. 10, 2014.
- [23] H. Gao and T. Chen, "H_∞ estimation for uncertain systems with limited communication capacity," *IEEE Transactions on Automatic Control*, vol. 52, no. 11, pp. 2070–2084, 2007.
- [24] S. Wang, B. Chen, and T. Lin, "Robust stability of uncertain time-delay systems," *Techniques of Automation & Applications*, vol. 46, no. 3, pp. 963–976, 2002.
- [25] C. Lin, Q. G. Wang, and H. L. Tong, "Stabilization of uncertain fuzzy time-delay systems via variable structure control approach," *IEEE Transactions on Fuzzy Systems*, vol. 13, no. 6, pp. 787–798, 2005.
- [26] C. Yeroglu, C. Onat, and N. Tan, "A new tuning method for PI^λD^μ controller," in *Proceedings in 2009 International Conference on Electrical and Electronics Engineering*, pp. 312–316, Bursa, Turkey, August 2009.
- [27] N.-S. Pai, S.-C. Chang, and C.-T. Huang, "Tuning PI/PID controllers for integrating processes with deadtime and inverse response by simple calculations," *Journal of Process Control*, vol. 20, no. 6, pp. 726–733, 2010.
- [28] I. Kaya and D. P. Atherton, *Simple Analytical Rules for PI-PD Controllers to Tune Integrating and Unstable Plants*, University of Strathclyde Publications, Glasgow, Scotland, 2006.
- [29] N. Tan, "Computation of stabilizing PI-PD controllers," *International Journal of Control, Automation and Systems*, vol. 7, no. 2, pp. 175–184, 2009.

- [30] S. Srivastava and V. S. Pandit, "A PI/PID controller for time delay systems with desired closed loop time response and guaranteed gain and phase margins," *Journal of Process Control*, vol. 37, no. 1, pp. 70–77, 2016.
- [31] C. Onat, S. E. Hamamci, and S. Obuz, "A practical PI tuning approach for time delay systems," *IFAC Proceedings Volumes*, vol. 45, no. 14, pp. 102–107, 2012.
- [32] C. Onat, "A new concept on PI design for time delay systems: weighted geometrical center," *International Journal of Innovative Computing, Information & Control*, vol. 9, no. 4, pp. 1539–1556, 2013.
- [33] C. Onat, "WGC based robust and gain scheduling PI controller design for condensing boilers," *Advances in Mechanical Engineering*, vol. 6, Article ID 659051, 2015.
- [34] C. Onat, "A new design method for PI-PD control of unstable processes with dead time," *ISA Transactions*, vol. 84, no. 1, pp. 69–81, 2019.
- [35] A. Shariati, H. D. Taghirad, and A. Fatehi, "A neutral system approach to H_{∞} PD/PI controller design of processes with uncertain input delay," *Journal of Process Control*, vol. 24, no. 3, pp. 144–157, 2014.
- [36] M. M. Ozyetkin, "A simple tuning method of fractional order $PI^{\lambda}-PD^{\mu}$ controllers for time delay systems," *ISA Transactions*, vol. 74, pp. 77–87, 2018.
- [37] X. Yu, F. Yang, L. Ou, Q. Wu, and W. Zhang, "General stabilization method of fractional-order $PI^{\lambda}D^{\mu}$ controllers for fractional-order systems with time delay," *International Journal of Robust and Nonlinear Control*, vol. 28, no. 16, pp. 4999–5018, 2018.
- [38] I. Kaya, "Simple and optimal PI/PID tuning formulae for unstable time delay processes," in *Proceedings of the 2017 10th International Conference on Electrical and Electronics Engineering*, pp. 847–851, IEEE, Bursa, Turkey, December 2017.
- [39] A. Visioli, "Optimal tuning of PID controllers for integral and unstable processes," *IEE Proceedings—Control Theory and Applications*, vol. 148, no. 2, pp. 180–184, 2001.